Deoxygenation and organic carbon burial in past oceans
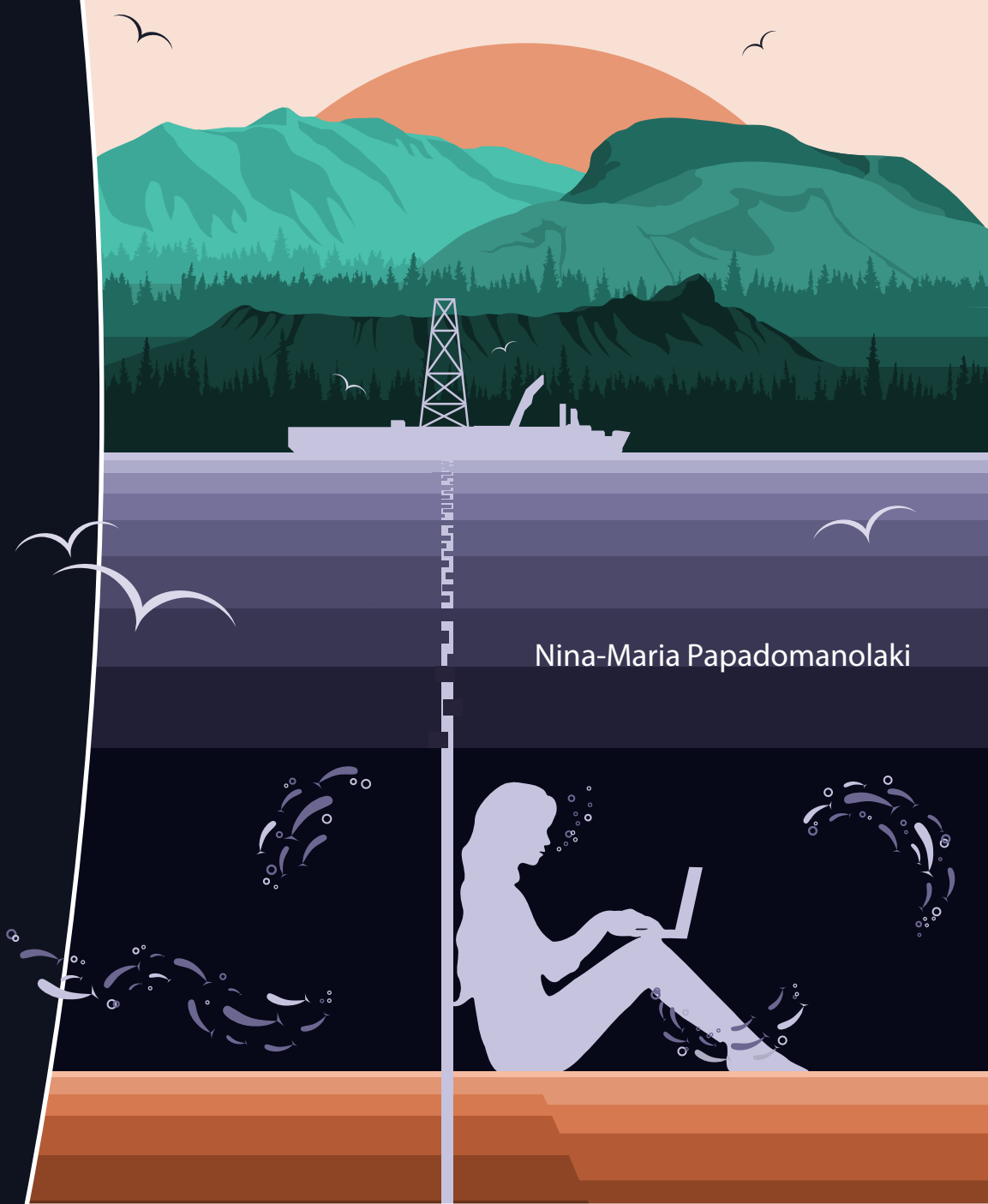
Nina-Maria Papadomanolaki

Deoxygenation and organic carbon burial in past oceans

Nina-Maria Papadomanolaki

Νίνα-Μαρία Παπαδομανωλάκη

Cover Illustrations by Nina-Maria Papadomanolaki. *Featuring Diamond Head (Hawai'i), Ben Nevis (Scotland), Ψηλορείτης (Psiloritis; Crete), the Dom (Utrecht) and the Joides Resolution.*

Cover Design by Margot Stoete and Nina-Maria Papadomanolaki.

Deoxygenation and organic carbon burial in past oceans

**Zuurstofverlies en begraving van organische koolstof
in oceanen van het verleden**

(met een samenvatting in het Nederlands)

**Αποξυγόνωση και ταφή οργανικού άνθρακα
στους ωκεανούς του παρελθόντος**

(με περίληψη στα ελληνικά)

Proefschrift

ter verkrijging van de graad van doctor aan de Universiteit Utrecht
op gezag van de rector magnificus, prof.dr. H.R.B.M. Kummeling,
ingevolge het besluit van het college voor promoties
in het openbaar te verdedigen op

donderdag 24 juni 2021 des middags te 4.15 uur

door

Nina-Maria Papadomanolaki

geboren op 3 juni 1993 te Rethymnon, Griekenland

|Promotoren|

Prof. dr. ir. Caroline. P. Slomp
Prof. dr. Appy Sluijs

You may walk and you may run
You leave your footprints all around the sun
And every time the storm and the soul wars come
You just keep on walking

"Year of the Flood"
Runrig

For my *-Heart of Olden Glory-*

CONTENTS

The paleoclimate record shouts to us that, far from being self-stabilizing, the Earth's climate system is an ornery beast which overreacts even to small nudges.
Wallace S. Broecker

1
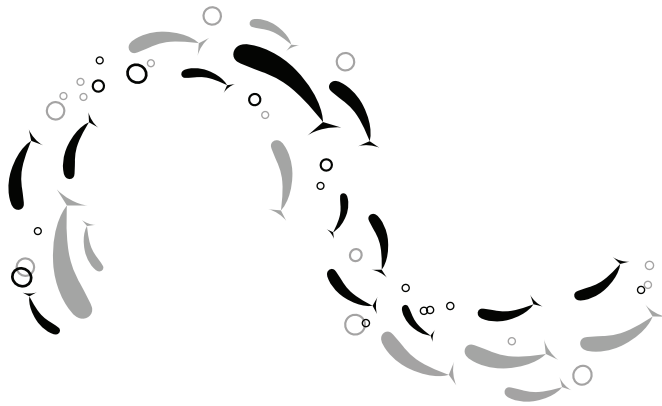
Introduction

1. MARINE CYCLES OF CARBON, OXYGEN AND PHOSPHORUS

The oceans cover more than 70% of our planet and play an important role in the biogeochemical cycles of numerous major and minor elements. Three of these elements, carbon (C), oxygen (O) and phosphorus (P), are key building blocks for life on Earth. Oxygen, in the form of O_2, is also vital for the survival of most multicellular marine organisms.

Carbon, in the form of CO_2, and O_2 is exchanged between the surface ocean and the atmosphere, while rivers also supply C, mostly as bicarbonate (HCO_3^-) (Figure 1). In the photic zone, the layer of the surface ocean that light penetrates, dissolved C is used for the production of organic matter through photosynthesis, and for the synthesis of calcium carbonate ($CaCO_3$) by calcifying organisms. The former process consumes CO_2, while the latter produces CO_2. Photosynthesis is controlled by the availability of P, which is mainly supplied as phosphate (PO_4^{3-}) by rivers, and other limiting nutrients such as nitrogen and iron, and produces O_2. Oxygen is subsequently consumed by the oxidation (degradation) of organic matter in the water column and in sediments. On geological time scales, marine sediments constitute the main sink for organic C (C_{ORG}) and $CaCO_3$, and P, which is buried as organic P (P_{ORG}) and in association with iron oxides, authigenic apatite or other minerals (e.g. Ruttenberg, 2003).

The cycles of these three major elements are partially co-dependent, as evidenced by the impact of dissolved C and P on the production of O_2 through photosynthesis, and are also greatly affected by climate change. An increase in atmospheric CO_2 will eventually translate into an increase in uptake by the surface ocean, leading to ocean acidification as ocean pH decreases (e.g. Broecker and Clark, 2001; Caldeira and Wickett, 2003; Doney *et al.*, 2009; Bates *et al.*, 2014). The uptake of CO_2 can also result in decreased carbonate (CO_3^{2-}) concentrations which, in combination with lowered pH, will reduce the production and preservation of $CaCO_3$ (e.g. Orr *et al.*, 2005).

Rising temperatures reduce the solubility of O_2 (Weiss, 1970) and affect dissolved O_2 concentrations in surface waters (Fig. 1.2). Warming also enhanced density stratification of the ocean, which can be locally intensified by freshening of surface waters due to an increase in precipitation or glacial melt (e.g. Manabe and Stouffer, 1995; Jacobs *et al.*, 2002). Stratification impedes oxygenation of sub-surface and deep waters by reducing the mixing with surface waters and deep water formation (e.g. Wilkin *et al.*, 1997; Sarmiento *et al.*, 1998; Matear *et al.*, 2000; Keeling and Garcia, 2002), whereas the consumption of O_2 through organic matter degradation may be favored in a warmer climate (e.g. Marsay *et al.*, 2015; Lønborg *et al.*, 2018). A reduction in O_2 availability favors the preservation and burial of C_{ORG}, while it also enhances the regeneration of P from organic matter and the recycling of P from sediments back to the water column.

The impact of human-induced climate change on ocean biogeochemistry is already becoming apparent. Since the start of the Industrial Revolution approximately 30% of human CO_2 emissions have been taken up by the surface ocean (Sabine *et al.*, 2004; Sabine and Feely, 2007; Khatiwala *et al.*, 2013; De Vries, 2014). The projected decrease in pH for the 21st century is about 0.3 – 0.4 units and marine CO_3^{2-} concentrations are expected to drop by 50%, within the same timeframe (Orr *et al.*, 2005). There is increasing evidence that biological calcification

will be inhibited, potentially affecting several marine organisms including marine primary producers (Doney *et al.*, 2009; Hendriks *et al.*, 2010; Harvey *et al.*, 2013).

A. CARBON AND OXYGEN CYCLES
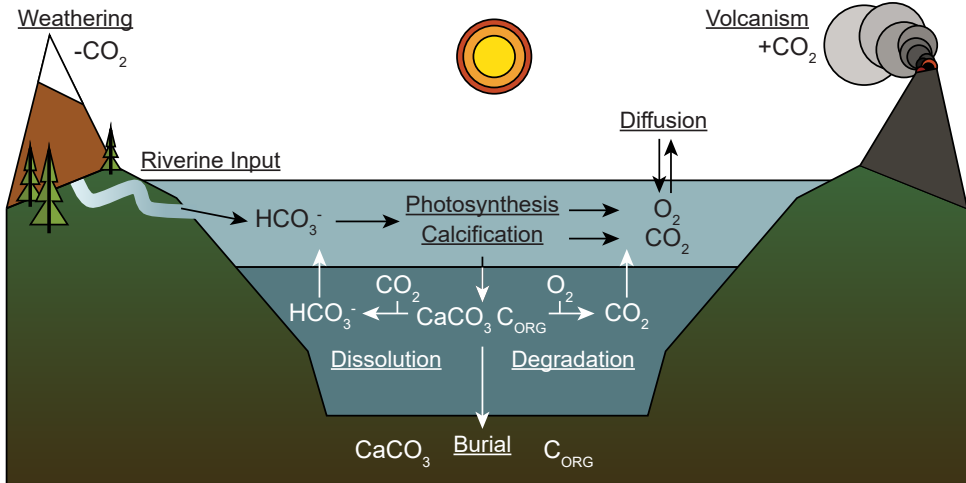
B. PHOSPHORUS CYCLE
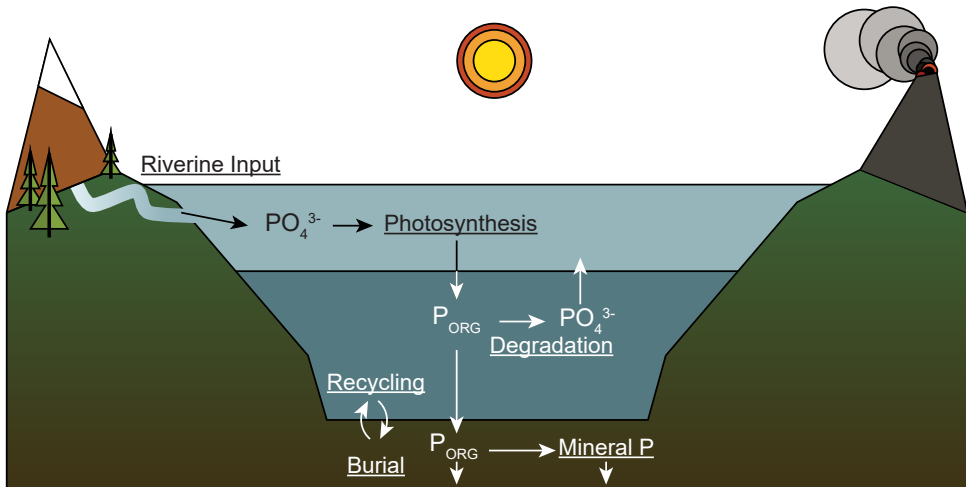
Figure 1.1| Major processes in the biogeochemical cycles of carbon (C) and oxygen (O_2) (A), and phosphorus (P) (B) in the ocean – atmosphere system. Arrows indicate the direction of fluxes. For details see Sarmiento and Gruber (2006) and Ruttenberg (2003). Symbols are explained in the text.
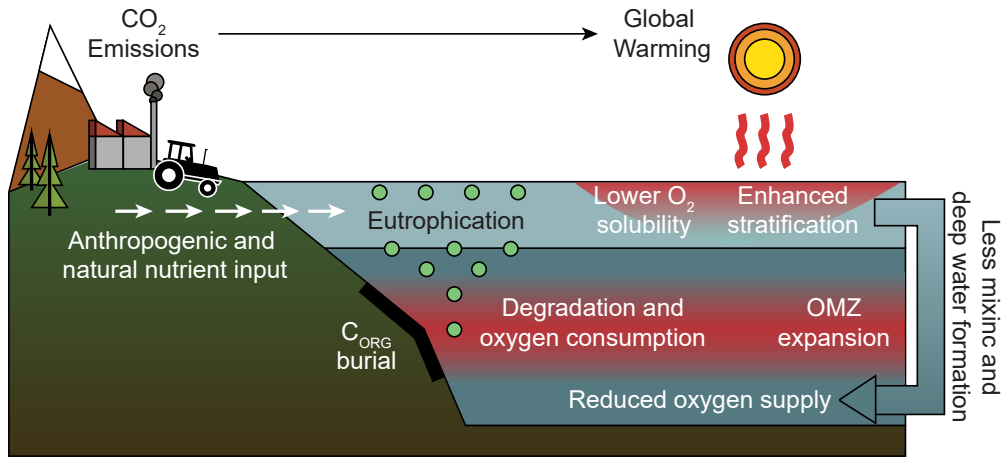
Figure 1.2| Schematic illustration of processes affecting, directly and indirectly, the O_2 inventory of the continental shelf and open ocean (modified from Stramma *et al.*, 2010). OMZ: Oxygen Minimum Zone.

The open ocean has lost ~2% of its O_2 inventory over the last 50 years (Schmidtko *et al.*, 2017) and naturally occurring Oxygen Minimum Zones (OMZs) are expanding (Stramma *et al.*, 2012). This follows from the increased outgassing of O_2 from the surface ocean (Bopp *et al.*, 2002), increased stratification (Li *et al.*, 2020) and a slow-down in Atlantic Meridional Overturning Circulation (e.g. Caesar *et al.*, 2021). Coastal hypoxia ([O_2] ≤63 µmol liter^{-1}) has spread exponentially since the 1960s as sewage and fertilizer fluxes into the ocean favor eutrophication (Diaz and Rosenberg, 2008), which causes increased production of organic matter, followed by increased O_2 consumption as the organic matter is remineralized (e.g. Rosenberg *et al.*, 1990). The current trends in ocean deoxygenation are projected to continue unless significant reductions to greenhouse gas emissions and nutrient discharges are made (e.g. Breitburg *et al.*, 2018), and the combined effects of deoxygenation and acidification will impose limits to the distribution and diversity of marine biota (Steckbauer *et al.*, 2020).

2. FEEDBACKS WITHIN THE CLIMATE SYSTEM

The lifetime of CO_2 in the atmosphere, the magnitude of the resulting climate system perturbation and the subsequent response in marine biogeochemistry, all rely heavily on the influence of feedbacks (IPCC, 2013). Feedback loops constitute processes wherein the consequence of an initial system change reduces the strength of (negative feedback; Fig. 3a) or amplifies (positive feedback; Fig. 3b) that initial perturbation. The large range of climate model projections for the future is caused largely by the presence of these climate feedbacks and the uncertainty surrounding them (Cubasch and Cess, 1990). Three key feedbacks are discussed in the context of this thesis: the terrestrial weathering feedback, the drawdown of CO_2 through C_{ORG} burial and the effect of redox-driven P recycling on deoxygenation.

The weathering of terrestrial calcium and magnesium silicate rocks is one of the most important feedbacks with the Earth system (Fig. 3c) (Ebelmen, 1845; Urey, 1952; Berner and

A. NEGATIVE FEEDBACK
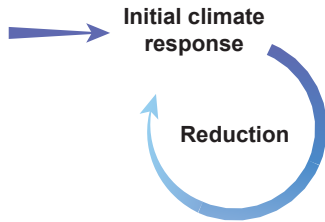
C. EXAMPLE 1: WEATHERING
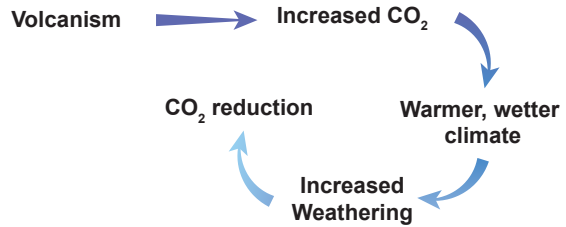
D. EXAMPLE 2: C_{ORG} BURIAL
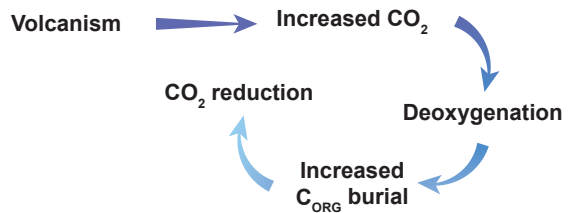
B. POSITIVE FEEDBACK
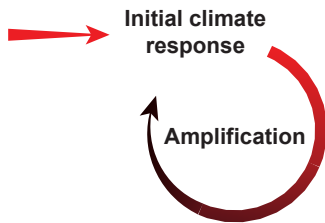
E. EXAMPLE 3: P RECYCLING
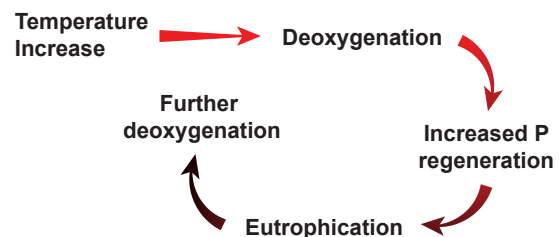
Figure 1.3| Schematic representation for the functioning of negative (A; blue) and positive (B; red) feedbacks in the climate system (left), and examples (right). Progressively lighter colors represent reduction in intensity, while progressively darker colors indicate amplification. The first negative feedback (C) is based on work by Ebelmen (1845) and Urey (1952), the second negative feedback (D) on Slomp and Van Cappellen (2007) and Komar and Zeebe (2017), and the positive feedback (E) on Van Cappellen and Ingall (1994).

Berner, 1997). High CO_2 concentrations and a warmer, wetter climate promote weathering, which in turn draws down CO_2. Due to the dependence of this process on a number of parameters such as temperature and soil pH, its exact response under greenhouse conditions is a subject of ongoing research (e.g. Winnick and Maher, 2018). The timescale of the weathering feedback is very long, making it a relatively slow climate feedback. An initial estimate of the timescale was on the order of $300 - 400 \times 10^3$ years (kyr) (Sundquist, 1991), but currently it is thought to be $170 - 380$ kyr (Zachos *et al.*, 2005; Colbourn *et al.*, 2015).

The production of C_{ORG} constitutes a second negative feedback on atmospheric CO_2 concentrations (Fig. 3d). Elevated atmospheric CO_2 concentrations favor the weathering of apatite rocks (Guidry and Mackenzie, 2000), stimulating the input of P to the ocean, the production of C_{ORG} and deoxygenation. As reducing conditions favor the preservation of C_{ORG} in marine sediments (Ingall *et al.*, 1993; Hartnett *et al.*, 1998), this can lead to a significant accumulation of C_{ORG} in sediments, leading to a net loss of atmospheric CO_2 (Walsh *et al.*, 1981; Ingall and Jahnke, 1997). The burial of C_{ORG} is a more rapid feedback on the C cycle than weathering, in the range of tens of thousands of kyr (e.g. Komar and Zeebe, 2017).

The redox-driven recycling of P from marine sediments functions as a positive feedback on dissolved O_2 concentrations (Fig. 3e). Under anoxic conditions ($[O_2]$ = 0) the retention of P in sediments, as P_{ORG} or iron-bound P, is generally reduced and recycling to the water column increases (e.g. Gächter and Meyer, 1993; Ingall *et al.*, 1993; Ingall and Jahnke, 1997; Slomp *et al.*, 2002). Subsequently, the increased availability of P will promote surface water eutrophication and enhance the production of organic matter. Degradation of the additional organic matter will consume O_2, enhancing bottom water deoxygenation and intensifying the release of P from sediments. The response time of ocean biogeochemistry depends on the residence time of P in the ocean, which is estimated between ~9 and 100 kyr (Froelich *et al.*, 1982; Broecker, 1982; Ruttenberg, 1993; Wallmann, 2003; Ruttenberg, 2003).

3. PAST PERTURBATIONS OF OCEAN BIOGEOCHEMISTRY

Current emissions of greenhouse gasses are without precedent in the last 66 million years (Myr), pushing the climate system into a state to which our species is unaccustomed (e.g. IPCC, 2013; Zeebe *et al.*, 2016). Yet, while the cause (i.e. human activity) is novel, Earth's climate and oceans have experienced many upheavals during the past 4.5 billion years. The study of the Earth's past, and specifically intervals experiencing similar changes to those projected for the future, allows us to assess the impact of global feedbacks on the onset and recovery of changes in the C cycle, climate and marine biogeochemistry (e.g. Burke *et al.*, 2018).

Past triggers of changes in the global C cycle and climate include the emplacement of Large Igneous Provinces (LIPs) (e.g. Turgeon and Creaser, 2008), seafloor spreading (e.g. Kasting and Richardson, 1985), methane hydrate destabilization (e.g. Dickens *et al.*, 1997) and variations in the Earth's orbital cycles (e.g. Ganopolski and Calov, 2011), as well as modes of internal climate variability, such as the Pacific El Niño (e.g. Larkin and Harrison, 2005) and the North Atlantic Oscillation (e.g. Hurrel and Deser, 2010). As a result, CO_2 levels have been as low as 100 ppm and as high as 2000 – 5000 ppm in the last 450 Myr (Foster *et al.*, 2017) and fluctuated between ~170 – 300 ppm over the last 800 kyr (Lüthi *et al.*, 2008). Mean ocean pH has not been constant in the past, falling well below the pre-industrial value of ~8.15 (Hönisch *et al.*, 2012) and several C cycle and climate perturbation events have resulted in instances of ocean acidification (e.g. Zachos *et al.*, 2005; Trecalli *et al.*, 2012; Bauer *et al.*, 2017), with a potentially devastating impact on marine fauna such as deep-sea benthic foraminifera (e.g. Thomas and Schakleton, 1996).

Multiple intervals of widespread deoxygenation have been identified throughout Earth's history (e.g. Schlanger and Jenkyns, 1976; Berry and Wilde, 1978; Condie *et al.*, 2001; Jenkyns, 2010; Sluijs *et al.*, 2014; Cheng *et al.*, 2020), often coincident with the deposition of C_{ORG}-rich sediments (e.g. Arthur *et al.*, 1990; Jenkyns, 2010; Cartapanis *et al.*, 2016). Increased temperatures (e.g. McInerney and Wing, 2011; Ullmann *et al.*, 2020) and increased precipitation and runoff (e.g. van Helmond *et al.*, 2014; Carmichael *et al.*, 2017) promoted stratification and limited O_2 supply to surface and deep water masses (e.g. Sluijs *et al.*, 2008).

In addition to such global events, instances of basinal deoxygenation can also leave traces in the geological record. The Eastern Mediterranean sapropels are examples of organic-rich deposits that are the result of such basin-scale anoxia (e.g. Rohling, 1994). The rhythmical reoccurrence of these organic-rich sedimentary layers alludes to their main cause: the intensification of the North African monsoon as a result of changes in Earth's orbital cyclicity (e.g Rossignol-Strick *et al.*, 1985; Hilgen, 1991; Gasse, 2000). The strengthened monsoon enhanced riverine discharge from the Nile, promoting stratification and circulation slowdown, while also supplying nutrients for primary productivity (e.g. Rohling and Hilgen, 1991; Rohling, 1994; Calvert and Pedersen, 1992). Bottom water conditions during sapropel deposition resulted in an increased efflux of P from sediments (e.g. Slomp *et al.*, 2004; Reed *et al.*, 2011).

4. CASES OF PAST DEOXYGENATION IN THIS THESIS

It is vital to understand the aforementioned climate feedbacks and their impact on ocean biogeochemistry over a range of temporal and spatial scales. This thesis focuses on three key systems and time intervals, in particular: the Holocene Baltic Sea and the ocean during the Paleocene – Eocene Thermal Maximum and Cretaceous Oceanic Anoxic Event 2. With this selection I cover different geological time intervals — from thousands (Holocene) to millions (Paleogene and Cretaceous) of years ago — and event durations — from hundred to hundreds of thousands of years. Additionally, the Holocene Baltic Sea is an example of deoxygenation in a single basin (e.g. Zillén *et al.*, 2008), whereas the PETM and OAE2 were intervals of widespread deoxygenation (e.g. Dickson, 2017).

4.1 Holocene: The Baltic Sea

Located in Northern Europe, the Baltic Sea is a landlocked, brackish-marine basin with a permanently stratified water column and restricted exchange with the open ocean (Fig. 1.4) (Stigebrandt and Gustafsson, 2003; Döös *et al.*, 2004). As a result, the deeper areas in particular are preconditioned to bottom-water deoxygenation. Saline inflows from the North Sea periodically oxygenate bottom waters (Matthäus and Franck, 1992), but also strengthen stratification (Gerlach, 1994; Conley *et al.*, 2002). Furthermore, the oxygenation state of Baltic Sea is negatively affected by the warming and eutrophication caused by human activities, making it the world's largest human-induced 'dead zone' (Diaz and Rosenberg, 2008; Gustafsson *et al.*, 2012; Carstensen *et al.*, 2014). Despite reductions in terrestrial nutrient inputs since the 1980s (HELCOM, 2007), P concentrations in the Baltic Sea have not decreased due to recycling of P in the system (Conley *et al.*, 2002). As a result of the abundant

A. Holocene Baltic Sea

B. Late Paleocene - Early Eocene

B. Late Cretaceous (Cenomanian – Turonian)
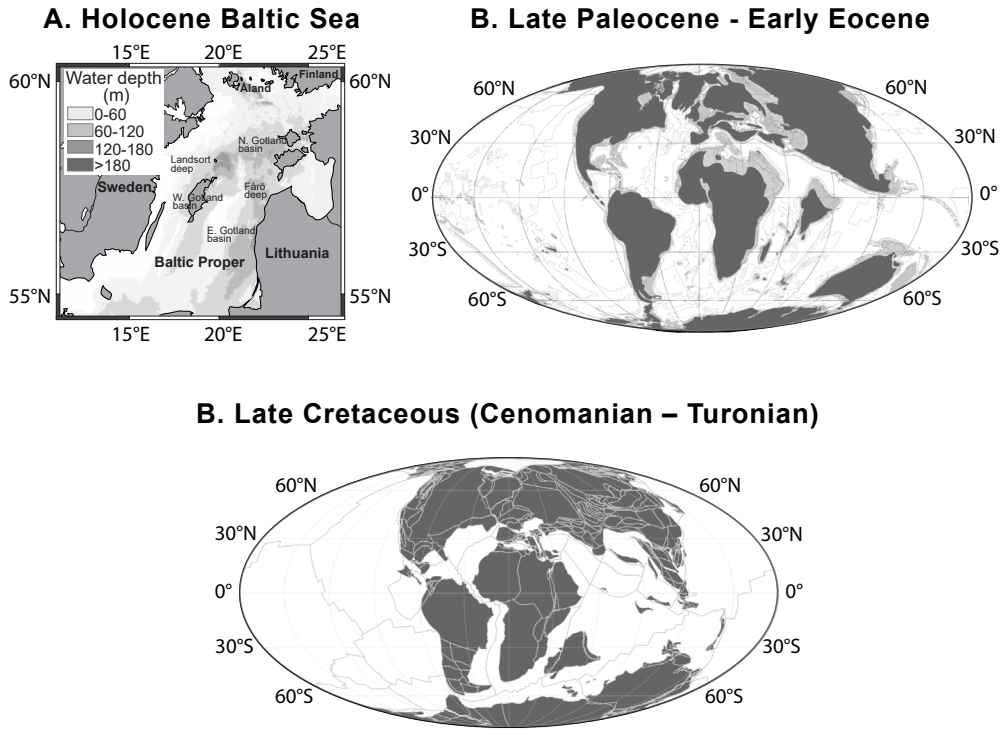
Figure 1.4| Maps of the central Baltic Sea during the Holocene (A) and the global continental configuration for the Late Paleocene and Early Eocene (B; modified from Marwick, 2007), and the Late Cretaceous (C; map created using GPlates and 94 Ma settings; with the continental polygons and rotation frame of Matthews *et al.*, 2016).

presence of P in surface waters, cyanobacterial blooms persist and contribute to the rain of C_{ORG} to sediments (Eilola *et al.*, 2009; Funkey *et al.*, 2014).

The modern, brackish-marine Baltic Sea was established in the last 10,000 years, following sea level rise at the end of the Last Glacial Maximum and intrusion of marine waters from the North Sea into the freshwater Ancylus Lake (Andrén *et al.*, 2011 and references therein). Laminated, C_{ORG}-rich sediments deposited within this interval indicate that the Baltic Sea has experienced two pre-modern stages of widespread hypoxia (e.g. Andrén *et al.*, 2000). These stages occurred between 8 – 4 kyr ago (ka) and 1.2 – 0.75 ka, coinciding with two separated intervals of warming that affected mainly the mid- and high latitudes pf the Northern Hemisphere termed the Holocene Thermal Maximum (HTM) and the Medieval Climate Anomaly (MCA) (e.g. Wanner *et al.*, 2008; Zillén *et al.*, 2008; Mann *et al.*, 2009). The occurrence of hypoxia during the HTM is mainly attributed to the establishment of a halocline as saline North Sea waters entered the freshwater basin and high primary productivity (Emeis *et al.*, 2003; Funkey *et al.*, 2014). The younger hypoxic period of the MCA

has been linked to higher temperatures (Kabel *et al.*, 2012) as well as the growing human population which led to intensified agriculture and P input from land, and eutrophication (Zillén *et al.*, 2008; Funkey *et al.*, 2014).

4.2 Paleogene: The Paleocene-Eocene Thermal Maximum

The Paleocene-Eocene Thermal Maximum (PETM; 56 Ma) (Fig. 4) was a geologically short (≥200 kyr; e.g. Röhl *et al.*, 2007; Zeebe and Lourens, 2019) C cycle perturbation (McInerney and Wing, 2011 and references therein) with increased temperatures (e.g. Fricke *et al.*, 1998; Wing *et al.*, 2005; Frieling *et al.*, 2017) and ocean acidification (e.g. Zachos *et al.*, 2005; Gibbs *et al.*, 2010). In addition to these changes in the climate system, the PETM is also associated with faunal turnover, such as the large scale extinction of deep sea benthic foraminifera (e.g. Thomas, 1989; 2007). Sediments deposited during the PETM record a large negative $\delta^{13}C$ excursion, associated with the addition of a significant mass of ^{13}C-depleted C to the ocean-atmosphere system (Dickens *et al.*, 1995; McInerney and Wing, 2011 and references therein). Potential source reservoirs for this C are methane hydrates (e.g. Dickens *et al.*, 1995; 1997), possibly destabilized by orbitally controlled warming (Sluijs *et al.*, 2007; Lunt *et al.*, 2011; Zeebe and Lourens, 2019), thermogenic methane (Svensen *et al.*, 2004) and volcanism (e.g. Bralower *et al.*, 1997).

Several lines of evidence indicate that ocean deoxygenation spread during the PETM, especially in restricted basins such as the Arctic Ocean and peri-Tethys (Sluijs *et al.*, 2014; Yao *et al.*, 2018). Causes for this include warming and salinity stratification (Sluijs *et al.*, 2008), and increased primary and export production of organic matter (e.g. Bains *et al.*, 2000; Gibbs *et al.*, 2006; Ma *et al.*, 2014). These processes, in combination with higher sedimentation rates, led to substantial accumulation of C_{ORG} in marine sediments, in particular in marginal settings (e.g. Sluijs *et al.*, 2008; John *et al.*, 2008; Dickson *et al.*, 2014; Dunkley Jones *et al.*, 2017). This burial of ^{13}C-depleted marine C_{ORG} is hypothesized to have contributed to the rapid recovery of $\delta^{13}C$ and the C cycle to their background state at the end of the PETM (Bowen and Zachos, 2010; Gutjahr *et al.*, 2017; Komar and Zeebe, 2017).

4.3 Cretaceous: Oceanic Anoxic Event 2

The Cenomanian-Turonian Oceanic Anoxic Event 2 (OAE2; ~94 Ma) was among the largest C cycle perturbations of the Mesozoic and is the most extensively studied OAE (Schlanger and Jenkyns, 1976; Arthur *et al.*, 1990; Jenkyns, 2010). The outgassing of CO_2 during the emplacement of Large Igneous Provinces (LIPs) and from mid-ocean spreading centers (e.g. Ingram *et al.*, 1994; Sinton and Duncan, 1997; Jones and Jenkyns, 2001; Turgeon and Creaser, 2008), led to a rise in atmospheric CO_2 (Barclay *et al.*, 2010) and global temperatures (e.g. Voigt *et al.*, 2004; Forster *et al.*, 2007; van Helmond *et al.*, 2014a). The consequent intensification of weathering (von Strandmann *et al.*, 2013; Jenkyns *et al.*, 2017) provided nutrients that supported increased primary productivity (e.g. Sepúlveda *et al.*,2009; Trabucho-Alexandre *et al.*, 2010; Monteiro *et al.*, 2012; Ruvalcaba-Baroni *et al.*, 2014), while warming and an intensified hydrological cycle (e.g. van Helmond *et al.*, 2014a; 2015) strengthened stratification. As a consequence, anoxic and euxinic conditions spread (Owens *et al.*, 2013; Dickson *et al.*, 2016; Clarkson *et al.*, 2018), especially in the restricted proto-North Atlantic and continental seas such as the Western Interior Seaway (e.g. van Helmond *et al.*, 2014a; b; 2015).

The reducing conditions and increased primary productivity during OAE2 supported the deposition of sediments with high ^{13}C-depleted C_{ORG} content (e.g. Takashima *et al.*, 2006). The widespread increase in C_{ORG} burial led to an exogenic C pool depleted in ^{12}C and (strongly) enriched in ^{13}C, and a positive excursion in sedimentary δ^{13}C records globally (Jenkyns, 2010). The increased recycling of P from reducing sediments sustained anoxia and C_{ORG} burial, extending the duration of OAE2 (Mort *et al.*, 2007; Tsandev and Slomp, 2009; Kraal *et al.*, 2010). The deposition of large amounts of C_{ORG} in marine systems is also proposed to have caused a decrease in atmospheric CO_2 (Sinninghe Damsté *et al.*, 2008; 2010; Jarvis *et al.*, 2011). This drawdown of CO_2 and/or changes in circulation (Zheng *et al.*, 2013; 2016; O'Connor *et al.*, 2020) were associated with one or more pulses of cooling, including the Plenus Cold Event (Gale and Christensen, 1996; O'Connor *et al.*, 2020 and references therein), and likely re-oxygenation of bottom waters (Friedrich *et al.*, 2006; Van Helmond *et al.*, 2014b; Clarkson *et al.*, 2018; Sweere *et al.*, 2020).
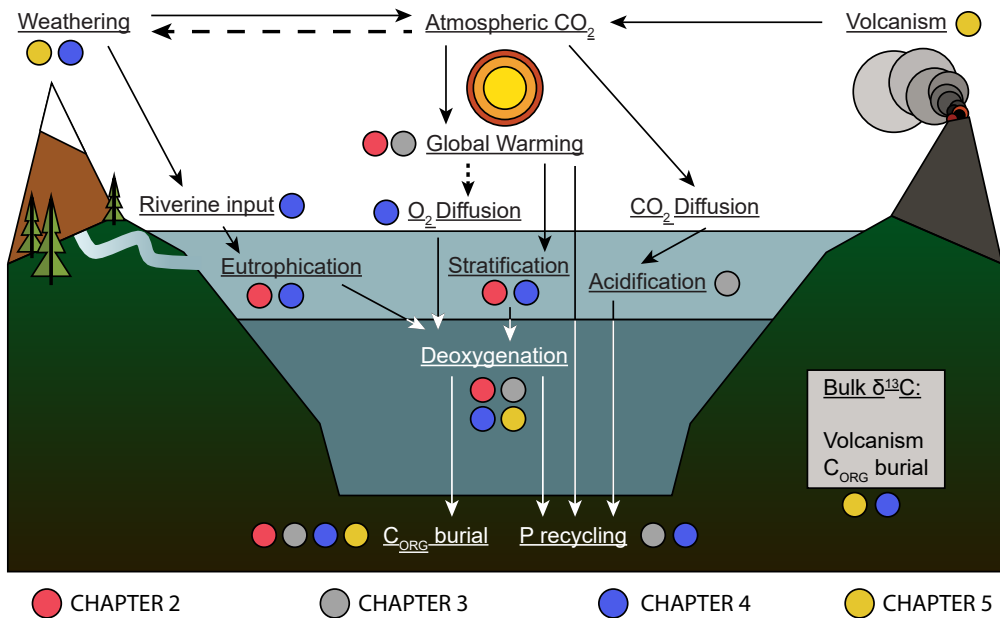
Figure 1.5| Schematic representation of the processes, feedbacks and C cycle components studied in this thesis. Solid arrows represent process intensification and dashed arrows represent reduction. Boxes indicate the chapters in which these processes are discussed in detail.

5. SCOPE AND OUTLINE OF THESIS

Within the content of this thesis, I aim to qualitatively and quantitatively assess the driving mechanisms and consequences of marine deoxygenation and C_{ORG} burial in a greenhouse world (Fig. 1.5). The focus lies on instances of locally and globally enhanced deoxygenation (Fig. 1.6): the Holocene Baltic Sea (**Chapter 2**), three sapropels deposited
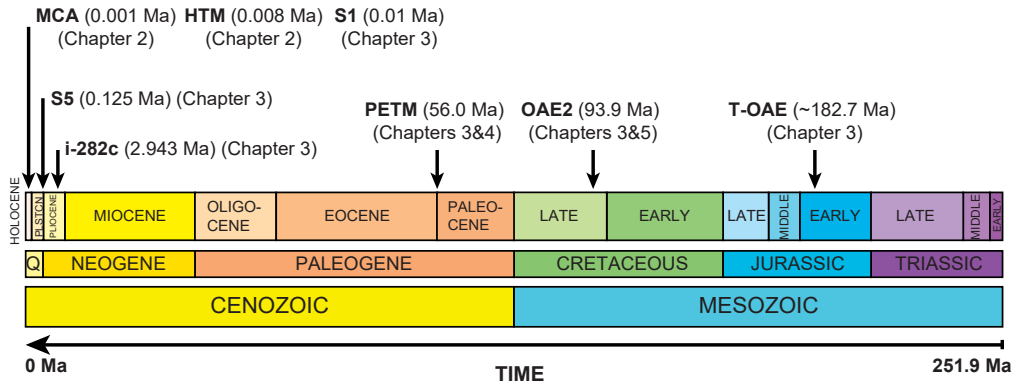
Figure 1.6| The geological time scale (Gradstein *et al.*, 2012) spanning the Cenozoic and Mesozoic, the two Eras that encompass the events studied in this thesis. Arrows indicate the position of the studied intervals and the corresponding thesis chapters. The oldest intervals are on the right and the youngest on the left. PLSTCN: Pleistocene.

in the Pliocene and Quaternary Mediterranean Sea (**Chapter 3**), the PETM (**Chapters 3 and 4**), OAE2 (**Chapters 3 and 5**) and Toarcian Oceanic Anoxic Event (**Chapter 3**). Key questions I aim to answer are the causes of deoxygenation on a local (**Chapter 2**) and global (**Chapter 4**) scale, the controls of P mineral formation on P recycling under anoxia (**Chapter 3**) and the global impact of enhanced redox-driven P recycling (**Chapters 3 – 5**), and the effect of redox-driven C_{ORG} burial on the global carbon cycle (**Chapters 4 and 5**).

In order to unravel the causes of extensive deoxygenation and its impact on C_{ORG} burial, I paired new geochemical and palynological sediment analyses, with the analysis of existing data sets and biogeochemical box modelling. Samples from international cruises (DSDP, ODP and IODP) and outcrops, for the PETM and Holocene Baltic Sea, were analyzed for their C_{ORG} content and total elemental composition. Specifically, the content of trace metals was used to reconstruct changes in redox conditions for these sediments (Brumsack, 2006; Tribovillard *et al.*, 2006). For the Holocene Baltic Sea, the temperature evolution was assessed using TEX_{86} and the abundance and diversity of cysts produced by dinoflagellates, single-celled eukaryotic organisms, were primarily quantified to reconstruct variations in surface salinity (e.g. Zonneveld *et al.*, 2013). The recycling of P relative to C_{ORG} was assessed for OAE2, the PETM, sapropels, as well as the modern deep, euxinic Black Sea and the Arabian Sea Oxygen Minimum Zone, based on a data compilation of the C_{ORG}/P_{TOT} proxy (Ingall *et al.*, 1993; Algeo and Ingall, 2007).

Changes in marine biogeochemical cycles during the PETM and OAE2 were investigated using two separate box-models. I built a new biogeochemical model, with an ocean-box configuration specific for the PETM, which covers the cycles of C_{ORG}, O_2 and P in the deep ocean and along continental margins. This model was used specifically to investigate the mechanisms causing widespread deoxygenation and C_{ORG} burial during the PETM. A second model, the long-term ocean-atmosphere sediment C cycle reservoir model (LOSCAR-P;

Zeebe *et al.*, 2009; 2012; Komar and Zeebe, 2017), was used to test the response of bulk marine C isotope ratios to enhanced light C input and burial.

6. THESIS SYNOPSIS

The two pre-modern hypoxic intervals in the Baltic Sea are well described and documented (Zillén *et al.*, 2008), but their cause(s), particularly potential climatic forcing, remains heavily debated. C**hapter 2** investigates the role and relative timing of salinity stratification, increased temperature and nutrient loading as causes for the anoxic conditions in the deepest basin of the Baltic Sea (Landsort Deep) during the Holocene Thermal Maximum (HTM) and Medieval Climate Anomaly (MCA). At the start of the HTM, melting ice sheets and rising sea levels caused the intrusion of saline marine waters from the North Sea into the still freshwater Baltic Sea. Dinoflagellate cyst abundance and morphology reconstruct a major increase in salinity during peak anoxia in the Landsort Deep. A coeval increase in temperature underlines the importance of reduced O_2 solubility and temperature stratification, together with salinity stratification, in reducing the O_2 supply to the deep basin. The anoxia resulted in the accumulation of dark, C_{ORG}-rich sediments during the HTM. The bottom waters became oxygenated again when salinity stratification weakened and the climate cooled again. In contrast to the HTM, the occurrence of anoxia during the MCA appears to have been mainly linked to warm temperatures. This study highlights the fact that climate change will intensify deoxygenation in the Baltic Sea, and coastal seas in general, likely counteracting the impact of reduced nutrient input.

The Baltic Sea is a modern basin where deoxygenation has greatly enhanced P recycling (e.g. Mort *et al.*, 2010). Yet proxy studies have shown that P recycling was also increased during certain hypoxic intervals in the geological past (Algeo and Ingall, 2007). **Chapter 3** explores why P recycling during key greenhouse and deoxygenation intervals exceeded the modern process in magnitude. Traditionally, enhanced recycling of P is only linked to low O_2 concentrations, which are known to drive the preferential regeneration relative to C_{ORG}, and the dissolution of iron oxides. Such changes in P recycling can be traced back through sediment ratios of C_{ORG}/P_{ORG} (for the last few millions of years) and C_{ORG}/P_{TOT}. While high values of C_{ORG}/P_{TOT} are observed in sediments of the modern Black Sea and Arabian Sea OMZ, those in ancient sediments exceed the modern range, as observed, for example, for the T-OAE, OAE2 and two sapropels (i-282c and S5). Geochemical calculations for the saturation state of past porewaters, show that high temperatures and lower pH, which were typical for the studied organic-rich sediments of the past, combined with low O_2 concentrations negatively impact the formation of carbonate fluorapatite, the main long-term sink for P. This presents a warning in view of the continuing expansion of low-O_2 areas in the modern ocean, coupled with ongoing acidification and warming as a consequence of human-induced climate change.

Deoxygenation during the PETM was less intense and extensive in comparison to OAE2 (Owens *et al.*, 2013; Dickson, 2017; Clarkson *et al.*, 2018; Yao *et al.*, 2018; Clarkson *et al.*, 2021), but deoxygenation was likely widespread, on continental shelves in particular (Sluijs *et al.*, 2014). Most C_{ORG} burial takes place along continental margins (e.g. Hedges and Keil, 1995; Burdige, 2005) and low O_2 conditions promote this process (e.g. Ingall *et al.*, 1993; Hartnett *et*

al., 1998). Thus the rapid initial recovery of δ^{13}C at the end of the event (Bowen and Zachos, 2010) may have been aided by C_{ORG} accumulation in marine sediments. **Chapter 4** studies the spatial and temporal extent of increased primary productivity and deoxygenation, and their combined effect on C_{ORG} burial, during the PETM. The work in this chapter shows that productive, low-O_2 environments occurred mostly on the continental margins and in restricted basins, and persisted into the recovery phase. The resulting increase in C_{ORG} burial was also focused in these marginal environments and of a magnitude sufficient to affect the bulk δ^{13}C signal of the ocean. The large amount of C_{ORG} buried during the PETM also indicates that a large amount of light carbon must have been emitted to produce the plateau in δ^{13}C records.

Carbon-isotope records are used to reconstruct changes in the exogenic carbon cycle. Transient negative excursions may provide quantitative assessments of the mass of ^{13}C-depleted carbon injected into the global exogenic carbon pool (e.g., Dickens *et al.*, 1997; Dickens, 2001), while positive excursions can be used to constrain the mass of ^{13}C-depleted C_{ORG} burial (e.g. Nederbragt *et al.*, 2004; Owens *et al.*, 2018). In either case, it is important to consider the effect of both CO_2 emissions and removal on δ^{13}C. In **Chapter 5**, we explore the links between Large Igneous Province volcanism, C_{ORG} burial and the carbon isotopic record for OAE2. The temporal proximity of the emplacement of one or more LIPs and the evidence for increased mantle input of elements such as osmium is the basis for the hypothesis that increased volcanism triggered the spread of anoxia and the geochemical cascade of OAE2. In this study, we develop a volcanic CO_2 emission and C_{ORG} burial scenario for OAE2 using the model LOSCAR-P that optimally reproduces the key features of the OAE2 δ^{13}C and CO_2 record. Our best-fit scenario implies a two-pulse volcanism scenario and redox-sensitive C_{ORG} and P burial. The combination of high C_{ORG} burial and an intermittent decrease in LIP activity results in the documented drop in atmospheric CO_2, followed by the characteristic negative Plenus isotopic excursion. These features provide the first combined constraints on the magnitude, rate and duration of volcanism and C_{ORG} burial, consistent with δ^{13}C and CO_2 records for OAE2.

7. CONCLUDING REMARKS
In summary, this thesis provides a framework for the causes and consequences of marine deoxygenation and C_{ORG} burial. Warming, both regional (**Chapter 2**) and global (**Chapters 3 and 4**), promotes the loss of dissolved O_2 from ocean waters and the accumulation of C_{ORG} in marine sediments. Deoxygenation enhances P recycling relative to C_{ORG}. This recycling was more pronounced during greenhouse periods than at present (**Chapters 2 – 4**). During the PETM (**Chapter 4**) and OAE2 (**Chapter 5**), the geochemical cascade leading to the buildup of C_{ORG} in marine sediments was caused by increased CO_2 emissions. The burial of C_{ORG} had a profound effect on the exogenic carbon cycle, resulting in the drawdown of CO_2 from the atmosphere.

The findings presented in this thesis provide indications for the possible future evolution of marine biogeochemical cycles. The projected increase in temperature (IPCC, 2013) will lead to loss of O_2 from open ocean waters, while it may also hinder the recovery of coastal areas (e.g. the Baltic Sea) from deoxygenation, upon nutrient input reductions (**Chapter**

2). Acidification will not only affect calcifying organisms and marine alkalinity, but may enhance P recycling and, hence, eutrophication (**Chapter 3**). As the oceans warm and $CaCO_3$ dissolution spreads into more areas of the deep ocean (e.g. Sulpis *et al.*, 2018), P recycling from deep marine sediments may increase. The impact of C_{ORG} burial on atmospheric CO_2 (**Chapters 4 and 5**), even during a mild deoxygenation event such as the PETM (**Chapter 4**), underlines the importance of including this process and its causes in global biogeochemical and climate models when assessing the lifetime of our emissions in the atmosphere.

1

To aim for the highest point is not the only way to climb a mountain.
Nan Shepherd – The Living Mountain

2
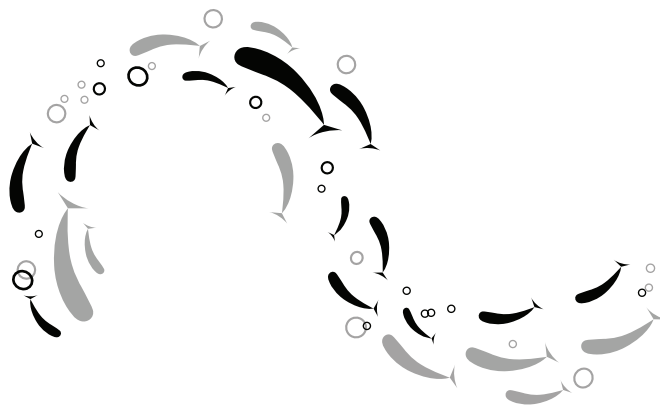
Controls on the onset and termination
of past hypoxia in the Baltic Sea

Controls on the onset and termination of past hypoxia in the Baltic Sea

Nina M. Papadomanolaki, Nikki Dijkstra, Niels A.G.M. van Helmond, Mathilde Hagens, Thorsten Bauersachs, Ulrich Kotthoff, Francesca Sangiorgi, Caroline P. Slomp

ABSTRACT

The Baltic Sea is currently the largest marine hypoxic ($O_2 < 2$ mg L^{-1}) 'dead zone' following excessive nutrient input from anthropogenic activities over the past century. Widespread hypoxia has previously developed in the Baltic Sea during the Holocene Thermal Maximum (HTM; 8 — 4 ka before present; BP) and the Medieval Climate Anomaly (MCA; 1.4 — 0.7 ka BP). Here we study the mechanisms that contributed to the onset and termination of this past hypoxia using geochemical and marine palynological data from a sediment record retrieved from the Landsort Deep during IODP Expedition 347 (Site M0063). Dinoflagellate cyst records and TEX_{86}^{L}-based sea surface temperature reconstructions indicate a major increase in salinity and temperature prior to and across the onset of the HTM hypoxic interval, underlining the importance of both temperature and salinity stratification in providing conditions conducive to the onset of hypoxia. Both salinity and temperature decline during the termination of the HTM hypoxic interval. In contrast, we find no evidence for significant changes in surface salinity during the MCA hypoxic interval and both the onset and termination of hypoxia appear to have been primarily driven by changes in temperature. Our results indicate that temperature and salinity changes were key drivers of past hypoxia in the Baltic Sea and imply that ongoing climate change will delay recovery from the modern, nutrient-driven hypoxic event in the Baltic Sea.

1. INTRODUCTION

Hypoxia, i.e. dissolved oxygen concentrations in seawater <2 mg L^{-1} (e.g. Rabalais *et al.*, 2010), has been a recurring natural phenomenon in marine environments throughout Earth's history (e.g. Jenkyns, 2010). In the past decades, anthropogenic activities and global climate change have led to widespread hypoxia in coastal waters with harmful consequences for marine life (Diaz and Rosenberg, 2008).

The modern Baltic Sea is a key example of such a human-induced dead-zone (e.g. Conley *et al.*, 2009; Carstensen *et al.*, 2014a). Current efforts to mitigate the effects of hypoxia focus on reducing nutrient inputs from agriculture and sewage (Andersen *et al.*, 2017). In addition, elevated temperatures contribute to the spread of hypoxia in multiple ways, e.g. by reducing the solubility of oxygen and stimulating marine productivity. Seawater temperatures are expected to increase further in the Baltic Sea region over the coming decades (BACC II Author Team, 2015), and may partly counteract the positive impact of nutrient reduction. As a consequence, the timeline of recovery from hypoxia in the Baltic Sea remains uncertain (Meier *et al.*, 2012).

Past intervals of hypoxia, recorded in marine sedimentary archives, provide the opportunity to study the various factors that control the development of hypoxia. In the Baltic Sea, two distinct intervals of widespread hypoxia are recognized prior to the modern hypoxic period (Zillén *et al.*, 2008). Both intervals occurred in the ca. 8 ka following the transition from the freshwater Ancylus lake phase to the brackish-marine Littorina phase (A/L transition, e.g. Björck, 1995). The first hypoxic interval was dated at 8 — 4 ka before present (BP) and coincided with the warm, dry period of the Holocene Thermal Maximum (HTM; e.g. Anderson *et al.*, 1988; Zillén *et al.*, 2008; Jilbert and Slomp, 2013). Diatom assemblages and the isotopic composition of organic matter from laminated sediments in the Gotland Basin record maxima in salinity, suggesting that the influx of saline North Sea waters after the A/L transition caused the expansion of hypoxia through water-column stratification (Emeis *et al.*, 2003; Zillén *et al.*, 2008). Hypoxia resulted in enhanced recycling of sedimentary phosphorus (P) and increased marine productivity, thereby acting as a positive feedback on de-oxygenation (Sohlenius *et al.*, 2001; Jilbert and Slomp, 2013). The termination of the HTM hypoxic interval (HTM$_{HI}$) has been attributed to reduced salinity and weakened stratification (Zillén *et al.*, 2008; Carstensen *et al.*, 2014a), and to the shoaling of the northern Åland Sea sill (Jilbert *et al.*, 2015). This shoaling is thought to have led to reoxygenation of the Bothnian Sea and, consequently, to an increase in the burial of P imported from the Baltic Proper. The associated decline in P availability in the Baltic Proper may have contributed to a decline in marine productivity and subsequent oxygen demand in deeper waters (Jilbert *et al.*, 2015).

A large fraction of the Baltic Proper became hypoxic again between 1.4 and 0.7 ka BP, during the Medieval Climate Anomaly (MCA), when mean air temperatures were 0.9 — 1.4°C higher than temperatures recorded in the period 1961–1990 (e.g. Mann *et al.*, 2009; Jilbert and Slomp, 2013). Population estimates indicate that around the onset of the MCA hypoxic interval (MCA$_{HI}$) the human population in the Baltic Sea watershed expanded significantly and the associated release of nutrients from agriculture may have enhanced marine productivity (Zillén *et al.*, 2008; Zillén and Conley, 2010). Kabel *et al.* (2012) proposed

that a decrease in sea surface temperature (SST) at the end of the MCA$_{HI}$ reduced marine productivity in the Baltic Sea and resulted in the termination of the hypoxic interval. A decrease in external nutrient loading due to a large population decline following the outbreak of the Black Death may have contributed to the termination as well (Zillén *et al.*, 2008).

Various studies have focused on understanding environmental changes in the Baltic Sea region and their impact on the development of hypoxia during the HTM$_{HI}$ and the MCA$_{HI}$ using sediment records (e.g. Sohlenius *et al.*, 2001; Zillén *et al.*, 2008; Zillén and Conley, 2010) or climate modeling (Schimanke *et al.*, 2012). However, major uncertainties remain regarding temporal changes in surface and bottom water salinity (Gustafsson and Westman, 2002; Emeis *et al.*, 2003) and marine productivity (e.g. Brenner, 2005). Furthermore, currently only three SST records exist for the Baltic Sea. Two of these records are from the Baltic Proper, covering the past 1000 yr, excluding the HTM$_{HI}$ and the early MCA$_{HI}$ (Kabel *et al.*, 2012), while the third is a low resolution record from an estuary in the Bothnian Sea (Warnock *et al.*, 2017). Differences in sampling resolution and dating uncertainties further complicate comparison of the available records.

During Integrated Ocean Drilling Program (IODP) Expedition 347 a suite of long sediment cores was recovered from the Baltic Sea (Andrén *et al.*, 2015a). Here, we present a high-resolution, multi-proxy study of sediments from the Landsort Deep (Site M0063, Fig. 1), capturing profiles of the onset and termination of the HTM$_{HI}$ and MCA$_{HI}$. The combination of geochemical, lipid and palynological data allows the simultaneous reconstruction of variations in salinity and SST. We find that hypoxia during the HTM shows a strong link with changes in both salinity and temperature, while MCA hypoxia appears to have responded mainly to temperature changes.

2. MATERIALS AND METHODS

2.1. Study site and sample selection

For the past ~ 8 ka the Baltic Sea has been a restricted marginal sea that is strongly influenced by river runoff and saline inflows from the North Sea (Bergström and Carlsson, 1994; Gustafsson and Westman, 2002; Zillén *et al.*, 2008). The deepest basin of the Baltic Sea is the Landsort Deep (459 m), which currently has a density stratified water column and bottom waters that are permanently euxinic (no oxygen and presence of free sulfide) (e.g. Zillén *et al.*, 2008). The studied sediment record was retrieved from the central part of the Landsort Deep at Site M0063 (58°37.34´N, 18°15.25´E; 437 m water depth; Fig. 2.1) during IODP Expedition 347 in October 2013 (Andrén *et al.*, 2015a).

The HTM$_{HI}$ and MCA$_{HI}$ were previously identified at this site based on sedimentary enrichments in organic carbon (C$_{ORG}$), sulfur (S) and molybdenum (Mo) contents in ~ 9 m and ~ 4 m laminated intervals respectively (Dijkstra *et al.*, 2016). Here, we focus on a selection of samples around the onset and termination of the HTM$_{HI}$ and MCA$_{HI}$. These include 12 subsamples (~20 cm resolution; Hole C) previously studied by Dijkstra *et al.* (2016) and additional subsamples taken at 5 cm depth resolution from the sediments from Hole C at the IODP Core Repository in Bremen. While Andrén *et al.* (2015b) and Dijkstra
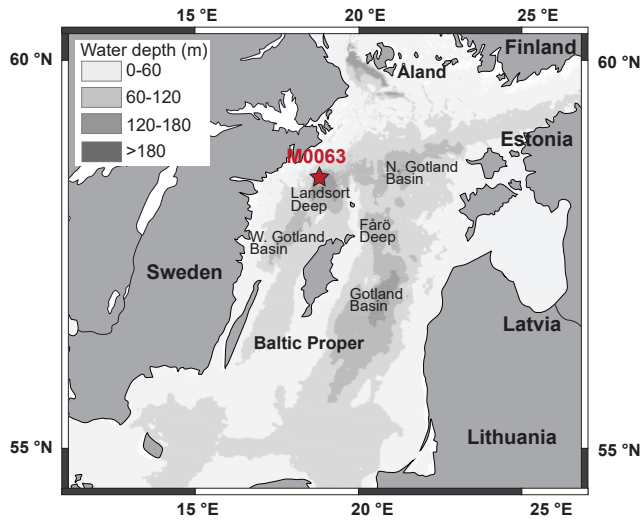
Figure 2.1| Bathymetric map of the Baltic Proper. Site M0063 (red star) of IODP Expedition 347 is located in the Landsort Deep at a water depth of 437 m. (For interpretation of the references to color in this figure legend, the reader is referred to the web version of this article.)

et al. (2016) provided meters below seafloor (mbsf) depths, we use the new adjusted meters below seafloor (ambsf) depth scale. The difference in the two depth scales is caused by gas expansion of sediments during their recovery, which resulted in apparent depth overlap between consecutive sections (Obrochta *et al.*, 2017). The ambsf depth scale eliminates this overlap. The chosen intervals cover the changes in C_{ORG} and Mo at the onset and termination of the HTM_{HI} and MCA_{HI} (Dijkstra *et al.*, 2016): 27 — 24 ambsf, 21 — 17 ambsf, 7.2 — 6.3 ambsf and 3.9 — 3.3 ambsf. We also present geochemical data for 58 subsamples published by Dijkstra et al. (2016): 27 — 24 ambsf, 21 — 17 ambsf, 7.2 — 6.3 ambsf and 3.9 — 3.3 ambsf. TEX_{86}^{L}–based SSTs were determined for a total of 54 subsamples.

2.2. Sediment geochemistry

Sediment samples were freeze-dried and powdered with an agate mortar and pestle. Between 100 and 125 mg of sample was weighed in Teflon destruction vessels, after which 2.5 ml concentrated mixed acid ($HClO_4$:HNO_3; 3:2) and 2.5 ml 40% HF were added. The mixture was then heated to 90°C and left overnight. Subsequently, the acids were evaporated at a temperature of 140°C, after which the residue was dissolved in 25 ml 4.5% HNO_3. Finally, the concentrations of iron (Fe), molybdenum (Mo) and aluminum (Al) were measured using Inductively Coupled Plasma-Optical Emission Spectrometry (ICP-OES) using a Perkin Elmer 9224 Optima 3000. Sedimentary Mo and Fe contents were normalized over Al. The relative standard deviation for the elements presented in this study was <5% based on duplicate analysis.

Approximately 300 mg of powdered freeze-dried sediment was weighed in centrifuge tubes for decalcification prior to organic carbon analysis. The samples were mixed twice with 7.5 ml of 1 M HCl, shaken overnight and subsequently washed twice with 10 ml demineralized water (Van Santvoort *et al.*, 2002). Afterwards, the samples were dried in an oven at 50 °C. Between 5 and 10 mg of decalcified sediment was weighed in tinfoil cups and analyzed using a Fisons Instruments CNS NA 1500 analyzer. Sedimentary C_{org} content was calculated after correcting the sediment weight for carbonate loss. Duplicate analyses indicated that the relative standard deviation for C_{org} was <5%.

A total of 54 sediment samples were freeze-dried, homogenized and extracted using a modified Bligh and Dyer technique (Rütters *et al.*, 2002) at the Christian-Albrechts University. Up to 10 g of sediment was extracted ultrasonically for 10 min with a solvent mixture of methanol (MeOH): dichloromethane (DCM): phosphate buffer (2:1:0.8, v/v/v). The extract and residue were separated by centrifuging at 1500 rpm for 5 min, after which the supernatant was decanted into a new vial. This procedure was repeated until the extract was colorless. Subsequently, DCM and phosphate buffer were added to the combined extract to a volume ratio of 1:1:0.9 (v/v/v), which resulted in a phase separation. After centrifugation (2500 rpm, 5 min), the lipid-containing bottom layer was collected and the aqueous phase was washed twice with DCM. Subsequently, the combined DCM phases were reduced under rotary vacuum and transferred to glass vials, in which elemental sulfur was removed for 24 h by the addition of activated copper turnings. The obtained Bligh and Dyer extracts (BDEs) were then evaporated to dryness under a stream of nitrogen and stored at −20°C until further processing.

All BDEs were separated into apolar and polar lipid fractions using activated Al_2O_3 as stationary phase and hexane:DCM (9:1, v/v) and DCM:MeOH (1:1, v/v) as respective eluents. The polar fractions, containing glycerol dialkyl glycerol tetraethers (GDGTs), were dried under N_2, re-dissolved in a mixture of hexane:propan-2-ol (99:1, v/v) to a concentration of 2 mg ml^{-1} and filtered through a 0.45 μm PTFE filter prior to analysis.

GDGTs were separated using a Waters Alliance 2695 high performance liquid chromatography (HPLC) system equipped with a Prevail Cyano column (150 mm × 2.1 mm i.d., 3 μm; Grace, Deerfeld, Il, USA) and following the analytical protocol described by Hopmans *et al.* (2000) and the gradient profile of Liu *et al.* (2012). Detection of isoprenoid and branched GDGTs was achieved using a Micromass ZQ single quadrupole mass spectrometer (MS) equipped with an APCI source operated in positive ion mode. MS conditions were as detailed in Heyng *et al.* (2015). All GDGTs were detected via single ion recording (SIR) of their protonated molecules (dwell time 234 ms) as described by Schouten *et al.* (2007).

TEX_{86}^{L} values were calculated following the formula of Kim *et al.* (2010) and transferred to SSTs using the Baltic Sea calibration of Kabel *et al.* (2012).

To determine the robustness of the TEX_{86}^{L}, we calculated the Branched and Isoprenoid Tetraether (BIT) index according to Hopmans *et al.* (2004). Empirical studies indicate that in settings where the BIT index exceeds the threshold of 0.3 (Weijers *et al.*, 2006) or shows

a correlation with TEX_{86}^L or its derivatives (Schouten *et al.*, 2013) the reconstruction of SSTs using the distribution of isoprenoid GDGTs may be inaccurate.

2.3. Palynology

An aliquot of the freeze-dried sediment sample was gently crushed using an agate pestle and mortar. Subsequently, between 0.2 and 6.5 g of sediment was spiked with *Lycopodium clavatum* spores for quantification of palynomorph abundance (Wood *et al.*, 1996). Samples were treated with HCl (10%) and HF (38%) to dissolve carbonates and silicates, respectively. The samples were centrifuged for 5 min at 2200 rpm and decanted to remove the acids. The samples were subsequently sieved over a 10-µm sieve and placed in an ultrasonic bath for 5 min to aid disaggregation of organic matter and remove minerals (e.g. pyrite). The retrieved residues were mounted on slides with glycerin gel and analyzed under a light microscope at a 400 × magnification. Identification was performed to genus and species level following Rochon *et al.* (1999), Fensome and Williams (2004) and Marret *et al.* (2004). Averages of 189 (Maximum: 352; Minimum: 45, pre-A/L transition) and 118 (Maximum: 199; Minimum: 75) dinoflagellate cysts (dinocysts) were counted for the HTM and MCA, respectively. These averages are lower than the value of 300 counts usually considered sufficient to generate reliable diversities (e.g. Mertens *et al.*, 2009). However, due to the low dinocyst diversity of Baltic Sea samples (Willumsen *et al.*, 2013; Ning *et al.*, 2015; Sildever *et al.*, 2015), we are confident that these counts are representative of the sample content.

2.4. Proxy interpretation

2.4.1. Geochemical proxies

Changes in the sedimentary Fe and Mo contents can provide insight into past bottom water redox conditions (e.g. Helz *et al.*, 1996; Lyons and Severmann, 2006; Scott and Lyons, 2012). In surface sediments on oxic shelves, Fe is generally present in the form of Fe-oxides. When oxygen concentrations decrease, Fe may be mobilized and transported to adjacent deep basins as nanoparticle Fe-oxides or complexed Fe(III) (Raiswell and Canfield, 2012). Increased Fe contents relative to a detrital background in deep basin sediments can therefore be used as an indicator of hypoxic conditions on the surrounding shelf (Lyons and Severmann, 2006; Raiswell and Canfield, 2012). The fraction of reactive Fe that is present as pyrite (FeS_2) (degree of pyritization; Raiswell *et al.*, 1988) can be used to distinguish between sediments deposited under anoxic (>0.38) and euxinic (0.7) bottom waters (Poulton and Canfield, 2011). Sediment Mo content can also be used to track past bottom water redox conditions (Scott and Lyons, 2012).

2.4.2. Palynological proxies

About 15 to 20% of extant dinoflagellates produce a fossilizable organic-walled dinocyst (e.g. Head, 1996). The distribution of dinoflagellates and their dinocysts is sensitive to a variety of environmental parameters, such as SST, salinity and marine productivity (Zonneveld *et al.*, 2013), so that the presence and abundance of dinocyst species in down-core sediments can be employed to reconstruct paleoenvironmental conditions (e.g. de Vernal and Marret, 2007).

The process length of *Operculodinium centrocarpum* cysts in the Baltic Sea has been related to surface water salinity and is therefore applied as a (paleo-)salinity proxy (e.g. Mertens *et*

al., 2011; Willumsen *et al.*, 2013; Jansson *et al.*, 2014; Ning *et al.*, 2015). Here, we define an *O. centrocarpum* index, which we use as a qualitative indicator of salinity changes. The index is based on the relative abundance of morphotypes with processes over cysts without processes and is calculated as:(1)

We also used the cysts of *Gonyaulax apiculata* as an indicator for freshwater conditions. This species is a freshwater dinoflagellate (Evitt *et al.*, 1985) and its cyst has been found in lake sediments (e.g. Kouli et al., 2001).

2.5. Age model

For Site M0063, an age model was created for Hole D using the bulk ^{14}C method (Obrochta *et al.*, 2017). We could not transfer this model to Hole C (this study), because of the large and variable depth offset between holes. Furthermore, an offset of on average 0.9 ± 0.75 ka is observed for the onset and termination of the HTM$_{HI}$ and MCA$_{HI}$ when compared to earlier work (Jilbert and Slomp, 2013; Funkey *et al.*, 2014; Lenz *et al.*, 2015). These studies used an age model for Gotland Basin sediments developed using three different geochronological methods (Lougheed *et al.*, 2012). Given the relative proximity of the Gotland Basin to the Landsort Deep, we expect the timing of the onset and termination of the hypoxic intervals to have been similar and we therefore use the ages of Lougheed *et al.* (2012).

3. RESULTS

3.1. Ancylus/Littorina transition and the Holocene Thermal Maximum

The sediments deposited in the lower part of the A/L transition (27–26.6 ambsf) are low in Fe/Al (~0.6 wt%/wt%) and C$_{ORG}$ (<1 wt%), and depleted in Mo (2.2A–C). In the upper part (26.6–26.2 ambsf), Fe/Al increases (0.7 wt%/wt%) and the C$_{org}$ content doubles (2 wt%), while Mo remains absent. Reconstructed SST increases from 15.4°C to ~17°C (Fig. 2.2D). Cysts of *G. apiculata* initially dominate the dinocyst assemblage (>80%; Fig. 2.2E) but then decrease strongly (<5%; above 26.4 ambsf).

At the onset of the HTM$_{HI}$ (~26.2 ambsf), a distinct maximum in Fe/Al (>0.9 wt%/wt%), Mo/Al and C$_{ORG}$ (>6 wt%) is observed. Sea surface temperatures are generally above 16 °C but decrease intermittently to 14.3°C. A second maximum in Fe/Al, Mo/Al and C$_{org}$ occurs between 25 and 24.7 ambsf. The *O. centrocarpum* index displays marked minima (<0.1) during peak values of Fe/Al and Mo/Al (Fig. 2.2F).

The termination of the HTM$_{HI}$ (~19.5–17.2 ambsf) is reflected in a decline to relatively low values of Fe/Al, Mo/Al and C$_{ORG}$ (~0.7 wt%/wt%, <0.0003 wt%/wt% and ~2 wt%, respectively). Prior to the termination, SST is 17.6°C and during the termination a decline in SST to <14°C is observed. *G. apiculata* is mostly absent and there is no clear trend in the *O. centrocarpum* index.

3.2. The Medieval Climate Anomaly

Sediments deposited between 7.2 and 6.5 ambsf are relatively poor in Fe/Al (0.7 wt%/wt%), Mo/Al and C$_{ORG}$ (1.5 wt%), and record SSTs around 14.7°C (Fig. 2.3A–D). A few cysts of *G.*

apiculata are infrequently present (Fig. 2.3E; H). The *O. centrocarpum* index (Fig. 2.3F) varies between 0.3 and 0.4.
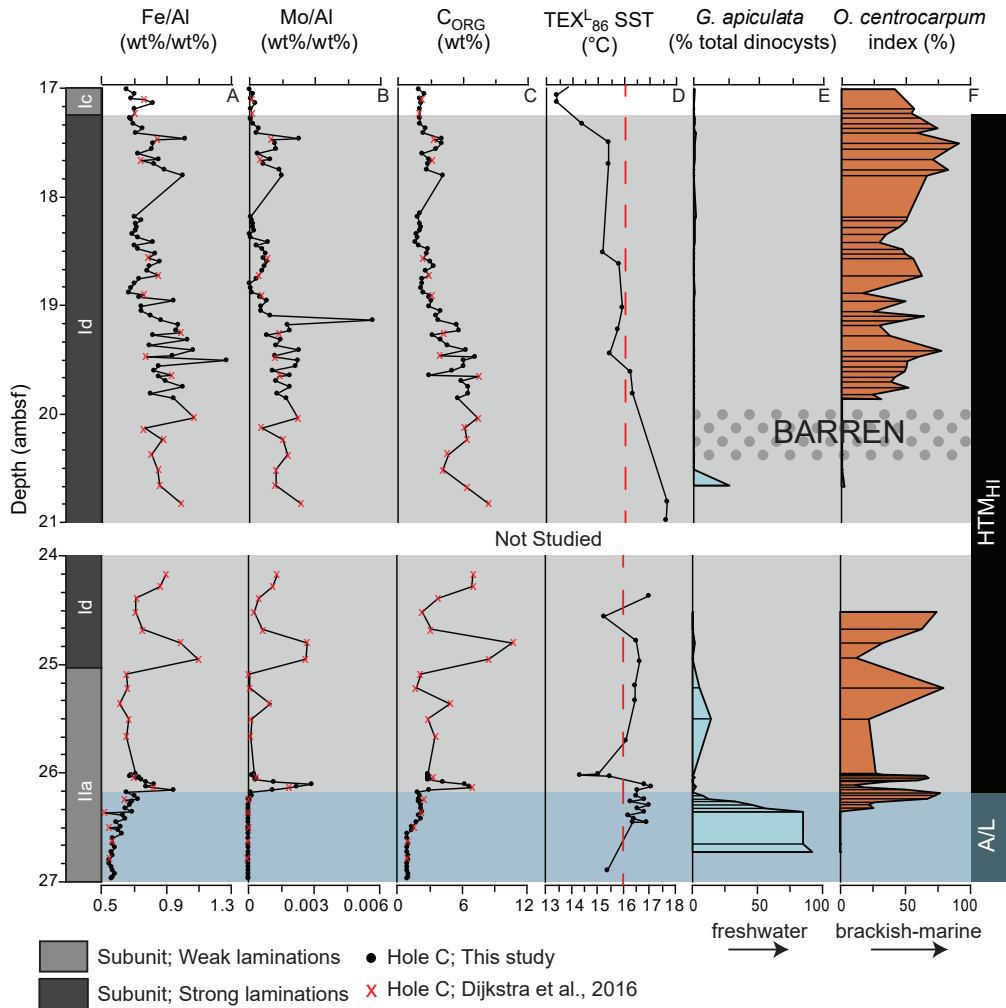
Figure 2.2| Overview of geochemical and palynological data from Hole C, Site M0063 of the Landsort Deep for the depth intervals 27–24 ambsf and 21–17 ambsf. The onset (~26.2 ambsf) and termination (~17.2 ambsf) of the Holocene Thermal Maximum hypoxic interval (HTM$_{HI}$) are dated at approximately 8 ka and 4 ka BP, respectively. A. Iron over aluminum ratio (Fe/Al) B. Molybdenum over aluminum ratio (Mo/Al) C. Total organic carbon content (C$_{ORG}$) D. TEX$_{86}^L$ sea surface temperatures E. Relative abundance of freshwater *Gonyaulax apiculata* cysts F. *Operculodinium centrocarpum* surface water salinity index. The dotted interval indicates barren samples that were devoid of palynomorphs. Red symbols in panels A–C represent data from Dijkstra et al. (2016) Units (Ic-IIa) represent the core lithology (Andrén *et al.*, 2015b). A/L: Ancylus/Littorina transition (Dijkstra *et al.*, 2016).
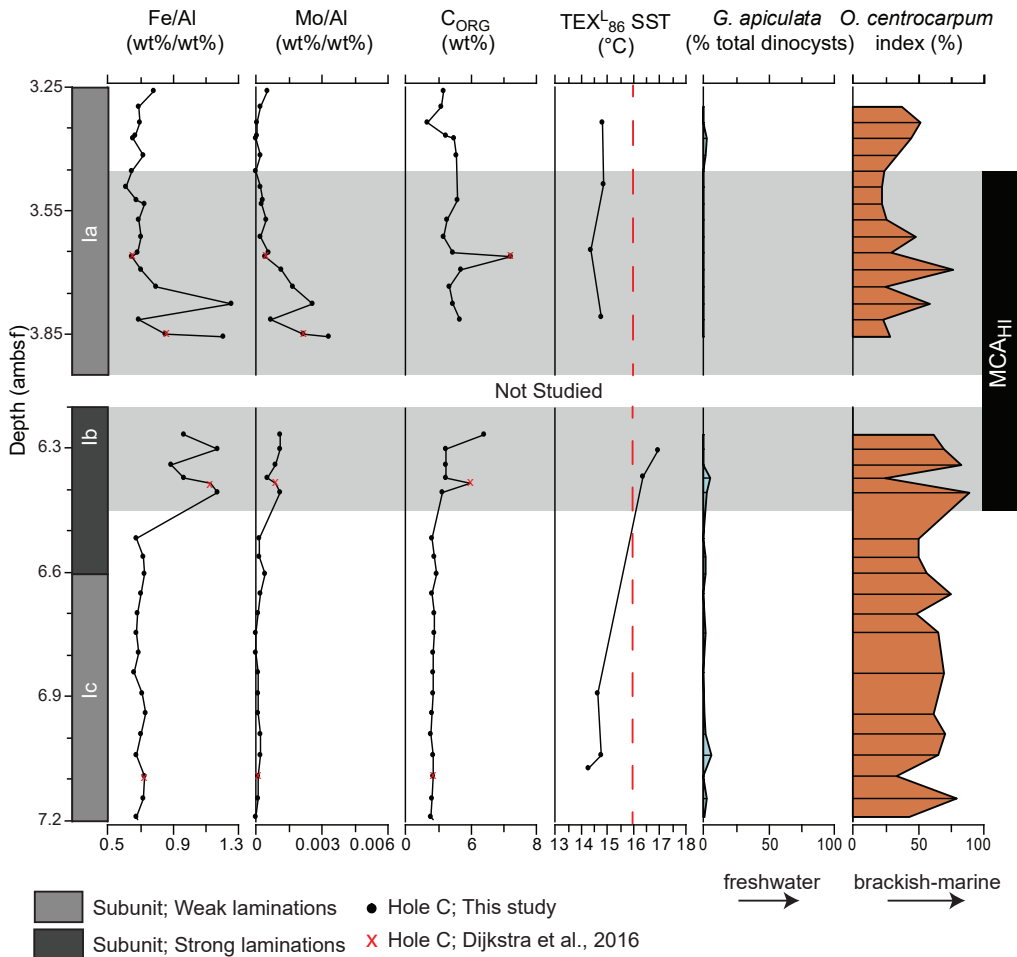
Figure 2.3| Overview of geochemical and palynological data from Hole C, Site M0063 of the Landsort Deep for the intervals of 7.2–6.3 ambsf and 3.9–3.3 ambsf. The onset (~6.5 ambsf) and termination (~3.5 ambsf) of the Medieval Climate Anomaly hypoxic interval (MCA$_{HI}$) are dated at approximately 1.4 ka and 0.7 ka BP, respectively. A. Iron over aluminum ratio (Fe/Al) B. Molybdenum over aluminum ratio (Mo/Al) C. Total organic carbon content (C$_{ORG}$) D. TEX$_{86}^{L}$ sea surface temperatures E. Relative abundance of freshwater *Gonyaulax apiculata* cysts F. *Operculodinium centrocarpum* surface water salinity index Red symbols in panels A–C indicate data from Dijkstra *et al.* (2016). Units (Ia–Ic) represent the core lithology (Andrén *et al.*, 2015b). (For interpretation of the references to color in this figure legend, the reader is referred to the web version of this article.)

Across the onset of the MCA$_{HI}$ (6.5–6.3 ambsf), increases in Fe/Al (>1 wt%/wt%), Mo/Al and C$_{ORG}$ (>2 wt%) are observed. Sea surface temperatures rise from ~14.6°C to 16.5°C. *G. apiculata* cysts disappear from the record. The C$_{ORG}$ maximum (~5 wt%) is preceded by two maxima in the *O. centrocarpum* index (~0.7).

The termination of the MCA_{HI} (3.9–3.5 ambsf) is characterized by a general decrease in Fe/Al and Mo/Al. Values of C_{org} are relatively constant at ~ 2.9 wt%. Following the termination, values for Fe/Al and C_{org} are on average 0.7 wt%/wt% and 2 wt%, respectively. Mo is only intermittently present. TEX_{86}^{L}-reconstructed SSTs between 14 °C and 15 °C precede the termination. There is no clear trend in the *O. centrocarpum* index.

2

4. DISCUSSION

4.1. Environmental conditions during the transition to the brackish-marine Littorina Sea

The onset of the brackish-marine Littorina Sea is recorded in Landsort Deep sediments by the gradual appearance of benthic foraminifera and brackish-marine diatoms in Unit IIb (Andrén *et al.*, 2015b) and by a strong decline in the abundance of freshwater *G. apiculata* cysts (26.4–26.2 ambsf, Fig. 2.2E). This disappearance of *G. apiculata* was previously observed in the Gotland Basin, where it is dated at ca. 7.6–7.4 ka BP (Brenner, 2005). This date matches the timing of the rise in bottom water salinity at our site (ca. 7.5 ka BP; Egger *et al.*, 2017).

The increase in Fe/Al during the A/L transition (Fig. 2.2A) likely reflects a decrease in oxygen concentrations on the shelf surrounding the Landsort Deep and an associated increase in the lateral transfer of Fe from the shelf and subsequent burial in the deep basin ("Fe shuttling"; Raiswell and Canfield, 2012; Lenz *et al.*, 2015). The decrease in shelf bottom water oxygen was likely the result of decreased oxygen solubility and increased stratification due to the incursion of saline North Sea waters, in combination with increasing SSTs (Fig. 2.2D; Renssen *et al.*, 2012; Kotthoff *et al.*, 2017). The reconstruction of SSTs from TEX_{86}^{L} is validated by the BIT index (Supplements, Supp. Table 2.3) which is generally below 0.16 (Supplementary Fig. 2.1, Supplementary Fig. 2.2), with the exception of the sample at 26.89 ambsf which had a BIT value of 0.32. As SSTs increased they crossed the temperature threshold for cyanobacterial bloom formation of 16 °C (Fig. 2.2D; Wasmund, 1997). This, together with increased P availability (e.g. Bianchi *et al.*, 2000; Sohlenius *et al.*, 2001) likely stimulated an increase in cyanobacterial productivity, which contributed to bottom water deoxygenation upon degradation (Funkey *et al.*, 2014).

4.2. Onset and termination of hypoxia during the Holocene Thermal Maximum

4.2.1. Onset of the HTM_{HI}
The onset of the HTM_{HI} (ca. 8 ka BP; Zillén *et al.*, 2008; Jilbert and Slomp, 2013) is reflected in a continued increase in Fe/Al in the Landsort Deep, indicating an intensification of the Fe shuttle in response to widespread hypoxia in the Baltic Proper. In addition, elevated Mo/Al values (Fig. 2.2B) throughout the onset, combined with the high degree of pyritization (> 0.7, Dijkstra *et al.*, 2016) indicates that bottom waters in the Landsort Deep were euxinic during the HTM_{HI} (Poulton and Canfield, 2011; Scott and Lyons, 2012).

The onset of the HTM_{HI} occurred after the establishment of brackish-marine conditions in the Baltic Proper and Landsort Deep, within an extended period characterized by high SSTs that started during the A/L transition. We therefore infer that the emplacement of a permanent halocline was the main cause for the development of widespread hypoxia, while temperature-

driven stratification provided conditions conducive to hypoxia. In addition, maxima in C_{org}, Fe/Al and Mo/Al (26.2 ambsf; 25–24.7 ambsf) coincide with low *O. centrocarpum* index values, suggesting relatively low sea surface salinity (Fig. 2.2F). This trend would be opposite to the increasing trend in bottom water salinity (Gustafsson and Westman, 2002; Egger *et al.*, 2017), leading to a larger density difference between surface and bottom waters, thus stimulating water-column stratification. Possible causes for lower surface water salinity are a high North Atlantic Oscillation (NAO) index and the retraction of Norwegian glaciers due to HTM warming (e.g. Hänninen *et al.*, 2000; Nesje, 2009), which would both lead to enhanced freshwater input.

4.2.2. Termination of the HTM$_{HI}$

The termination of the HTM$_{HI}$ in the Landsort Deep and the surrounding shelf area is reflected in a phased decrease in Fe/Al and Mo/Al (Fig. 2.2A,B). This suggests a muted Fe shuttle, due to retreating shelf hypoxia, and less reducing conditions in the bottom waters of the Landsort Deep, respectively, in agreement with previous studies (Funkey *et al.*, 2014; Lenz *et al.*, 2015; Dijkstra *et al.*, 2016).

The absence of a correlation between the geochemical parameters and the *O. centrocarpum* index, and the lack of a clear trend in the *O. centrocarpum* index itself, suggest that sea surface salinity neither changed considerably nor contributed to the termination of the HTM$_{HI}$ therefore surface water salinity. However, decreasing bottom water salinity during the termination, due to a weakened connection between the Baltic Sea and North Sea from ca. 5.5 ka BP onwards (Gustafsson and Westman, 2002; Egger *et al.*, 2017), would have weakened stratification. The steady decline in SSTs further reduced stratification, increased oxygen solubility and likely caused a decrease in cyanobacterial productivity as SSTs dropped below 16 °C (Westman *et al.*, 2003; Funkey *et al.*, 2014).

4.3. Onset and termination of hypoxia during the Medieval Climate Anomaly

4.3.1. Onset of the MCA$_{HI}$

The onset of the MCA$_{HI}$ in the Landsort Deep is characterized by an increase in Mo/Al, S and C_{ORG} at 6.45 ambsf (Dijkstra *et al.*, 2016). The high values of Fe/Al and the intermittent presence of Mo (Fig. 2.3A–B) below this depth indicates that this site and its surrounding area were already experiencing low oxygen conditions prior to the MCA$_{HI}$. The increase in Mo/Al across the onset and the average degree of pyritization of 0.64 throughout the MCA$_{HI}$ (Dijkstra *et al.*, 2016) imply that bottom waters in the Landsort Deep were anoxic and possibly euxinic.

Model simulations indicate that the onset of the MCA$_{HI}$ occurred within a long-term period of decreasing bottom water salinity (Gustafsson and Westman, 2002; Egger *et al.*, 2017). The absence of a correlation between Fe/Al, Mo/Al and the *O. centrocarpum* index suggests that stratification resulting from salinity differences was not important for the development of the MCA$_{HI}$. We infer that climatic warming, leading to lower gas solubility and promoting water column stratification, was the primary cause of the MCA$_{HI}$. The prevailing high SSTs (>16°C) coupled with the terrestrial input of P as a result of an expanding human population

and associated marine productivity may have contributed to the development of hypoxia (e.g. Zillén *et al.*, 2008; Zillén and Conley, 2010; Funkey *et al.*, 2014).

4.3.2. Termination of the MCA$_{HI}$

A coeval decrease in Fe/Al and Mo/Al marks the retreat of shelf hypoxia in the Landsort Deep as well as the onset of less reducing conditions in the deep basin itself. Similar changes in both ratios were recorded in sediments from other sites in the Baltic Proper (Jilbert and Slomp, 2013; Funkey *et al.*, 2014; Lenz *et al.*, 2015) at the end of the MCA$_{HI}$.

Due to the continued decrease in bottom water salinity (Gustafsson and Westman, 2002; Egger *et al.*, 2017) and the lack of a signal in the *O. centrocarpum* index we conclude that salinity changes did not contribute to the termination of the MCA$_{HI}$. Sea surface temperatures during the termination are significantly lower than during the onset (Fig. 2.3D), in line with lower air temperatures (e.g. Seppä *et al.*, 2009), suggesting that the actual drop in SST preceded the termination of the MCA$_{HI}$. A large SST decrease, similar in shape to the decline we observe in our Fe/Al and Mo/Al records, was reported previously for the nearby Gotland Basin (Kabel *et al.*, 2012), supporting the conclusion that a decline of SST at or near the end of the MCA$_{HI}$ would have resulted in weakened water column stratification, facilitating bottom water ventilation. The SST decrease (<16°C) would also have reduced cyanobacterial productivity (Funkey *et al.*, 2014).

4.4. Causes of hypoxia and consequences for the future Baltic Sea

In the modern Baltic Sea, widespread hypoxia is primarily linked to the high loading of nutrients through river discharge and the resulting enhanced marine productivity, with global warming playing a secondary role (Carstensen *et al.*, 2014b). During the HTM$_{HI}$ and MCA$_{HI}$ we find that changes in salinity and SST were key causes of hypoxia, underscoring their possible importance in facilitating the spread of oxygen-depleted bottom waters in the future Baltic Sea. Model simulations indicate that the average salinity in the Baltic Sea will probably decrease over the coming century, presumably weakening stratification (Meier, 2006; Meier *et al.*, 2011; BACC II Author Team, 2015). Yet, future changes in global and local sea level, as well as a different NAO mode, may result in opposite trends in surface and bottom water salinity. This could potentially lead to enhanced water column stratification and facilitate a further expansion of hypoxia in the Baltic Sea (Meier *et al.*, 2016), as observed during the HTM$_{HI}$.

Our results highlight that changes in SST contributed to the onset and termination of both the HTM$_{HI}$ and MCA$_{HI}$. Warming surface waters already contribute to bottom water deoxygenation today (Conley *et al.*, 2002) and the projected temperature rise for the Baltic Sea in the coming century (Meier *et al.*, 2012; BACC II Author Team, 2015) is within or above the range of SST change for the HTM and MCA (~2°C; this study; Kabel *et al.*, 2012). Warmer future SSTs may therefore cause a further decline in oxygen concentrations through decreased oxygen solubility, enhanced stratification and by supporting cyanobacterial blooms.

Despite a reduction in external nutrient loads, the ecological status for large parts of the Baltic Sea is showing only gradual improvement (Andersen *et al.*, 2017). This is mostly attributed to internal storage and recycling of P under hypoxic conditions (Andersen *et al.*, 2017). Our

findings are in agreement with previous studies (e.g. Andersson *et al.*, 2015 and references therein), and indicate that mitigation schemes must also account for changes in salinity and temperature and their possible effect on Baltic Sea oxygen concentrations.

5. CONCLUSIONS

Our study highlights that changes in salinity and sea surface temperature (SST) were key drivers of past intervals of widespread hypoxia in the Baltic Sea. During the Holocene Thermal Maximum (HTM), the hypoxic interval followed the transition to a warmer and more saline Baltic Sea. The onset of HTM hypoxia coincided with a period of relatively fresh surface waters, suggesting that enhanced stratification due to the larger salinity difference between surface and bottom water played a key role. During the Medieval Climate Anomaly the onset of widespread hypoxia correlated with changes in SST. Both onsets likely coincided with enhanced marine productivity, because the critical SST (>16°C) for the development of cyanobacterial blooms was reached. We infer that both terminations were mainly caused by decreased stratification due to lower SSTs and, at the end of the HTM_{HP}, a weaker salinity gradient. Our findings underline the potential impact of ongoing global climate change on bottom water oxygen concentrations in the Baltic Sea. Importantly, they indicate that current efforts to address hypoxia by curbing nutrient input from land may be countered by rising temperatures and an increased gradient between surface and bottom water salinity, linked to sea level change. These results underscore the importance of understanding future climate dynamics when designing mitigation schemes for eutrophic systems.

Chapter 2
Supplementary Materials

2
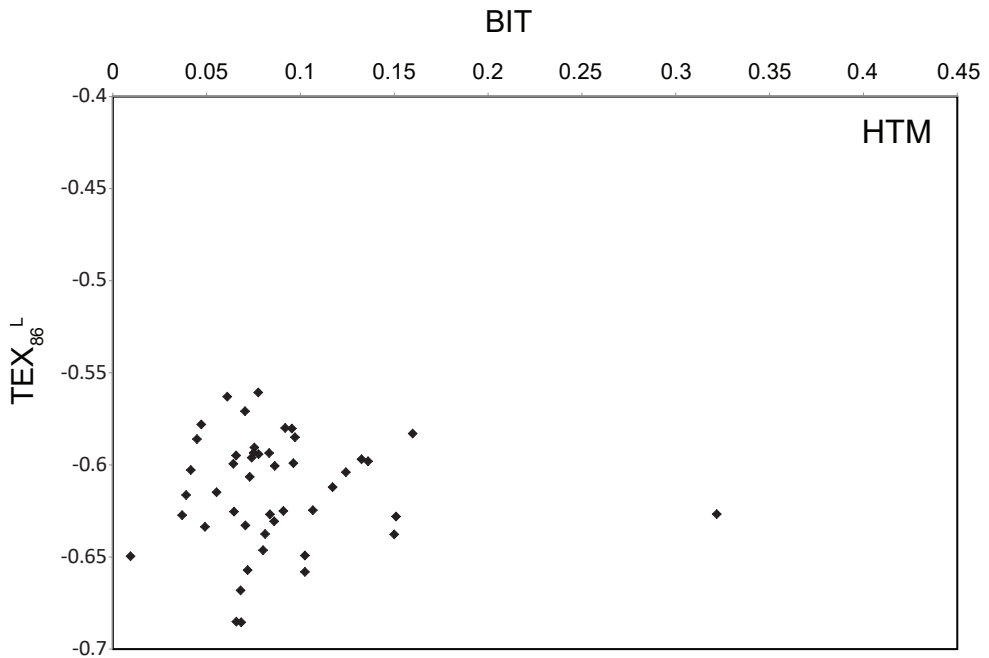
Supplementary Figure 2.1| Crossplot of TEX_{86}^L versus BIT index values for the Holocene Thermal Maximum (15.2 – 21 ambsf and 20.8 – 27 ambsf).
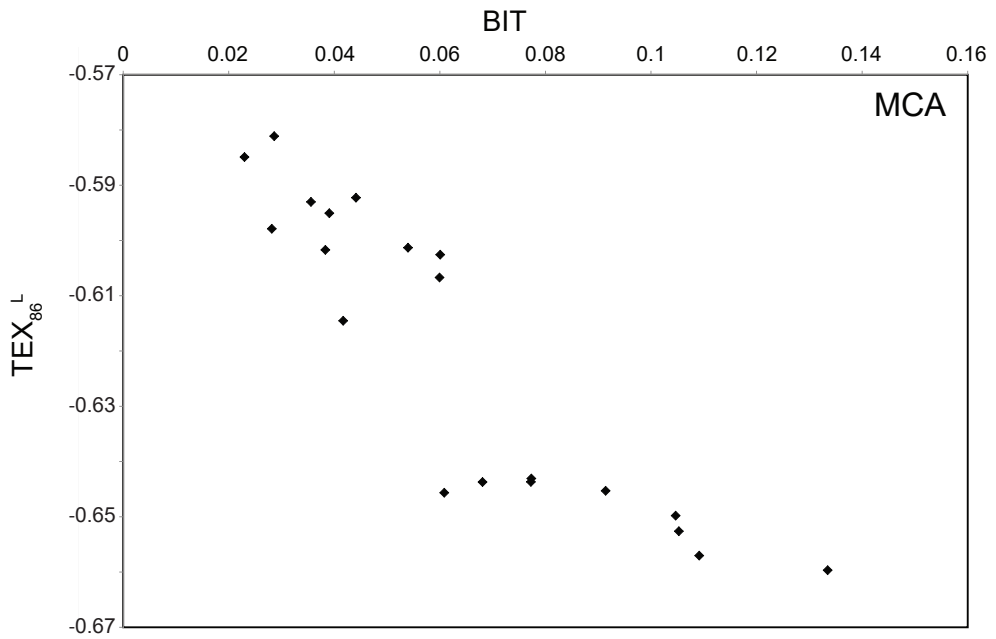
Supplementary Figure 2.2| Crossplot of TEX_{86}^L versus BIT index values for the Medieval Climate Anomaly (3.3 – 4.2 ambsf and 6.1 – 7.4 ambsf).

Supplementary Table 2.1| Palynological data for Site M00063 (Landsort Deep), IODP Expedition 347. ambsf = adjusted meters below surface, MCA$_{HI}$= Medieval Climate Anomaly hypoxic interval, HTM$_{HI}$= Holocene Thermal Maximum hypoxic interval.

Depth (ambsf)	G. apiculata (%)	O. centrocarpum index (%)	O. centrocarpum processes (cysts per gram)	O. centrocarpum no processes (cysts per gram)
MCA$_{HI}$ Termination				
3.30	0	0.37	7404	12555
3.34	0	0.52	18094	16998
3.38	2.36	0.45	11350	14074
3.41	1.77	0.34	9541	18581
3.45	0	0.24	10180	31814
3.49	0	0.31	29537	64445
3.49	0	0.13	7161	46544
3.53	0	0.22	8801	30803
3.57	0	0.26	11310	32044
3.61	0	0.48	8988	9805
3.65	0	0.29	4584	11002
3.69	0	0.76	43834	13947
3.73	0	0.25	664	1992
3.78	0	0.59	6522	4566
3.82	0	0.23	3760	12783
3.86	0	0.29	2010	5025
MCA$_{HI}$ Onset				
6.27	0	0.62	11029	6740
6.30	0	0.70	1439	617
6.34	0	0.83	6329	1266
6.37	5.71	0.25	487	1462
6.41	2.40	0.90	7696	880
6.52	0	0.50	3165	3165
6.56	1.68	0.50	3004	3004
6.60	1.85	0.56	6057	4711
6.65	0	0.75	9779	3260
6.70	0.77	0.48	11176	11921
6.75	1.58	0.65	9814	5196
6.84	0	0.70	11078	4847
6.94	1.31	0.62	5704	3565

6.99	1.37	0.71	11115	4577
7.04	6.11	0.65	18562	9827
7.09	0	0.33	6347	12694
7.14	2.90	0.80	11400	2850
7.19	1.15	0.44	18169	23513
7.24	3.84	0.22	1178	4122
HTM$_{HI}$ Termination				
17.01	0.48	0.42	80144	110865
17.19	0.33	0.57	93248	71584
17.23	0	0.54	58344	48934
17.28	0.71	0.61	54021	33896
17.32	0.48	0.69	122576	56119
17.37	0	0.75	66387	22524
17.42	1.94	0.59	52034	35846
17.51	0.66	0.92	97080	8726
17.56	0.59	0.84	94672	18250
17.66	1.26	0.71	31237	12830
17.75	0	0.83	69065	13813
17.80	0	0.67	36273	18137
18.19	1.40	0.52	80042	74706
18.22	0.63	0.51	60439	58115
18.28	0.74	0.45	55854	68267
18.35	0.53	0.35	49383	92744
18.41	1.20	0.29	70189	170208
18.49	0	0.48	39686	43406
18.52	0	0.50	65696	65696
18.56	0	0.56	48608	37898
18.72	0.40	0.63	119721	69581
18.89	0.57	0.17	63000	306782
18.96	0	0.50	72181	72181
19.05	0	0.25	61253	185871
19.10	0	0.64	91548	51322
19.14	0	0.47	24387	27436
19.18	0	0.30	83101	197365
19.28	0	0.38	45689	75133
19.42	0	0.78	282547	79591
19.46	0	0.61	107406	68932

19.51	0	0.51	34733	33079
19.56	0	0.51	148860	143814
19.61	0	0.49	44902	46629
19.65	0	0.42	94001	132049
19.70	0	0.38	74444	119111
19.75	0	0.52	27509	25216
19.81	0	0.24	197334	617464
19.86	0	0.31	99678	224914
20.24	0	0.00	0	0
20.37	0	0.00	0	0
20.51	0	0.00	0	0
20.67	27.14	0.03	193	7516

HTM$_{HI}$ Onset

24.52	0	0.74	93540	33407
24.68	0	0.62	28319	17109
24.80	1.36	0.33	16447	33809
24.95	0	0.12	40790	292950
25.22	5.27	0.79	41265	11218
25.50	14.37	0.22	1715	6175
26.00	1.21	0.27	2227	6013
26.01	0	0.32	2201	4586
26.03	0.41	0.65	13180	7189
26.04	2.05	0.67	48645	23744
26.06	0	0.59	11930	8123
26.08	0	0.37	72348	123691
26.10	0.74	0.11	45534	355162
26.13	2.43	0.18	67252	308237
26.15	0.54	0.50	55721	55721
26.18	0	0.76	56257	17388
26.21	7.89	0.73	45991	23762
26.23	12.57	0.67	1197	599
26.26	32.66	0.27	978	2690
26.29	46.27	0.22	209	732
26.32	55.72	0.25	629	1887
26.36	85.19	0	0	0
26.65	84.62	0	0	0
26.72	92.31	0	0	0

Supplementary Table 2.2| Geochemical data for Site M00063 (Landsort Deep), IODP Expedition 347. ambsf = adjusted meters below surface, MCA$_{HI}$= Medieval Climate Anomaly hypoxic interval, HTM$_{HI}$= Holocene Thermal Maximum hypoxic interval.

Depth (mbsf)	Fe (μmol/g)	Fe/Al (wt%/wt%)	Mo (μmol/g)	Mo/Al (wt%/wt%)	Al (μmol/g)
		MCA$_{HI}$ **Termination**			
3.26	1052	0.78	0.40	0.0005	2790
3.30	952	0.69	0.15	0.0002	2843
3.34	994	0.70	0.05	0.0001	2944
3.38	940	0.65	0	0	2981
3.41	996	0.72	0.15	0.0002	2875
3.45	860	0.65	0	0	2738
3.49	870	0.61	0.16	0.0002	2940
3.53	986	0.72	0.21	0.0003	2818
3.57	902	0.69	0.38	0.0005	2713
3.61	992	0.70	0.18	0.0002	2917
3.65	892	0.69	0.44	0.0006	2687
3.69	916	0.71	0.88	0.0012	2677
3.73	642	0.80	0.79	0.0017	1658
3.78	826	1.26	0.99	0.0026	1361
3.82	864	0.69	0.51	0.0007	2598
3.86	1184	1.21	1.90	0.0033	2029
		MCA$_{HI}$ **Onset**			
6.27	993	0.97	0.66	0.0011	2118
6.30	793	1.17	0.43	0.0011	1402
6.34	915	0.89	0.53	0.0009	2129
6.37	955	0.97	0.29	0.0005	2040
6.41	982	1.18	0.54	0.0011	1728
6.52	978	0.68	0.15	0.0002	2993
6.56	1020	0.72	0.14	0.0002	2927
6.60	1002	0.73	0.34	0.0004	2848
6.65	931	0.71	0.16	0.0002	2720
6.70	1080	0.68	0.09	0.0001	3285
6.75	1053	0.68	0	0	3211
6.79	1034	0.69	0	0	3098
6.84	1002	0.67	0.07	0.0001	3116
6.89	938	0.72	0.08	0.0001	2714

6.94	1153	0.73	0.12	0.0001	3247
6.99	1088	0.71	0.19	0.0002	3193
7.04	893	0.67	0.16	0.0002	2743
7.09	1043	0.76	0.10	0.0001	2827
7.14	932	0.72	0.08	0.0001	2691
7.19	955	0.68	0	0	2911
7.24	1008	0.70	0.06	0.0001	2994
7.30	1002	0.68	0	0	3047
7.35	1008	0.67	0.05	0.0001	3104
7.40	1044	0.67	0.06	0.0001	3231
7.46	984	0.67	0	0	3059
7.51	1001	0.67	0	0	3101
7.57	994	0.69	0	0	2997
7.61	998	0.67	0	0	3092
7.66	963	0.68	0.08	0.0001	2924
7.72	961	0.66	0	0	2995

HTM$_{HI}$ Termination

17.01	954	0.65	0	0	3038
17.05	955	0.69	0.12	0.0002	2846
17.10	1033	0.68	0.06	0.0001	3145
17.14	1213	0.81	0.22	0.0003	3081
17.19	1067	0.70	0.06	0.0001	3153
17.23	1072	0.70	0.08	0.0001	3181
17.28	1024	0.67	0.04	0	3178
17.32	1097	0.69	0.14	0.0002	3298
17.37	1097	0.75	0.35	0.0004	3038
17.42	966	0.70	0.24	0.0003	2840
17.46	965	1.01	1.26	0.0023	1974
17.51	819	0.81	0.67	0.0011	2095
17.56	810	0.81	0.70	0.0012	2082
17.61	1046	0.72	0.29	0.0003	3011
17.65	1054	0.84	0.68	0.0009	2584
17.70	1050	0.82	0.46	0.0006	2656
17.75	1074	0.88	0.98	0.0014	2519
17.80	910	1.00	0.78	0.0015	1886
18.19	1071	0.70	0.06	0.0001	3175
18.22	1029	0.74	0.10	0.0001	2870
18.25	1064	0.71	0.15	0.0002	3114

18.28	1003	0.71	0.13	0.0002	2926
18.31	1053	0.71	0.18	0.0002	3088
18.34	1077	0.68	0	0	3262
18.38	1105	0.72	0.05	0.0001	3162
18.41	1008	0.81	0.60	0.0008	2575
18.45	1074	0.70	0.29	0.0003	3182
18.49	965	0.72	0.45	0.0006	2764
18.52	911	0.83	0.48	0.0007	2275
18.56	1018	0.76	0.44	0.0006	2763
18.60	925	0.85	0.50	0.0008	2249
18.64	860	0.79	0.42	0.0007	2247
18.68	1000	0.77	0.42	0.0006	2670
18.72	1083	0.83	0.27	0.0004	2687
18.76	999	0.73	0.27	0.0003	2838
18.80	1075	0.70	0	0	3179
18.84	1067	0.68	0.06	0.0001	3249
18.89	1028	0.66	0.12	0.0001	3221
18.93	1005	0.73	0.36	0.0004	2862
18.96	1247	0.94	0.60	0.0008	2756
19.01	1065	0.74	0.45	0.0005	2964
19.05	1112	0.76	0.42	0.0005	3040
19.09	726	0.80	0.50	0.0009	1884
19.14	651	0.86	2.47	0.0056	1559
19.18	1115	0.97	1.15	0.0017	2385
19.23	983	0.95	1.10	0.0018	2136
19.28	1010	0.81	0.58	0.0008	2568
19.32	1080	1.02	0.88	0.0014	2187
19.37	906	0.79	0.80	0.0012	2366
19.41	1003	1.06	1.24	0.0022	1965
19.46	899	0.93	0.66	0.0012	2000
19.51	1101	1.27	1.13	0.0022	1801
19.56	714	0.85	1.03	0.0021	1740
19.61	681	0.82	0.52	0.0011	1719
19.65	630	0.85	0.56	0.0013	1542
19.70	767	0.89	0.61	0.0012	1778
19.75	833	1.00	0.90	0.0019	1726
19.81	830	0.80	0.78	0.0013	2159
19.86	1079	0.95	1.14	0.0017	2345

HTM$_{HI}$ Onset					
26.00	1044	0.71	0.21	0.0002	3035
26.01	1019	0.68	0.13	0.0001	3095
26.03	987	0.68	0.24	0.0003	3003
26.04	903	0.73	0.28	0.0004	2560
26.06	1007	0.75	0.25	0.0003	2787
26.08	771	0.77	0.67	0.0012	2063
26.10	741	0.83	1.50	0.0029	1855
26.13	685	0.78	1.15	0.0022	1829
26.15	1252	0.95	0.86	0.0011	2735
26.18	1003	0.65	0.10	0.0001	3173
26.21	1066	0.71	0.13	0.0002	3115
26.23	1142	0.73	0	0	3254
26.26	1088	0.69	0	0	3261
26.29	1058	0.68	0	0	3224
26.32	1016	0.65	0	0	3243
26.36	1081	0.69	0	0	3229
26.39	992	0.63	0	0	3242
26.42	1044	0.65	0	0	3330
26.45	899	0.60	0	0	3128
26.49	973	0.62	0	0	3260
26.52	945	0.61	0	0	3217
26.56	998	0.63	0	0	3296
26.60	940	0.57	0	0	3389
26.65	940	0.57	0	0	3385
26.68	940	0.58	0	0	3345
26.72	911	0.56	0	0	3345
26.76	927	0.57	0	0	3370
26.80	921	0.56	0	0	3380
26.84	901	0.55	0	0	3375
26.87	902	0.56	0	0	3316
26.89	916	0.57	0	0	3309
26.93	948	0.59	0	0	3344
26.97	915	0.57	0	0	3347

2

Supplementary Table 2.3| BIT and data for Site M00063 (Landsort Deep), IODP Expedition 347. ambsf = adjusted meters below surface, MCA_{HI}= Medieval Climate Anomaly hypoxic interval, HTM_{HI}= Holocene Thermal Maximum hypoxic interval.

Depth (ambsf)	BIT	TEX_{86}^{L}	TEX_{86}^{L}-SST (°C)
MCA_{HI} Termination			
3.34	0.07	-0.64	14.8
3.49	0.08	-0.64	14.8
3.65	0.11	-0.66	14.4
3.81	0.06	-0.65	14.8
MCA_{HI} Onset			
6.30	0.03	-0.58	17
6.37	0.03	-0.6	16.4
6.89	0.1	-0.65	14.6
7.04	0.09	-0.65	14.8
7.07	0.13	-0.66	14.3
HTM_{HI} Termination			
17.06	0.07	-0.69	13.4
17.12	0.07	-0.69	13.4
17.32	0.07	-0.66	14.4
17.50	0.04	-0.63	15.4
17.69	0.08	-0.63	15.4
18.52	0.05	-0.63	15.2
18.62	0.06	-0.61	15.8
19.02	0.12	-0.61	15.9
19.22	0.04	-0.62	15.8
19.44	0.06	-0.63	15.4
19.61	0.04	-0.6	16.2
19.81	0.06	-0.6	16.3
20.81	0.08	-0.56	17.7
20.98	0.06	-0.56	17.6
HTM_{HI} Onset			
24.37	0.09	-0.58	17
24.56	0.09	-0.63	15.3
24.78	0.07	-0.59	16.5
24.97	0.08	-0.59	16.6
25.20	0.11	-0.62	16.4
25.34	0.07	-0.6	16.4

25.70	0.07	-0.61	16.1
26.00	0.08	-0.64	15
26.01	0.1	-0.66	14.3
26.03	0.09	-0.62	15.5
26.10	0.04	-0.59	16.8
26.13	0.05	-0.58	17.1
26.15	0.08	-0.59	16.5
26.21	0.08	-0.59	16.5
26.23	0.1	-0.6	16.8
26.26	0.09	-0.6	16.3
26.29	0.1	-0.58	17
26.32	0.08	-0.59	16.5
26.36	0.1	-0.58	16.8
26.39	0.12	-0.6	16.2
26.42	0.13	-0.6	16.4
26.45	0.16	-0.58	16.9
26.45	0.14	-0.6	16.4
26.89	0.32	-0.63	15.4

2

Certain books, like certain landscapes, stay with us even when we left them,
changing not just our weathers but our climates.
Robert Macfarlane – Landmarks
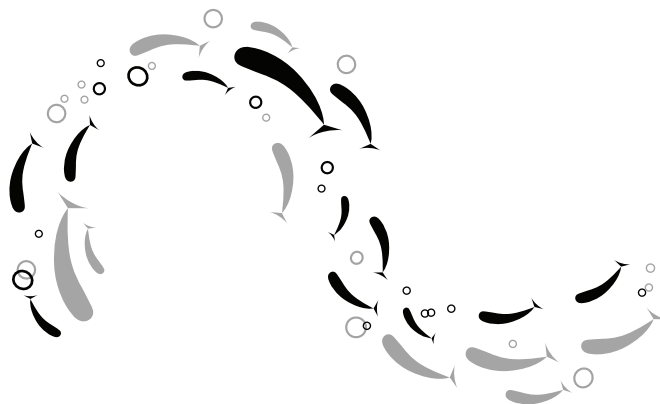
3

Ocean warming and acidification enhanced phosphorus recycling during past anoxic events

Ocean warming and acidification enhanced phosphorus recycling during past anoxic events

Nina M. Papadomanolaki, Mariette Wolthers, Caroline P. Slomp

ABSTRACT

Enhanced recycling of phosphorus as ocean deoxygenation expanded under past greenhouse climates, contributed to widespread organic carbon burial and drawdown of atmospheric CO_2. Phosphorus recycling was more efficient in ancient anoxic marine environments, compared to modern anoxic settings, for reasons that remain unclear. Here we show that ocean warming and acidification reduce the saturation state of sediment porewaters with respect to carbonate fluorapatite. We argue that this, combined with less calcium carbonate as a template for carbonate fluorapatite formation, amplified recycling of phosphorus and increased organic carbon burial upon marine anoxia during the Toarcian Oceanic Anoxic Event and Cretaceous Oceanic Anoxic Event 2. Future changes in temperature and ocean biogeochemistry, induced by elevated atmospheric CO_2, may similarly increase phosphorus availability and accelerate ocean deoxygenation and organic carbon burial.

1. INTRODUCTION

Phosphorus (P) is a key nutrient for marine phytoplankton and the ultimate limiting nutrient on geological timescales (Tyrrell, 1999). Through its control on primary productivity, P availability can impact organic carbon (C_{ORG}) burial and atmospheric carbon dioxide (CO_2) and oxygen (O_2) (Van Cappellen and Ingall, 1996). The availability of P in the surface ocean, in turn, is determined by riverine P input, P burial in sediments and recycling of P (Ruttenberg. 2003). Sinking of organic matter is the main route of delivery of P and C_{ORG} to sediments (Ruttenberg. 2003). Recycling of P relative to C_{ORG} from sediments is enhanced upon ocean deoxygenation (Van Cappellen and Ingall, 1994; Tyrrell, 1999; Algeo and Ingall, 2007). Enhanced recycling of P upon oceanic anoxia is the combined result of less efficient anaerobic degradation of organic carbon (Hartnett, 1998), preferential release of P from organic matter (Ingall *et al.*, 1993; Steenbergh *et al.*, 2011) and less retention of P in mineral form, either as iron (Fe) oxide bound P (Algeo and Ingall, 2007) or carbonate fluorapatite (Ruttenberg, 2003; Algeo and Ingall, 2007) (CFA). Organic P (P_{ORG}), Fe-bound P, CFA and detrital P together make up the total P (P_{TOT}) pool in marine sediments.

Changes in P recycling are reflected in elevated C_{ORG} over total P (C_{ORG}/P_{TOT}) ratios, as demonstrated for modern marine sediments (Ingall *et al.*, 1993; Algeo and Ingall, 2007). Importantly, the range of C_{ORG}/P_{TOT} values for deposits formed during past oceanic anoxia is wider than that for modern sediments (Algeo and Ingall, 2007; Kraal *et al.*, 2010a; Flögel *et al.*, 2011). For example, C_{ORG}/P_{TOT} ratios for sediments from the Cretaceous Oceanic Anoxic Event 2 (OAE2; 94 Ma) range up to at least 1200 mol/mol (Kraal *et al.*, 2010a), whereas modern C_{ORG}/P_{TOT} ratios are generally <400 (Algeo and Ingall, 2007). Various explanations for these elevated C_{ORG}/P_{TOT} ratios, which occur in both shallow and deep marine settings (Kraal *et al.*, 2010a), have been proposed. Higher atmospheric CO_2 may have increased the ratio of C_{ORG} to P_{ORG} of phytoplankton (Flögel *et al.*, 2011). Alternatively, lower atmospheric O_2 in Earth's past could have caused more reducing conditions near the seafloor (Algeo and Ingall, 2007) and an increased release of P from Fe oxides and organic matter, relative to modern anoxic systems. However, many modern anoxic systems are rich in hydrogen sulfide and hence contain negligible Fe oxide bound P (Kraal *et al.*, 2017). Furthermore, ratios of C_{ORG} to P_{ORG} (C_{ORG}/P_{ORG}), which are indicators of P release from organic matter (Algeo and Ingall, 2007), in such modern sediments range up to at least 1200 (Kraal *et al.*, 2017) and thus are similar to the C_{ORG}/P_{TOT} ratios of ancient anoxic environments (Kraal *et al.*, 2010a). This suggests that, in these ancient sediments, a smaller proportion of the P released from organic matter and iron oxides was retained as CFA. Thus, variations in CFA formation must have played a key role in modulating the response of C_{ORG}/P_{TOT} to bottom water redox conditions.

Importantly, rates of CFA formation are not directly redox-sensitive. Instead, the degree of supersaturation of porewaters with respect to CFA plays a key role (Koutsoukos *et al.*, 1980; Jahnke, 1984; Ruttenberg, 2003). CFA is a form of fluorapatite with carbonate substituting for phosphate and fluoride ($Ca_{10-a-b}Na_aMg_b(PO_4)_{6-x}(CO_3)_{x-y-z}(CO_3F)_y(SO_4)_zF_2$) (Jarvis *et al.*, 1994). Saturation depends on solute concentrations of the dominant components of CFA, as well as various environmental conditions such as temperature and pH (Jahnke, 1984). Notably, past oceanic anoxia typically occurred during periods of high temperatures and/or potential ocean acidification (Forster *et al.*, 2007; Zachos *et al.*, 2008; Trecalli *et al.*, 2012; Ettinger *et al.*, 2020; Sullivan *et al.*, 2020).

Here, we assess the impact of ocean warming and acidification on P recycling during multiple periods of past anoxia. We use a data compilation of sediment C_{ORG}/P_{TOT} and the redox proxy iron over aluminum (Fe/Al) (Raiswell *et al.*, 2018), combined with calculations of saturation indices for CFA and box-model simulations of the oceanic C and P cycles. Through a comparison with Mediterranean sapropels and modern anoxic environments, we show that in severely anoxic marine settings, higher temperatures and lower pH can explain why the rates of CFA authigenesis are lower than expected based on the P input to the sediment, and hence, the large discrepancy between ancient and modern P recycling.

2. ANCIENT AND MODERN ENVIRONMENTS

For the past ocean, we focus on sediments deposited directly before and during three deoxygenation events: the Toarcian Oceanic Anoxic Event (T-OAE; 183 Ma), OAE2 (94 Ma) and the Paleocene-Eocene Thermal Maximum (PETM; 56 Ma) (Table S1). These events are associated with elevated atmospheric CO_2, warmer deep ocean temperatures, and lower than modern ocean pH (Forster *et al.*, 2007; Zachos *et al.*, 2008; Friedrich *et al.*, 2012; Trecalli *et al.*, 2012; Zeebe and Tyrrell, 2019; Ettinger *et al.*, 2020; Sullivan *et al.*, 2020), conditions which are likely to lower the saturation state of porewaters with respect to CFA (Jahnke, 1984). Furthermore, redox-driven P recycling likely contributed to the deposition and burial of large quantities of C_{ORG} during each event (Ruvalcaba Baroni *et al.*, 2014; Komar and Zeebe, 2017; Ruvalcaba Baroni *et al.*, 2018). In addition to these ancient sediments, we investigate three Mediterranean sapropels (i-282c at 2.943 Ma, S5 at 125 ka and S1 at 10 ka) which provide C_{ORG}/P_{TOT} ratios for past hypoxic to euxinic (anoxic and sulfidic) settings with similar to modern atmospheric CO_2 and O_2 (Algeo and Ingall, 2007; Zachos *et al.*, 2008). The PETM and sapropel S1 sediments were deposited under mild ocean deoxygenation, relative to the other four past events (Jenkyns, 2010; Rohling *et al.*, 2015). For further comparison, we also present data on modern sediments from the Arabian Sea and Black Sea, where CFA formation is known to occur in the Oxygen Minimum Zone and deep euxinic basin, respectively (Kraal *et al.*, 20172; Kraal *et al.*, 2017). Sediment P speciation is only considered for sapropels and modern sediments, since for more ancient events, interpretation is hampered by long-term diagenesis and oxidation during storage (Kraal *et al.*, 2009) . For more information on the chosen events and locations, we refer the reader to the Supplementary Text.

3. REDOX-DEPENDENT PHOSPHORUS RECYCLING

Median C_{ORG}/P_{TOT} ratios for all ancient sediments and sapropels are elevated compared to values preceding the onset of widespread deoxygenation (Fig. 3.1A and B), in accordance with a transition towards enhanced P recycling. Similarly, median C_{ORG}/P_{TOT} values are higher in the modern Arabian Sea OMZ and euxinic Black Sea basin, when compared to values for their respective oxic sediments (Fig. 3.1C). Importantly, median values for T-OAE, i-282c and S5 (169, 655 and 315, respectively), and maximum C_{ORG}/P_{TOT} ratios for all ancient sediments, exceed the Redfield ratio of 106 mol/mol, indicating sediment deposition in anoxic bottom waters[6] (Fig. 3.1A and B; Supplementary Table 3.2). Higher than modern C_{ORG}/P_{TOT} values are observed for the T-OAE and OAE2, and the i-282c and S5 sapropels. Such values are not found during the PETM and sapropel S1. The highest maxima, in excess of 1000 mol/mol, are observed for T-OAE, OAE2 and i-282c sediments (1099, 1835 and 1156, respectively).
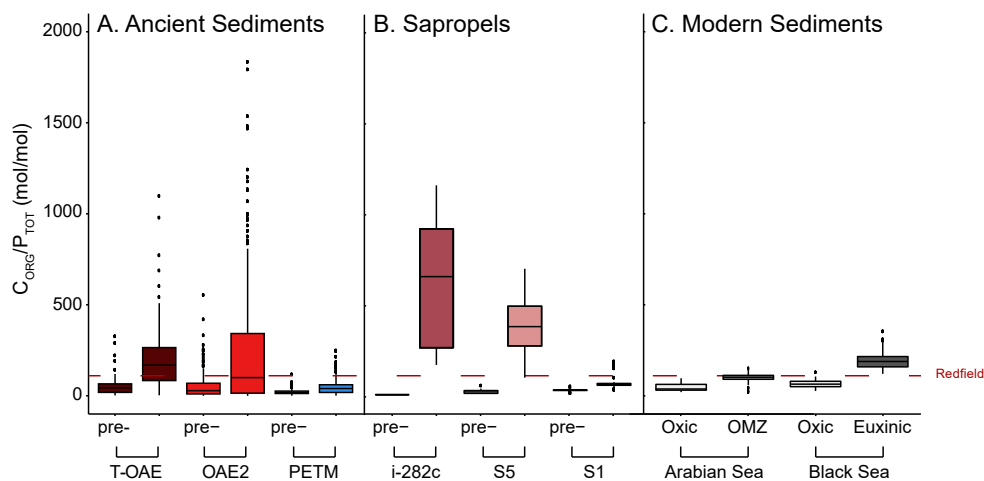
Figure 3.1| Compilation of C_{ORG}/P_{TOT} values for ancient sediments (A), sapropels (B) and modern sediments (C). Ancient sediments were deposited during the Toarcian Oceanic Anoxic Event, Oceanic Anoxic Event 2 and the Paleocene-Eocene Thermal Maximum. The three Eastern Mediterranean sapropels are: i-282c, S5 and S1; pre-event C_{ORG}/P_{TOT} values are presented separately. Modern sediments were deposited in and below the Arabian Sea OMZ, on the oxic Black Sea shelf and in the adjacent euxinic basin. Horizontal lines within the boxplots represent median values. The horizontal red line indicates the Redfield C_{ORG}/P_{ORG} ratio of 106:1.

The lowest median values, and smallest spread, are observed for the PETM and sapropel S1 (40 and 53, respectively). This agrees with earlier work demonstrating more widespread and intense anoxia during the T-OAE, OAE2 and the i-282c and S5 sapropels, when compared to the PETM and sapropel S1 (Jenkyns, 2010; Rohling *et al.*, 2015). Median ratios of C_{ORG}/P_{TOT} for the Arabian Sea OMZ and the euxinic Black Sea are 103 and 189 mol/mol, respectively, and thus fall within the range of median values for the paleo-environments. However, the overall range in C_{ORG}/P_{TOT} ratios in modern sediments from anoxic settings is much lower than during the paleo-events and remains below 400, as observed previously (Algeo and Ingall, 2007).

A comparison of C_{ORG}/P_{TOT} ratios with the corresponding Fe/Al for each study site shows that median ratios of Fe/Al>0.66, indicating anoxic and euxinic facies (Raiswell *et al.*, 2018), are generally observed for ancient sediments with median C_{ORG}/P_{TOT}>106 (Fig 3.2A, B and inset; Supplementary Table 3.3). Most (70%) median Fe/Al>0.66 correspond to sediments from T-OAE, OAE2, i-282c and S5. While median values of C_{ORG}/P_{TOT} and Fe/Al are moderately correlated (R^2=0.47; Fig. 3.2 inset), supporting the utility of C_{ORG}/P_{TOT} ratios as a redox proxy, we note that individual values of Fe/Al>0.66 are observed at almost all sites. This supports the utility of C_{ORG}/P_{TOT} ratios as a redox proxy, but the lack of a stronger correlation also emphasizes the need for an additional mechanism leading to high C_{ORG}/P_{TOT} under anoxic conditions, apart from enhanced recycling of organic and Fe oxide bound P (Ingall *et al.*, 1993; Hartnett, 1998; Algeo and Ingall, 2007; Steebergh *et al.*, 2011). In the next section,
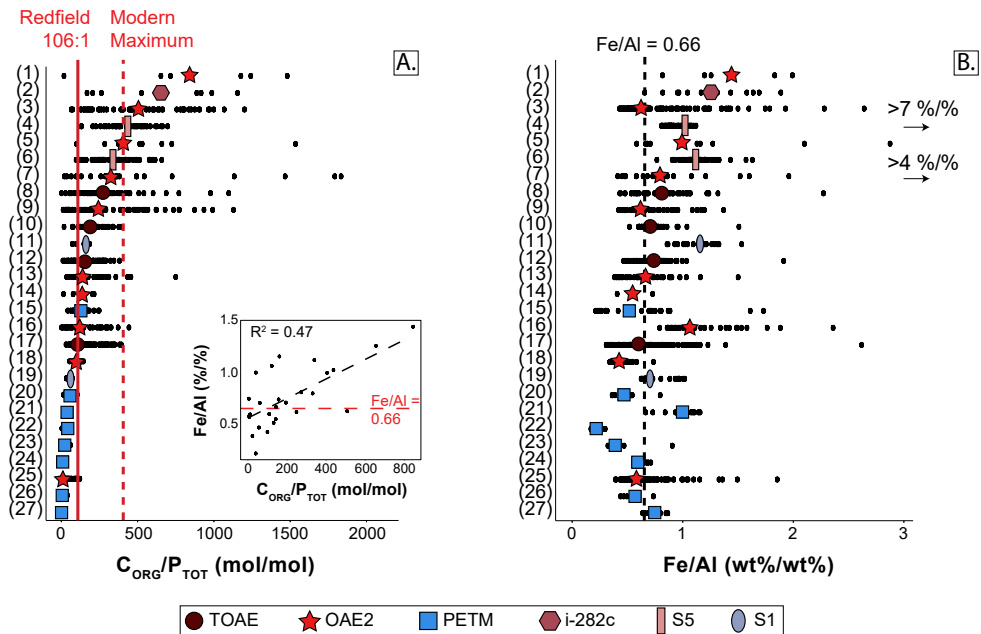
Figure 3.2| Site-specific compilation of C_{ORG}/P_{TOT} (A) and Fe/Al (B) values for the T-OAE (circle), OAE2 (star), PETM (square) and i-282c (rhombus), S5 (rectangle) and S1 (oval) sapropels. Colors are additional indicators of the corresponding events. Two samples with high Fe/Al values of 4 and 7 wt%/wt% are indicated in the right-hand panel with arrows. The vertical lines in (A) and (B) indicate the Redfield C_{ORG}/P_{ORG} value (solid red), the modern maximum C_{ORG}/P_{TOT} value of 400 (red dashed; Algeo and Ingall, 2007) and the Fe/Al threshold for sediments overlain by euxinic bottom waters (black dashed; Raiswell *et al.*, 2018). The figure inset depicts the correlation between the median values of the C_{ORG}/P_{TOT} and Fe/Al ratios for each site. The red dashed line represents the euxinic Fe/Al threshold and the black dashed line is the linear regression line (R2 = 0.47). The sites are sorted from highest median C_{ORG}/P_{TOT} to lowest. The site names corresponding to each number are given in Supplementary Table 3.3.

we argue that variations in CFA formation, under specific environmental conditions, provide such a mechanism.

4. FORMATION OF CFA AS A MODULATOR OF SEDIMENT C_{ORG}/P_{TOT}

While in-situ mechanisms of CFA formation in marine sediments are difficult to resolve because of the multitude of biogeochemical processes involved and slow rates of formation (Ruttenberg, 2003; Van Cappellen and Berner, 1991), a higher degree of supersaturation of the porewater with respect to CFA will promote mineral formation (Supplementary Text). Potential controls on the saturation state include porewater $[PO_4]$, $[F^-]$ and $[Ca^{2+}]$ (Schuffert *et al.*, 1990; Ruttenberg and Berner, 1993; Slomp *et al.*, 1996; Zhao *et al.*, 2020). Furthermore,
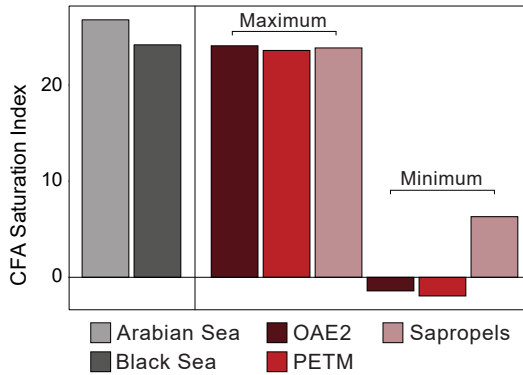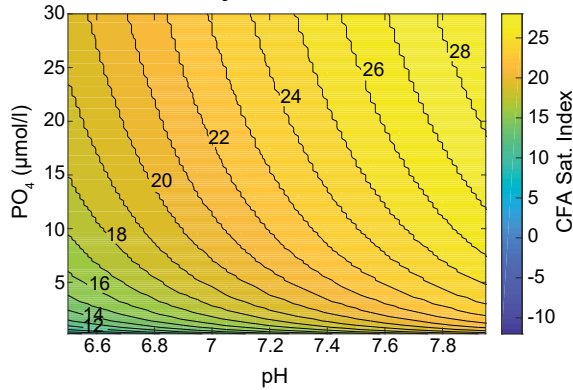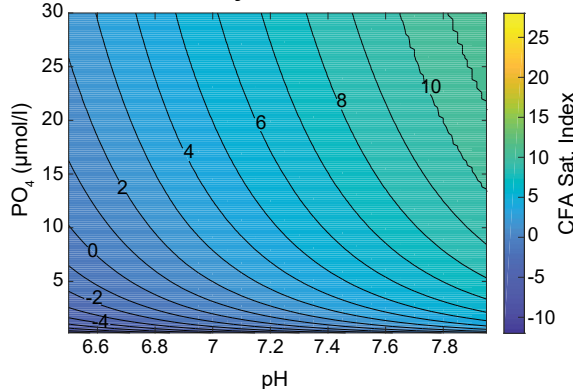
Figure 3.3| Saturation Indices (SI) for carbonate fluorapatite (CFA) as calculated with PHREEQC for A) the modern Arabian Sea and Black Sea anoxic sediments and estimated for OAE2, the PETM and eastern Mediterranean sapropels; for the Arabian Sea OMZ at 9°C (B) and 25°C (C), for a range of [PO_4] (0.2 - 30 µmol l^{-1}) and pH (6.5 - 7.95) values. Input values for the simulations are given in Supplementary Table 3.4.

authigenesis of CFA, or a precursor phase, is promoted by the presence of nucleation surfaces, provided by calcium carbonate ($CaCO_3$) or microbially-derived organic matter (Gunnars *et al*., 2004; Mänd *et al*., 2018). Finally, laboratory experiments have revealed a strong sensitivity of CFA solubility to temperature and pH (Jahnke, 1984).

Here, we use PHREEQC to calculate the response of porewater saturation states, with respect to CFA, at our study sites to variations in pH, temperature and porewater chemistry (Supplementary Text; Supplementary Table 3.4). For modern Arabian Sea OMZ and euxinic Black Sea surface sediments, where CFA formation is observed (Kraal *et al*., 2012; Kraal *et al*., 2017), we find an average saturation index (SI) of ca. 24 and 27, respectively, indicating supersaturation of the porewaters with respect to CFA (Fig. 3.3A; Supplementary Text). A subsequent sensitivity analysis for porewaters of the anoxic Arabian Sea OMZ Station 1B, reveals that an increase in temperature and decrease in pH and $[PO_4]$ results in SI reduction. Within the tested ranges (T: 9 – 25°C; pH: 6.5 – 7.95; $[PO_4]$: 0.2 – 30 µmol l^{-1}), temperature has the largest impact on the SI (Fig. 3.3B – C). For any given pH and $[PO_4]$ combination, the SI at 9°C is 17 units higher than at 25°C, whereas the difference in SI is ~9.5 units between the lowest and highest pH, and ~11 units between the highest and lowest $[PO_4]$. Notably, above a $[PO_4]$ of ca. 5 µmol l^{-1} the changes in SI for further increases in $[PO_4]$ are relatively small when compared to a change in pH. Undersaturation is achieved at 25°C (Fig. 3C), when $[PO_4]$ < 10 µmol l^{-1} and for pH < 7.8.

Increasing evidence demonstrates that many of our ancient sediments, characterized by intense anoxia and high C_{ORG}/P_{TOT} (Fig. 1, 2), were deposited under higher than modern temperatures and lower pH. During OAE2, the equatorial Atlantic ocean warmed to 35 – 36°C (Forster *et al*., 2007) (surface waters) and 20 – 25°C (Friedrich *et al*., 2008) (intermediate waters; 500 – 1000 m). Deep water temperatures were likely in the 12 – 24°C range (Haupt and Seidov, 2001; Friedrich *et al*., 2012). As a result, most OAE2 sites in our data compilation (Fig. 3.2), including those located at great depths (van Helmond *et al*., 2014) (>2000 m), probably experienced temperatures in excess of 20°C. Similarly, during the T-OAE, the European Shelf, where our study sites were located, was subject to substantial warming (Beerling *et al*., 2002; Bailey *et al*., 2003; Suan *et al*., 2008; Krencker *et al*., 2015), with bottom temperatures in the western Tethys increasing by 3.5°C and exceeding 20°C (Ullmann *et al*., 2020). Finally, the deposition of the i-282c and S5 sapropels likely coincided with warming of bottom waters in the Eastern Mediterranean (Dwyer *et al*., 1995 Emeis *et al*., 2003), exceeding the modern day temperature of ~14˚C (MEDAR, 2003). Constraints on pH are more uncertain, but evidence suggests an increase in ocean pH from ~7.5 to 8.2 over the last ca. 100 Myr (Zeebe and Tyrrell, 2019) and a decrease in oceanic pH due to ocean acidification during the T-OAE (Trecalli *et al*., 2012) and the PETM (Zachos *et al*., 2005). Furthermore, pH values in modern surface sediments frequently range between 6.9 and 8.0, and are generally lower than the pH of the overlying waters (Shao *et al*., 2016). Our calculations point towards supersaturation of porewaters with respect to CFA for OAE2, PETM and sapropel sediments at low temperatures (14°C) and maximum pH and PO_4 values (Figure 3.3A; Supplementary Table 3.4). Conversely, when assuming warming to 25°C (17°C for the Eastern Mediterranean), a pH of 6.9 and $[PO_4]$ of 1 µmol l^{-1}, the SI values decrease dramatically, indicating undersaturation with respect to CFA for OAE2 and the PETM. Such conditions would likely have hindered increased CFA authigenesis, which would have had

I. Original Model

II. Inhibited apatite authigenesis
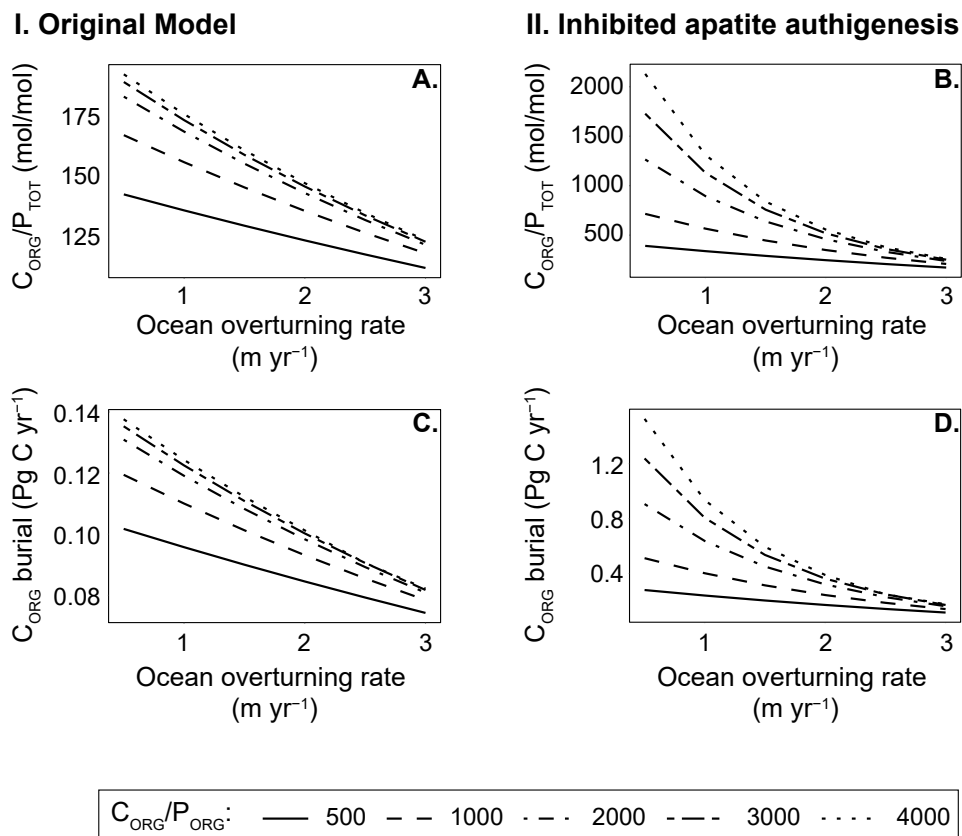
Figure 3.4| Box model output for simulations using the original Van Cappellen and Ingall (1994) model (I) and with reduced apatite authigenesis (II). The C_{ORG}/P_{TOT} (A-B) and C_{ORG} burial rate (C-D) are shown for increasing ocean overturning rates and maximum C_{ORG}/P_{ORG} (lines). Results are shown for ocean overturning rates in the range of $0.5 - 3$ m yr^{-1}, and C_{ORG}/P_{ORG} of 500 to 4000 mol/mol.

a larger impact on sediment P recycling during OAE2 than the PETM because of the more intense anoxia during the former event (Jenkyns, 2010). The effects of other major ions on the SI of CFA, were negligible (Supplementary Text).

The presence of calcium carbonate ($CaCO_3$) in sediments affects the potential for CFA authigenesis, by providing suitable nucleation surfaces (Kraal *et al.*, 2017). Calcium carbonate contents for the most anoxic ancient sediments (T-OAE, OAE2, i-282c and S5) are generally much lower than for modern Arabian and Black Sea sediments, with average values for the two OAEs and i-282c below 20% at most sites (Supplementary Table 3.5). Additionally, an inverse correlation between sediment $CaCO_3$ contents and C_{ORG}/P_{TOT} ratios is observed for i-282c (Supplementary Fig. 3.1), similar to S5 (Kraal *et al.*, 2010b). The low sediment $CaCO_3$ was the consequence of reduced $CaCO_3$ input from overlying waters, as high pCO_2 and oceanic anoxia impacted phytoplankton species (Erba and Tremolada, 2004),

and $CaCO_3$ dissolution upon a decreased pH (Zachos *et al.*, 2005; Trecalli *et al.*, 2012). We propose that the low $CaCO_3$ content at euxinic sites during the T-OAE, OAE2 and sapropel formation, hindered an increase in CFA authigenesis, rendering it insufficient to retain the increased P supply to sediments.

Importantly, a hindrance of CFA formation only leads to extremely high C_{ORG}/P_{TOT} values upon intense anoxia, when recycling of P is enhanced. Under oxic conditions, when P is retained in Fe-oxides and in organic matter and C_{ORG}/P_{ORG} ratios remain close to the Redfield ratio of 106:1, C_{ORG}/P_{TOT} will remain low regardless of whether CFA formation is hindered. Therefore, as anoxia during the PETM and sapropel S1 was not as intense (Jenkyns, 2010; Rohling *et al.*, 2015), C_{ORG}/P_{TOT} ratios remained lower compared to the T-OAE, OAE2, and the i-282c and S5 sapropels (Fig. 3.1, 3.2). To illustrate the effect of C_{ORG}/P_{ORG} on P retention, and the impact of enhanced P recycling on C_{ORG} burial, we use a one-box biogeochemical model for the oceanic C and P cycles (Van Cappellen and Ingall, 1994). We demonstrate that, in simulations for an oxic ocean, C_{ORG}/P_{TOT} values always remain within the modern range (Fig. 3.4A, B). Under increasing deoxygenation, here generated by decreasing the rate of ocean overturning (Van Cappellen and Ingall, 1994), only simulations with high maximum C_{ORG}/P_{ORG} values and inhibited authigenic P burial capture the range of C_{ORG}/P_{TOT} values for ancient sediments (max. 2000 mol/mol) (Fig. 3.4B). When authigenic P burial is not hindered, C_{ORG}/P_{TOT} values remain in the lower half of the modern range (<200 mol/mol). In our model simulations for an ocean that is largely anoxic, the hindrance of authigenic P formation results in an almost tenfold increase in the burial rate of C_{ORG} (Fig. 3.4C, D).

5. CONCLUSIONS

In conclusion, our data compilation and modeling indicate that higher ocean temperatures, lower porewater pH and low(er) $CaCO_3$ contents hampered CFA formation and P retention in the sediment during past periods of oceanic anoxia. This explains the more efficient recycling of P compared to modern times as reflected in higher C_{ORG}/P_{TOT} ratios and contributed to widespread deposition of organic carbon (Fig. 3.4D). Under ongoing climate change, a similar combination of ocean deoxygenation, warming and acidification is projected for the future ocean. The lack of high rates of CFA formation during sapropel formation (Slomp *et al.*, 2004) in particular is a warning that much faster recycling of P relative to C_{ORG} is possible in the modern ocean. This could contribute to a further acceleration of ocean deoxygenation by stimulating primary productivity (Van Cappellen and Ingall, 1994), organic carbon burial and other key feedbacks in the global carbon and oxygen cycles.

Chapter 3
Supplementary Materials

1. SEDIMENT DESCRIPTION

The aim of this study is to elucidate what mechanisms led to stronger P recycling in ancient anoxic marine environments when compared to modern low oxygen settings. For this purpose, we selected intervals from the geological record that varied strongly in their degree of deoxygenation, sediment composition and climatic conditions during deposition. Specifically, we compiled C_{ORG}, P, Fe/Al and $CaCO_3$ data for sediments from the Toarcian Oceanic Anoxic Event (T-OAE), Oceanic Anoxic Event 2 (OAE2) and the Paleocene-Eocene Thermal Maximum (PETM), as well as for three Mediterranean sapropels (i-282c, S5 and S1) and two modern anoxic marine areas: the Arabian Sea and the Black Sea. The ancient and sapropel data cover sediments deposited before and during the spread of deoxygenation. For the Arabian Sea, we focus on sediments from within and below the OMZ, while the Black Sea data include sediments from the oxic shelf and the euxinic deep basin. The ancient and modern sediments cover both shallow and deep depositional settings (Supp. Table 3.1). The full list of references for the data used in this study is given per site in Supp. Table 3.1, and at the end of this document.

The T-OAE and OAE2 are two of the most severe deoxygenation events in Earth's history (Jenkyns, 2010). Sulfur isotope values increased by 5 — 7‰ for the T-OAE (Gill *et al.*, 2011) and up to 5‰ for OAE2 (Owens *et al.*, 2013). This increase was interpreted as a spread of euxinic conditions over 2-5% of the ocean seafloor, close to the estimate of ≤2% based on molybdenum isotopes (Dickson *et al.*, 2016). For comparison, in the modern ocean sulfidic waters cover ~0.15% of the seafloor (Clarkson *et al.*, 2018). Uranium isotopes for OAE2 suggest that 8 — 15% of the seafloor was anoxic (Clarkson *et al.*, 2018). These conditions were caused by enhanced volcanic CO_2 and methane emissions, which resulted in high atmospheric pCO$_2$ and a warmer and, in some areas, wetter climate (Jenkyns, 2010). The greenhouse climate resulted in water column stratification, while increased continental weathering also led to an increase in nutrient supply to the oceans (Jenkyns, 2010). The combination of these factors stimulated the spread of oceanic anoxia (Jenkyns, 2010). Most of the known locations that were characterized by anoxic bottom waters during the T-OAE were shallow and epicontinental (Ruvalcaba Baroni *et al.*, 2018). The sulfur isotope record, however, suggests a larger areal extent of anoxia (Gill *et al.*, 2011), potentially including deep sites. Anoxic bottom waters occurred in both shallow and deep settings during OAE2 (Kraal *et al.*, 2010a).

During the PETM, similar perturbations of the exogenic C cycle resulted in widespread deoxygenation (Sluijs *et al.*, 2014), yet it was less severe in comparison to the two OAEs. The sulfur isotope excursion was 1‰ (Yao *et al.*, 2018), suggesting a minor expansion in sulfidic bottom water area, and molybdenum isotopes also support less-extensive euxinia during the PETM, than during the two OAEs (Dickson *et al.*, 2017). Additionally, uranium isotopes indicate that less than 2% of the seafloor was overlain by anoxic bottom waters (Clarkson

et al., 2021). Regardless, it is hypothesized that the sediment burial of C_{ORG} resulted in CO_2 drawdown during all three events (Bowen and Zachos, 2010; Jarvis *et al.*, 2011; Ruvalcaba Baroni *et al.*, 2018).

In contrast to the large spatial extent of the anoxia during the three chosen events, the conditions that led to sapropel formation were restricted mostly to the Eastern Mediterranean. Intense rainfall during stronger monsoon intervals resulted in stratification and deoxygenation, which in turn increased the burial of C_{ORG} and the recycling of P (Rohling, 1994; Slomp *et al.*, 2004). Bottom water conditions during the formation of S1 were generally less reducing than for S5 and i-282c (Slomp *et al.*, 2004; Andersen *et al.*, 2020).

Other examples of intervals that experienced deoxygenation are the Late Permian, OAE1a and the glacial-interglacial cycles. However, various indicators, such as the lack of high C_{ORG}/P_{TOT} suggest anoxia was likely not as severe and P recycling was not as enhanced, as during the T-OAE and OAE2 (Palastanga *et al.*, 2013; Beil *et al.*, 2020; Schobben *et al.*, 2020). These events are therefore not included in this study, as the PETM, and also sapropel S1, already provide examples for milder deoxygenation and P recycling. Additionally, there is more data available on the degree and extent of these changes for the PETM (Sluijs *et al.*, 2014).

2. DATA COMPILATION

In modern marine sediments, the ratios of organic carbon (C_{ORG}) to organic P (P_{ORG}) (C_{ORG}/P_{ORG}) and to total P (C_{ORG}/P_{TOT}) track bottom water redox conditions (Anderson *et al.*, 2001). A low $[O_2]$ favors the preservation of C_{ORG}, while promoting the preferential regeneration of P_{ORG} (Ingall *et al.*, 1993). This results in elevated C_{ORG} contents relative to P_{ORG} and an increased C_{ORG}/P_{ORG} ratio (Ingall *et al.*, 1993). The rate of authigenic mineral formation determines what proportion of the P released from organic matter is retained in the sediment (in the absence of Fe oxides, see main text). Sediment P speciation can provide insight in the response of different P sinks to environmental conditions during deposition (Ruttenberg, 2003).

The application of P speciation, however, is limited by sample storage (Kraal *et al.*, 2009) and sediment age (Kraal *et al.*, 2010b). As degradation of organic matter continues during burial, sediment P_{ORG} values gradually decrease on time scales of kyrs to Myrs. This can result in high C_{ORG}/P_{ORG} values that do not reflect the original conditions during deposition (Kraal *et al.*, 2010b). The P that is released from organic matter during long-term burial is typically retained as authigenic apatite (Kraal *et al.*, 2009). hence C_{ORG}/P_{TOT} values are not affected. This long-term diagenetic sink-switching precludes the use of P speciation data for the T-OAE, OAE2 and PETM. The age of sapropel S5, however places it in the 600 – 700 kyr window, in which C_{ORG}/P_{ORG} ratios for the Mediterranean Sea mostly reflect depositional conditions (Kraal *et al.*, 2010b). For sapropel i-282c, C_{ORG}/P_{ORG} values could be somewhat affected by diagenesis, though C_{ORG} and barium records suggest this is not the case (Slomp *et al.*, 2004).

For the i-282c and S1 sapropels, apatite (both authigenic and biogenic) make up at least a third of total P burial (Slomp *et al.*, 2004). A large proportion of this authigenic apatite is thought to be a background flux from dust (Eijsink *et al.*, 2000; Slomp *et al.*, 2004). During

formation of the S5 sapropel, authigenic apatite decreased and recycling of P to the water column increased (Kraal *et al.*, 2010b). In the Arabian Sea, in contrast, the down-core increase of apatite at the most anoxic sites (1B and 2) indicates apatite authigenesis (Kraal *et al.*, 2012). This process also occurs in the deep euxinic basin of the Black Sea, where it begins in the upper centimeters of the sediment column (Kraal *et al.*, 2017), as it does in other areas in the modern ocean (Jahnke *et al.*, 1983; Ruttenberg and Berner, 1993; Slomp *et al.*, 1996). We compare C_{ORG}/P_{ORG} and C_{ORG}/P_{TOT} ratios for the S5 and i-282c sapropels, both of which have $C_{ORG}/P_{TOT} > 400$ mol/mol, to those in the modern Black Sea and Arabian Sea below. Data for C_{ORG}/P_{TOT} as shown in Fig. 3.1 are given in Supp. Table 3.2.

Various proxies are used for the reconstruction of global and local bottom water redox conditions. While global proxies are useful for a comparison of the spatial extent of anoxic waters at the global scale between events (as discussed above), local redox information is required to evaluate whether differences in redox conditions can explain differences in C_{ORG}/P_{TOT} values between sites. To assess the local occurrence and intensity of bottom water anoxia, three proxies are often used: sediment molybdenum (Mo), uranium (U) and the ratio of iron (Fe) over aluminum (Al). However, Mo records can be affected by basinal restriction, as shown for two of our studied events (McArthur *et al.*, 2008; van Helmond *et al.*, 2014; Goldberg *et al.*, 2016; Ruvalcaba Baroni *et al.*, 2018), for which a decoupling of Mo values from variations in deoxygenation was observed (Algeo and Lyons, 2006). As U data are only sparsely available, we elected to use the Fe/Al ratio. High Fe/Al (>0.66 on a weight basis) is assumed to reflect enhanced input of Fe and its sequestration as pyrite in sediments under anoxic and sulfidic bottom waters (Lyons and Severmann, 2006; Raiswell and Canfield, 2012).

3. CARBONATE FLUORAPATITE FORMATION

The formation of carbonate fluorapatite (CFA) (r_{CFA}) depends on the saturation state of porewaters (Van Cappellen and Berner, 1991), and can be expressed as (Zhao *et al.*, 2020):

$$r_{CFA} = k_{CFA}(\Omega_{CFA}-1)$$

where k_{CFA} is a rate constant and Ω_{CFA} is the saturation state with respect to CFA (with supersaturation when $\Omega_{CFA} > 1$). This formula suggests that the growth rate of CFA is nearly linearly dependent on the saturation state, but this is likely an oversimplification. For fluorapatite, for example, the rate of crystal growth can accelerate above a certain, threshold saturation state (Van Cappellen and Berner, 1991). It is therefore likely that the rate of formation of CFA also increases more strongly at higher degrees of supersaturation, especially in the presence of suitable nucleation surfaces (Mänd *et al.*, 2018).

The thermodynamic effects of temperature and pH on solubility of CFA can be partially offset by kinetic effects acting in the opposite direction, increasing the rate constant for CFA formation (Van Cappellen and Berner, 1991). Importantly, the compound result of such kinetic effects expected for OAE2 and the PETM do not compensate for the effect of the decrease in SI and hence Ω_{CFA} (Supp. Table 3.4) on the rate of CFA formation. The kinetic effects become irrelevant when undersaturation is reached and CFA formation comes to a halt.

4. SATURATION INDEX CALCULATIONS FOR CFA

We calculate the porewater saturation index (SI, which is equal to log Ω_{CFA}) for the ancient and modern sediments with the PHREEQC model (Parkhurst and Appelo, 2013) in combination with the Lawrence Livermore National Laboratory (LLNL) database for thermodynamic data, using Davies equations for activity coefficients. Currently there are no parameters available for phosphate in the PHREEQC Pitzer database. However, for calculations of the SI for other Ca-containing phases such as gypsum, results are comparable when using either the Pitzer or the LLNL database, up to salinities of about a 100 (Appelo and Postma, 2004; Grothe *et al.*, 2020; Wolthers, personal observations), because the ion-pairs are considered when using the LLNL database, resulting in similar free ion activities. The porewater saturation state was calculated for carbonate bearing CFA with the following formula:

$$Ca_{10}(PO_4)_{5.83-0.57X}(CO_3)_X F_{2.52-0.3X}$$
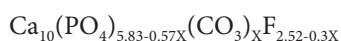
where X is 1.45. This solid composition, with 1.45 CO_3^{2-} for every ten Ca^{2+}, is comparable to a carbonate-rich francolite (Jahnke, 1984; Zhao *et al.*, 2020). Solubility coefficients for CFA were taken from (Jahnke, 1984), which includes solubility products (Ksp) for 9°C, 14°C and 25°C for PO_4^{3-}. Due to the fixed composition of our solid CFA, Ksp only varies with temperature. Ksp can also vary with $[CO_3^{2-}]$, however the influence of this is relatively small (Zeebe and Tyrrell., 2019; Zhao *et al.*, 2020).

For this study, Ksp values were recalculated for HPO_4^{2-} and additional values were extrapolated along an exponential trendline. These values can be used safely between 9 – 25˚C. The saturation indices obtained were calculated by PHREEQC as:

$$SI = \log IAP - \log K_{sp}$$

where IAP is the activity product of the ions making up the CFA. As a result, an SI increase of one unit results in an order of magnitude increase in the degree of supersaturation.

The use of PHREEQC to calculate the saturation state with respect to CFA allows for a comparison of geological settings while minimizing the number of assumptions required. For our calculations, we estimate the likely range of values for the pH and $[PO_4^{3-}]$, $[CO_3^{2-}]$ and $[F^-]$ for the chosen paleo-depositional environments, based on what is known about their biogeochemistry. The aim of these PHREEQC calculations is to determine whether porewaters in ancient sediments were likely undersaturated with respect to CFA, effectively preventing the formation of CFA, or whether the degree of supersaturation was insufficient for CFA formation to keep pace with the supply of P to sediments.

5. PHREEQC SENSITIVITY RANGES

We used measured porewater concentrations for the modern sediments and estimated values for the ancient sediments as input for the PHREEQC calculations, as detailed below. Obviously, porewater and seawater concentrations and environmental characteristics for ancient marine systems cannot be measured directly and hence must be derived from, e.g.,

proxy and modelling studies. Here, we use a range of values for $[PO_4]$, pH, temperature and key solute concentrations. Where possible, these ranges are based on estimates for seawater and porewater values from earlier studies.

For the modern Arabian Sea and Black Sea, porewater concentrations were obtained through sampling and analyses in 2009 (Kraal *et al.*, 2012) and 2015 (Kraal *et al.*, 2017), respectively. For OAE2, the PETM, and the i-282c and S5 sapropels, we estimated minimum and maximum porewater concentrations of major ions from model and proxy data for bottom waters (Supp. Table 3.4). Note that we did not include the T-OAE because of a lack of sufficient data on seawater composition. For $[PO_4]$, our range (1 µmol l^{-1} and 11 µmol l^{-1}) captures the values used by (Monteiro *et al.*, 2012) for OAE2 simulations, the low bottom water $[PO_4]$ of the modern SE Mediterranean (~2 µmol l^{-1}) (MEDAR Group, 2003), the maximum porewater concentrations estimated for sapropel S1 based on diagenetic modelling (6.5 µmol l^{-1}) (Reed *et al.*, 2011) and the average value for modern porewaters in sediments of the euxinic basin of the Black Sea (~10 µmol l^{-1}), where CFA authigenesis occurs. For OAE2, we also tested the effect of the much higher $[PO_4]$ concentrations that are found in porewaters of the Arabian Sea (80 µmol l^{-1}). Our range of values is thus wide enough to account for both low $[PO_4]$ in porewaters in deep sea sediments and increased porewater $[PO_4]$ following deoxygenation.

The maximum pH values used for OAE2 (7.6) and the PETM (7.7) correspond to the estimated, average ocean pH during their respective time periods (Shao *et al.*, 2016), while for sapropels the value corresponds to the water column pH of the modern Eastern Mediterranean (8.2) (MEDAR Group, 2003). The minimum pH value used for all ancient sediments is 6.9 and accounts for the generally lower pH values in porewaters (Shao *et al.*, 2016). These ranges cover the pH values for modern marine surface sediments (top 10 cm) (Shao *et al.*, 2016).

The chosen temperature range for OAE2 is based on proxy and model reconstructions of temperature during the event (Haupt and Seidov, 2001; Forster *et al.*, 2007; Friedrich *et al.*, 2008). The range of bottom water temperatures for the PETM is similar to OAE2 (Tripati and Elderfield, 2005; Friedrich *et al.*, 2012; Jones *et al.*, 2013). Therefore we use a minimum temperature of 14°C and a maximum temperature of 25°C for both events. Sapropel i-282c was deposited during a period of warming (Dwyer *et al.*, 1995) and the deposition of sapropel S5 corresponds to a solar insolation maximum (Frant *et al.*, 2016). We, therefore, assign a maximum temperature of 17°C to our sapropel calculations, which is a few degrees higher than the modern bottom value of 14°C for the Eastern Mediterranean south of Crete (MEDAR Group, 2003). The full list of values and their references can be found in Supp. Table 3.4.

We also tested the effect of changes in alkalinity and $[Ca^{2+}]$, $[Mg^{2+}]$ and $[SO_4^{2-}]$ on the saturation index of CFA using the corresponding average ocean value for each time period (Zeebe and Tyrrell, 2019). Overall the effects of changes in these parameters were small to negligible when compared to those of temperature, pH and $[PO_4]$. For OAE2, an increase in $[Ca^{2+}]$ from 17 mmol Ca kg^{-1} to 29 mmol Ca kg^{-1}, the maximum range tested here, had the largest effect of the three ion concentrations, yet we only observed an increase in SI of ~2

units. Furthermore, as ocean $[Ca^{2+}]$ during the ancient events (>10 mmol Ca l^{-1}) was higher than that in the modern Arabian Sea (~10 mmol Ca l^{-1}) and Black Sea (~7 mmol Ca l^{-1}), changes in $[Ca^{2+}]$ cannot have contributed to the reduction in CFA authigenesis during past deoxygenation events.

Within the ranges tested, the effect of temperature on SI was an increase of ~13 units for OAE2 and the PETM and ~3 units for the sapropels, or an increase of roughly 1 unit per 1°C. Similarly, the effect of a change in pH was 4.7 for OAE2, 5.3 for the PETM and ~8 for the sapropels. Within the 1 – 11 μmol l^{-1} range for $[PO_4]$, the change in SI was equal to 5 for all ancient sediments. However, as we note in the main text, the effect of changes in $[PO_4]$ was largest at low concentrations, whereas the effect of a change in pH and temperature remained constant. This is why, even with much higher $[PO_4]$ (80 μmol l^{-1}), the change in SI is only 4 units. For the sapropels, due to the larger range for pH and the smaller temperature range, the effect of $[PO_4]$ is relatively more important. However, for OAE2 and the PETM the combined effect of temperature and pH is more significant, producing lower SI values irrespective of the $[PO_4]$.
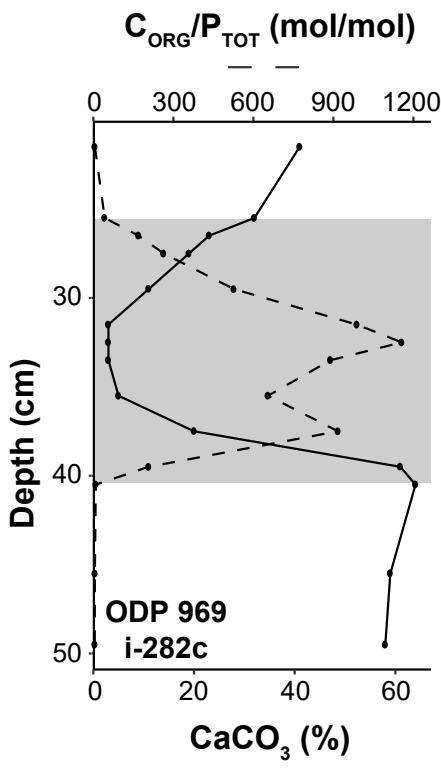
Supplementary Figure 3.1| Calcium carbonate content ($CaCO_3$; solid line) and C_{ORG}/P_{TOT} values (dashed line) for sapropel i-282c sediments from ODP Site 969 (Slomp *et al.*, 2004). The grey area indicates the position of the sapropel.

6. Sediment CaCO$_3$

Average CaCO$_3$ contents for all sites are given in Supp. Table 3.5. Profiles of C$_{ORG}$/P$_{TOT}$ and CaCO$_3$ for sapropel i-282c (ODP Site 969) (Slomp *et al.*, 2004) are shown in Supp. Fig. 3.1.
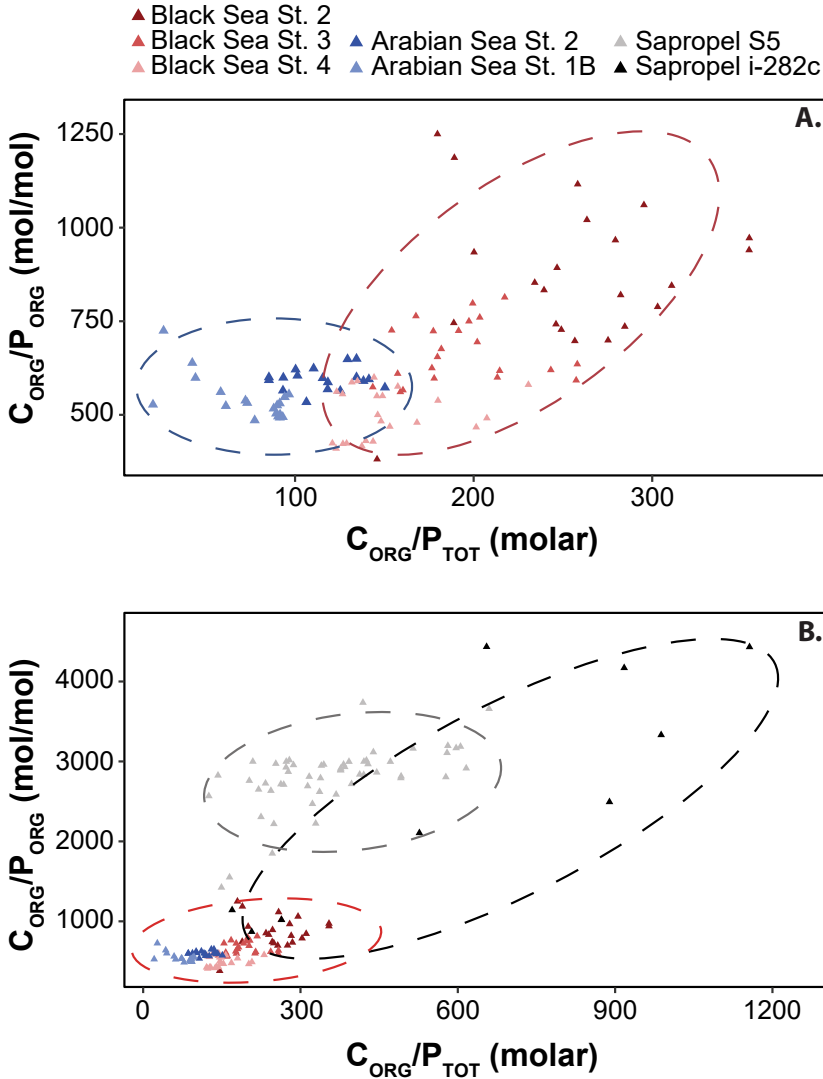
Supplementary Figure 3.2| Relationship between sediment C$_{ORG}$/P$_{TOT}$ and C$_{ORG}$/P$_{ORG}$ for (A) three sites in the euxinic basin of the Black Sea (Kraal *et al.*, 2017) and two sites from the Arabian Sea OMZ (Kraal *et al.*, 2012), and (B) the Black Sea and Arabian Sea data combined with data for the i-282c (Slomp *et al.*, 2004) and S5 sapropels (Kraal *et al.*, 2010b). Dashed circles indicate the approximate extent of values for each area or event, as well as the general trend.

7. RECYCLING OF P RELATIVE TO C_{ORG} AND ITS IMPACT ON OCEANIC CARBON CYCLING

Organic matter is the dominant source of P to sediments (Ruttenberg, 2003). Hence, enhanced recycling of P from organic matter under low $[O_2]$, which is reflected in high C_{ORG}/P_{ORG}, is a prerequisite for high sedimentary C_{ORG}/P_{TOT}.

Variations in the rate of formation of authigenic carbonate fluorapatite (CFA) will then further determine the range of C_{ORG}/P_{TOT} values encountered in a given anoxic or euxinic setting and the impact on the marine P and C cycles. For example, in sediments of the Arabian OMZ, C_{ORG}/P_{ORG} values exceed 500 mol/mol but C_{ORG}/P_{TOT} values are <200 mol/mol (Kraal *et al.*, 2012). Similarly, in sediments of the euxinic Black Sea basin, maximum C_{ORG}/P_{ORG} values are well above 1000 mol/mol but C_{ORG}/P_{TOT} does not exceed 400 mol/mol (Kraal *et al.*, 2017) (Supp. Fig. 3.2). These differences in C_{ORG}/P_{ORG} and C_{ORG}/P_{TOT} values in the Arabian Sea and Black Sea are in accordance with the less intense anoxia and the higher rates of CFA formation in the former system.

Values of C_{ORG}/P_{ORG} and C_{ORG}/P_{TOT} values for the two most intense sapropels (i-282c and S5) in contrast, range up to nearly 4300 mol/mol and 1200 mol/mol, respectively, and hence are at least an order of magnitude higher than those for the Arabian Sea and Black Sea (Supp. Fig. 3.2). If authigenesis of CFA was capable of retaining the P released from organic matter, C_{ORG}/P_{TOT} values for the sapropels should not have exceeded the modern maximum. We attribute the high C_{ORG}/P_{TOT} values during formation of these sapropels to the effects of ocean warming and acidification on CFA authigenesis.

We illustrate the potential consequences of lower rates of CFA authigenesis for oceanic P and C cycling with results from the Van Cappellen and Ingall (1994) ocean box model. In our simulations, we used two versions of the model: (A) the original version in which CFA formation is only related to the rate of organic matter decay, following:

$$FP_4 = kp_4 \times FP_2^{2.5} \qquad (4.1)$$

where FP_4 is the rate of CFA authigenesis, kp_4 is a rate constant and FP_2 is the rate of organic matter decay (see (Van Cappellen and Ingall, 1994) for the full model description); (B) a version with a modified rate law which adds a dependency to the formation of authigenic CFA (1) which is assumed to reflect the impact of the simultaneous warming and decrease in

$$FP_4 = (1 - DOA) \times kp_4 \times FP_2 \qquad (4.2)$$

pH that accompanies the change in bottom water redox conditions:

where *DOA* is the degree of anoxia. A DOA value of 0 describes a fully oxic ocean whereas a fully anoxic ocean results in a value of 1. In our simulations, we assessed the sensitivity of DOA, C_{ORG}/P_{TOT} and C_{org} burial to changes in the rate of ocean overturning and changes in the maximum C_{ORG}/P_{ORG} for burial under anoxic conditions over a range of 500 to 4000. The steady state simulations with the original model show that lower mixing rates and higher C_{ORG}/P_{ORG} values result in an increase in the DOA, C_{ORG}/P_{TOT} and C_{ORG} burial (Supp. Fig.

3.3; Fig. 3.4). Importantly, C_{ORG}/P_{TOT} stays below a value of 200, despite the wide range of C_{ORG}/P_{ORG}. In contrast, in model simulations with inhibited CFA formation, the increase in DOA is stronger and an order of magnitude higher C_{ORG}/P_{TOT} values and C_{org} burial rates are observed. Hence, without inhibited CFA authigenesis, C_{ORG}/P_{TOT} values remain well within the modern range even for the more extreme scenarios. Values similar to those found for OAE2 (up to at least 1200 mol/mol, see main text) are only observed for scenarios with inhibited authigenesis and strong anoxia, as reflected in high values of DOA, and C_{ORG}/P_{ORG} >2000 mol/mol. These results highlight that a combination of severe deoxygenation and inhibited CFA formation are required to explain the high C_{ORG}/P_{TOT} values found in ancient sediments. They also demonstrate that the high rates of C_{ORG} burial in the ocean during ancient anoxia are likely linked to the low rates of CFA authigenesis.
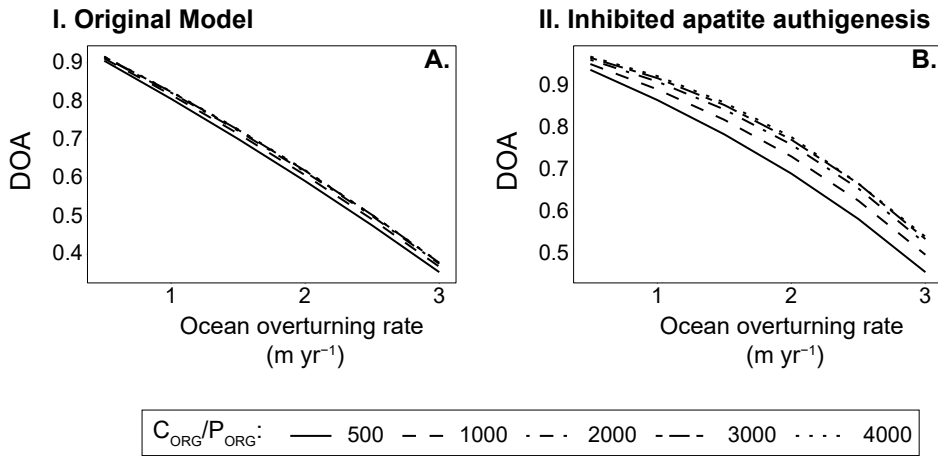
Supplementary Figure 3.3| Steady state box model output for simulations using the original model by (Van Cappellen and Ingall1 1994) (I) and with inhibited apatite authigenesis (I). The degree of anoxia (DOA; A-B) is shown for increasing ocean overturning rates and maximum C_{ORG}/P_{ORG} (lines). Results are shown for ocean overturning rates in the range of 0.5 – 3 m yr^{-1}, and C_{ORG}/P_{ORG} of 500 to 4000 mol/mol.

Supplementary Table 3.1| Complete list of sources for the data shown in: Fig. 3.1 (C_{ORG}/P_{TOT}), Fig. 3.2 (C_{ORG}/P_{TOT} and Fe/Al) and Supp. Fig. 3 ($CaCO_3$). Full references are given in the Supplementary Information.

Site	Event/Basin	Depositional setting	C_{org}/P_{tot} (molar)	Fe/Al (%/%)	$CaCO_3$ (%)
Schandelah			[1]	[1]	[4] ([1])
Dotternhausen	T-OAE	Epicontinental Shelf	[2] ([1])	[2] ([1])	[2] ([1])
Rietheim			[3]	[3] ([1])	[3]
Yorkshire			[2] ([1])	[2] ([1])	[2] ([1])
ODP 1260		Continental slope	[5]	[10]	[10]
Tarfaya S57		Continental shelf	[5]	[11] ([5])	[11] ([5])
DSDP 641			[6]	[6]	[16]
DSDP 603			[5]	[12]	[7] ([5])
DSDP 386	OAE2	Deep ocean	[6]	[6]	[16]
DSDP 367			[7] ([6])	[12]	[17]
ODP 1276			[6]	[6]	[16]
DSDP 530			[5]	[13]	[18]
Bass River		Continental shelf	[8]	[14]	[14]
Wunstorf		Epicontinental shelf	[9]	[15]	[15]
Bass River		Continental shelf	[19]	[19]	[24]
IODP M006, ACEX	PETM		[19]	[23]	[23]
IB10		Epicontinental shelf	[20]	[20]	[20]
ODP 959		Continental slope	[21]	[21]	[21]

Site	Event/Basin	Depositional setting	C_{org}/P_{tot} (molar)	Fe/Al (%/%)	$CaCO_3$ (%)
IODP 1403		Deep ocean	[19]	[19]	[25]
ODP 1172	PETM	Continental shelf	[19]	[19]	[19]
ODP 752		Continental slope	[19]	[19]	[19]
Forada			[22]; [19]	[19]	[22]
ODP 969	i-282c	Deep ocean	[26]	[26]	[26]
PS25PC	S5	Deep ocean	[27]	[28]	[28]
KC16C			[27]	[27]; [29]	[30]
MS21PC	S1	Deep ocean	[31]	[32]	[32]
KC19C			[27]	[27]; [29]	[30]
1B (OMZ)					
2 (OMZ)					
3					
4					
5	Arabian Sea	Continental Slope (Oxygen Minimum Zone)		[33]	
6B					
7					
8					
9					
10					
2 (Anoxic)	Black Sea	Deep ocean		[34]	
3 (Anoxic)		Continental slope			

3

Site	Event/Basin	Depositional setting	C_{org}/P_{tot} (molar)	Fe/Al (%/%)	CaCO$_3$ (%)
4 (Anoxic)		Continental slope			
6A	Black Sea			[34]	
6B		Continental shelf			
7					

[1] Ruvalcaba Baroni *et al.*, 2018; [2] Harding, 2004 (thesis) [3] Montero-Serrano *et al.*, 2015; [4] Papadomanolaki *et al.*, unpublished; [5] Kraal *et al.*, 2010a; [6] van Helmond *et al.*, 2014a; [7] Kuypers *et al.*, unpublished; [8] van Helmond *et al.*, 2014b; [9] van Helmond *et al.*, unpublished (2015) [10] van Bentum *et al.*, 2009; [11] Kolonic *et al.*, unpublished (2005) [12] Owens *et al.*, 2012; [13] Kraal *et al.*, unpublished; [14] van Helmond *et al.*, unpublished (2014b); [15] Hetzel *et al.*, 2011 [16] van Helmond *et al.*, unpublished (2014a); [17] Kraal *et al.*, 2009; [18] Forster *et al.*, 2008; [19] Papadomanolaki *et al.*, 2021; [20] Frieling *et al.*, 2017; [21] Frieling *et al.*, 2018; [22] Giusberti *et al.*, 2007; [23] Sluijs *et al.*, 2008; [24] John *et al.*, 2008; [25] Penman *et al.*, 2016; [26] Slomp *et al.*, 2004; [27] Kraal *et al.*, 2010b; [28] Slomp, unpublished; [29] Passier *et al.*, 1998; [20] De Lange *et al.*, unpublished; [31] Zwiep *et al.*, 2018; [32] Hennekam, personal communication; [33] Kraal *et al.*, 2012; [34] Kraal *et al.*, 2017

Supplementary Table 3.2| Median and maximum C_{ORG}/P_{TOT} values for the Black Sea, Arabian Sea, T-OAE, OAE2, PETM and i-282c, S5 and S1 sapropels, as shown in Fig. 3.1. For references, see Supp. Table 3.1. OMZ: Oxygen Minimum Zone.

Area/Event		C_{ORG}/P_{TOT} (mol/mol)	
		Median	Maximum
T-OAE	pre-	44	327
	event	169	1099
OAE2	pre-	28	554
	event	100	1835
PETM	pre-	17	118
	event	40	249
i-282c	oxic	6	9
	sapropel	655	1156
S5	oxic	18	55
	sapropel	315	698
S1	oxic	27	50
	sapropel	53	187
Arabian Sea	below OMZ	38	97
	OMZ	103	151
Black Sea	oxic	64	130
	euxinic	189	354

3

Supplementary Table 3.3| Median C_{ORG}/P_{TOT} and Fe/Al values for the T-OAE, OAE2, PETM and i-282c, S5 and S1 sapropels, as shown in Fig. 3.2. For references, see Supp. Table 3.1. Numbers correspond to those given on the vertical axis of Fig. 3.2.

Event	Site	Number	C_{ORG}/P_{TOT} (mol/mol)	Fe/Al (%wt/%wt)
T-OAE	Schandelah	8	272	0.81
	Dotternhausen	10	194	0.71
	Rietheim	12	157	0.74
	Yorkshire	17	109	0.60
OAE2	ODP 1260	7	331	0.80
	Tarfaya S57	3	507	0.63
	DSDP 641	14	142	0.55
	DSDP 603	9	248	0.62
	DSDP 386	1	844	1.44
	DSDP 367	5	405	1.00
	ODP 1276	13	144	0.67
	DSDP 530	16	122	1.06
	Bass River	18	100	0.43
	Wunstorf	25	7	0.58
PETM	Bass River	22	40	0.22
	IODP M006, ACEX	15	131	0.52
	IB10	23	23	0.39
	ODP 959	20	56	0.47
PETM	IODP 1403	27	5	0.75
	ODP 1172	21	40	1.00
	ODP 752	24	11	0.60
	Forada	26	7	0.57
i-282c	ODP 969	2	655	1.26
S5	PS25PC	6	340	1.12
	KC19C	4	438	1.02
S1	MS21PC	19	61	0.71
	KC19C	11	161	1.16

Supplementary Table 3.4| Input values for the PHREEQC Saturation Index (SI) calculations, as shown in Fig. 3.3A. For OAE2, the PETM and the sapropels, a number of different combinations were tested, with values and SI results that fall between the ones presented in the table. For the Black Sea and Arabian Sea, calculations were performed for four depths between 0.25 cm and 32.5 cm. The average SI for each location is shown here. Numbers between brackets refer to references as given below the table. Full references are given in the Supplementary Information.

Basin/Event	Site	Description	T(°C)	pH	PO₄ (μmol/l)	Ca (mmol/kg)	Alk (mmol/kg)	Mg (mmol/kg)	SO₄ (mmol/kg)	SI
OAE2	-	Min[a]	25[1]	6.9[2]*	1.1[3]	17[2]	2[2]	40[2]	14[2]	-1.2
		Max[a]	14[1]	7.6[2]	11[3]	29[2]	2.5[2]	30[2]	8[2]	24.3
		Test			80					28.6
PETM		Min[a]	25[4,5]	6.9[6]*	2.5[6]	15[2]	2[6]	40[2]	15[2]	0.05
		Max[a]	14[4,5]	7.7[6]	3[6]	22[2]	2.5[6]	30[2]	10[2]	21
Saprope;s		Min[a]	17[7-11]	6.9*	1[7]	10[2]	2[2]	50[2]	26[2]	6.3
		Max[a]	14[7-11]	8.2[12,13]	6.5[14]	13[2]	3[2]	45[2]	23[2]	22.9
Arabian Sea	Station 1B	Modern[b]	10[17]	7.65[17]	66.7[17]	~10[10]	3.3[17]	77.8[17]	28.5[17]	26.8
		Future	25	6.9						4.3
Black Sea	Station 2	Modern[b]	9.1[15]	7.43[16]	10.3[15]	6.64[15]	5[15]	32.4[15]	16.3[15]	24.2
		Future	25	6.9						3.4

a: Values that result in minimum and maximum SI values; b: Depth averaged values; *: Shao et al., 2016; 1: Friedrich et al., 2012; 2: Zeebe and Tyrrell, 2019; 3: Monteiro et al., 2012; 4: Tripati and Elderfield, 2005; 5: Dunkley Jones et al., 2013; 6: Komar and Zeebe, 2017; 7: MEDAR/ MEDATLAS, 2003; 8: Dwyer et al., 1995; 9: Herbert et al., 2015; 10: Sangiorgi et al., 2013; 11: Emeis et al., 2003; 12: Techtmann et al., 2015; 13: Abdel-Halim and Aly-Eldeen, 2016; 14: Reed et al., 2011; 15: Kraal et al., 2017; 16: Hermans et al., unpublished; 17: Kraal et al., 2012

3

Supplementary Table 3.5| Calcium carbonate contents ($CaCO_3$: average, maximum, minimum) for all sites presented in Fig. 3.2. For the T-OAE, OAE2, PETM and the sapropels, the pre-event/sapropel values are also given. The values given for the Arabian Sea and Black Sea cover the sampled depths at each station. References are listed in Supp. Table. 3.1.

Site	Event/Basin	$CaCO_3$					
		Pre-event/sapropel			Event/sapropel		
		Average	Max.	Min.	Average	Max.	Min.
Schandelah	T-OAE	0	0	0	20	41	0
Dotternhausen		26	42	12	33	79	11
Rietheim		40	55	19	23	47	6
Yorkshire		3	8	0.5	8	35	1
ODP 1260 (NIOZ)	OAE2	69	98	55	60	94	23
ODP 1260		62	96	49	53	92	5
Tarfaya S57 (Bremen)		76	100	50	84	100	28
Tarfaya S57 (ICBM)		65	92	40	74	92	50
DSDP 641		26	39	16	18	30	12
DSDP 603		0.9	2	0.3	0.5	2	0.2
DSDP 386		7	30	0.9	10	14	7
DSDP 367		5	22	1	8	20	0.6
ODP 1276		17	33	0.8	1	9	0
DSDP 530		1	18	0	0.6	9	0
Bass River		14	18	12	17	26	10
Wunstorf		10	11	10	8	11	2
Bass River	PETM	5	8	1	10	21	0.95
IODP M006 ACEX		0.3	0.4	0.2	0.3	0.5	0.1
IB10		9	42	1	3	7	2
ODP 959		13	25	3	0	0	0
ODP 1403		0.4	0.7	0.3	17	33	0.2
ODP 1172		1.11	9.5	0.3	0.94	1.61	0.41
ODP 752					3	11	0
Forada		47	60	28	36	74	0
969	i-282c	61	65	58	16	61	3
PS25PC	S5	38	41	34	35	42	26
KC19C		50	52	47	39	44	29

1B			53	59	44
2			59	61	57
3			62	64	60
4			58	60	57
5	Arabian Sea		71	73	69
6B	(Carbonates)	-	63	66	59
7			46	51	44
8			47	50	45
9			42	47	40
10			43	48	40
1B			27	33	21
2			45	51	41
3			49	51	47
4			45	50	40
5	Arabian Sea		62	66	56
6B	(from Ca)	-	52	56	45
7			30	35	26
8			47	50	45
9			26	33	21
10			27	36	21
2			52	81	18
3	Black Sea		42	69	11
4			64	64	9
6A		-	50	88	17
6B			45	94	13
7	Black Sea		63	86	30

3

Βουνά και κάμπους αγαπώ   Ένας ανθός της Άνοιξης
γιατί `ναι από χώμα   και του Χειμώνα χιόνι
και είναι κομμάτι απ' αυτά   δείχνουνε πως η ομορφιά
και το δικό μου σώμα.   της φύσης δεν τελειώνει.
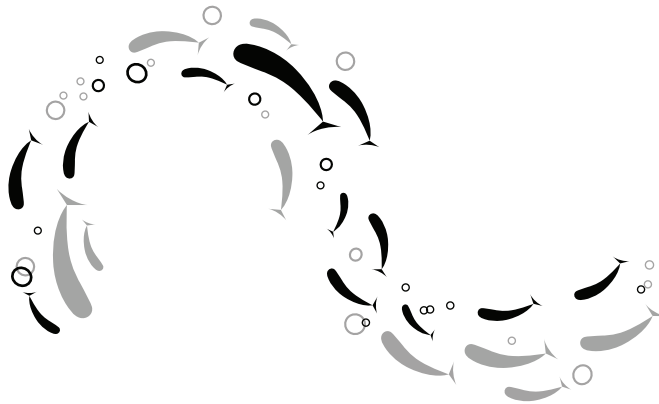
Νίκος Στρατάκης, Δέσποινα Σπαντιδάκη - Φύση

4

Eutrophication and deoxygenation forcing of marginal marine organic carbon burial during the PETM

Eutrophication and deoxygenation forcing of marginal marine organic carbon burial during the PETM

Nina M. Papadomanolaki, Appy Sluijs, Caroline P. Slomp

ABSTRACT

The Paleocene-Eocene Thermal Maximum (PETM) is recognized globally by a negative excursion in stable carbon isotope ratios ($\delta^{13}C$) in sedimentary records, termed the carbon isotope excursion (CIE). Based on the CIE, the cause, duration and mechanisms of recovery of the event have been assessed. Here, we focus on the role of increased organic carbon burial on continental margins as a key driver of CO_2 drawdown and global exogenic $\delta^{13}C$ during the recovery phase. Using new and previously published sediment proxy data, we show evidence for widespread enhanced primary production, low oxygen waters and high organic carbon (C_{ORG}) burial in marginal and restricted environments throughout the $\delta^{13}C$ excursion. With a new biogeochemical box model for deep and marginal environments, we show that increased phosphorus availability and water column stratification on continental margins can explain the increased C_{ORG} burial during the PETM. Deoxygenation and recycling of phosphorus relative to C_{ORG} were relatively mild when compared to modern day anoxic marine systems. With the model, we estimate a burial of 6000 Pg across the PETM, in excess over late Paleocene burial, and ~3,300 Pg C for the critical first 40 kyr of the recovery, primarily located on continental margins, in accordance with field data. This value is consistent with prior modelling estimates (~2000 — 3000 Pg C). Such an increased C_{ORG} burial implies an injection of 5,790 Pg of methane ($\delta^{13}C$ = -55‰) or 7,030 Pg of mixed sources ($\delta^{13}C$ = -55‰ and -25‰) to reconstruct the shape and magnitude of the CIE.

1.INTRODUCTION

The Paleocene-Eocene Thermal Maximum (PETM; ~56 Ma) was a geologically short-lived (~150 – 250 kyr; e.g., Röhl *et al.*, 2007; Murphy *et al.*, 2010; Zeebe & Lourens, 2019) phase characterized by global warming, an enhanced hydrological cycle and biotic turnover (e.g., McInerney and Wing, 2011; Carmichael *et al.*, 2017). A key feature of the event is a negative stable carbon isotope ($\delta^{13}C$) excursion (CIE) recovered in both marine and terrestrial records (Koch *et al.*, 1992). In combination with dissolution of seafloor carbonates (e.g., Zachos *et al.*, 2005), the CIE indicates the injection of large quantities of ^{13}C-depleted carbon (C) into the ocean-atmosphere system (Dickens *et al.*, 1995; 1997). Proposed sources for this carbon include methane hydrates (e.g. Dickens *et al.*, 1995; Lunt *et al.*, 2011; Frieling *et al.*, 2019), terrestrial organic carbon (C_{ORG}) (DeConto *et al.*, 2012; Kurtz *et al.*, 2003), thermogenic methane (Svensen *et al.*, 2004) and volcanic CO_2 (e.g. Bralower *et al.*, 1997; Gutjahr *et al.*, 2017) or a combination of sources (e.g., Sluijs *et al.*, 2007; Panchuk *et al.*, 2008). Many records show a rapid onset of the CIE followed by a 'plateau' phase of stable, low $\delta^{13}C$ values (e.g., Bowen *et al.*, 2001; Thomas *et al.*, 2002) with a duration of up to 170 kyr (Zeebe and Lourens, 2019) (Figure 4.1). The plateau, or rather the lack of immediate recovery, implies a long-term additional source of ^{13}C-depleted carbon, such as methane from hydrates, thermogenic sources or terrestrial carbon oxidation (Zeebe, 2013; Frieling *et al.*, 2016; Lyons *et al.*, 2019). The subsequent recovery to — almost — background $\delta^{13}C$ values may span up to ~120 kyr (e.g. Farley and Elgroth, 2003), though many records suggest stable post-excursion values within ~100 kyr (Bowen, 2013).

The time scale of recovery (Dickens *et al.*, 1997; Zachos *et al.*, 2005, Bowen, 2013) as well as sedimentary evidence (e.g. Ravizza *et al.*, 2001; Kelly *et al.*, 2005) indicate that intensified weathering of terrestrial silicate rocks likely drove CO_2 drawdown during the PETM. However, the rapid recovery of the CIE observed in some marine and terrestrial records (e.g. Giusberti *et al.*, 2007; Abdul-Aziz *et al.*, 2008), suggests that C_{ORG} burial played an important role as well, especially within the first 30 – 40 kyr of the recovery (Bowen and Zachos, 2010, Bowen 2013). Along with terrestrial C_{ORG} burial (Bowen and Zachos, 2010), marine C_{ORG} burial might have been a major sink (e.g., John *et al.*, 2008).

In the modern ocean, over 90% of all C_{ORG} burial in the marine realm takes place at depths shallower than 1000 m (Sarmiento and Gruber, 2006). Climate change during the PETM likely led to increased weathering-driven river inputs of phosphorus (P) to coastal zones (e.g., Sluijs *et al.*, 2014; Khozyem *et al.*, 2015; Carmichael *et al.*, 2017), stimulating primary productivity. The resulting increase in organic matter remineralization near the sea floor, decreased bottom water oxygen concentrations, enhancing the recycling of phosphorus relative to C_{ORG}, and C_{ORG} burial (e.g. Ingall *et al.*, 1993; Sluijs *et al.*, 2008a; 2014). Warming and stronger (salinity) stratification also contributed to a drop in seawater oxygen concentrations (e.g., Thomas *et al.*, 2002; Sluijs *et al.*, 2006; Carmichael *et al.*, 2017). Given the high sea level across the late Paleocene and early Eocene (e.g. Miller *et al.*, 2020), particularly during the PETM (e.g. Sluijs *et al.*, 2008b), even more nutrients were likely trapped along margins. Collectively, if marine C_{ORG} sequestration was of relevance to carbon drawdown during the PETM, it was most likely concentrated along continental margins.

Some studies suggest a rise in primary or export production (Bains *et al.*, 2000; Ma *et al.*, 2014) and mild deoxygenation (e.g. Chun *et al.*, 2010; Pälike *et al.*, 2014) in the open ocean, thus potentially increasing C_{ORG} sequestration. However, most observations point towards increased C_{ORG} burial on continental shelves and slopes (John *et al.*, 2008; Dunkley Jones *et al.*, 2018), notably in restricted basins such as the Arctic (Sluijs *et al.*, 2008a) and in epicontinental seas such as the peri-Tethys (Gavrilov *et al.*, 1997). Sedimentary records from various margins point towards eutrophic conditions (e.g. Schmitz *et al.*, 1997; Gibbs *et al.*, 2006; Nicolo *et al.*, 2010; Soliman *et al.*, 2011; Dickson *et al.*, 2014). Bottom waters at such locations were at least intermittently low in oxygen and in some cases even euxinic ($[O_2]=0$ and sulfidic), which in combination with elevated clay supply, enhanced C_{ORG} burial (Sluijs *et al.*, 2014).

The rapid recovery of $\delta^{13}C$ during the CIE through elevated C_{ORG} burial in marine sediments was recently assessed with two Earth System models. Using cGENIE, Gutjahr *et al.* (2017) and Dunkley Jones *et al.* (2018) assumed an ad hoc increase in burial to simulate the desired $\delta^{13}C$ response. In an application of LOSCAR, Komar and Zeebe (2017) simulated a reduction in deep water O_2 and associated increased P recycling and primary production as a mechanism for enhanced C_{ORG} burial. These studies conclude that the burial of ~2000 to 8000 petagrams (10^{15} g; Pg) of C_{ORG} is required to reconstruct the initial, rapid $\delta^{13}C$ recovery, in agreement with Bowen and Zachos (2010). However, neither cGENIE nor LOSCAR include a representation of the continental shelves and all C_{ORG} burial in these models occurs in deep marine sediments. As a result, the models do not capture the primary locale of C_{ORG} burial for the PETM which may affect both interpretations of the scale and nature of the driving mechanisms, as well as the actual magnitude of the C_{ORG} burial.

In this study, we first expand existing global scale data compilations of changes in primary production, and deoxygenation during the PETM (Dickson *et al.* 2012; Sluijs *et al.*, 2014; Carmichael *et al.*, 2017), based on the currently available published information and new data, with a focus on marginal sites. We then present a new biogeochemical box model with separate boxes for the open ocean and continental margins, the Arctic Ocean and the Eurasian Epicontinental Seas (EES). With the model, we simulate changes in primary production and water column redox conditions during the PETM, with a specific focus on the resulting burial of C_{ORG} on continental margins during the key first 40 kyr of the recovery phase.

2. MATERIALS AND METHODS

2.1 Data compilation
We generated new seafloor oxygenation proxy records and combined them with published information on changes in primary production and redox conditions during the PETM (Supp. Table 4.1). The compilation also includes new geochemical records for the deep North Atlantic (International Ocean Discovery Program (IODP) Site 1403) and marginal settings in the Pacific, Tethys, Atlantic, Arctic, Southern and Indian Oceans (Lodo Gulch, Forada, Bass River, Lomonosov Ridge IODP Site M004, Ocean Drilling Program (ODP) Sites 1172 and
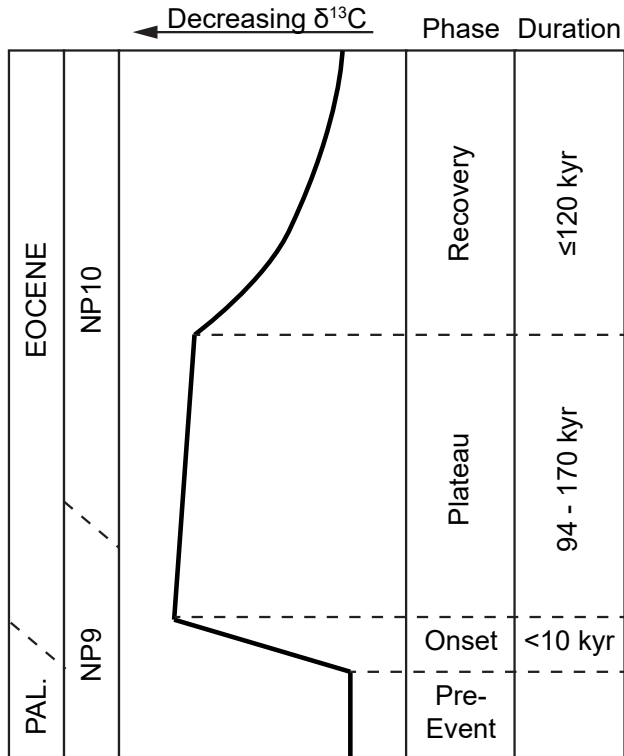
Figure 4.1| Idealized representation of the carbon isotope excursion (CIE) associated with the PETM. The four key phases of the CIE are shown: the pre-event stable background, the $\delta^{13}C$ decrease across the onset, the stable or slightly increasing values of the 'plateau' and the increasing $\delta^{13}C$ of the recovery. As this $\delta^{13}C$ curve does not represent a specific site, the boundaries between the Paleocene and Eocene, and Zones NP9 and NP10, are approximate. The duration for the onset (Kirtland Turner, 2018 and refs. therein), plateau (Zeebe and Lourens, 2019 and refs. therein) and recovery (e.g. Zeebe *et al.*, 2009; Murphy *et al.*, 2010; Bowen, 2013) of the PETM are also given.

752) (see Supplementary Materials for site descriptions and methodology). For the recovery phase, we exclude sites lacking appropriate chronology.

To determine the redox conditions in the water column during the PETM, we use sediment Fe/Al and the trace metal Mo, changes in benthic foraminiferal assemblages and abundance, pyrite contents, sediment lamination and the presence of biomarkers such as isorenieratene and derivatives. The continued presence of benthic foraminifera is used as an indicator of bottom waters that were not permanently anoxic (e.g. Bernhard and Gupta, 1999). Laminations generally form as meso- and macrofauna disappear from sediments when bottom water oxygen is low (e.g. Savrda and Bottjer, 1991). In this study we only use the classification 'anoxic' for sites where Mo is present, pyrite contents are high, and/or isorenieratene (or derivatives) is detected. The presence of the first two indicators may point
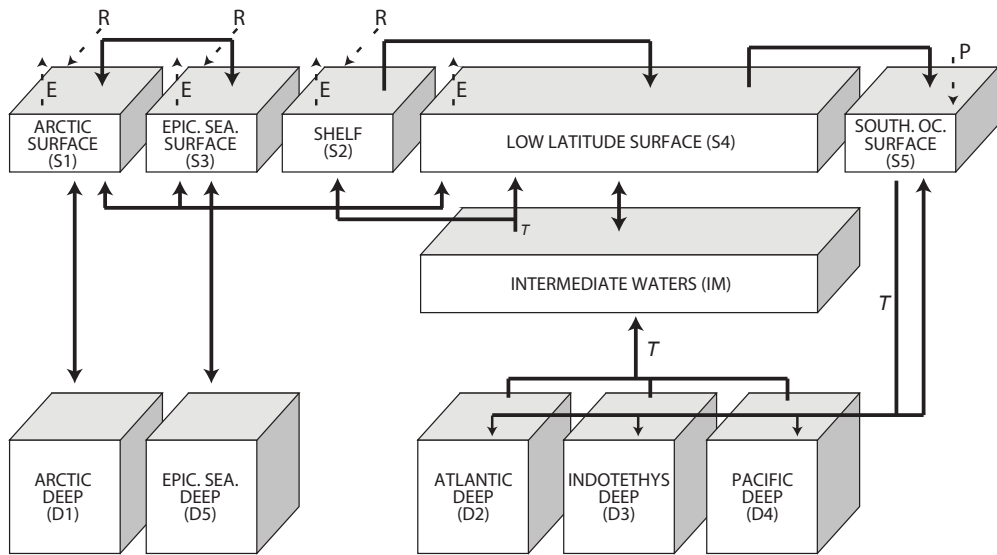
Figure 4.2| Setup of model boxes with names (codes) and fluxes determining the exchange between them. Fluxes between the boxes are indicated with solid lines and riverine fluxes (R), evaporation (E) and precipitation (P) are indicated by dashed lines. Thermohaline circulation assumes deep-water formation in the Southern Ocean (Bice and Marotzke, 2001). towards sulfidic surface sediments and anoxic bottom waters (e.g. Bertine, 1972; Crusius *et al.*, 1996; Roychoudhury *et al.*, 2003). Although isorenieratene indicates lower photic zone euxinia, where present in sediments at shallow sites, euxinia likely reached down to the seafloor (e.g., Sluijs *et al.*, 2014).

We exclude records that aim to reconstruct primary production using C_{ORG} records, as these can be influenced by changes in preservation of organic matter and sediment supply. We compile all studies that interpret proxy records purely as reflections of primary or export production, including those of barite and specific groups of plankton (e.g. foraminifera), to assess trophic levels, without a specific distinction between increased or high primary production.

2.2 Model description
We developed an 11-box biogeochemical model with representations of the coupled marine cycles of C_{ORG}, P and O_2 to track changes in ocean biogeochemistry during the PETM in response to increased atmospheric CO_2 and weathering. To this end, we formulated a steady state mass balance model for the late Paleocene and parameterized processes through simple rate laws (e.g. Van Cappellen and Ingall, 1994; Ruvalcaba Baroni *et al.*, 2014). To simulate the PETM, we applied transient atmospheric pCO$_2$ perturbations to assess the response to enhanced P weathering, higher temperatures and increased stratification.

Our open ocean box layout is similar to that of the Walker and Kasting (1992) carbon-cycle model with separate boxes for the surface waters in the mid and low latitude ocean and Southern Ocean, a thermocline box and three boxes for the Atlantic, Indian and Pacific deep
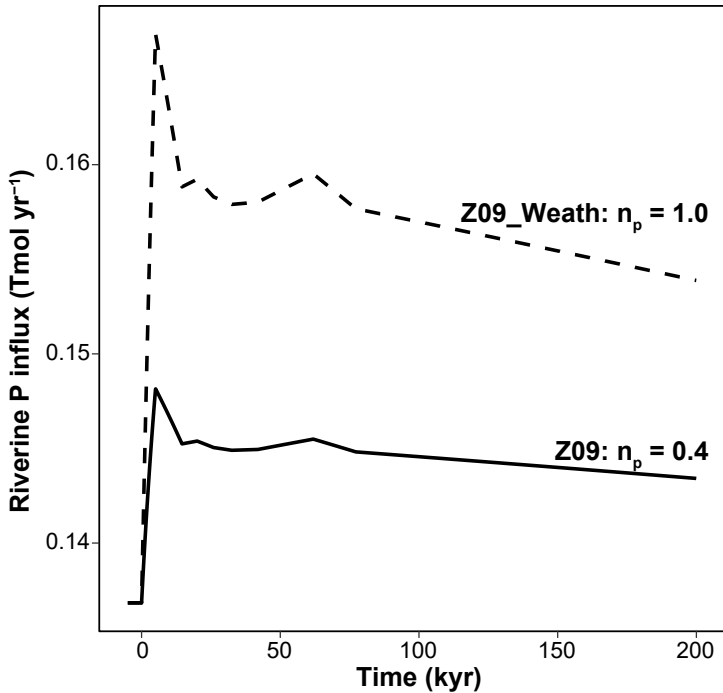
Figure 4.3| Overview of the increased riverine P influx that is used, together with rising temperatures and stratification, to simulate the PETM in our model. The standard scenario (Z09; solid line) uses a lower P weathering sensitivity of $n_p = 0.4$ than the Z09_Weath scenario in which $n_p = 1.0$.

oceans (Fig. 4.2). The original Indian Ocean box of Walker and Kasting (1992) is increased in size, however, to include the Tethys Ocean (Indotethys). The continental margins, with the exception of the Arctic Ocean and EES (which includes the peri-Tethys region), are represented by a single box. We hereafter refer to it as the continental margin. The Arctic Ocean and EES are each represented by two boxes, a shallow one that includes the shelf area and a deep box. The continental margin, the surface Arctic Ocean and the surface EES will be referred to collectively as the marginal boxes. Further details are provided in the Supplementary Information.

2.3 Simulation setup

The standard simulation which we present here is forced by the atmospheric CO_2 curve as modelled by Zeebe *et al.*, 2009 (Z09) (Supp. Table 4.2). The increase in pCO_2 during the PETM causes an increase in P_{weath} and, subsequently, total riverine P input (Fig. 4.3). Additionally, the accompanying increase in water temperature leads to a reduction in O_2 solubility and we enforce an increase in stratification in the Arctic surface and EES surface boxes. The combined changes in P input, O_2 solubility and stratification cause the variations in primary productivity and deoxygenation associated with the PETM. The four key parameters of which the values chosen strongly affect our simulation results for the PETM are f_{OrgP} (0.75), f_{CaP}

(0.4), n_p (0.4) and f_{strat} (S1: 0.1; S2: 1; S3: 0.4) (Supp. Table 4.2). The sensitivity analyses that we conducted before choosing these final values are presented in the Supplementary Information. Additionally, we tested the impact of changes in these parameters in combination with riverine P inputs associated with three alternative facts atmospheric pCO$_2$ curves (F16: Frieling *et al.*, 2016; G17: Gutjahr *et al.*, 2017; K170: which is the Z09 scenario but using the 170 kyr duration of Zeebe and Lourens (2019) for the plateau of the CIE. The results of these simulations can also be found in the Supplementary Information. The rate of C$_{ORG}$ burial from Z09 was implemented in LOSCAR as a time dependent variable, to examine the effect on bulk δ^{13}C.

We also performed five experiments using the Z09 scenario (Supp. Table 4.2), with the aim to assess the sensitivity of C$_{ORG}$ burial to of increased P supply, primary productivity, stratification and reduced O$_2$ solubility. In our first experiment (Z09_Weath), we enhanced the sensitivity of P weathering to atmospheric CO$_2$, thereby increasing riverine P supply to the ocean. For this run, we increased the value of np from 0.4 to 1. In the second experiment (Z09_cOOPP), we kept open ocean (S4 and S5) primary productivity constant at the corresponding steady state value. As a result, the relative contribution of marginal (S1 – 3) productivity to total organic matter production increased. In this run, excess C$_{ORG}$ burial is influenced solely by marginal productivity and deoxygenation in marginal and deep boxes. The third experiment tested the combined effect of decreased O$_2$ solubility and increased P weathering, without increased stratification (Z09_cStrat). In this experiment, f_{strat} was set to 1 for all marginal boxes (S1 – 3), while n_p was kept at the standard value. For the next experiment (Z09_Weath_Only), we tested the impact of only enhanced P weathering on productivity and, subsequently, on C$_{ORG}$ burial. To test this, we kept all boxes fully oxic (constant DOA and [O$_2$] at steady state values), thus eliminating the contribution of preservation of C$_{ORG}$ and P recycling. Our last experiment tested the effect of reduced O$_2$ solubility under higher temperatures (Z09_O2Sol) assuming no increased stratification and no increased P weathering by setting f_{strat} to 1 for all marginal boxes (S1 – 3) and np to 0.

2.4 LOSCAR δ¹³C simulations

To test the response of increased C$_{ORG}$ burial rates on dissolved inorganic carbon δ^{13}C, we used the carbon cycle box model LOSCAR (Zeebe *et al.*, 2009). The C$_{ORG}$ burial in the original LOSCAR version is constant throughout the simulations. For the purpose of this study, we changed this setup to include a time-dependent C$_{ORG}$ burial factor that emulated the relative changes in C$_{ORG}$ burial, as simulated by our Z09 scenario. We tested a Z09 simulation with and without C$_{ORG}$ burial, as well as two further emission scenarios, one for a larger second pulse of methane (see Komar and Zeebe, 2009) and one where the second pulse is caused by C$_{ORG}$ oxidation (Lyons *et al.*, 2019). Both of these scenarios are combined with Z09 C$_{ORG}$ burial rates for the onset, plateau and first 40 kyr of the recovery phase. We use the LOSCAR δ^{13}C fractionation value of -33‰ for C$_{ORG}$ burial.
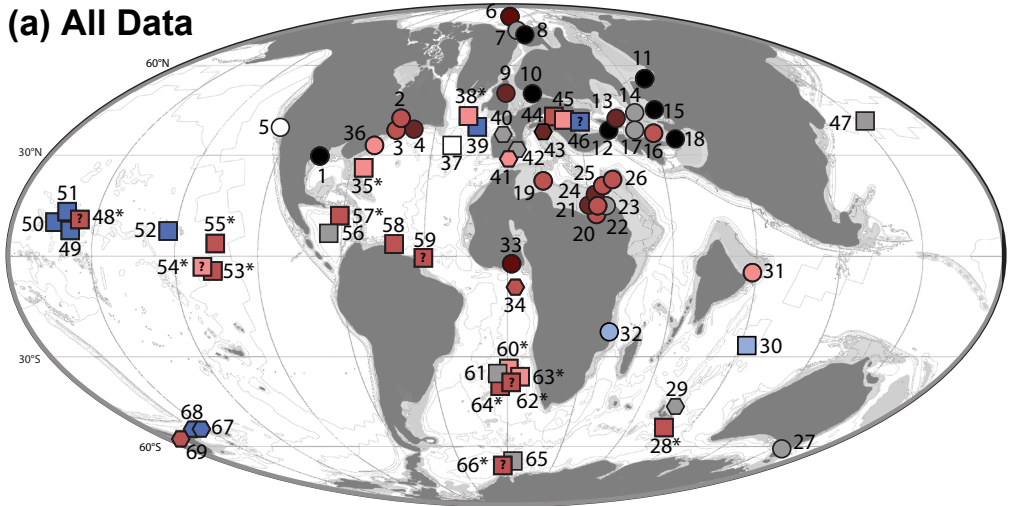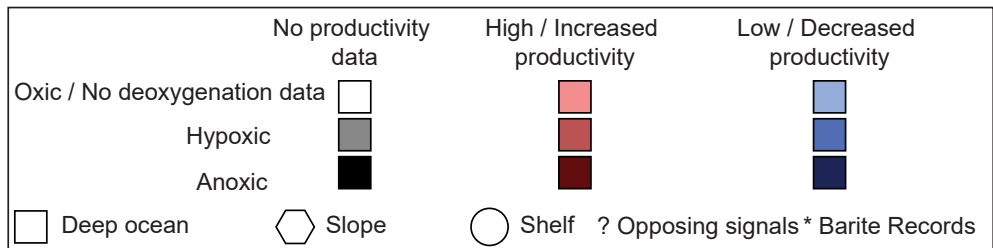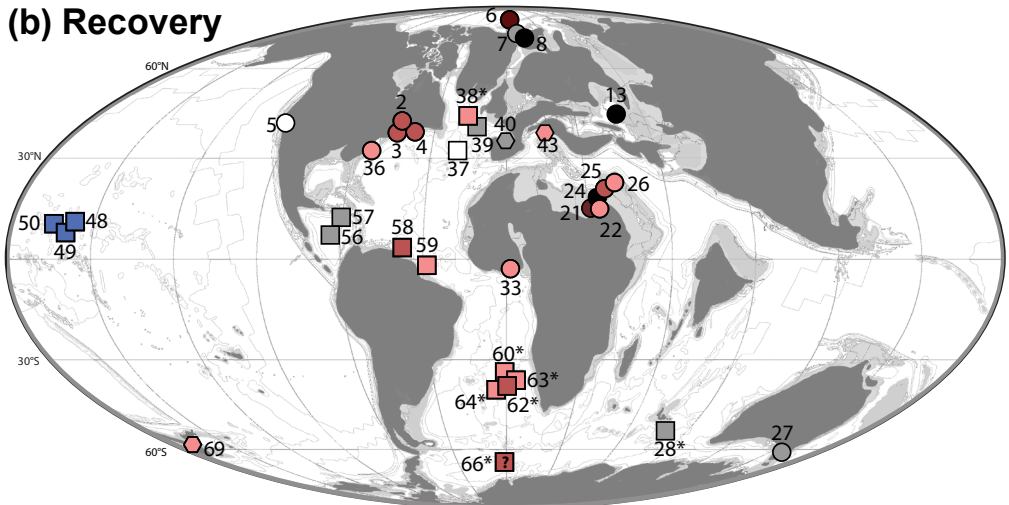
Figure 4.4| Global overview of sites of proxy records on changes in primary productivity (PP) and bottom water redox conditions for the PETM. Records for all phases of the PETM (a) and records for the recovery as identified from the δ¹³C excursion (b) are indicated separately. The lightest colors indicate oxic conditions or sites where no data on deoxygenation is

available. Intermediate shades are used for hypoxic sites while the darkest shades indicate anoxic or euxinic conditions (see text for criteria). Grey colors are used for sites without data on PP changes, red colors indicate high or increased PP and blue is used for sites with low or decreased PP. Sites with records that use barite to reconstruct PP are indicated by stars (*) and sites where proxy records offer contradicting results by question marks (?). Symbol shapes represent the depth domain: shelf (circle), slope (polygon) and deep (square). For the full reference list and site names (here indicated by numbers) see Supp. Table 4.1. Map after Markwick (2007), modified by Sluijs *et al.* (2014).

3. RESULTS

3.1 Geochemical data

The $\delta^{13}C$ data for our newly generated PETM records show that we capture both the onset and recovery of the PETM at five out of seven sites (Supp. Fig. 4.1). At the Lomonosov Ridge, C_{ORG}/P_{TOT} values well in excess of the Redfield ratio, and high Mo concentrations indicate severe deoxygenation. The high C_{ORG}/P_{TOT} values found at Lodo Gulch and the presence of Mo at Bass River and ODP Sites 1172 and 752 suggest reducing conditions as well. Average C_{ORG} contents are mostly at or below ~0.5% at all sites except for Site 1172 and the Lomonosov Ridge where C_{ORG} contents range up to ~1.3 and 3.4 wt%, respectively. For more details on the proxy records for our seven sites, see Supplementary Information.

3.2 Data compilation

Most sites in in our compilation (Fig. 4.4a) experienced some degree of deoxygenation during the PETM. Hypoxic conditions on the sea floor at open ocean sites are concentrated mainly in the areas of the Equatorial Pacific and Atlantic, Walvis Ridge in the Southern Atlantic and the Southern Ocean. Most sites on the continental shelf and slope experienced hypoxia at some stage during the PETM, with only a few (<5) exceptions. Intermittent to permanent anoxia developed at sites in the Arctic Ocean, the North Sea, the Peri-Tethys, the New Jersey shelf and the North-African shelf. However, sites on the New Jersey and North-African shelves provide evidence for hypoxia rather than anoxia. Lower photic zone euxinia was identified at a total of four sites.

Signs of eutrophication are found in all basins and at all water depth intervals, during different stages of the PETM. About 13 sites experienced high productivity throughout the entire PETM (Supp. Table 4.1). Clusters of high productivity occur around the Walvis Ridge, on the New Jersey Shelf and the North African Shelf. Most sites with evidence for increased productivity also experienced deoxygenation, with a few exceptions. A much smaller number of records capture the recovery phase of the PETM (Fig. 4.4b). At some sites, notably in the deep ocean and the (peri)Tethyan realms, proxies indicate oxic conditions during the recovery, but a large number of sites in various ocean basins, notably on the North African Shelf, the New Jersey Shelf and in the Arctic remained hypoxic or anoxic.

Overall, there is abundant evidence for eutrophication and deoxygenation in marginal and restricted environments, also during the recovery phase of the PETM. This contributed to high sediment C_{ORG} contents in these environments (Fig. 4.5). Records containing C_{ORG} >0.5
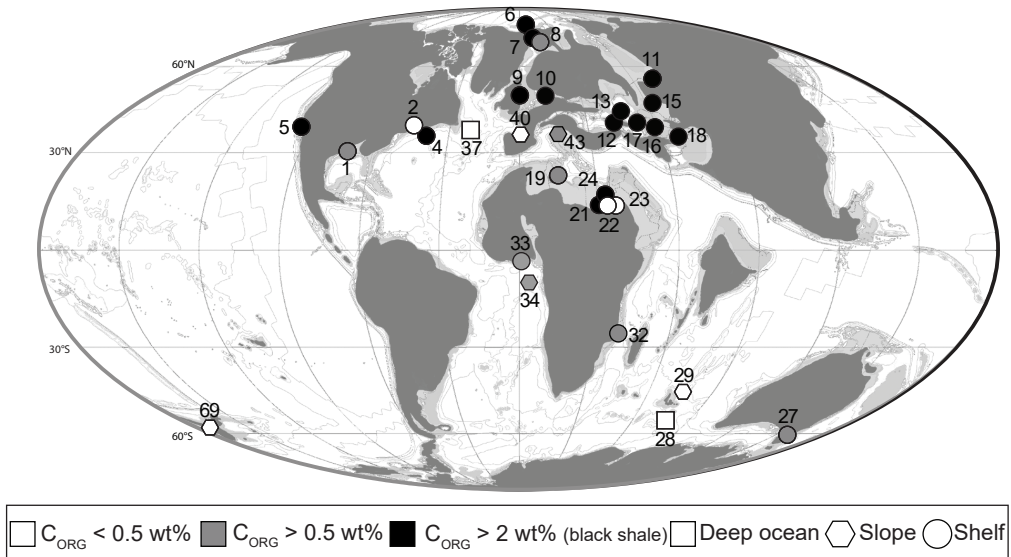
Figure 4.5| Compilation of sediment C_{ORG} contents for the PETM. Colors represent maximum values for each site: less than 0.5 wt% (white), more than 0.5 wt% (grey) and more than 2 wt% (black). Shapes indicate the depth domain: shelf (circle), slope (polygon) and deep (square). For the full reference list and site names (here indicated by numbers) see Supp. Table ST1. Map after Markwick (2007), modified by Sluijs *et al.* (2014).

wt%, and especially C_{ORG} >2 wt%, are found mainly in marginal environments during the PETM (Fig. 4.5).

3.3 Modeling results
We present results for the Z09 simulations here (Fig. 4.6). Those for the F16, G17 and K170 simulations are very similar and can be found in the Supplementary Materials.

3.3.1 Z09 simulation
Dissolved PO_4 concentrations in all basins and primary production rates in the surface boxes increase by a factor of ~1.6 during the first 80 to 100 kyr of the event, before decreasing (Figs. 4.6a, 4.6b). Phosphate concentrations become highest in the deep boxes of the restricted basins (D1, D5; ~3 µmol kg^{-1}), somewhat lower in the thermocline (> 2 µmol kg^{-1}) and remain low in the Southern Ocean (<1 µmol kg^{-1}; Fig. 4.6a). Total primary productivity increases from ~49 Pg C yr^{-1} to 77 Pg C yr^{-1}. This increase results in excess production of ~4.3 x 10^6 Pg C, with 78% produced in S4 and 12% in S2.

Deoxygenation occurs in all surface (Fig. 4.6c) and deep (Fig. 4.6d) boxes. The DOA is highest in box S1 (0.94), compared to S2 (0.38) and S3 (0.74). The DOA for S2 begins to decrease at about 100 kyr. For S1 and S3, the recovery begins around 60 kyr into the event. Oxygen concentrations in the deep Arctic Ocean (D1) and EES (D5) decrease to zero within the first ~10 kyr and ~20 kyr of the PETM simulation, respectively. Both boxes remain fully anoxic
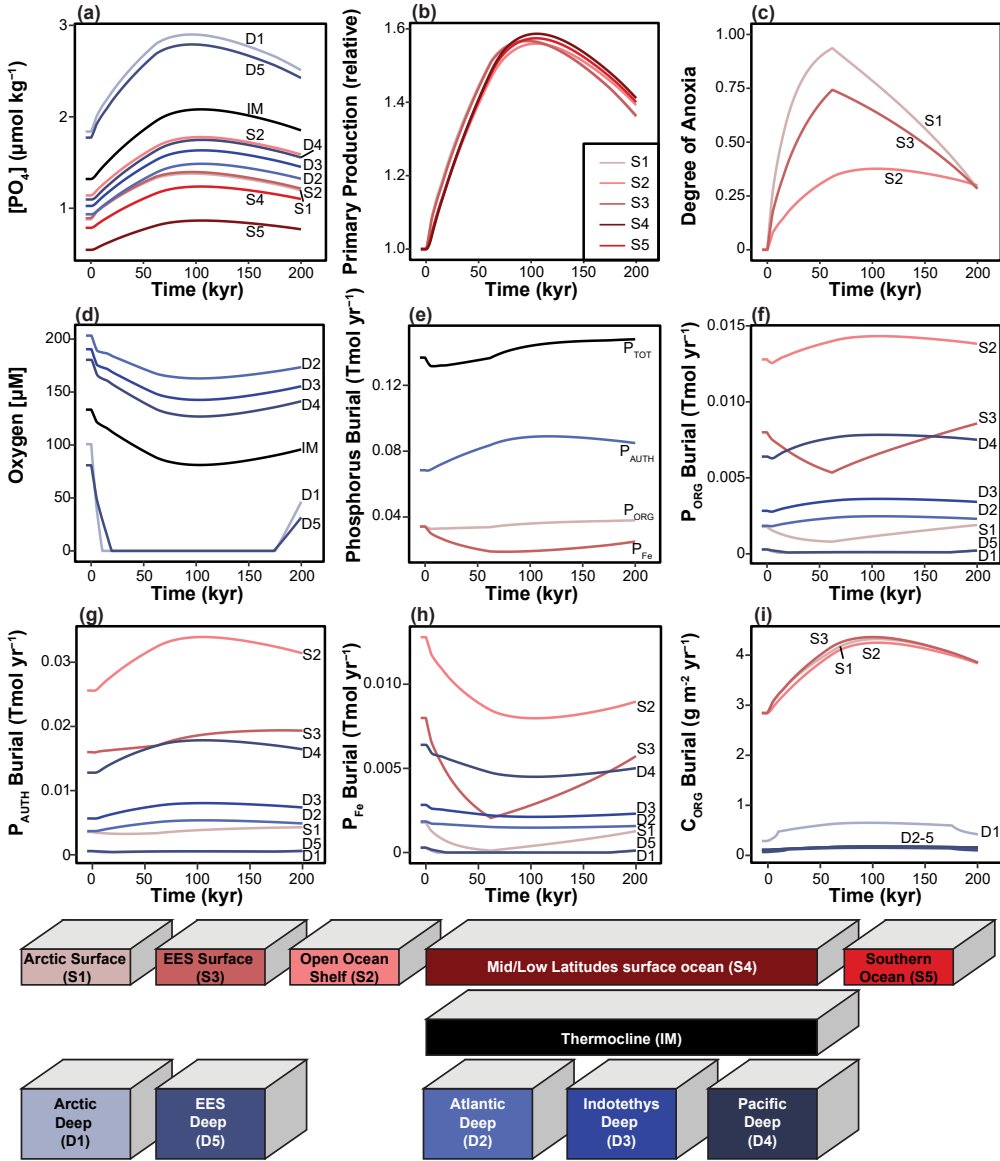
Figure 4.6| Key results for PETM simulation Z09: phosphate concentrations in μmol kg^{-1} (a), relative change in primary productivity (b), degree of anoxia for the marginal boxes (c), oxygen concentrations in μM for the deep boxes (d), total phosphate burial rates for the different pools in Tmol yr^{-1} (e), organic P (P$_{ORG}$) burial rates in Tmol yr^{-1} (f), authigenic P (P$_{AUTH}$) burial rates in Tmol yr^{-1} (g), iron-bound P (P$_{Fe}$) burial rates in Tmol yr^{-1} (h) and organic carbon (C$_{ORG}$) burial rates in g C m^{-2} yr^{-1} (i). Red colors are used for surface boxes, black for the thermocline and blue colors for the deep boxes. The color association is also shown in boxes at the bottom of this figure.
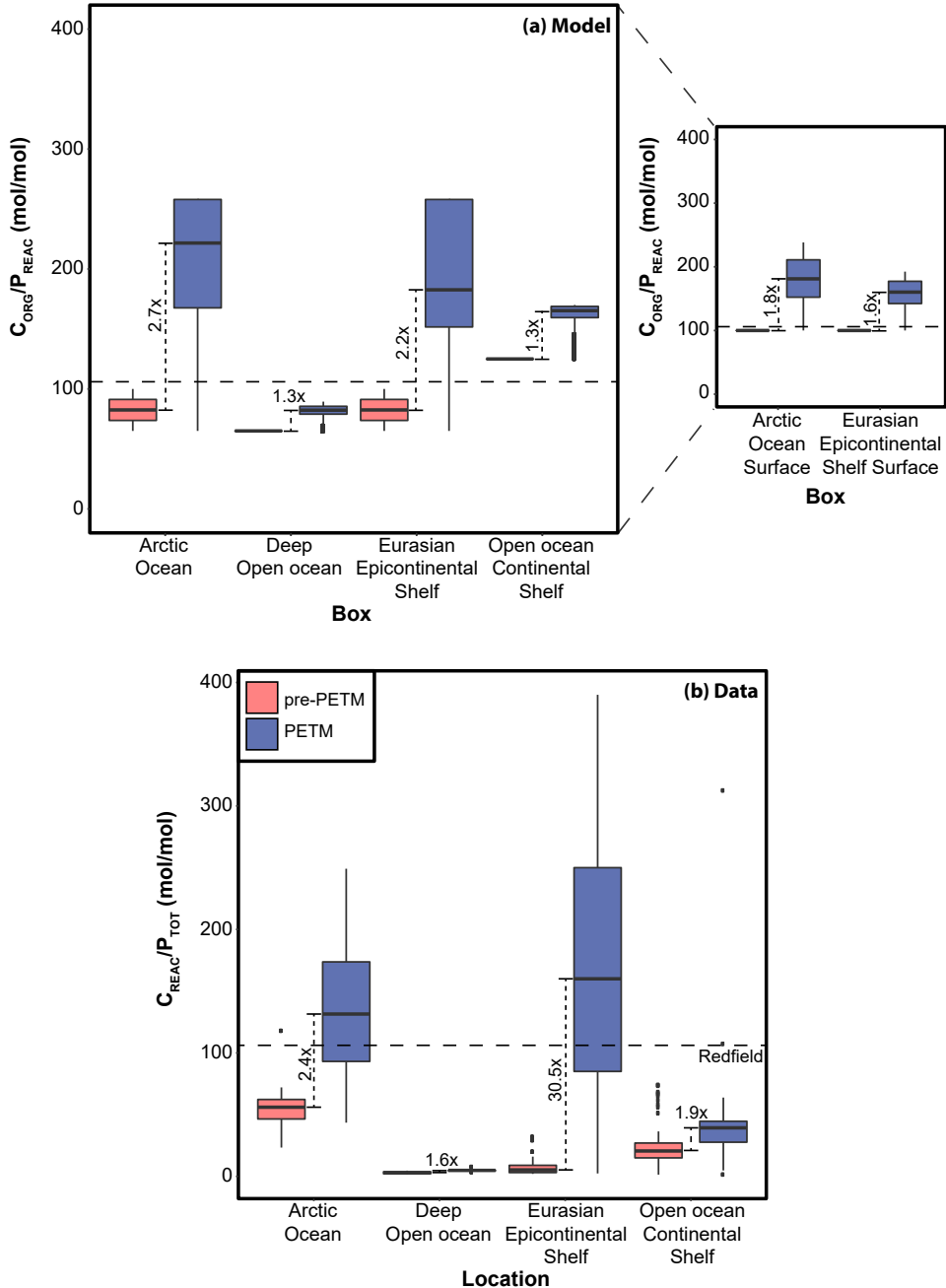
Figure 4.7| Simulated and measured values of C_{ORG}/P_{TOT} for marginal and deep ocean regions based on our model scenario Z09 (a) and data compilation (b). In the data set, total P (P_{TOT}) is equal to reactive P (P_{REAC}) plus detrital P. The latter phase is not included in the total P in our model. Values are shown for the late Paleocene (pink)

and the PETM (blue). The dashed line indicates the Redfield value (106). The relative change in median values is indicated. The inset for panel (a) shows the values for the Arctic and EES surface boxes, which in (a) are combined with the values for the respective deep boxes. Horizontal lines within the boxplots indicate median values. until ca. 30 kyr before the end of the event. The thermocline becomes nearly hypoxic (min. 80 μmol kg^{-1}). Oxygen concentrations in the deep open ocean boxes decrease but remain >60 μmol kg^{-1}. Oxygen concentrations for the thermocline and deep open ocean (IM, D2 – 4) begin their recovery from ~100 kyr onward.

The burial of P_{TOT} decreases at the onset of the PETM and remains below the late Paleocene level for the first ~60 kyr of the event, followed by a rise (Fig. 4.6e). Variations in total P_{ORG} burial are minor compared to the rise in P_{AUTH} and decrease in P_{Fe} burial. Interestingly, while P_{ORG} burial increases in the deep ocean boxes D2, D3 and D4, and the shallow box S2, it decreases in D1, S1 and S3 (Fig. 4.6f). The burial of P_{AUTH} shows little change in D1, D5 and S1 but increases in all the other boxes (Fig. 4.6g). Burial of P_{Fe} decreases in all boxes, but most prominently in S2 and S3 (Fig. 4.6h).

The rate of C_{ORG} accumulation increases in all boxes (Fig. 4.6i). In the marginal boxes, the rate increases from an average of 2.8 g C m^{-2} yr^{-1} to 4.3 g C m^{-2} yr^{-1}. In the deep boxes, the largest change occurs in the restricted basins, where rates more than double from 0.29 g C m^{-2} yr^{-1} to 0.65 g C m^{-2} yr^{-1} in D1 and from 0.07 g C m^{-2} yr^{-1} to 0.15 g C m^{-2} yr^{-1} in D5.

Burial C_{ORG}/P_{TOT} values during the PETM generally exceed the Redfield ratio of 106 in all boxes, except for the deep open ocean (D2 – 4) (Fig. 4.7a). Maximum values (260 mol/mol) are reached in the Arctic and Eurasian Epicontinental Seaway and the maximum relative increase (2.7) occurs in the Arctic. The lowest maximum value (83 mol/mol) and the lowest relative change (1.27) occur in the deep open ocean.

3.3.2 Excess C_{ORG} burial

Most excess burial of C_{ORG} for the standard scenario (Z09) occurs in the marginal boxes (Fig. 4.8a), which account for more than 70% of total burial. Over the entire PETM, excess burial amounts to 13,300 Pg C (Fig. 4.8b). During the first 40 kyr of the recovery, excess burial is 3300 Pg C. For the sensitivity tests, we show results for simulations with a P weathering sensitivity of either $n_p = 0.4$ (as in the standard run) and, only where it is explicitly stated, $n_p = 1.0$ (as in Z09_Weath) (Fig. 4.8c). An increase in weathering sensitivity from 0.4 to 1.0 generally increases the amount of excess C_{ORG} burial. When this increase is applied to the standard scenario (Z09_Weath), it results in total excess burial of ~21,100 Pg C, while for the first 40 kyr of the recovery excess burial increases to 5000 Pg C. Generally, excess burial is at least 1.4 times higher for a weathering sensitivity that is 2.5 times higher. When open ocean productivity is kept constant (Z09_cOOPP), excess C_{ORG} burial shifts towards the restricted basins. Due to a decreased retention of phosphorus in the open ocean, more of it becomes available for production in the restricted basins instead. Total excess C_{ORG} burial is 16,000 Pg C for the entire PETM and ~4000 Pg C for the early recovery.

The effect of changes in stratification on excess C_{ORG} burial is large and is required to reproduce the spatial extent and severity of deoxygenation in the Arctic and EES. Without
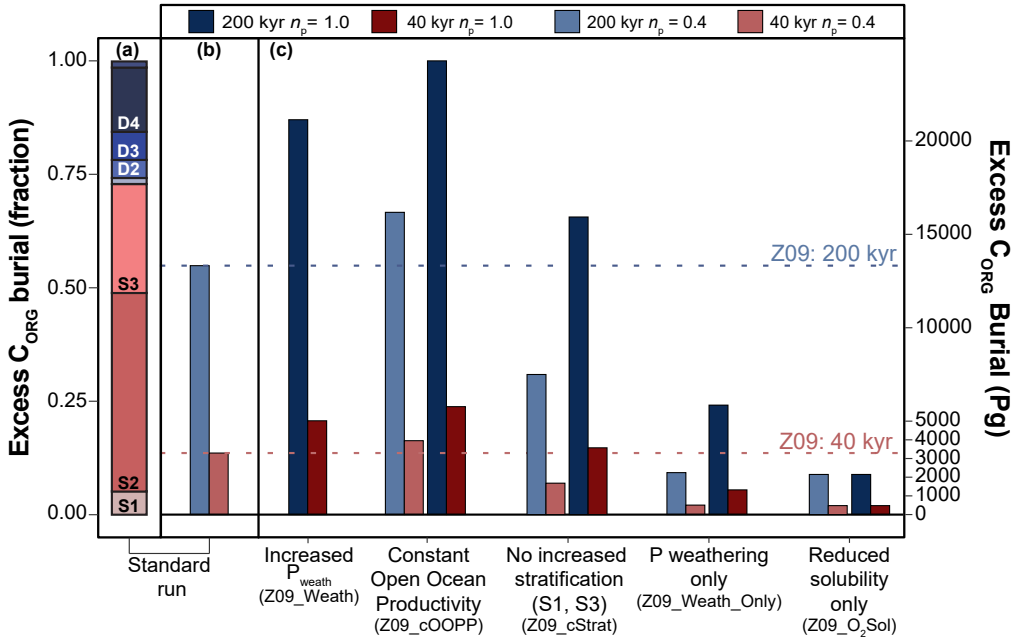
Figure 4.8| Barplot for excess C_{ORG} burial associated with the PETM for the standard simulation Z09 (a and b) and the sensitivity analyses (c) in units of Pg C and as a relative fraction when compared to Z09). The codes for the boxes contributing to the excess C_{ORG} burial are as described in Fig. 2. Blue colors are used for excess burial across the entire PETM while red indicates excess burial during the first 40 kyr of the recovery. Light colors in (b) and (c) are used for the lower P weathering sensitivity (np = 0.4) while darker shades correspond to the higher sensitivity (n_p = 1.0). See the Methods section for an explanation on the calculation of excess burial. Scenario codes are given in brackets and explained in Supp. Table 4.2.

increased stratification in S1 and S3 (Z09_cStrat), total excess C_{ORG} burial over the entire PETM is 7500 Pg C and 1700 Pg C of this is buried during the 40 kyr interval. The CO2-driven increase in P_{WEATH} and associated riverine input of P is the only factor controlling biogeochemical changes in the ocean in the model run with oxic conditions and without increased stratification (Z09_Weath_Only). Total primary productivity increases to 53 Pg C yr^{-1} and excess C_{ORG} burial amounts to 2200 Pg C (entire event) and 500 Pg C (first 40 kyr of recovery). The effect of reduced O_2 solubility on C_{ORG} burial, due to warming only (Z09_O2Sol), is similar to that of increased P_{WEATH} only (Z09_Weath_Only). Excess C_{ORG} burial by the end of the PETM is 2100 Pg C and roughly 480 Pg C are buried during the 40 kyr early recovery interval.

The sensitivity tests show that increased weathering of P is a key driver of biogeochemical change during the PETM. However, the redox-driven recycling of P amplifies this effect, resulting in the patterns of increased productivity and deoxygenation that we observe in the data.
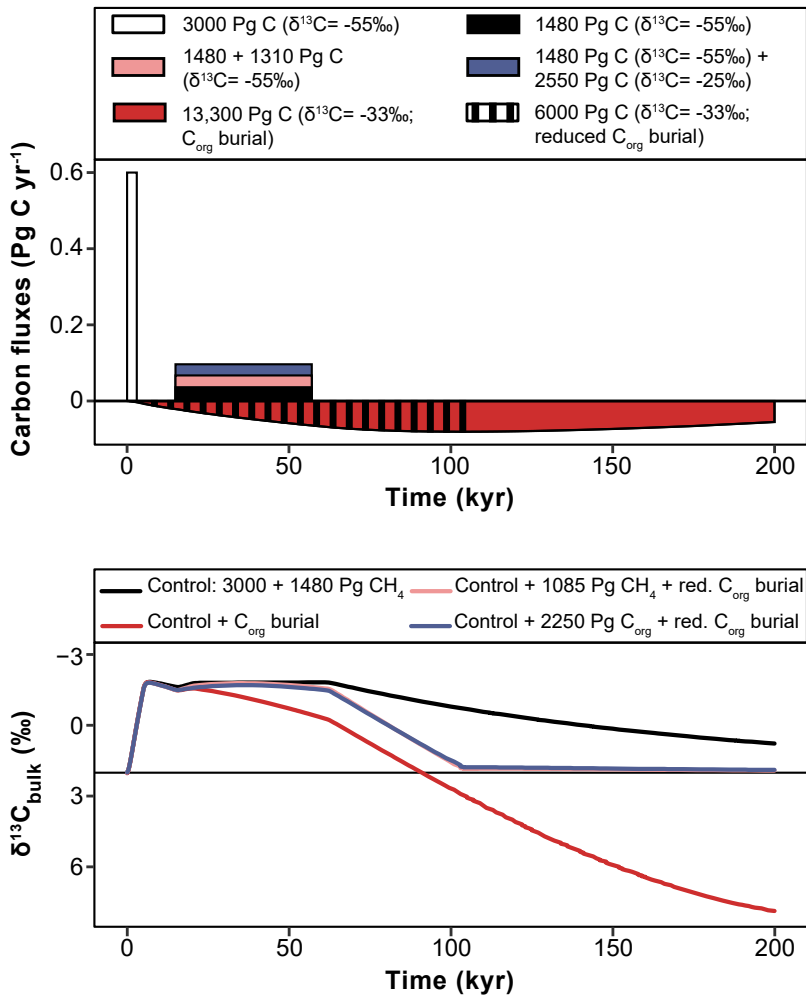
Figure 4.9| Bulk carbon isotope response to four PETM forcing scenarios. The forcing scenarios (a) include methane (CH4; $\delta^{13}C$ = -55‰) and Corg ($\delta^{13}C$ = -25‰) emissions, and C_{ORG} burial. White bar: an initial pulse of 3000 Pg C of CH_4 emission (Zeebe *et al*., 2009), used in all scenarios. Black bar: a "leak" of 1480 Pg C of CH_4 (Zeebe *et al*., 2009). Pink bar: an additional "leak" of 2020 Pg C of methane. Blue bar: an additional "leak" of 1020 Pg C of CH_4 and 2400 Pg C of C_{ORG}. Purple bar: reduced burial, excess C_{ORG} burial of 6000 Pg C, over the onset, plateau and first 40 kyr of the recovery. Red bar: excess C_{ORG} burial of 7,300 Pg C, together with the purple bar it accounts for the burial of 13,300 Pg C over the entire PETM. The bulk $\delta^{13}C$ responses (b) correspond to combinations of these scenarios. Black line: Control scenario with a forcing of 3000 Pg C plus 1480 Pg C of CH_4. Red line: Control scenario with the inclusion of the complete C_{ORG} burial scenario simulated in this study. Pink line: Control scenario plus 2020 Pg C of CH_4 and reduced burial. Blue line: Control scenario plus 1020 Pg C of CH_4 and 2400 Pg C of C_{ORG}, with reduced burial. O.: Onset.

3.4 LOSCAR δ¹³C simulations

The inclusion in LOSCAR of C_{ORG} burial rates simulated in this study, results in a preferential removal of ^{13}C-depleted carbon and thus an earlier and more rapid recovery of the CIE (red line in Fig. 4.9). The shape of the CIE broadly matches observations (Fig. 4.1). However, by the end of the PETM, $\delta^{13}C$ values have increased by 2‰ above the pre-event value, which is in stark contrast with observations and thus implies the need for the addition of several thousand Pg of ^{13}C-depleted C during the plateau and recovery phases to match the shape of the CIE. Truncating C_{ORG} burial rates after the first 40 kyr of the recovery (blue, pink lines), leads to a better match with the target. An addition of ~1000 Pg C with a $\delta^{13}C$ value of -55‰ (blue line), or 2400 Pg C of -25‰ (pink line), results in a plateau phase similar to the scenario without C_{ORG} burial.

4. DISCUSSION

4.1 Primary production

Our data compilation shows that primary production increased in both open ocean and marginal marine areas during the PETM (Fig. 4.4). Roughly 70% of all studied sediment records reveal increased production based on at least one proxy. Some work has suggested that barite records (partly) record export rather than primary production (Ma *et al.*, 2014) - though it seems unlikely that export production increased without a pronounced increase in primary production, particularly in a warmer water column (e.g, Laws *et al.*, 2000b) - or a global increase in the Ba inventory (Dickens *et al.*, 2003; Frieling *et al.*, 2019). Even when barite records are excluded, 60% of all sites still show an increase in primary production. Importantly, almost two thirds of all high or increased productivity sites are located on the continental margin and in the restricted basins of the EES and Arctic Ocean, where almost all sites show an increase during the PETM. This is especially true for areas such as the North African shelf (sites 19 – 26) and the New Jersey shelf (sites 2 – 4), where increased productivity marks all sites but one (23).

Our simulations indicate an equal relative increase of primary productivity in all surface boxes. The absolute increase in maximum rates of primary production per unit of surface area is highest in marginal boxes (S1 – 3), but most production takes place in the low and mid latitudes of the open ocean (S4) (Supp. Table 4.3). These environments cover the largest surface area of the ocean and proxy records for high or increased primary production are found in the North and the South Atlantic, as well as the tropical Pacific.

4.2 Deoxygenation

Deoxygenation is recorded by proxies at 90% of the sites compiled for this study (Fig. 4.4). Sulfur isotope ratios have been interpreted to suggest that large parts of the ocean became sulfidic during the PETM (Yao *et al.*, 2018) with an expansion of the OMZ to 10 – 20% of the ocean volume (modern: 1%). While there is local evidence for hypoxia at intermediate depths in the open ocean (Fig. 4.4) there are no signs of euxinic, or even anoxic conditions on such a scale. (Intermittent) euxinic conditions are almost entirely restricted to specific sections of the continental shelf: the Arctic, the eastern EES and peri-Tethys region, the North Sea, the North African Shelf and the Gulf of Mexico.

4

The results of our simulations are in general agreement with the data, as all boxes show signs of deoxygenation. The deep boxes of the open ocean also exhibit a decrease in $[O_2]$ but remain oxic (>60 μM) during the PETM. Intermediate waters (box IM) also remain oxic. As our model provides average changes for all basins, this result is not inconsistent with the observed hypoxic areas ($[O_2]$ <60 μM) as others remained oxic (e.g. Pälike *et al.*, 2014). The deep Arctic and EES become fully anoxic and the DOA rises for all surface boxes, consistent with observations. At present, there is no data available for the deep Arctic basin, however our model does not allow for an oxic, or even hypoxic, deep Arctic when the surface box experiences a large increase in DOA. As surface deoxygenation for the Arctic is supported by work on multiple sites (Fig. 4.4; see Supp. Table 4.1 for all references), it is likely that the deep Arctic experienced similar conditions.

The changes in the hydrological cycle that are associated with the PETM likely resulted in increased river runoff to the marine realm which, in combination with higher temperatures, would have caused water column stratification (e.g., Sluijs *et al.*, 2006). In our model, stratification plays a large role in increasing the DOA of surface boxes (Supp. Table 4.3). Marginal environments where evidence suggests that salinity varied, are mainly located in the Arctic (Pagani *et al.*, 2006; Sluijs *et al.*, 2008a; Harding *et al.*, 2011) and on the New Jersey Shelf (Kopp *et al.*, 2009; Sluijs and Brinkhuis, 2009). But evidence of intense hydrological change on land (e.g., Bowen *et al.*, 2004; Foreman *et al.*, 2012; Schmitz and Pujalte, 2007; Chen *et al.*, 2018) and an increase in the supply of terrestrial siliciclastic and organic material to the margins has been found in numerous locations (see overview in Sluijs *et al.*, 2014), likely accompanied by large-scale (seasonal) salinity stratification along margins. Very strong stratification is required in our simulations to create severe anoxia in the Arctic, so as to correspond to the conditions that were dominant at Lomonosov Ridge (Stein *et al.*, 2006; Sluijs *et al.*, 2006; 2008; Dickson *et al.*, 2012) and Spitsbergen (Cui *et al.*, 2011; Harding *et al.*, 2011). A somewhat lower DOA for the EES, again mostly due to stratification, encompasses the larger range of redox conditions deduced from proxies for this region (Fig. 4), though anoxia occurred (intermittently) at nearly half of all sites there. Without stratification, our model does not capture such conditions for the EES. Despite the fact that we did not enforce stratification on the continental margin (box S2), stratification elsewhere also results in a somewhat higher DOA for S2.

4.3 Phosphorus recycling

Phosphorus is considered the main limiting nutrient in the ocean on long timescales (Tyrrell, 1999). Records of C_{ORG}/P_{TOT} indicate that P recycling relative to C_{ORG} increased from the late Paleocene into the PETM (Fig. 4.7b). Typical values of C_{ORG}/P_{TOT} were lower than those in modern anoxic to euxinic basins, however, where they generally far exceed the Redfield ratio, reaching values of up to 400 mol/mol (Algeo and Ingall, 2007). Values in excess of 300 mol/mol do occur at Guru Fatima, Kheu River (Dickson *et al.*, 2014) and Lodo Gulch (Supp. Fig. 4.1). This confirms that throughout the PETM, complete anoxia was only experienced locally, while most locations experienced at most a switch to hypoxia.

Overall, the absolute range of C_{ORG}/P_{TOT} simulated by our model corresponds well to the range of the data (Fig. 4.7), when taking the exclusion of detrital P in our model into account. In contrast, the relative increase in the modeled median C_{ORG}/P_{TOT} value is much lower

than the increase in the data. This is especially true for the EES where the relative change in median data values is more than a factor 30, versus a modeled increase of 1.6 – 2.5 times the late Paleocene median C_{ORG}/P_{TOT} value (Fig. 4.7b; Dickson *et al.*, 2014). Here, we must add that in addition to deoxygenation and P recycling, an increase in the input of detrital P would lower sedimentary C_{ORG}/P_{TOT} while increased terrestrial organic matter fluxes would have the opposite effect (Ruttenberg and Goñi, 1997; Burdige, 2005). An increase in the contribution of terrestrial organic material is found at some sites during the PETM (e.g., Crouch *et al.*, 2003; Arreguín-Rodríguez *et al.*, 2014). Furthermore, the locally intensified hydrological cycle (Carmichael *et al.*, 2017) would have led to an increased influx of both detrital P and terrestrial organic matter, with uncertain effects on marine C_{ORG}/P_{TOT}. The extremely large change for the EES in particular, combined with an increased abundance of terrestrial biomarkers and highly weathered lithogenic material (Dickson *et al.*, 2014), suggests that PETM values were affected by an increase in terrestrial material. We therefore infer that the strength of P recycling within our model falls within a reasonable range for the PETM.

The ability of biota to utilize the excess availability of P during the PETM may have depended on the cycling of other nutrients such as N and Fe as well. Nitrogen isotope ($\delta^{15}N$) records suggest an increased availability of ammonium in the photic zone and potentially a P-driven increase in N_2 fixation during the PETM (Knies *et al.*, 2008; Junium *et al.*, 2018). The cycling of Fe in the past ocean is even harder to trace, however local transitions to a (seasonally) drier climate (Carmichael *et al.*, 2017) likely resulted in enhanced wind-driven Fe deposition in nearby marine environments. Additionally, deoxygenation may have led to elevated fluxes of bioavailable Fe from continental shelf sediments to ocean waters (Homoky *et al.*, 2012; Raiswell *et al.*, 2018; Lenstra *et al.*, 2019).

4.4 Organic carbon burial

In our standard scenario, the combination of eutrophication and deoxygenation results in excess burial of ~13,000 Pg Corg across the entire PETM (Fig. 4.8b). The fraction of produced C_{ORG} that is buried increases from 1% (late Paleocene) to 3% (Supp. Table ST3). An increase in riverine P input from ~0.15 Tmol P yr^{-1} (Z09) to ~0.17 Tmol P yr^{-1} (Z09_Weath), leads to a rise in excess C_{ORG} burial of 7800 Pg C across the entire PETM. Our results emphasize the importance of redox-driven P recycling for the burial of C_{ORG}. When P burial is decoupled from [O_2] and DOA (Z09_Weath_Only), increased terrestrial nutrient input and subsequently higher primary productivity, fuel excess C_{ORG} burial that is ~16% of the Z09 value (Fig. 4.8b, c).

More than 70% of all excess burial in our model occurs in the three marginal boxes (S1 – 3) (Fig. 4.8a). Despite its large area and consequently large production, burial in the Pacific Ocean makes up only 10% of excess C_{ORG} burial. In fact, when open ocean production is kept constant (Z09_cOOPP), the resulting increase in nutrients in the marginal boxes leads to increased total global production and excess C_{ORG} burial. Such a change in the trophic resource continuum was postulated by Gibbs *et al.* (2006) to explain the different productivity trends between Wilson Lake on the New Jersey Shelf and ODP Site 1209 in the Pacific Ocean. In contrast to previous suggestions (e.g., Bains *et al.*, 2000), our study further supports the notion that deep ocean organic carbon burial played a very minor role in the recovery of the PETM.

The amount of total excess C_{ORG} burial in our Z09 simulation (13,300 Pg C) is higher than that determined from marginal marine sediment records and previous model simulations (4000 – 6000 Pg C; John *et al.*, 2008; Komar and Zeebe, 2017). By contrast, excess C_{ORG} burial in the Arctic (690 Pg C in surface; 870 Pg C in total) is very similar to the value (770 Pg C) of Sluijs *et al.* (2008a). We must note here that the sediment cores cover just a minor fraction of the full extent of the margins and their mass accumulation rate values may not be representative for other localities. Additionally, if we calculate the mass accumulation rates for our model, the maximum change in rate between the late Paleocene and the PETM are similar between our model and the data: 1.51 g m^{-2} yr^{-1} (Sluijs *et al.*, 2008a) and 1.48 g m^{-2} yr^{-1} for the Arctic (Fig. 4.6i), and 1.1 g m^{-2} yr^{-1} (John *et al.*, 2008) and 1.4 g m^{-2} yr^{-1} for the continental margin (Fig. 4.6i). As it is this difference that determines excess burial, and our rates fall well within the modern ranges (e.g. de Madron *et al.*, 1999; Alperin *et al.*, 2002), we are confident that our C_{ORG} burial results are realistic for the PETM. Collectively, we conclude that our simulated C_{ORG} burial, caused by changes in productivity and deoxygenation that are in good agreement with field data, is realistic for the PETM.

4.5 Can C_{ORG} burial explain the shape of the CIE?

The burial of C_{ORG}, and the $\delta^{13}C$ signature that is used, determines the reconstruction of the CIE and the estimation of carbon emissions. Zeebe *et al.* (2009) proposed a methane addition scenario of 4480 Pg C, which Komar and Zeebe (2017) adjust to 5500 Pg C following the inclusion of C_{ORG} sequestration ($\delta^{13}C_{ORG}$ = -33‰, as in this study). For their work on C_{ORG} burial and its effect on $\delta^{13}C$, Gutjahr *et al.* (2017) used a $\delta^{13}C_{ORG}$ value of -30.5‰, resulting in an, mostly volcanic, emission scenario of 10,000 Pg of C_{ORG}, whereas Dunkley Jones *et al.* (2018) used a $\delta^{13}C_{ORG}$ of -22‰. In this study, the burial of 13,300 Pg C, in excess of the late Paleocene, combined with the Zeebe *et al.* (2009) methane emission scenario, captures the general CIE shape and the rapid recovery but not the stable CIE plateau (Fig. 4.9).

Previous work (Bowen and Zachos, 2010; Gutjahr *et al.*, 2017; Komar and Zeebe, 2017; Dunkley Jones *et al.*, 2018) has highlighted that the burial of C_{ORG} (at least 2000 Pg C but up to 8000 Pg) is required to explain the relatively fast recovery within the first 30 – 40 kyr of the CIE. Our main PETM simulation, that now includes the correct locus for marine C_{ORG} burial, resulted in a similar amount of excess burial (3300 Pg C) within 40 kyr, buried mainly on the continental margin and the EES. The range of values for our sensitivity analyses is ~500 – 6000 Pg C, most of which is caused by redox feedbacks on C_{ORG} and P burial (Fig. 4.8).

The total increase of $\delta^{13}C$ during the recovery interval results in an overshoot relative to pre-PETM values. This occurs largely in the second half of the recovery, a time interval for which there are few constraints on the extent and degree of productivity and deoxygenation (see Supp. Table 4.1). When C_{ORG} burial rates up to and covering the first 40 kyr of the recovery are used, this δ13C overshoot is not simulated. (Figs. 4.1; 4.9). This truncation of C_{ORG} burial rates also results in lower total excess C_{ORG} burial (~6000 Pg C) similar to the 5000 Pg C suggested by Komar and Zeebe (2017). We therefore propose that this is a better estimate for the PETM than 13,300 Pg C. Importantly, the excess C_{ORG} burial during the key 40 kyr phase reproduces the more rapid recovery of $\delta^{13}C$ of ~2‰ as noted by Bowen and Zachos (2010). The C emissions required to recreate the CIE plateau of the PETM, with 6000 Pg excess C_{ORG} burial, is 5790 Pg of methane ($\delta^{13}C$: -55‰), or 7,030 Pg C of mixed sources: 4480 Pg C of

methane and 2,550 Pg C of C_{ORG} ($\delta^{13}C$: -25‰). Including emissions of volcanic origin ($\delta^{13}C$: -5‰) would require an even larger mass.

5. CONCLUSIONS

We compiled new and published proxy data for eutrophication and deoxygenation during the PETM and combined the results with biogeochemical modeling to simulate the effect on phosphorus and carbon burial over the event. We find that signs of increased primary productivity and spreading low oxygen conditions are largely concentrated in marginal and restricted sections of the ocean following the onset of the PETM and its recovery (final ~120 kyr). Our modeling results demonstrate that this spread of productive, low oxygen waters on the continental margin, the Arctic Ocean and Eurasian Epicontinental Seas could be caused by increased CO_2-driven riverine input of phosphate and water column stratification, further enhanced by phosphorus recycling linked to deoxygenation. Data and simulations show that deep sea organic carbon burial was quantitatively unimportant during the PETM. Our best estimate for excess C_{ORG} burial across the PETM is 6000 Pg C. Finally, our model suggests that eutrophication and deoxygenation within the first 40 kyr of the recovery phase could have led to the additional sequestration of 3300 Pg of C_{ORG}. This corroborates previous studies in showing that C_{ORG} burial of this order of magnitude is required to explain a rapid increase in global exogenic $\delta^{13}C$ at the beginning of the recovery phase.

4

<div style="background:#333;color:#fff;text-align:center;">

Chapter 4
Supplementary Materials

</div>

1. SITE DESCRIPTION

We generated new seafloor oxygenation proxy records for a selection of sites to fill gaps recognized in the compilation by Sluijs *et al*. (2014). These include the deep North Atlantic (International Ocean Discovery Program (IODP) Site 1403) and marginal settings in the Pacific, Tethys, Atlantic, Arctic, Southern and Indian Oceans (Lodo Gulch, Forada, Bass River, Lomonosov Ridge IODP Site M004, Ocean Drilling Program (ODP) Sites 1172 and 752).

Site 1403 was drilled during IODP Expedition 342 and recovered the late Paleocene and Early Eocene off the Newfoundland (Norris *et al*., 2014). The PETM was recognized by a negative $\delta^{13}C_{ORG}$ excursion and a break in carbonate sedimentation (Penman *et al*., 2016). The interval corresponding to the PETM comprises $CaCO_3$-poor and $CaCO_3$-rich (nannofossil) claystones and was deposited at a paleodepth of ca. 4400 m (Penman *et al*., 2016).

The Lodo Gulch section on the west coast of North America is comprised mostly of siltstone deposited at <200m water depth (Berggren and Aubert, 1983; John *et al*., 2008). The CIE extends from approximately 6m to 20m and the onset and core of the CIE are marked by an increase in grain size, $CaCO_3$ and C_{ORG} (John *et al*., 2008). The recovery interval is truncated by a glauconite-rich sand bed (John *et al*., 2008).

The PETM at Forada spans ca. 5 m of clay, marl and limestone deposited at ca. 1000 m depth and is characterized by a $\delta^{13}C_{CaCO3}$ excursion between ~39.5m and 44m (Giusberti *et al*., 2007). The core of the CIE occurs within a thick unit of clays and marls (the clay marl unit), which was the result of increased terrigenous flux to the site (Giusberti *et al*., 2007).

Paleogene siliciclastic sediments with some biogenic carbonate at Bass River, New Jersey shelf (ODP Leg 174AX) were deposited close to the shelf edge (Miller *et al*., 1998; Miller *et al*., 2004). The PETM $\delta^{13}C_{CaCO3}$ excursion occurs in a clay-rich interval between ~347 mbsf and 357 mbsf (Cramer *et al*., 1999; John *et al*., 2008).

The upper Paleocene and lower Eocene green and gray clay- and siltstones at ODP Site 1172 are rich in organics but devoid of calcareous and siliceous microfossils and were deposited in a shallow marine environment (Shipboard Scientific Party, 2001; Röhl *et al*., 2004). The thickness of the CIE is between 65 and 90 cm, depending on the definition of the termination (Sluijs *et al*., 2011).

Upper Paleocene to lower Eocene chalks, deposited at mid to lower bathyal depths, were recovered during ODP Expedition 121 Site 752 on the Broken Ridge in the Indian Ocean (Shipboard Scientific Party, 1989). The Paleocene-Eocene boundary is tentatively identified
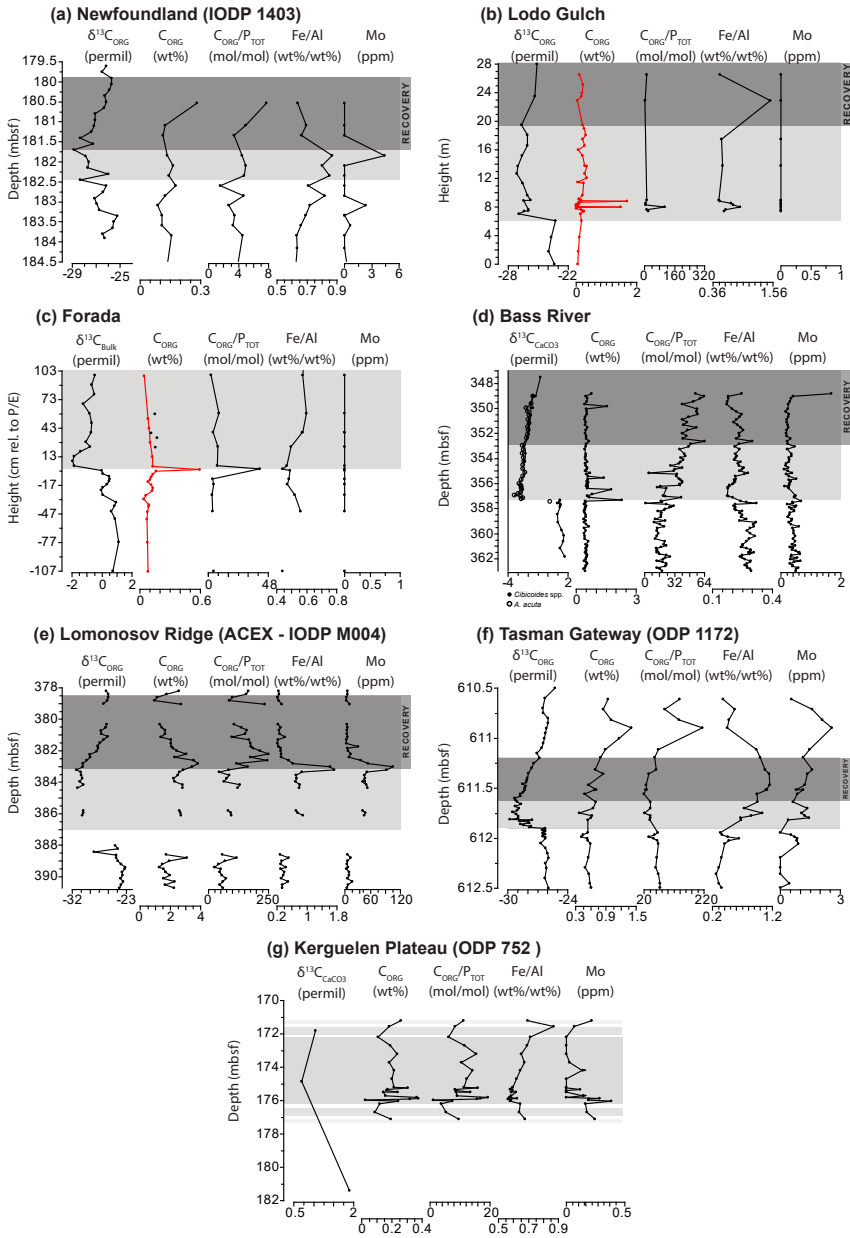
Supplementary Figure 4.1| PETM δ¹³C stratigraphy with bulk geochemical data: total organic carbon content (C_ORG), C_ORG/P_TOT, Fe/Al Mo concentrations. δ¹³C records are from Penman *et al.*, 2016 (IODP 1403), John *et al.*, 2008 (Lodo Gulch), Giusberti *et al.*, 2007 (Forada), Cramer *et al.*, 1999 (Bass River), Sluijs *et al.*, 2006 (Lomonosov Ridge), Sluijs *et al.*, 2011 (ODP 1172) and Seto *et al.*, 1991 (ODP 752). Organic carbon content for Lodo Gulch and Forada (red) are from John *et al.*, 2008 and Giusberti *et al.*, 2007, respectively. Grey bars indicate the extent of the PETM. Dark bars indicate the presumed extent for the recovery

phase in each record (recovery phase I at Bass River, Stassen *et al.*, 2012). The lighter bands for ODP 752 indicate the uncertainty in the extent of the PETM.

at 171.1 mbsf based on biostratigraphy and a negative shift in bulk carbonate $\delta^{13}C$ (Shipboard Scientific Party, 1989; Seto *et al.*, 1991).

2. GEOCHEMICAL ANALYSIS METHODS

Sediment samples were freeze-dried and powdered with an agate mortar and pestle. Between 100 and 125 mg of sample was weighed in Teflon destruction vessels, after which 2.5 ml concentrated mixed acid ($HClO_4$:HNO_3; 3:2) and 2.5 ml 40% HF were added. The mixture was then heated to 90 °C and left overnight. Subsequently, the acids were evaporated at a temperature of 140°C, after which the residue was dissolved in 25 ml 4.5% HNO_3. Finally, the concentrations of iron (Fe), molybdenum (Mo), phosphorus (P) and aluminum (Al) were measured using Inductively Coupled Plasma-Optical Emission Spectrometry (ICP-OES) using a Perkin Elmer 9224 Optima 3000. Sedimentary Fe contents were normalized over Al. The relative standard deviation (RSD) calculated from duplicates for the elements presented in this study was generally ≤ 5%.

Approximately 300 mg of powdered freeze-dried sediment was weighed in centrifuge tubes for decalcification prior to organic carbon analysis. The samples were mixed twice with 7.5 ml 1 M HCl, shaken overnight and subsequently washed twice with 10 ml demineralized water (Van Santvoort et al., 2002). Afterwards, the samples were dried in an oven at 50°C. Between 5 and 10 mg of decalcified sediment was weighed in tinfoil cups and analyzed using a Fisons Instruments CNS NA 1500 analyzer. Sedimentary C_{ORG} content was calculated after correcting the sediment weight for carbonate loss. Duplicate analyses set the RSD for C_{ORG} as ≤ 5%.

3. NEW GEOCHEMICAL DATA

The $\delta^{13}C$ data for our newly generated PETM records show that we capture both the onset and recovery of the PETM at five out of seven sites (Supplementary Figure 4.1). Average C_{ORG} contents are mostly at or below ~0.5% at all sites except for ODP 1172 and the Lomonosov Ridge site where C_{ORG} contents range up to ~1.3 and 3.4 wt%, respectively. At this latter site, values for C_{ORG} decrease during the recovery phase, but remain high (>1%). At the remaining sites, fluctuations in C_{ORG} content show no discernible trend.

Values for C_{ORG}/P_{TOT} are, likewise, low at most sites and generally below the Redfield ratio of 106. Average C_{ORG}/P_{TOT} in excess of this value is only found at the Lomonosov Ridge while a maximum C_{ORG}/P_{TOT} in excess of the Redfield value is only observed at this site and at Lodo Gulch. Although the C_{ORG}/P_{TOT} is low, the increase with time observed at IODP Site 1403, Bass River and ODP Site 752 does suggest more reducing conditions during the PETM. Maxima in C_{ORG}/P_{TOT} at Lodo Gulch and Forada may indicate brief deoxygenation. Increases in Fe/Al occur at IODP Site 1403, Lodo Gulch, Lomonosov Ridge and ODP Sites 1172 and 752. Molybdenum is present at Bass River, Lomonosov Ridge and ODP Sites 1172 and 752, with highest concentrations, up to 120 ppm, at the Lomonosov Ridge.

Five of our sediment records capture the recovery phase of the PETM. A minor increase in C_{ORG} and C_{ORG}/P_{TOT} at IODP Site 1403 and a single peak in Fe/Al at Lodo Gulch occur during the recovery. At Bass River, only C_{ORG}/P_{TOT} shows a change over the recovery, stabilizing at high values. Values of C_{ORG}, Fe/Al and Mo decrease during the recovery at the Lomonosov Ridge, but C_{ORG}/P_{TOT} reaches its maximum value in the same interval, before eventually recovering as well. Similar to Bass River, Fe/Al at ODP Site 1172 stabilizes at its maximum value before declining, while C_{ORG}, C_{ORG}/P_{TOT} and Mo show a minor increase across the entire recovery.

4. MODEL WATER CYCLE

Dimensions for the open ocean boxes were derived from LOSCAR (Zeebe, 2012). Shallow boxes represent the mixed surface layer and have an average depth of either 150 or 200m (Supp. Table 4.4). The thermocline box extends for 900m below the mid/low latitude surface ocean box. Assuming that the late Paleocene – early Eocene shelf area was approximately 1.5 – 2 times the size of the modern shelf (John *et al*., 2008), we set the total shelf size to 4.35 x 10^6 km². The Arctic Ocean was assigned an area of 0.3 x 10^6 km² (Sluijs *et al*., 2008a) and a total depth similar to the average depth of the modern basin (e.g. Abulaitijiang *et al*., 2019). The continental margin box was assigned an area twice (2.7 x 10^6 km²) that of the EES (1.35 x 10^6 km²) based on tectonic and sea level reconstructions for the Early Eocene (e.g. Seton *et al*., 2012; Miller *et al*., 2020). The deep section of the EES, with a depth of 750m, is represented by a separate box due to the uncertainty surrounding the depth of the EES and peri-Tethys, and the large number of sites in this area from a range of water depths (e.g., Gavrilov *et al*., 1997; 2003; Dickson *et al*., 2014).

The direction and value of the open ocean water fluxes were mostly based on LOSCAR (Zeebe, 2012) with remaining fluxes calculated by assuming steady state (Supp. Table 4.5). Deep water formation in the open ocean is located in the Southern Ocean (e.g., Pak and Miller, 1992; Thomas *et al*., 2003), with formation cells in each of the three major deep basins (Atlantic, Indotethys, Pacific). Deep water exchange between the major deep ocean basins was most likely much restricted relative to the modern given Southern Ocean tectonic boundary conditions, but there likely was some (e.g., Zeebe and Zachos, 2007; Luo *et al*., 2016). We have not included any exchange in the model for simplicity. Upwelling is divided into coastal (80%) and equatorial (20%) upwelling. The upwelled water partially evaporates, returning as precipitation in the Southern Ocean, while the remainder flows from the margins, through the low latitudes to the Southern Ocean. The restricted Arctic and Epicontinental basins have limited surface exchange, also with the low latitude open ocean, and no deep water exchange with the open ocean (Fig. 4.2). Rivers flow into the Arctic, EES and open ocean marginal boxes at rates approximately proportional to the size of each basin; the Arctic receives a somewhat larger fraction (10%) than dictated by its size (5%), as the modern Arctic makes up only 1% of the global seawater volume but receives 11% of global river outflow (Kalinin and Shiklomanov, 1974). The total riverine flux is increased relative to the modern value (Miliman and Farnsworth, 2013), assuming a stronger hydrological cycle for the late Paleocene (e.g. Pierrehumbert, 2002; Carmichael *et al*., 2017). Precipitation and evaporation are added for steady state.

5. LATE PALEOCENE STEADY STATE FOR MODEL

The simplified cycles of C, P and O_2 in our model include production, degradation and burial of organic matter (both C_{ORG} and P_{ORG}), as well as the burial of authigenic apatite (P_{AUTH}) and iron- bound P (P_{Fe}) (Supp. Table 4.4). Terrestrial Corg and detrital P are not included. Total primary production in the model is 49 Pg C yr^{-1}, which is close to the modern estimate for net primary production by coastal and oceanic phytoplankton (~54 Pg C yr^{-1}; Middelburg, 2019). We assume that production of P_{org} is linked to C_{org} through the Redfield ratio of 106:1, resulting in a total production of 38.7 Tmol P yr^{-1}. Roughly 80% of the organic matter is produced in the low latitude ocean (S4) and Southern Ocean (S5), with the remainder occurring in the three marginal boxes (S1 – 3). In the modern ocean, the open ocean accounts for a somewhat higher proportion of total production (87%; Middelburg, 2019). In the warmer world of the late Paleocene (e.g. Cramwinckel *et al.*, 2018) with much higher sea level (e.g. Müller *et al.*, 2008; Miller *et al.*, 2020) production may have been shifted towards the shelves, as it did during the PETM itself (e.g. Gibbs *et al.*, 2006) and as projected for the future ocean (Bindoff *et al.*, 2019).

Approximately 92% of total C_{ORG} production is recycled in the surface ocean (modern ocean: ~80%; Middelburg, 2019). The percentage of organic carbon that decays in the surface boxes varies from 84% in S1 to 96% in S2. Export production is ~3.6 Pg C yr^{-1} (modern ocean: 1.6 – 3.4 Pg C yr^{-1}; Laws *et al.*, 2000a; 9 – 13 Pg C yr^{-1}; Laws *et al.*, 2011) and ~99% of the C_{ORG} is degraded in intermediate and deep boxes. Therefore, only 1% of export production (0.036 Pg C yr^{-1}) is buried in the sediments of the deep Arctic, EES, Atlantic, Indotethys and Pacific Oceans (D1-5). A further 0.124 Pg C yr^{-1} is buried in the marginal boxes, in boxes S1 – 3, amounting to a total burial of ca. 0.3% of total primary production, or 0.16 Pg C yr^{-1} (Burdige, 2007).

In order to calculate the steady state burial fluxes for the three P phases, we set the initial $(C_{ORG}/P_{ORG})_{oxic}$ burial ratio for deep boxes to 260 (Komar and Zeebe, 2017), to 400 for the surface Arctic and EES (Slomp and Van Cappellen, 2007), and to 500 for the continental margin. The resulting C_{ORG}/P_{TOT} ratios in our model are close to the Redfield value of 106 suggesting that we obtain a good approximation of reactive P burial in oxic marginal settings (Algeo and Ingall, 2007). Additionally, we assume that P_{ORG} burial is 25% of the total, P_{AUTH} is 50% and the remaining 25% is buried as P_{Fe} (Ruttenberg, 2003; Slomp and Van Cappellen, 2007). The total P_{ORG} and P_{Fe} burial in our model are 0.034 Tmol P yr^{-1} each, while P_{AUTH} is 0.068 Tmol P yr^{-1}. Therefore, total P burial in the global ocean amounts to 0.136 Tmol P yr^{-1}, which falls within the range assumed for reactive (i.e. biologically active) P burial in previous studies for the pre-anthropogenic ocean (e.g. 0.09 Tmol P yr^{-1}; Slomp and Van Cappellen, 2007; 0.30 Tmol yr^{-1}; Ruttenberg, 2003). The burial of P is balanced by riverine input. The resulting residence time for P in the ocean is ~11 kyr, which is at the lower end of the range typically considered (10 – 40 kyr) (Ruttenberg, 2003; Tsandev *et al.* 2008) and also lower than the residence time in LOSCAR (~40 kyr; Komar and Zeebe, 2017).

The degradation of organic matter consumes O_2 and we model this explicitly in the intermediate and deep boxes (IM, D1 – 5) as O_2 respiration. The steady state value for respiration is calculated using the corresponding value of C_{ORG} decay and the $(C/O_2)_{Redfield}$ value (Supp. Table 4.6).

Dissolved P and O_2 are exchanged between all boxes. This transfer is directly linked to the water cycle and is equal to the product of the water flux and the concentration of the chemical constituent in the source box. Initial concentrations of dissolved P and O_2, the latter only for the intermediate and deep boxes, are calculated from the water flux and all other initial fluxes in the C, P and O_2 cycles, assuming steady state (Supp. Table 4.4). Oxygen concentrations in surface waters depend on temperature and are calculated using the equations for the solubility of O_2 derived by Weiss (1970) for the modern ocean-atmosphere system, as in LOSCAR (Zeebe, 2012). The initial concentrations are comparable to those in the modern ocean (Garcia *et al.*, 2018a; 2018b).

6. MODEL RATE LAWS

In the dynamic version of the model, used to assess the effect of perturbations, the exchange of dissolved P and O_2 between boxes was calculated as the product of the water flux and the concentration of the dissolved constituent in the source box (see Slomp and Van Cappellen, 2007 and references therein). As an example, the upwelling of dissolved P from the deep Atlantic onto the continental margin is the product of the upwelling rate and the $[PO_4]$ of the deep Atlantic.

Assuming that P is the limiting nutrient on geological timescales (e.g. Tyrrell, 1999), the formation of P_{org} through primary production in each surface box is dependent on $[PO_4]$ and a rate constant (Supp. Table 4.6):

$$PP = [PO_4] \times k_{bio} \qquad (4.1)$$

A set fraction f_{exp} of primary production is exported directly to the deep ocean (from S1, S3, S5) or to the thermocline (from S2, S4). Primary production and export of C_{ORG} are linked to P_{ORG} through the Redfield ratio. In all boxes, the fraction of C_{ORG} and P_{ORG} that is not exported (S1 – 5; IM) or buried (S1 – 3; D1 – 5) is remineralized.

In the thermocline and deep ocean, the remineralization of C_{ORG} consumes O2 at the Redfield ratio of 106:138 (Supp. Table 4.6). The additional effects of stratification and C_{ORG} degradation on deoxygenation at the sediment – water interface are captured in the degree of anoxia (DOA) (Van Cappellen and Ingall, 1994). A value of zero describes fully oxic conditions while a value of 1 is linked to complete anoxia:

$$DOA = 1 - \left(\frac{f_{strat} \times [O_2]}{[O_2]_0}\right) \times \left(\frac{PP_0}{PP}\right) \qquad (4.2)$$

where PP_0 is the steady state value for primary production and PP is primary production as calculated in (1). The term f_{strat} captures the effect of increased water column stratification as a result of rising temperatures and reduced salinity. A value of 1 implies a lack of stratification, whereas a value of zero is assigned when there is no vertical exchange within the water column of a box, hence stratification is complete. In complex models, this effect is described by a vertical diffusion coefficient which is generally dependent on density and ocean floor topography (e.g. Bouttes *et al.*, 2009). Such complexities are, however, beyond the capabilities of box models such as ours. We therefore assign a time dependent increase to a maximum

value within the plateau of the PETM, and a time dependent linear decrease back to 1 during the recovery.

In the marginal boxes (S1 – 3), a fraction of P is buried in sediments in the form of P_{ORG}, P_{AUTH} and P_{Fe}. The burial rates for all three phases are dependent on the degree of anoxia (DOA) in each box. Burial of P_{org} depends on the rate of primary production (PP), a rate constant (k_{orgP}) and DOA, assuming that only a fraction f_{orgP} of P_{org} burial is redox-dependent:

$$P_{ORG} = k_{orgP} \times PP \times \left((1 - f_{orgP}) + f_{orgP} \times (1 - DOA) \right) \tag{4.3}$$

The burial rate of P_{AUTH} depends on the remineralization of organic matter (R), a rate constant (k_{authP}) and DOA assuming a redox dependent fraction f_{authP}:

$$P_{AUTH} = k_{authP} \times R \times \left((1 - f_{authP}) + f_{authP} \times (1 - DOA) \right) \tag{4.4}$$

Burial of P_{Fe} depends linearly on DOA:

$$P_{Fe} = P_{Fe,0} \times (1 - DOA) \tag{4.5}$$

The burial rate of C_{ORG} is linked to that of P_{ORG} through the C_{ORG}/P_{ORG} burial ratio, with a value that depends on bottom water redox conditions (Van Cappellen and Ingall, 1994):

$$C_{ORG} = P_{ORG} \times \frac{C/P_{oxic} \times C/P_{anoxic}}{C/P_{anoxic} \times (1 - DOA) + C/P_{oxic} \times (DOA)} \tag{4.6}$$

In the deep ocean, burial of P_{ORG}, P_{AUTH}, P_{Fe} and C_{ORG} are modelled in a similar manner but here they depend on O_2 concentrations instead of DOA. Furthermore, P_{org} burial depends on P export rather than productivity:

$$P_{ORG} = k_{orgP} \times E \times \left((1 - f_{orgP}) + f_{orgP} \times \left(\frac{[O_2]}{[O_2]_0} \right) \right) \tag{4.7}$$

$$P_{AUTH} = k_{authP} \times R \times \left((1 - f_{authP}) + f_{authP} \times \left(\frac{[O_2]}{[O_2]_0} \right) \right) \tag{4.8}$$

$$P_{Fe} = P_{Fe,0} \times \left(\frac{[O_2]}{[O_2]_0} \right) \tag{4.9}$$

$$C_{ORG} = P_{ORG} \times \frac{C/P_{oxic} \times C/P_{anoxic}}{C/P_{anoxic} \times \left(\frac{[O_2]}{[O_2]_0} \right) + C/P_{oxic} \times \left(1 - \frac{[O_2]}{[O_2]_0} \right)} \tag{4.10}$$

Weathering of silicate and carbonate rocks on land is linked to atmospheric pCO_2 and provides reactive P to the ocean through rivers. The response of weathering of carbonates (W_{CARB}) and silicates (W_{SIL}) to changes in pCO_2 is modelled as in LOSCAR, by assuming a non-linear dependence on a factor n_{cc} and n_s, respectively:

$$W_{CARB} = W_{CARB,0} \times \frac{pCO_2}{pCO_{2,0}}^{n_{cc}} \qquad (4.11)$$

$$W_{SIL} = W_{SIL,0} \times \frac{pCO_2}{pCO_{2,0}}^{n_s} \qquad (4.12)$$

The response of P weathering (P_{WEATH}), in turn, depends on carbonate and silicate weathering modulated by a factor n_p :

$$P_{WEATH} = (P_{WEATH,0} \times \frac{W_{CARB} + W_{SIL}}{W_{CARB,0} + W_{SIL,0}})^{n_p} \qquad (4.13)$$

The riverine flux of P (P_{in}) to each marginal box (S1-S3) is a function of P_{WEATH} and of its coastline and area and an estimation of the number of rivers draining into the region, which are combined in the factor fin:.

$$P_{IN} = P_{WEATH} \times f_{in} \qquad (4.14)$$

Parameter values are either taken from previous publication (e.g. Komar and Zeebe, 2017) or calculated from steady state values of the fluxes and concentrations and their corresponding rate laws. Key parameter values can be found in Supp. Table 4.6.

A key output of the model is the excess burial of C_{ORG}: the amount of C_{ORG} buried in addition to the burial mass of late Paleocene (steady state) conditions. Excess C_{ORG} burial for a given time-step is the difference between the C_{ORG} burial rate at that time-step and the steady state burial rate, times the duration of the time-step. By adding the excess buried mass for all time-steps within a certain interval of the PETM (e.g. the recovery), we obtain the excess C_{ORG} burial for that interval. Other excess mass values, such as riverine P influx (**Fig. 3**) and primary production are calculated in a similar manner.

7. ADDITIONAL MODEL SIMULATIONS

The standard simulation presented in the main text is forced by the increased weathering of phosphorus (P), as a result of increased CO_2 following the curve presented by Zeebe *et al.* (2009) (Z09). We tested the biogeochemical response to three more CO_2 curves and present them here. Two of the curves are published by Frieling *et al.* (2016) (F16) and Gutjahr *et al.* (2017) (G17) whereas the third is an adjusted version of the Zeebe *et al.* (2009) curve with a 170 kyr duration for the stable isotope phase (Zeebe and Lourens, 2019) (K170). The forcing is, as in the standard Z09 simulation, an increase in weathering of P (Supp. Fig. 4.2A) which is then supplied to the marginal boxes (S1 – 3) of our model.

The results for the three additional simulations are very similar to those of the standard Z09 simulation, as evidenced by excess C_{ORG} burial during the full event and the first 40kyr of the recovery (Supp. Fig. 4.2B; see also Supp. Tables 4.3, 4.7). The similarities are largely due to the similar magnitude of the CO_2 change for the four different simulations. The different shapes of the CO_2 curves, in particular those of Frieling *et al.* (2016) and Gutjahr *et al.* (2017), result in a slight increase in excess C_{ORG} burial. The main difference is in the higher overall excess burial for K170, versus that of Z09, F16 and G17 (Supp. Fig. 4.2B). This is due to the longer
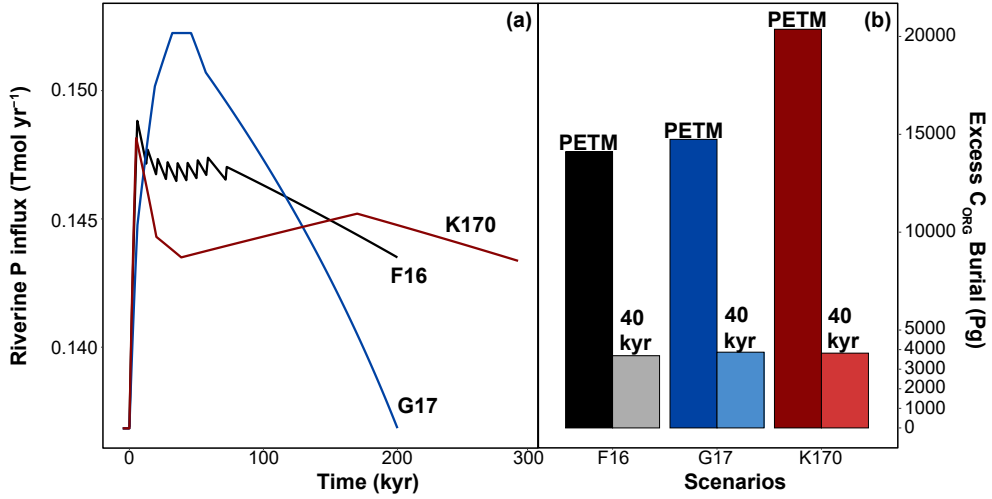
Supplementary Figure 4.2| Overview of two key input and output parameters for three additional PETM scenarios. The increased riverine phosphorus flux (A) is forced using pCO_2 curves from Frieling *et al.*, 2016 (F16; black), Gutjahr *et al.*, 2017 (G17; blue) and Zeebe *et al.*, 2009, with the longer plateau duration of Zeebe and Lourens, 2019 (K170; red). Darker colors for excess organic carbon (C_{ORG}) burial (B) indicate burial calculated over the entire PETM interval. Lighter colors indicate burial for the first 40 kyr of the recovery.

duration of the stable $\delta^{13}C$ phase of this scenario, giving more time for enhanced C_{ORG} burial to occur over.

8. REDOX SENSITIVITY OF P_{ORG} AND P_{AUTH} BURIAL

A key biogeochemical feedback driving C_{ORG} burial is the increase in redox-driven P recycling (see main text). In turn, the model response of P recycling to deoxygenation depends on the assigned sensitivity. The change in iron-bound P (P_{Fe}) burial due to deoxygenation is usually modelled as a linear relationship (Ingall and Van Cappellen, 1994). In the standard equations for organic P (P_{ORG}) and authigenic P (P_{AUTH}) burial (1, 2), the sensitivity is denoted as f_{OrgP}

$$P_{ORG} = k_{orgP} \times PP \times \left(\left(1 - f_{orgP}\right) + f_{orgP} \times (1 - DOA) \right) \qquad (4.15)$$

$$P_{AUTH} = k_{authP} \times R \times \left(\left(1 - f_{authP}\right) + f_{authP} \times (1 - DOA) \right) \qquad (4.16)$$

and f_{authP}:

Different values have been given to these two factors across a number of publications. In a study of the sensitivity of P cycling to ocean circulation in a model for the modern ocean (Slomp and Van Cappellen, 2007), the values for f_{OrgP} and f_{auth} were set at 0.25 and 0.5, respectively. Ruvalcaba Baroni *et al.* (2014), while modelling biogeochemical changes during
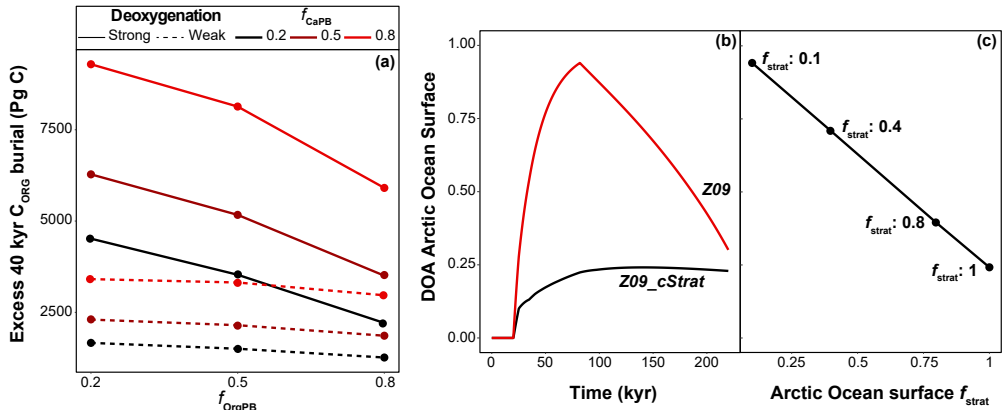
Supplementary Figure 4.3| Overview of sensitivity tests performed for our carbon-cycle box model. The effect of increased redox sensitivity of P burial on excess C_{ORG} burial within the first 40 kyr of the recovery (A) was tested under strong (high Degree of Anoxia or DOA; solid line) and weak deoxygenation (low DOA; dashed line). The values that were tested for the redox sensitivity of organic P burial (f_{OrgPB}) are 0.2, 0.5 and 0.8. The same values were tested for the redox sensitivity of authigenic P burial (f_{CaPB}; black, dark red and red, respectively). The effect of constant versus increased stratification (B) and different degrees of increased stratification (C) was tested on the DOA of the surface Arctic Ocean (box S1). Black line: constant stratification (Z09_cStrat). Red line: increased stratification with a maximum value of f_{strat} = 0.1 (Z09).

Oceanic Anoxic Event 2 (OAE2), used an f_{OrgP} value of 0.4, a coastal f_{auth} value of 0.82 and an open ocean f_{auth} value of 0.18. Again for OAE2, Tsandev and Slomp (2009) use values of 0.75 and 0.9 for f_{OrgP} and f_{auth}, respectively. These last two values were also used by Komar and Zeebe (2017) for PETM simulations.

The choice of P burial sensitivity depends on the design of the model and the sensitivity of the C_{ORG}/P_{TOT} ratio to anoxia inferred for the time period from the geological record or other considerations. For example, the higher values used by Ruvalcaba Baroni *et al.* (2014) and Tsandev and Slomp (2009) are explained by the severe and widespread nature of OAE2 deoxygenation (e.g. Takashima, 2004) and the reported high values of C_{ORG}/P_{TOT} ratios (up to 2000). To recreate these conditions in a model requires intense P recycling relative to C_{ORG} (Ruvalcaba Baroni *et al.*, 2014). On the other hand, the study of Komar and Zeebe (2017) focusses on C_{ORG} burial in the deep ocean which, with late Paleocene circulation, does not become hypoxic easily. As a result, intense P recycling is required to obtain the target value of excess C_{ORG} burial and the corresponding $\delta^{13}C$ curve.

In this study, we chose values of 0.75 for f_{OrgP} (Tsandev and Slomp, 2009) and 0.4 for f_{authP}, which is closer to the Slomp and Van Cappellen (2007) value than the high Komar and Zeebe (2017) value. The lower sensitivity for P_{AUTH} when compared to early studies is in line with milder deoxygenation during the PETM, compared to OAE2 (e.g. Jenkyns, 2010). These values resulted in excess C_{ORG} burial and relative C_{ORG}/P_{TOT} changes in line with the data and

previous publications. We also tested the response of our model to different values of f_{OrgP} and f_{authP}, using the Z09 forcing scenario, under strong (including increased stratification) and weak (without increased stratification) deoxygenation (Supp. Fig. 4.3A). A higher value of f_{authP} and stronger deoxygenation both cause an increase in excess C_{ORG} burial, as they promote P recycling and primary productivity. The response to increasing f_{OrgP} is opposite which appears counterintuitive. As P_{ORG} recycling gets stronger (higher f_{OrgP}), the supply of new organic matter is not sufficient to counteract the decreasing P_{ORG} burial. This effect is further strengthened under strong deoxygenation. The degree of deoxygenation also controls the value of C_{ORG}/P_{ORG} and as P_{ORG} gets lower at higher sensitivity, the corresponding C_{ORG} is also reduced. In all cases, C_{ORG} burial will still be higher than the late Paleocene value.

9. MODEL STRATIFICATION SENSITIVITY

Sluijs *et al.* (2006), among others, showed that stratification increased during the PETM, likely as a result of an enhanced hydrological cycle (e.g. Carmichael *et al.*, 2017). Stratification can be a key cause for deoxygenation in marginal marine areas and for this reason we have parameterized it in our model by adding a factor f_{strat} to the DOA for the surface Arctic and EES boxes. The Arctic Ocean and EES experienced severe deoxygenation, even anoxia (e.g. Sluijs *et al.*, 2008; Dickson *et al.*, 2014), which our model did not simulate without the addition of f_{strat}. We chose to use an exponential increase in f_{strat}, to match the shape of the increase in DOA without f_{strat} (Supp. Fig. 4.3B). As stratification is linked to a warmer, wetter climate due to rising pCO_2, we force a recovery of f_{strat} back to 1 (no increased stratification) at the beginning of the PETM recovery phase (Supp. Fig. 4.3B).

The value of DOA is approximately the same for all three marginal boxes, when increased stratification is not enforced (Supp. Table 4.3). The relationship between f_{strat} and DOA is broadly linear (Supp. Fig. 4.3C) and the effect of f_{strat} is the same, regardless of the box it is enforced on. This is evident when comparing the maximum DOA value of the surface Arctic (Supp. Fig. 4.3C) and the surface EES (Fig. 4.6) for an f_{strat} of 0.4. We chose to use a lower f_{strat} value for the surface EES (0.4), compared to the surface Arctic (0.1), resulting in a lower DOA for the EES.

Supplementary Table 4.1 | Compilation of published and new proxy records. Records cover proxies that are used to reconstruct changes in primary productivity and redox conditions. Site numbers correspond to the ones used in Figs. 4 and 5, and all references for these figures are given here as well. The key explains symbols and letters used to indicate increased, decreased or constant productivity and deoxygenation. We also provide information on the timing of these changes relative to the following stages of the $\delta^{13}C$ excursion: onset (O), core (B), early recovery (Ta) and late recovery (Tb). For an overview of these phases, see Fig. 1 of the main text. For changes in redox conditions we also provide the interpretations given in the original studies. Complete references are given at the end of the main text. N.A.: nannofossil assemblages.

Nr.	Site	Setting/ Paleodepth	Primary Productivity				Oxygen				Author oxygen condition definition	C_ORG
			Change	Data	Timing	Reference	Change	Data	Timing	Reference		
1	Harrell Core, Gulf Coastal Plain	Shelf					~	Isorenieratane Foram linings Glauconite	B (1/2)	Sluijs et al., 2014	Seasonal photic zone euxinia	Sluijs et al., 2014
2	Wilson Lake, New Jersey Shelf	Shelf	+ +?	 Benthic forams	O-Ta (/2) O-Ta (/2)	Gibbs et al., 2006 Stassen et al., 2012; 2015	- -	Benthic forams Biogenic single domain magnetite	O-Ta (/2) O-B (/2)	Stassen et al., 2012 Lippert & Zachos, 2007	Dysoxic (biogroups) Non-steady state redox/ Oxic-anoxic trans. shifted	Lippert & Zachos, 2007
3	Ancora, New Jersey Shelf	Shelf	+	Benthic forams	O-Tb (/2)	Stassen et al., 2012	- -	Benthic forams Biogenic single domain magnetite	O-Ta (/2) O-Ta (/2)	Stassen et al., 2012 Stassen et al., 2012	Dysoxic (biogroups) Non-steady state redox/ Oxic-anoxic trans. shifted	-
4	Bass River	Shelf	+	Benthic forams	O-Tb (/2)	Stassen et al., 2012; 2015	- =/~	Benthic forams Biogenic single domain magnetite Trace elements	O-Ta (/2) Ta (?) O-Tb (/2)	Stassen et al., 2012 This study	Dysoxic (biogroups)	This study/ John et al., 2008

4

No.	Location	Setting	+/−	Organic carbon	=/~	Trace elements	O-Tb	This study		This study
5	Lodo Gulch	Shelf				Isorenieratane	B-Ta	Sluijs et al., 2006	Photic zone euxinia	This study
6	IODP Site M0004, Lomonosov Ridge	Shelf	+	Organic carbon — O-T (low resol though) — Stein et al., 2006	−	Redox-sensitive trace elements; Laminations; Foram linings	B-Ta (/)	Sluijs et al., 2008	Anoxia	This study
						Pyrite	B-Ta	Stein et al., 2006	Euxinic	
					−/~	Redox-sensitive trace elements	B/Ta	This study		
7	Longyear-byean, Spitsbergen	Shelf			~	Amorphous organic matter; Phytoclasts; Th/U; Laminations	T	Harding et al., 2011	(Seasonally) low oxygen	Harding et al., 2011
8	BH9-05, Spitsbergen	Shelf			−	Benthic forams; Laminations; Laminations; Th/U; Pyrite; pristane, phytane	?; ?; O-Ta?	Nagy et al., 2013; Dypvik et al., 2011; Cui et al., 2011	Hypoxia; Reducing conditions; Anoxia	Cui et al., 2011

#	Location	Setting		Biomarker	Reference		Proxy	Code	Reference	Redox interpretation	Reference
9	Central Basin, North Sea	Shelf	(=)+		Kender et al., 2012	-	Laminations	?	Sluijs personal	Anoxia	Kender et al., 2012
							Benthic forams/ amorphous Organic Matter?	O-B	Kender et al., 2012		
10	Denmark, North Sea	Shelf				-	Laminations Pyrite Isorenieratane	O-B	Schoon et al., 2015	Anoxic/ sulfidic	Schoon et al., 2015
11	Well 10, West Siberian Sea	Ep. Shelf				~	Isorenieratane total organic carbon Dinoflagellates	? (1/)	Frieling et al., 2014	Photic zone euxinia Intermi./seas. Anoxia	Frieling et al., 2014
12	Medani, Georgia	Ep. Shelf			Dickson et al., 2014	-	Redox-sensitive trace elements	? No d13C (B)	Gavrilov et al., 1997; 2003	Hypoxic?	Gavrilov et al., 1997
							Redox-sensitive trace elements	? No d13C (B)	Gavrilov et al., 1997; 2003		
13	Kheu River, Central Caucasus	Ep. Shelf	+	Pristane; Phytane Alkanes / B	Scherbinina et al., 2016	-	Redox-sensitive trace elements	O-Ta	Dickson et al., 2014	Anoxic/ episodic ventilation	Dickson *et al.,* 2014

4

No	Location	Setting	Benthic forams	Ref		Evidence		Ref	Low oxygen conditions	Ref
14	Kaurtakapy, Khazakstan	Ep. Shelf			-	Pyrite/ fish debris	?	Gavrilov et al., 1997; 2003		-
15	Aktumsuk, Uzbekistan	Ep. Shelf			-	Trace metals	? No d13C (B)	Gavrilov et al., 1997; 2003	Hypoxic?	
					=-	laminations	?	Gavrilov et al., 2003		Gavrilov et al, 1997
					-	Pyrite/ lycopane	?	Bolle et al., 2000	Anoxic	
16	Torangly, Turkmeni-stan	Ep. Shelf	+	Benthic forams	B	Speijer et al., 1997	Benthic forams	B	Speijer et al, 1997	Anaerobic/ dysaerobic	Gavrilov et al, 1997
					-	Redox-sensitive trace elements	? No d13C (B)	Gavrilov et al., 1997; 2003		
17	Dzenghutay				~	Redox-sensitive trace elements	B	Dickson et al., 2014	Suboxic	Dickson et al., 2014
18	Kurpai / Guru Fatima, Tadjik depression				-	Redox-sensitive trace elements	B	Dickson et al., 2014	Anoxia/ euxinia	Dickson et al., 2014; Gavrilov et al., 2014
						Redox-sensitive trace elements	? No d13C (B)	Gavrilov et al., 1997; 2003		

No	Location	Setting	Eutroph.	Eutroph. proxy	Eutroph. code	Eutroph. reference	Oxygenation proxy	Oxyg. code	Oxyg. reference	Oxygenation interpretation	Interpretation reference
19	Sidi Nasseur / Wadi Mezaz, Tunisia	Shelf	=+	Benthic forams	?	Stassen et al., 2012	Benthic forams	O/B-?	Stassen et al., 2012	Severe dysoxia	Stassen et al., 2012
							Benthic forams	B	Morsi et al., 2011	Low oxygen	
							Ostracodes				
							Laminations	?	Speijer & Schmitz, 1998	Hypoxic?	
							Forams	O-B (?)			
							Benthic forams		Speijer & Wagner, 2002		
20	Gebel Aweina, Egypt	Shelf	+	Forams	O-B (/2?)	Speijer & Schmitz, 1998	Fish remains	?	Ernst et al., 2006	-	-
21	Dababiya, Egypt	Shelf	+	Forams	?	Soliman et al., 2011	Benthic forams (and compl. Absence)	O-Ta	Ernst et al., 2006	Anoxic/ephemeral oxygenation	Ernst et al., 2006
				Trace elements	B	Soliman et al., 2011	Laminations				
				$\delta^{15}N$	O-T	Khozyem et al., 2015	Redox-sensitive trace elements	B	Soliman et al., 2011	Anoxic/Euxinic	Schulte et al., 2011
				Elements	T (?)	Khozyem et al., 2015	Redox-sensitive trace elements	B	Khozyem et al., 2015	Anoxic	

4

#	Location	Setting		Proxy		Reference		Proxy		Reference		Interpretation
22	Gebel Duwi, Egypt	Shelf		Forams	?	Speijer et al., 1996	?	Forams	?	Speijer et al., 1996		Bolle et al., 2000
			+	Opal	O-T	Bolle et al., 2000	-	Laminations	?			
			?	$\delta^{13}C$	?	Schmitz et al., 1997	-	Forams		Speijer & Wagner, 2002		
				Calcite								
23	Gebel Nezzi, Egypt	Shelf					-	Benthic forams		Soliman et al., 2011		Farouk et al., 2019
24	Gebel Qreiya, Egypt	Shelf	+	P	O-B?	Schulte et al., 2013	-	Benthic forams		Khozyem et al., 2015	Hypoxia?	Schulte et al., 2013
								Pyrite				
								Redox-sensitive trace elements		Knox et al., 2003		
								Redox-sensitive trace elements	? (no access)			
								Pyrite		Soliman, 2003		
								Redox-sensitive trace elements				
								Redox-sensitive trace elements	O-B/Ta	Schulte et al., 2013	Anoxia/brief euxinia	

No.	Site	Setting	Productivity (signal / proxy / timing / reference)	Oxygenation (signal / proxy / timing / reference)	Inferred O₂ state / reference
25	Wadi Nukhul, Egypt	Shelf	+ ; d15N ; O(-T) ; Khozyem et al., 2013 — Elements — Benthic forams ; O-B (?) ; Speijer et al., 1997	- ; Benthic forams ; O-B (?) ; Speijer et al., 1997 — Redox-sensitive trace elements ; O-T ; Khozyem et al., 2013 — d15N / Benthic forams ; Speijer & Wagner, 2002	Quasi-anaerobic / Dysaerobic ; -
26	Ben Gurion, Israel	Shelf	+ ; Barium, SiO₂, P₂O₅ ; O-B/Ta? (low resol) ; Schmitz et al., 1997	- ; Benthic forams ; Speijer & Wagner, 2002	-
27	ODP Site 1172, Tasman Plateau	Shelf		~ ; Redox-sensitive trace elements ; O-T ; This study	This study
28	ODP Site 738	Deep (1300m)	+ (XP) ; Barite ; B? (low resol) ; Ma et al., 2014	=- ; Mn/U enrichment factors ; ? ; Pälike et al., 2014 — - ; Forams ; Lu & Keller, 1993	Suboxic ; Shipboard Scientific Party, 1989
29	DSDP Site 752, Kerguelen Plateau	Shelf		? ; Redox-sensitive trace elements ; ? ; This study	This study

4

#	Site	Setting		Proxy	Class.	Reference		Proxy	Class.	Reference	Notes
30	DSDP 213, Indian Ocean		-	N.A.	O-B (/I)	Tremolada & Bralower, 2004					-
31	Khasi Hills, India		+	Ter. OM + Apecto.	N.A.	Prasad et al., 2006					-
32	TDP14		=-	N.A.	O-B	Bown & Pearson, 2009					Aze et al., 2014
33	IB10 Nigeria	Shelf	+	TOC + Dinofl.	O/T	Frieling et al., 2017	-	Redox-sensitive trace elements	O-B	Frieling et al., 2017	
34	ODP Site 959, West Africa	Slope	+	Dinofl.	B	Frieling et al., 2018	+(?-) / -	Foram linings / Redox-sensitive trace elements	B	Frieling et al., 2018	Decreased oxygen levels
35	1051	Deep	+ (**XP**)	Barite	B	Ma et al., 2014					-
36	South Dover Bridge		+	N.A.	O-B, T?	Self-Trail et al., 2012					-
37	IODP Site 1403,	Deep					-?	Redox-sensitive trace elements	O	This study	This study
38	DSDP Site 549, North Atlantic	Deep	+ (**XP**)	Barite	T	Ma et al., 2014					Shipboard Scientific Party, 1985 (but not PETM specifically)

#	Site	Setting	Proxy	Value	Desig.	Reference	Value	Proxy	Desig.	Reference	Oxygenation	Reference
39	DSDP Site 401, Bay of Biscay	Deep (2000m)	N.A.	-	O-B	Tremolada & Bralower, 2004	-	Mn, U enrichment factors	O-T	Pälike et al., 2014	Suboxic	-
40	Zumaia, Spain	Slope/Rise					-	Ichnofossils	O-B/Ta	Rodriguez-Tovar et al., 2011	Oxygen depletion (not full anoxia)	Dunkley Jones et al., 2018
							-	Forams	?	Canudo et al., 1995	Low oxygen	
41	Alamedilla, Spain	Slope/Rise	Epi vs infaunal	=+	?	Alegret et al., 2010	=+	Vr/Cr Ni/Co		Alegret et al., 2010	Oxic	-
42	Caravaca, Spain	Slope 200-600					-(?)	Laminations	?	Canudo et al., 1995	Low oxygen	-
43	Forada, Italy	Rise/Deep	N.A.	+	B	Agnini et al., 2007	=+	Forams	O-B	Giusberti et al., 2007	Oxic	This study
			Pl. forams	+/=+	O-B	Luciani et al., 2007	-	Redox-sensitive trace elements		Luciani et al., 2007	Oxygen depletion	
			Barite	~	O	Giusberti et al., 2007		Bioturbation	O	This study		
			Benthic forams	(=)+ (XP)	B-Ta	Giusberti et al., 2016	-	Forams	O/B	Giusberti et al., 2016	Brief anoxia	
			Benthic forams	+	B	Giusberti et al., 2016	-	Redox-sensitive trace elements				
							-	Benthic forams				

4

#	Location	Setting	Sym	Prod. material	Prod. qualifier	Prod. reference	Sym	Oxygen material	Oxygen qualifier	Oxygen reference	Interpretation	
				Diatoms								
44	Anthering, Austria	rise	+		? (low resol)	Egger et al., 2003	-	Benthic forams	? (low resol)	Egger et al., 2003	Oxygen depletion	-
45	Untersberg, Austria	rise	+		?	Egger et al., 2005						-
46	Bieszczady Mountains, Poland	rise	~	Barite; P_2O_5	? (no d13C)	Bak et al., 2004	+	Deep water agglutinated forams	O-B (?); T (?); (no d13C)	Bak et al., 2004	Low oxygen	-
47	Hokkaido Tokachi district	Deep (?)	-				-	Benthic forams	?	Kaiho, 1988		-
48	ODP Site 1209, Shatsky Rise; Central Pacific	Deep (2000m)	-/=-		O-B	Gibbs et al., 2006	=+	Mn, U enrichment factors	?	Pälike et al., 2014	Oxic	-
			-/=-		?	Petrizzo, 2007	-	Benthic forams	O-Ta	Takeda & Kaiho, 2007	Low oxygen	
			+ (**XP**)	Barite	? (low resol)	Ma et al., 2014	-/=-	Pyrite	O	Colosimo et al., 2005		
			-	Benthic forams	O-Ta	Takeda & Kaiho, 2007						
			=(+)			Stoll et al., 2007	-	Benthic forams	O-B	Kaiho et al., 2006		

4

#	Site	Depth		Proxy		Reference		Proxy		Reference	Redox
49	ODP Site 1210, Shatsky Rise; Central Pacific	Deep (2200m)	-/=- -	Pl. forams Benthic forams	? O-Ta(?)	Petrizzo, 2007 Takeda & Kaiho, 2007	=/- -	Pyrite Benthic forams	O O-B O-Ta(?)	Colosimo et al., 2005 Kaiho et al. 2006 Takeda & Kaiho, 2007	- Low oxygen
50	ODP Site 1211, Shatsky Rise; Central Pacific	Deep (2500m)	-	Benthic forams	O-Ta(?)	Takeda & Kaiho, 2007	-	Pyrite Benthic forams	O-B O-Ta(?)	Colosimo et al., 2005 Takeda & Kaiho, 2007	- Low oxygen
51	ODP Site 1212, Shatsky Rise; Central Pacific	Deep (2300m)	-	Benthic forams	?	Takeda & Kaiho, 2007	-	Pyrite Benthic forams	O ?	Colosimo et al., 2005 Takeda & Kaiho, 2007	- Low oxygen
52	ODP Site 865, Central Pacific	Deep (1100-1300m)	-/= ?	Pl. forams	?	Kelly et al., 1996	-/=- - (?)	Benthic forams Benthic forams	 ?	Thomas, 1998 Bralower et al., 1995	Low oxygen -
53	ODP Site 1220, Central Pacific	Deep (3200m)	+ (XP)	Barite	? (low resol)	Ma et al., 2014	-/=-	Bioturbation Benthic forams	?	Nomura et al., 2005	-
54	ODP Site 1221, Central Pacific	Deep	+ (XP)	Barite	O-B?	Ma et al., 2014	-/=- =+	Benthic forams Bioturbation Mn/U enrichment factors	?	Nomura et al., 2005 Pälike et al., 2014	Oxic

#	Site	Depth		Proxy		Reference		Method		Reference	Redox	
55	ODP Site 1215	deep 3000	+ (**XP**)	Barite	O-B	Ma et al., 2016	-?	Benthic forams	?	Shipboard Scientific Party, 2002		-
56	ODP Site 999, Carribean	Deep (1500-2500m)					-	Laminations	O-Ta(Tb?)	Bralower et al., 1997	Dysoxic/oxygen deficiency	-
57	ODP Site 1001, Carribean	Deep (1500-2500m)	+(**XP?**)	Barite	?	Bains et al., 2000	-	Laminations	O-Ta(Tb?)	Bralower et al., 1997	Dysoxic/oxygen deficiency	-
58	ODP Site 1258, Demerara Rise	Deep (3000m?)	=(+)	Cocco. Sr/Ca	=-	Stoll et al., 2007	=-	Mn/U enrichment factors		Pälike et al., 2014	Suboxic	-
59	ODP Site 1260, Demerara Rise	Deep (2500m?)	-/=- +	N.A.	? T	Schneider et al., 2013 Mutterlose et al., 2007	-	Laminations	?	Shipboard Scientific Party, 2004		-
60	DSDP 525, Walvis Ridge	deep	+ (**XP**)	Barite	B-T	Ma et al., 2014						
61	ODP Site 1262, Walvis Ridge	Deep (3600m)					-	Mn/U enrichment factors	O-B	Chun et al., 2010	Suboxic	-
62	ODP Site 1263, Walvis Ridge	Deep (1500m)	+ (**XP**) ?-	Barite	O-Ta ?	Ma et al., 2014 Raffi & De Bernardi, 2008	=-	Mn/U enrichment factors		Pälike et al., 2014	Suboxic	-

#	Site	Depth	±	Productivity proxy	Type	Reference	±	Deoxygenation proxy	Type	Reference	Redox	
63	ODP Site 1265, Walvis Ridge	deep	+ (XP)	Barite	O-Ta	Ma et al., 2014	-	Mn/U enrichment factors	O-B	Pälike et al., 2014/ Chun et al., 2010	Suboxic	-
64	ODP Site 1266, Walvis Ridge	Deep (2600)	+ (XP)	Barite	T	Ma et al., 2014	-	Benthic forams	?	Thomas &	Decreased oxygen levels	-
65	ODP Site 689, Maud Rise	Deep (1100m)					-	Benthic forams	?	Thomas, 1989	Low oxygen	-
66	ODP Site 690, Maud Rise	Deep (1800m)	+ (XP)	Barite	B	Ma et al., 2014	-	Mn/U enrichment factors	T	Pälike et al., 2014	Suboxic	-
					O-B (Ta?)	Bains et al., 2000		Benthic forams	?	Thomas &	Decreased oxygen levels	
					T	Torfstein et al., 2010						
			-	N.A.	O-T(a) (depends on taxon)	Bralower, 2002						
			+	N.A.	B	Kelly et al., 2005						

4

#	Site	Setting	PETM change	Productivity proxy	Timing	Reference	Low O₂ change	Indicator	Timing (low O₂)	Reference	Descriptor	
66	ODP Site 690, Maud Rise	Deep (1800m)	-	Pl. forams	O-B (depends on A. species)	Kelly, 2002	-		?	Thomas, 1989	Low oxygen	-
			+	Sr/Ca	O/B-T	Stoll & Bains, 2003; Stoll et al., 2007						
67	Mead Stream, New Zealand	slope 100-1000	=-/-	Marl + Carbonates	? (low resol)	Hollis et al., 2005	-	Laminations	O-B (?)	Nicolo et al., 2010	Oxygen depletion	-
68	Dee Stream, New Zealand	slope 100-1000	-	Marl + Carbonates	O?	Hancock et al., 2003	-	Laminations	O-B (?)	Nicolo et al., 2010	Oxygen depletion	-
								Forams	? (no d13C comp)	Hancock et al., 2003	Dysoxia	-
69	Tawanui, New Zealand	slope	+	Dinofl.	? (no d13C comp)	Crouch & Brinkhuis, 2005	-	Benthic Forams	? (no d13C comp)	Kaiho et al., 1996	Suboxic	Crouch et al., 2003
			+	N.A	B-T	Crouch et al., 2003						
			-/=?	Forams + N.A	? (no d13C comp)	Kaiho et al., 1996						

Key changes across PETM: (+) increase; (-) decrease; (=+) no change, high; (=-) no change, low; (~) variable/intermittent oxygenation.

Timing of low O₂ / high PP: (O) onset; (B) plateau; (T) termination; (Ta) first phase of termination; (Tb) second phase of termination; (/) unconformity or hiatus; (x/y) during x and/or y; (x-y) from x and until y.

Supplementary Table 4.2| Descriptions for the standard runs and sensitivity simulations performed within this study. An n_p value of 0.4 results in a maximum riverine P input rate of ~0.15 Tmol P yr^{-1} and a value of 1.0 gives a maximum rate of ~0.17 Tmol P yr^{-1}. Note that the following sensitivity analyses were also performed with an np value of 1.0: Z09_OOP, Z09_nostrat, Z09_noO2r, Z09_noPPr and Z09_river.

Code	CO$_2$ Forcing	f_{OrgP}^a	f_{CaP}^a	f_{strat}^a	n_p^a	O$_2$ dependence	Notes
Z09				0.1[b]; 1[c]; 0.4[d]	0.4	T; f$_{strat}$; PP	
Z09_weath				0.1[b]; 1[c]; 0.4[d]	**1**	T; f$_{strat}$; PP	Increased P weathering sensitivity
Z09_OOP	Zeebe et al., 2009	0.75	0.4	0.1[b]; 1[c]; 0.4[d]	0.4	T; f$_{strat}$; PP	PP in S4 and S5 constant
Z09_nostrat				**1[b]; 1[c]; 1[d]**	0.4	T; PP	No stratification
Z09_river				**1[b]; 1[c]; 1[d]**	0.4	-	No deoxygenation/stratification
Z09_O$_2$sol				**1[b]; 1[c]; 1[d]**	**0**	**T; PP**	No P weathering/stratification
F16	Frieling et al., 2016						
G17	Gutjahr et al., 2017	0.75	0.4	0.1[b]; 1[c]; 0.4[d]	0.4	T; f$_{strat}$; PP	Supp. Info.
K170	Zeebe et al., 2009 + 170 kyr body						

a: Sensitivity analysis in Supplementary Information; b: Arctic surface; c: Open ocean continental shelf; d: European Epicontinental shelf surface

4

Supplementary Table 4.3| Maximum and minimum (O_2 concentration) values for key model output, and excess C_{ORG} burial over the entire PETM and the first 40 kyr of the recovery, for our standard scenario and further sensitivity simulations. An explanation for the setup of the sensitivity analyses can be found in Table 4. The change in temperature is the same for all scenarios and given only for the standard run (Z09).

Maximum (minimum*) values	S1	S2	S3	S4	S5	IM	D1	D2	D3	D4	D5	Total
Z09												
Temperature (°C)	19.5	27.5	27.5	27.5	14.5	18.4	14.3	14.3	14.3	14.3	14.3	-
$[PO_4]$ ($\mu mol\,kg^{-1}$)	1.38	1.78	1.40	1.24	0.87	2.08	2.90	1.49	1.63	1.75	2.79	-
Primary Productivity ($Pg\,C\,yr^{-1}$)	0.9	9.1	3.6	60.7	3.1	-	-	-	-	-	-	77.4
Primary Productivity increase ($g\,C\,m^{-2}\,yr^{-1}$)	109.1	120.9	95.2	68.9	41.6	-	-	-	-	-	-	435.8
DOA	0.94	0.38	0.74	-	-	-	-	-	-	-	-	-
$[O_2]$ ((μM)*)	-	-	-	-	-	81.1	0.0	162.8	142.6	126.9	0.0	-
C_{org} burial ($Pg\,C\,yr^{-1}$)	0.01	0.11	0.06	-	-	-	0.002	0.01	0.01	0.03	0.002	0.25
C_{org} burial ($Pg\,C\,m^{-2}\,yr^{-1}$)	4.30	4.20	4.40	-	-	-	0.700	0.20	0.20	0.20	0.200	14.40
C_{org}/P_{tot} (rel)	2.4	1.4	1.9	-	-	-	4.0	1.3	1.3	1.4	4.0	-
Excess C_{org} burial (Pg C yr^{-1})	692	5833	3197	-	-	-	176	530	825	1890	181	13324
Excess C_{org} burial 40 kyr ($Pg\,C\,yr^{-1}$)	168	1439	791	-	-	-	43	132	205	470	45	3293
Z09_Weath												
$[PO_4]$ ($\mu mol\,kg^{-1}$)	1.62	2.12	1.65	1.48	1.04	2.49	3.41	1.78	1.96	2.10	3.29	-

Primary Productivity (Pg C yr^{-1})	1.1	10.9	4.2	72.5	3.8	-	-	-	-	-	92.4
Primary Productivity increase (g C m^{-2} yr^{-1})	162.5	186.4	142.3	105.8	63.9	-	-	-	-	-	661.0
DOA	0.95	0.48	0.78	-	-	-	-	-	-	-	-
$[O_2]$ (μM)⋆	-	-	-	-	56.5	0.0	145.9	121.7	103.0	0.0	-
C_{org} burial (Pg C yr^{-1})	0.02	0.13	0.07	-	-	0.002	0.01	0.02	0.04	0.002	0.29
C_{org}/P_{tot} (rel)	2.4	1.5	2.0	-	-	4.0	1.4	1.5	1.6	4.0	-
Excess C_{org} burial (Pg C yr^{-1})	-	-	-	-	-	-	-	-	-	-	21137
Excess C_{org} burial 40 kyr (Pg C yr^{-1})	-	-	-	-	-	-	-	-	-	-	5021

Z09_cOOPP

$[PO_4]$ (μmol kg^{-1})	1.89	1.93	1.92	1.80	1.07	2.26	3.98	1.47	1.56	1.63	3.85
Primary Productivity (Pg C yr^{-1})	1.2	9.9	4.9	38.5	2.0	-	-	-	-	-	56.5
Primary Productivity increase (g C m^{-2} yr^{-1})	221.6	149.3	194.6	0.0	0.0	-	-	-	-	-	565.5
DOA	0.95	0.42	0.81	-	-	-	-	-	-	-	-
$[O_2]$ (μM)⋆	-	-	-	-	124.0	0.0	190.9	177.9	168.2	0.0	-
C_{org} burial (Pg C yr^{-1})	0.02	0.12	0.08	-	-	0.003	0.01	0.01	0.02	0.003	0.26
C_{org}/P_{tot} (rel)	2.4	1.4	2.1	-	-	4.0	1.1	1.1	1.1	4.0	-
Excess C_{org} burial (Pg C yr^{-1})	-	-	-	-	-	-	-	-	-	-	5069

4

	1	2	3	4	5	6	7	8	9	10	11
Excess C_{org} burial 40 kyr (Pg C yr^{-1})	-	-	-	-	-	-	-	-	-	-	1337
Z09_cStrat											
[PO$_4$] (μmol kg^{-1})	1.12	1.48	1.14	1.02	0.71	1.72	2.36	1.22	1.34	1.44	2.27
Primary Productivity (Pg C yr^{-1})	0.7	7.6	2.9	50.1	2.6	-	-	-	-	-	63.9
Primary Productivity increase (g C m^{-2} yr^{-1})	53.4	63.9	47.0	36.0	21.7	-	-	-	-	-	222.0
DOA	0.24	0.25	0.24	-	-	-	-	-	-	-	-
[O$_2$] ((μM))*	-	-	-	-	-	103.3	56.7	178.1	161.4	148.4	41.3
C_{org} burial (Pg C yr^{-1})	0.01	0.10	0.05	-	-	-	0.001	0.01	0.01	0.03	0.001
C_{org}/P_{tot} (rel)	1.2	1.2	1.2	-	-	-	1.5	1.2	1.2	1.2	1.6
Excess C_{org} burial (Pg C yr^{-1})	-	-	-	-	-	-	-	-	-	-	7498
Excess C_{org} burial 40 kyr (Pg C yr^{-1})	-	-	-	-	-	-	-	-	-	-	1680
Z09_Weath_Only											
[PO$_4$] (μmol kg^{-1})	0.95	1.23	0.96	0.85	0.59	1.43	1.99	1.01	1.11	1.19	1.91
Primary Productivity (Pg C yr^{-1})	0.6	6.3	2.4	41.7	2.1	-	-	-	-	-	53.2
Primary Productivity increase (g C m^{-2} yr^{-1})	15.3	17.5	13.4	9.8	5.8	-	-	-	-	-	61.8
DOA	0	0	0	-	-	-	-	-	-	-	-
[O$_2$] ((μM))*	-	-	-	-	-	133.4	100.7	203.3	190.4	180.4	80.8
C_{org} burial (Pg C yr^{-1})	0.01	0.08	0.04	-	-	0.001	0.001	0.01	0.01	0.02	0.001

C_{org}/P_{tot} (rel)	1.02	1.02	1.02	1.02	1.02	1.02	1.02	1.02	1.02	1.02	1.02	-
Excess C_{org} burial (Pg C yr^{-1})	-	-	-	-	-	-	-	-	-	-	-	2245
Excess C_{org} burial 40 kyr (Pg C yr^{-1})	-	-	-	-	-	-	-	-	-	-	-	506
Z09_O2Sol												
[PO$_4$] (μmol kg^{-1})	0.95	1.24	0.96	0.86	0.60	1.44	1.99	1.02	1.12	1.20	1.92	-
Primary Productivity (Pg C yr^{-1})	0.6	6.3	2.4	41.9	2.2	-	-	-	-	-	-	53.5
Primary Productivity increase (g C m^{-2} yr^{-1})	15.3	18.7	13.5	10.6	6.4	-	-	-	-	-	-	64.4
DOA	0.10	0.10	0.10	-	-	-	-	-	-	-	-	-
[O$_2$] ((μM))*	-	-	-	-	120.3	83.0	189.4	175.6	164.9	65.6	-	-
C_{org} burial (Pg C yr^{-1})	0.01	0.08	0.04	-	-	0.001	0.01	0.01	0.02	0.001	-	0.17
C_{org}/P_{tot} (rel)	1.09	1.08	1.08	1.08	-	1.16	1.07	1.08	1.09	1.18	-	-
Excess C_{org} burial (Pg C yr^{-1})	-	-	-	-	-	-	-	-	-	-	-	2147
Excess C_{org} burial 40 kyr (Pg C yr^{-1})	-	-	-	-	-	-	-	-	-	-	-	479

4

Supplementary Table 4.4| Box characteristics with steady state concentrations and fluxes. Fluxes for carbon are given in Pg C yr⁻¹, for phosphorus in Tmol P yr⁻¹ and for oxygen in Tmol O₂ yr⁻¹. All values are rounded. PP: primary production; EXP: export; DC: Decay; BR: Burial; Resp.: respiration. Epi.: Epicontinental.

Box	Area (Tm²)	Depth (m)	[O₂]	[PO₄] (μmol kg⁻¹)	T (°C)	C_{ORG} PP	C_{ORG} DC	C_{ORG} EXP	C_{ORG} BR	River. [PO₄]	P.P.	P_{ORG} DC	P_{ORG} EXP	P_{ORG} BR	P_{AUTH} BR	P_{Fe} BR	O₂
S1	3	200	234	0.88	17	0.58[a]	0.48	0.09	0.009	0.014	0.45	0.38	0.07	0.002	0.004	0.002	-
S2	27	150	203.2	1.14	25	5.83[b]	5.58	0.17	0.077	0.075	4.58	4.43	0.14	0.013	0.026	0.013	-
S3	13.5	150	203.2	0.89	25	2.27[c]	2.14	0.09	0.038	0.048	1.78	1.7	0.07	0.008	0.016	0.008	-
S4	321.08	150	203.2	0.79	25	38.53[d]	35.45	3.08	-	-	30.29	27.87	2.42	-	-	-	-
S5	27.92	200	258.3	0.55	12	1.98[e]	1.78	0.2	-	-	1.56	1.4	0.16	-	-	-	-
IM	321.08	900	133.4	1.32	16	-	2.54	0.72	-	-	-	2	0.56	-	-	-	-
D1	13.5	1040	100.7	1.84	12	-	0.09	-	0.001	Sup-	-	0.07	-	-	0.001	-	9.28
D2	52.35	2940	203.3	0.93	12	-	0.15	-	0.006	-	-	0.12	-	0.002	0.004	0.002	-
D3	80.27	2000	190.4	1.03	12	-	0.22	-	0.009	-	-	0.18	-	0.003	0.006	0.003	24.4
D4	181.48	3610	180.4	1.1	12	-	0.51	-	0.02	-	-	0.41	-	0.006	0.013	0.006	-
D5	3	750	80.8	1.77	12	-	0.09	-	0.001	-	-	0.07	-	-	0.001	-	9.74
Total	-	-	-	-	-	49.19	49.03	4.35	0.16	0.137	38.67	38.63	3.42	0.034	0.068	0.034	

a: twice the modern value (Arrigo and van Dijken, 2011); b: somewhat higher than modern value (Wollast et al., 1998); c: tuned to obtain nutrient utilization efficiency <1; d: Wollast et al., 1998; e: Arrigo et al., 2008

Supplementary Table 4.5| Water fluxes for the box-model. Values are given in Tm^3 yr^{-1} (model input) and Sverdrup.

Flux	Code	Tm3/yr	Sv
Arctic surface - deep	F1/F2	70	2.2
Arctic surface to EES surface	F3	65	2.1
EES surface to Arctic surface	F4	63	2.0
Arctic surface - mid/low latitudes	F5/F6	43	1.4
EES surface - mid/low latitudes	F7/F8	154	4.9
EES surface -deep	F9/F10	80	2.5
Open ocean shelf to mid/low latitudes	F11	631	20.2
Open ocean shelf upwelling	F12	631	20.2
Mid/low latitudes Upwelling	F13	158	5.0
Mid/low latitudes - thermocline	F14/F15	3345	
Southern ocean - Atlantic	F16/F17	158	5.0
Southern ocean - Indotethys	F18/F19	158	5.0
Southern ocean - Pacific	F20/F21	252	8.1
Southern ocean deep water (Atlantic)	F22	131	4.2
Southern ocean deep water (Indotethys)	F23	202	6.5
Southern ocean deep water (Pacific)	F24	456	14.6
Thermocline upwelling (Atlantic)	F25	131	4.2
Thermocline upwelling (Indotethys)	F26	202	6.5
Thermocline upwelling (Pacific)	F27	456	14.6
Mid/low latitudes to Southern Ocean	F28	394	12.6
Riverine influx (Arctic)	RF1	5	0.2
Riverine influx (EES)	RF2	18	0.6
Riverine influx (Open ocean shelf)	RF3	28	0.9
Evaporation (Arctic)	EV1	3	0.1
Evaporation (EES)	EV2	20	0.6
Evaporation (Open ocean shelf)	EV3	28	0.9
Evaporation (Mid/low latitude)	EV4	394	12.6
Precipitation (Southern Ocean)	PR1	394	12.6

4

Supplementary Table 4.6| Key parameter values for the box model.

Parameter	Symbol	Value	Unit
Redfield C_{org}/P_{org}	$(C_{org}/P_{org})_{Redfield}$	106	mol/mol
Redfield C_{org}/O_2	$(C_{org}/O_2)_{Redfield}$	106/138	mol/mol
Fraction of export production decayed in thermocline	$tcpfract$	0.78	-
Surface particulate OM export fraction	f_{exp}	0.15[S1]; 0.03[S2]; 0.04[S3]; 0.08[S4]; 0.1[S5]	-
Fraction P_{riv} input	f_{in}	0.1[S1]; 0.55[S2]; 0.35[S3]	-
Anoxic C_{org}/P_{org}	$(C_{org}/P_{org})_{anoxic}$	1500	mol/mol
Burial C_{org}/P_{org}	$(C_{org}/P_{org})_{oxic}$	400[S1,S3]; 500[S2]; 260[D1-5]	mol/mol
Rate constant for primary productivity	k_{biol}	0.86[S1]; 0.99[S2]; 0.99[S3]; 0.8[S4]; 0.51[S5]	Tm^3/yr
Fraction primary/export productivity buried (P_{org})	k_{OrgP}	0.0039[S1]; 0.0028[S2]; 0.0045[S3]; 0.0041[D1,D5]; 0.0007[D2]; 0.001[D3]; 0.0024[D4]	-
Fraction decay buried (P_{auth})	k_{CaP}	0.009[S1,S3]; 0.006[S2]; 0.008[D1,D5]; 0.031[D2-4]	-
Steady state temperature	$T0$	17[S1]; 25[S2-4]; 12[S5]; 16[IM]; 12[D1-5]	°C
Gravimetric constants A	A	-177.7888; 255.5907; 146.4813; -22.2040	-
Gravimetric constants B	B	-0.037362; 0.016504; -0.0020564	-
Silicate weathering scaling factor	n_s	0.2	-
Carbonate weathering scaling factor	n_{cc}	0.4	-
Surface waters temperature relaxation time	$tlags$	20	-
Intermediate waters temperature relaxation time	$tlagim$	200	-
Deep waters temperature relaxation time	$tlagd$	1000	-
Temperature sensitivity to doubling of CO_2	s	3	-
Salinity	Sal	34.72	(psu)

Supplementary Table 4.7| Maximum and minimum (O_2 concentration) values for key model output for three additional pCO_2 forcing scenarios: F16 (Frieling *et al.*, 2016); G17 (Gutjahr *et al.*, 2017); K170 (Zeebe *et al.*, 2009 with long plateau as per Zeebe and Lourens, 2019).

Maximum (minimum*) values	S1	S2	S3	S4	S5	IM	D1	D2	D3	D4	D5	Total
					F16							
[PO$_4$] (μmol kg^{-1})	1.42	1.84	1.44	1.28	0.90	2.16	2.99	1.54	1.69	1.81	2.88	-
Primary Productivity (Pg C yr^{-1})	0.9	9.4	3.7	62.8	3.3	-	-	-	-	-	-	80.1
DOA	0.94	0.40	0.76	-	-	-	-	-	-	-	-	-
[O$_2$] ((μM)*	-	-	-	-	-	75.3	0.0	157.9	136.9	120.7	0.0	-
C$_{org}$ burial (Pg C yr^{-1})	0.01	0.12	0.06	-	-	-	0.002	0.01	0.01	0.03	0.002	0.25
C$_{org}$/P$_{tot}$ (rel)	2.4	1.4	1.9	-	-	-	4.0	1.3	1.4	1.4	4.0	-

4

Supplementary Table 4.8| Core information and new bulk geochemical measurements for study sites presented in this study and its supplements. The new data presented here cover: total organic carbon content (C_{ORG}), aluminum (Al), iron (Fe), manganese (Mn), molybdenum (Mo), phosphorus (P) and vanadium (V).

Leg	Site	Hole	Core	Section	Top Depth (cm)	Bottom Depth (cm)	Sample Code	Depth (mbsf)	C_{ORG} (%)	Al 394.401 (ppm)	Fe 259.941 (ppm)	Mn 257.611 (ppm)	Mo 203.909 (ppm)	P 177.495 (ppm)	V 292.464 (ppm)
							IODP Site U1403 Newfoundland								
342	1403	A	21X	2	25	26	1403A 21X-2 25-26	177.15		61980	43361	9239	0.0	1225	55
342	1403	A	21X	2	63	64	1403A 21X-2 63-64	177.53	0.14	49227	27182	2682	0.0	926	127
342	1403	A	21X	3	10	11	1403A 21X-3 10-11	178.5	0.14	62907	38591	2591	0.0	1104	161
342	1403	A	21X	3	93	64	1403A 21X-3 93-94	179.33	0.12	56769	39736	3001	0.0	944	138
342	1403	A	21X	4	119	120	1403A 21X-4 119-120	180.53	0.33	41920	27752	3117	0.0	778	86
342	1403	A	21X	4	144	145	1403A 21X-4 144-145	181.09	0.12	44170	28233	2572	0.0	646	80
342	1403	A	21X	4	63	64	1403A 21X-4 63-64	181.34	0.11	46770	32422	2677	0.0	858	82

342	1403	A	21X	5	119	120	1403A 21X-5 119-120	181.84	0.13	65122	55391	2119	4.4	2888	114
342	1403	A	21X	5	144	145	1403A 21X-5 144-145	182.09	0.16	58760	41706	1340	0.0	683	100
342	1403	A	21X	5	44	45	1403A 21X-5 44-45	182.34	0.14	46239	37864	1250	0.0	845	74
342	1403	A	21X	5	69	70	1403A 21X-5 69-70	182.59	0.18	54980	47686	2895	0.0	858	86
342	1403	A	21X	5	94	95	1403A 21X-5 94-95	182.84	0.12	62683	50250	3923	0.0	778	99
342	1403	A	21X	6	19	20	1403A 21X-6 19-20	183.09	0.09	64061	46048	5412	2.3	798	85
342	1403	A	21X	6	44	45	1403A 21X-6 44-45	183.34	0.11	64234	44490	6161	0.0	868	81
342	1403	A	21X	6	44	45	1403A 21X-6 44-45	183.34		65186	44875	6240	0.0	891	82
342	1403	A	21X	6	69	70	1403A 21X-6 69-70	183.59	0.11	65463	43050	6517	0.7	983	79

							Sample Code		C_ORG (%)	Fe 259.941 (ppm)	Mn 257.611 (ppm)	Mo 203.909 (ppm)	P 177.495 (ppm)	V 292.464 (ppm)
342	1403	A	21X	6	94	95	1403A 21X-6 94-95	183.84	0.16	60419	38105	7977	0.0	1480	69
342	1403	A	21X	7	25	26	1403A 21X-7 25-26	184.15		61928	39266	7539	0.0	1469	85
342	1403	A	22X	2	25	26	1403A 22X-2 25-26	186.85	0.08	60924	35764	9853	1.7	1499	54
342	1403	A	22X	3	25	26	1403A 22X-3 25-26	187.85	0.13	58680	36360	11537	0.0	1520	54

Forada

Sample Code	Height (cm)	C_ORG (%)	Al 394.401 (ppm)	Fe 259.941 (ppm)	Mn 257.611 (ppm)	Mo 203.909 (ppm)	P 177.495 (ppm)	V 292.464 (ppm)
BRI 280	278.5	0.12	53030	39077	528	0	507	88
BRI 155	153.5	0.12						
BRI 100	98.5		42965	24660	1081	0	543	73
BRI 60	58.5	0.15	56281	33701	518	0	449	108
BRI 40	38.5	0.11	51873	29786	794	0	791	91
BRI 40	38.5		52328	29814	799	0	771	91
BRI 35	33.5	0.17						
BRI 25	23.5	0.15	55018	27363	645	0	519	101
BRI 5	3.5		70011	32759	262	0	468	136

Black Lamina

		Al (ppm)	Fe (ppm)	Mn (ppm)	Mo (ppm)	P (ppm)	V (ppm)
Black Lamina	0	70681	31075	274	0	367	138
BRI 0	-1.5	23044	11236	113	0	b.d.	55
BRI-9	-10.5	30151	14529	910	0	743	63
BRI-14.5	-16	33024	15529	792	0	644	71
BRI-25.5	-27	46238	24021	501	0	520	89
BRI-42.5	-44	34911	19514	710	0	537	67
BRI-105.5	-107	39048	17094	656	0	461	82

IODP Site M0004 Lomonosov Ridge

Leg	Site	Hole	Core	Section	Top Depth (cm)	Bottom Depth (cm)	Sample Code	Depth (mbsf)	C_{ORG} (%)	Al 308.215 (ppm)	Fe 238.204 (ppm)	Mn 257.611 (ppm)	Mo 202.030 (ppm)	P 177.495 (ppm)	V 292.464 (ppm)
302	4	A	29X	1	39	40	29-1	376.19	2.56	99058	23586	142	5.71	398	249
302	4	A	29X	1	39	40	29-1	376.19	2.42	100055	23869	141	5.33	394	244
302	4	A	29X	1	59	60	29-1	376.39	1.77	96945	24353	156	5.82	292	242
302	4	A	29X	1	80	81	29-1	376.6	1.13	95337	20692	152	3.34	292	219
302	4	A	29X	1	99	100	29-1	376.79	0.96	92043	21864	174	3.42	290	236
302	4	A	29X	2	3	4	29-2	377.03	2.71	98973	31869	160	9.62	299	233
302	4	A	30X	1	1	3	30-1	380.31	1.28	91926	21349	160	4.75	309	229
302	4	A	30X	1	21	23	30-1	380.51	1.44	100729	30413	187	5.37	273	246
302	4	A	30X	1	40	41	30-1	380.7	1.65	105335	27021	184	4.42	269	253
302	4	A	30X	1	62	63	30-1	380.92	1.66	104213	27808	176	4.33	280	236
302	4	A	30X	1	82	83	30-1	381.12	1.38	98822	41271	220	5.42	362	241

4

302	4	A	30X	1	100	101	30-1	381.3	2.03	106851	23804	145	2.82	310	247
302	4	A	30X	1	122	123	30-1	381.52	2.04	112349	23998	166	3.46	303	240
302	4	A	30X	1	143	144	30-1	381.73	2.08	110375	27034	207	26.87	303	244
302	4	A	30X	2	3	4	30-2	381.84	2.18	107906	32909	222	5.01	304	234
302	4	A	30X	2	3	4	30-2	381.84	2.22						
302	4	A	30X	2	20	21	30-2	382.01	2.43	109633	33557	187	5.93	292	238
302	4	A	30X	2	40	41	30-2	382.21	3.04	109155	34793	184	11.95	315	242
302	4	A	30X	2	60	61	30-2	382.41	2.28	109136	33726	266	8.10	335	252
302	4	A	30X	2	80	81	30-2	382.61	3.55	104514	53860	209	31.99	374	280
302	4	A	30X	2	100	101	30-2	382.81	3.84	97421	61459	303	54.75	845	269
302	4	A	30X	2	120	121	30-2	383.01	3.44	81157	130844	969	105.33	547	218
302	4	A	30X	2	140	141	30-2	383.21	2.85	75859	131414	1171	92.17	883	184
302	4	A	30X	3	2	3	30-3	383.35	2.59	90872	79045	1437	53.39	1537	186
302	4	A	30X	3	22	23	30-3	383.55	2.50	94568	67324	1458	39.25	745	171
302	4	A	30X	3	42	43	30-3	383.75	2.21	94149	68192	1548	40.41	756	164
302	4	A	30X	3	62	63	30-3	383.95	2.29	92662	64455	1486	42.49	939	167
302	4	A	30X	3	82	83	30-3	384.15	2.81	90116	72718	1960	51.67	551	162
302	4	A	30X	3	103	104	30-3	384.36	2.81	93539	74635	2249	53.95	596	170
302	4	A	31X	1	10	12	31-1	383.3	2.59	95195	67744	1558	44.49	828	164
302	4	A	31X	1	10	12	31-1	383.3	2.52						
302	4	A	31X	1	23	24	31-1	383.43	2.65	91273	68663	1820	49.63	736	168
302	4	A	31X	1	40	41	32-1	383.6	2.71	80445	71349	1787	47.74	736	152
302	4	A	32X	1	59	60	32-1	388.59	1.73	104293	29892	154	4.96	773	299
302	4	A	32X	1	79	80	32-1	388.79	3.10	102033	51569	152	11.21	679	320

Site		Hole	Core	Section	Top	Bottom	Sample	Depth	C_ORG	Al 308.215	Fe 239.562	Mn 257.611	Mo 202.095	P 177.495	V 292.402
302	4	A	32X	1	100	101	32-1	389	1.93	104365	33664	180	5.51	733	296
302	4	A	32X	1	120	121	32-1	389.2	1.48	109452	32884	321	4.27	909	292
302	4	A	32X	1	140	141	32-1	389.4	1.27	106745	47186	490	6.03	1402	295
302	4	A	32X	2	0	1	32-2	389.5	1.54	105142	31076	312	3.02	792	281
302	4	A	32X	2	20	21	32-2	389.7	1.67	101664	40100	304	9.01	923	278
302	4	A	32X	2	40	41	32-2	389.9	1.98	101995	38405	445	8.52	938	292
302	4	A	32X	2	60	61	32-2	390.1	1.54	101010	31342	238	5.60	551	280
302	4	A	32X	2	80	81	32-2	390.3	2.29	98071	48994	574	15.12	981	302
302	4	A	32X	2	100	101	32-2	390.5	1.65	104912	35343	308	6.14	932	316
302	4	A	32X	2	119	120	32-2	390.69	2.23	104880	36468	459	4.10	950	324
302	4	A	32X	2	119	120	32-2	390.69	2.25	105597	36314	562	4.65	956	336

ODP 174AX Bass River

Sample Code	Top (feet)	Top (tenth of feet)	Bottom (feet)	Bottom (tenth of feet)	Depth (mbsf)	C_ORG (%)	Al 308.215 (ppm)	Fe 239.562 (ppm)	Mn 257.611 (ppm)	Mo 202.095 (ppm)	P 177.495 (ppm)	V 292.402 (ppm)
BR 22	1144	4	1144	5	348.83	0.77	70417	35913	79	1.69	367	135
BR 23	1145	1	1145	2	349.04	0.47	82458	30866	99	0.42	192	136
BR 24	1145	6	1145	7	349.19	0.57	81696	30386	107	0.33	246	134
BR 25	1146	4	1146	5	349.44	0.54	86068	30938	104	0.30	268	145
BR 26	1147	1	1147	2	349.65	0.44	84642	30145	104	0.25	282	141
BR 28	1148	4	1148	5	350.05	0.49	88555	36309	146	0.23	226	147
BR 29	1149	1	1149	2	350.26	0.52	89343	40361	202	0.17	242	147

4

BR 30	1149	7	1149	8	350.44	0.53	90664	46017	251	0.26	241	148
BR 31	1150	4	1150	5	350.66	0.45	88524	43352	230	0.25	248	150
BR 32	1151	1	1151	2	350.87	0.43	89239	40720	201	0.20	273	151
BR 33	1151	8	1151	9	351.08	0.47	89024	38066	185	0.20	268	150
BR 34	1152	5	1152	6	351.30	0.44	89048	41671	210	0.23	275	150
BR 35	1153	2	1153	3	351.51	0.56	90418	45224	238	0.24	262	153
BR 36	1153	9	1154		351.72	0.48	89718	47092	273	0.20	272	157
BR 37	1154	7	1154	8	351.97	0.45	89999	43364	252	0.18	292	154
BR 38	1155	4	1155	5	352.18	0.50	89986	43917	258	0.20	286	155
BR 39	1156	1	1156	2	352.39	0.50	91522	41614	249	0.31	316	156
BR 40	1156	8	1156	9	352.61	0.63	90682	56306	546	0.20	254	155
BR 41	1157	5	1157	6	352.82	0.51	89654	43053	269	0.23	266	159
BR 42	1158	2	1158	3	353.03	0.48	89785	39242	241	0.45	263	157
BR 43	1158	9	1159	0	353.25	0.44	93109	45227	291	0.22	301	159
BR 44	1160	1	1160	2	353.61	0.48	92974	41401	249	0.36	293	162
BR 45	1160	7	1160	8	353.80	0.48	93088	42774	259	0.35	288	165
BR 46	1161	2	1161	3	353.95	0.45	91398	40979	239	0.26	305	168
BR 47	1161	7	1161	8	354.10	0.48	91189	39566	235	0.28	299	163
BR 48	1162	2	1162	3	354.25	0.56	89124	44207	296	0.26	375	162
BR 49	1162	7	1162	8	354.41	0.46	91348	42964	276	0.18	322	165
BR 50	1163	2	1163	3	354.56	0.49	90421	43773	339	0.17	457	162
BR 51	1163	7	1163	8	354.71	0.56	90155	47964	379	0.24	356	169
BR 52	1164	2	1164	3	354.86	0.54	91984	47229	364	0.11	426	173
BR 53	1164	6	1164	7	354.99	0.46	92100	44983	331	0.23	387	181

BR 54	1165	1	1165	2	355.14	0.68	90706	52338	491	0.36	3674	186
BR 55	1165	5	1165	6	355.26	0.50	91129	49112	380	0.17	371	187
BR 56	1166	0	1166	1	355.41	0.58	93071	41500	276	0.27	440	187
BR 58	1166	7	1166	8	355.63	0.57	94706	42634	298	0.52	402	184
BR 59	1167		1167	1	355.72	0.57	90327	39068	319	0.27	381	171
BR 60	1167	4	1167	5	355.84	0.54	93915	41802	270	0.34	346	177
BR 61	1167	7	1167	8	355.93	0.60	98139	42569	292	0.31	387	180
BR 62	1168		1168	1	356.02	0.54	96105	39826	902	0.29	368	187
BR 63	1168	3	1168	4	356.11	0.59	97408	37382	213	0.28	399	197
BR 64	1168	6	1168	7	356.20	0.51	95642	36382	198	0.13	762	182
BR 65	1168	9	1169		356.30	0.58	95107	34816	212	0.27	1097	185
BR 66	1169	2	1169	3	356.39	0.55	95117	34812	216	0.27	617	180
BR 72	1171	1	1171	2	356.97	0.55	89956	32230	220	0.49	710	159
BR 73	1171	3	1171	4	357.03	0.57	88108	32926	212	0.47	663	144
BR 74	1171	6	1171	7	357.12	0.68	90383	37354	112	0.45	444	147
BR 78	1172	5	1172	6	357.39	0.45	71793	35688	93	0.67	655	114
BR 79	1172	8.5	1172	9	357.49	0.48	65701	36587	88	0.39	665	107
BR 80	1173	1	1173	2	357.58	0.45	54452	36158	115	0.40	8219	94
BR 81	1173	4	1173	5	357.67	0.40	65452	29137	92	0.21	449	96
BR 82	1173	7	1173	8	357.76	0.50	67828	29043	96	0.51	416	96
BR 83	1174		1174	1	357.85	0.48	66389	29305	93	0.48	443	92
BR 84	1174	2	1174	3	357.91	0.45	68437	30336	95	0.28	433	96
BR 85	1174	6	1174	7	358.03	0.45	66088	28916	93	0.35	519	94
BR 86	1174	9	1175		358.12	0.42	66346	29801	92	0.44	519	96

4

BR 87	1175	2	1175	3	358.22	0.39	61304	31500	93	0.44	728	91
BR 88	1175	5	1175	6	358.31	0.44	62049	30219	94	0.29	622	89
BR 89	1176	1	1176	2	358.49	0.49	58650	30075	91	0.28	724	87
BR 90	1176	6	1176	7	358.64	0.49	58842	29766	92	0.22	711	89
BR 91	1177	2	1177	3	358.83	0.38	53748	30094	92	0.37	887	86
BR 92	1177	6	1177	7	358.95	0.48	61610	30115	89	0.35	561	90
BR 93	1178	1	1178	2	359.10	0.41	47330	31216	90	0.27	1049	80
BR 94	1178	6	1178	7	359.25	0.52	49482	31188	91	0.34	803	82
BR 95	1179	1	1179	2	359.40	0.64	48540	30826	90	0.60	784	82
BR 96	1179	6	1179	7	359.56	0.40	50111	29788	88	0.38	776	82
BR 97	1180	3	1180	4	359.77	0.48	53492	30161	86	0.42	939	84
BR 98	1181	0	1181	1	359.98	0.41	50171	30064	89	0.43	708	83
BR 99	1181	7	1181	8	360.20	0.43	46289	29856	88	0.48	855	76
BR 100	1182	4	1182	5	360.41	0.42	51243	30083	90	0.40	950	83
BR 101	1183	1	1183	2	360.62	0.61	53303	29841	86	0.48	723	84
BR 102	1183	8	1183	9	360.84	0.47	57604	29964	88	0.37	589	88
BR 167	1184	2	1184	3	360.96	0.56	59083	30847	88	0.48	622	87
BR 103	1184	5	1184	6	361.05	0.54	61340	30880	88	0.30	797	93
BR 168	1184	8	1184	9	361.14	0.47	56674	31786	91	0.41	991	88
BR 104	1185	2	1185	3	361.26	0.51	50861	30700	93	0.37	967	82
BR 169	1185	6	1185	7	361.39	0.50	52371	31507	82	0.50	971	83
BR 105	1185	9	1186		361.48	0.44	54316	31650	82	0.62	892	86
BR 106	1186		1186	1	361.51	0.51	53439	34011	83	0.58	876	87

Sample				Depth (mbsf)	C$_{ORG}$ (%)	Al 308.215 (ppm)	Mn 257.611 (ppm)	Mn 260.569 (ppm)	Mo 202.095 (ppm)	Mo 203.909 (ppm)	P 178.287 (ppm)	V 292.402 (ppm)
BR 170	1186	4	5	361.63	0.51	54896	32368	87	0.0	0.63	831	89
BR 107	1186	7	8	361.72	0.55	62565	32194	83	0.0	0.35	610	95
BR 171	1187	0	1	361.81	0.52	67225	33299	83	0.0	0.34	498	104
BR 108	1187	4	5	361.93	0.50	65194	33685	81	0.0	0.54	578	98
BR 172	1187	7	8	362.03	0.48	61732	33583	82	0.0	0.32	614	94
BR 109	1188	1	2	362.15	0.41	56239	33812	81	0.0	0.66	817	88
BR 173	1188	5	6	362.27	0.52	55037	32761	81	0.0	0.44	695	85
BR 110	1188	8	9	362.36	0.56	57197	32379	80	0.0	0.30	625	89
BR 174	1189	2.5	3.5	362.50	0.51	60740	32784	82	0.0	0.39	567	92
BR 111	1189	5	6	362.57	0.48	57947	32636	80	0.0	0.39	554	87
BR 175	1189	9	0	362.70	0.44	58875	33406	82	0.0	0.59	899	89
BR 112	1190	3	4	362.82	0.38	55130	32958	77	0.0	0.51	589	84
BR 176	1190	8	9	362.97	0.45	56244	34075	82	0.0	0.49	617	85

ODP Site 752 Kerguelen Plateau

Leg	Site	Hole	Core	Section	A/W	Top Depth (cm)	Bottom Depth (cm)	Sample Code	Depth (mbsf)	C$_{ORG}$ (%)	Al 308.215 (ppm)	Mn 257.611 (ppm)	Mn 260.569 (ppm)	Mo 202.095 (ppm)	Mo 203.909 (ppm)	P 178.287 (ppm)	V 292.402 (ppm)
121	752	A	19X	1	W	10	12.5	A1	171.21	0.26	9807	293	302	0.0	0.5	601	36
121	752	A	19X	1	W	46	49	A2	171.58	0.18	9663	290	297	0.0	0.1	571	38
121	752	A	19X	1	W	110	112	A3	172.21	0.11	13597	339	360	0.0	0.0	457	61
121	752	A	19X	2	W	10	12	A4	172.71	0.19	18899	420	443	0.0	0.0	421	85
121	752	A	19X	2	W	60	62	A5	173.21	0.24	26338	517	548	0.0	0.0	397	119

4

121	752	A	19X	2	W	110	112	A6	173.71	0.18	24295	502	528	0.0	0.1	456	110
121	752	A	19X	3	W	10	12	A7	174.21	0.22	39552	728	750	0.3	0.0	394	188
121	752	A	19X	3	W	60	65	A8	174.73	0.20	41412	700	714	0.0	0.0	422	189
121	752	A	19X	3	W	110	112	A9	175.21	0.21	27981	507	536	0.0	0.0	481	113
121	752	A	19X	3		115	117	A10	175.26	0.30	28987	500	532	0.0	0.2	494	117
121	752	A	19X	3		122	124	A11	175.33	0.17	26318	519	553	0.0	0.0	532	104
121	752	A	19X	3		129	131	A12	175.4	0.16	22848	491	516	0.0	0.0	494	90
121	752	A	19X	3		138	140	A13	175.49	0.24	21006	494	528	0.0	0.0	455	82
121	752	A	19X	3		140	150	A14	175.55	0.14	20210	477	500	0.0	0.0	428	81
121	752	A	19X	4	W	12	14	A15	175.73	0.16	18773	498	523	0.0	0.3	452	76
121	752	A	19X	4	W	22	24	b1	175.83	0.37	21641	501	527	0.0	0.0	488	91
121	752	A	19X	4	W	27	29	b2	175.88	0.38	15086	464	488	0.0	0.6	574	64
121	752	A	19X	4	W	32	34	B3	175.93	0.32	21268	492	517	0.0	0.5	522	90
121	752	A	19X	4	W	37	39	B4	175.94	0.02	13115	451	470	0.0	0.4	544	54
121	752	A	19X	4	W	42	44	B5	176.03	0.24	16194	689	731	0.0	0.8	837	66
121	752	A	19X	4	W	58	60	A16	176.19	0.12	6024	334	345	0.0	0.3	836	20
121	752	A	19X	4	W	109	111	A17	176.7	0.09	6906	369	381	0.0	0.4	424	25
121	752	A	19X	4	W	30	32	A18	177.13	0.19	11167	304	310	0.0	0.5	513	43
121	752	A	19X	4	W	30	32	A18	177.13		11084	301	310	0.0	0.6	523	43

ODP Site 1172 Tasman Gateway

Leg	Site	Hole	Core	Section	Top Depth (cm)	Sample Code	Depth (mbsf)	C$_{ORG}$ (%)	Al 308.215 (ppm)	Fe 259.941 (ppm)	Mn 257.611 (ppm)	Mn 260.569 (ppm)	Mo 202.095 (ppm)	Mo 203.909 (ppm)	P 178.287 (ppm)	V 292.402 (ppm)
189	1172	D	15R	4	60	AP4	610.61	0.95	60743	47578	72	71	0.0	1.1	177	121
189	1172	D	15R	4	70	AP5	610.71	0.85	54036	64389	94	90	2.5	0.7	244	113
189	1172	D	15R	4	80	AP6	610.82	1.01	52778	51356	114	111	3.0	1.2	191	96
189	1172	D	15R	4	90	AP7	610.899	1.41	53474	49157	138	138	3.1	2.1	169	91
189	1172	D	15R	4	99	AP8	611	1.16								
189	1172	D	15R	4	110	AP9	611.115	0.89	50658	98191	304	322	0.0	2.9	343	123
189	1172	D	15R	4	120	AP10	611.195	0.79	49646	102736	355	374	0.0	2.3	373	129
189	1172	D	15R	4	131	AP11	611.315	0.69	32022	71453	259	270	1.9	1.3	293	90
189	1172	D	15R	4	135	AP12	611.355	0.85	53454	126684	525	552	1.1	1.6	617	162
189	1172	D	15R	4	146	AP13	611.47	0.55	55108	132142	520	528	0.0	2.5	518	179
189	1172	D	15R	5	0	AP14	611.514	0.71	56971	129140	516	544	0.4	1.2	658	187
189	1172	D	15R	5	0	AP14.1	611.514	0.72	56350	129194	519	547	1.0	1.2	680	187
189	1172	D	15R	5	5	AP15	611.559	0.68	60838	118514	450	468	0.0	1.7	595	200
189	1172	D	15R	5	13	AP16	611.639	0.48	60768	119403	425	443	0.0	1.3	439	217
189	1172	D	15R	5	20	AP17	611.7	0.70	65251	98702	384	402	1.5	1.2	412	201
189	1172	D	15R	5	24	AP18	611.75	0.65	55782	118856	301	318	0.0	2.1	443	244
189	1172	D	15R	5	28	AP19	611.775	0.38	59874	104479	351	368	0.0	2.4	389	217
189	1172	D	15R	5	29	AP20	611.795	0.63	65343	90131	218	225	0.0	2.9	377	225
189	1172	D	15R	5	31	AP21	611.815	0.60	57827	81062	166	167	0.6	0.2	351	232
189	1172	D	15R	5	44	AP27	611.945	0.54	61734	42899	74	70	0.0	0.0	209	169

4

189	1172	D	15R	5	47	AP28	611.965	0.54	60953	45631	71	66	1.0	0.0	208	168
189	1172	D	15R	5	48	AP29	611.985	0.45	60507	57441	76	73	1.4	0.0	295	182
189	1172	D	15R	5	51	AP30	612.005	0.42	57609	76885	81	77	1.3	0.4	267	209
189	1172	D	15R	5	52	AP31	612.025	0.53	59295	58392	78	74	1.6	0.0	214	183
189	1172	D	15R	5	55	AP32	612.055	0.54	62783	52881	108	104	1.7	0.1	228	182
189	1172	D	15R	5	60	AP33	612.195	0.59	61979	44989	73	68	0.0	0.0	230	197
189	1172	D	15R	5	69	AP34	612.195	0.55								
189	1172	D	15R	5	79	AP35	612.295	0.49	64595	41196	88	85	0.0	0.0	215	170
189	1172	D	15R	5	86	AP36	612.355	0.57	65235	35925	70	66	0.0	0.0	215	170
189	1172	D	15R	5	96	AP38	612.45	0.59	65605	41238	72	69	0.0	0.9	207	159
189	1172	D	15R	5	99	AP39	612.495	0.61	62842	45644	83	78	0.0	0.0	212	167
189	1172	D	15R	5	104	AP40	612.55	0.62	62443	46601	86	83	0.9	0.0	215	161

Sample Code	Depth (mbsf)	C_{ORG} (%)	Al 394.401 (ppm)	Fe 259.941 (ppm)	Mn 257.611 (ppm)	Mo 203.909 (ppm)	P 177.495 (ppm)	V 292.464 (ppm)
				Lodo Gulch				
LO-03-04	26.5		57920.251	29089.12	461.633	0	248.29	83.081
LO-03-42	22.9		64388.602	97034.574	199.806	0	525.826	355.981
LO-03-39	17.5		64482.706	34433.124	336.512	0	b.d.	107.475
LO-03-37	13.8		82795.705	45337.626	349.559	0	b.d.	119.773
LO-03-27/+150	9		78441.423	37382.393	406.345	0	295.667	110.504
LO-03-27/+130	8.8		94554.281	47069.845	286.222	0	b.d.	151.301
LO-03-27/+100	8.5		81508.695	58532.876	260.805	0	529.717	158.876
LO-03-27/+080	8.3		82102.445	62706.105	199.521	0	318.78	123.741

LO-03-27/+055	8	78420.164	70060.961	223.971	0	353.509	154.546
LO-03-27/+055	8	78662.753	71276.272	220.401	0	328.376	152.595
LO-03-27/+010	7.6	79667.541	48627.518	455.186	0	330.064	125.022
LO-03-27/-10	7.4	75272.28	44175.539	399.935	0	321.082	115.755

4

It's the job that's never started as takes longest to finish.
J.R.R. Tolkien - The Fellowship of the Ring
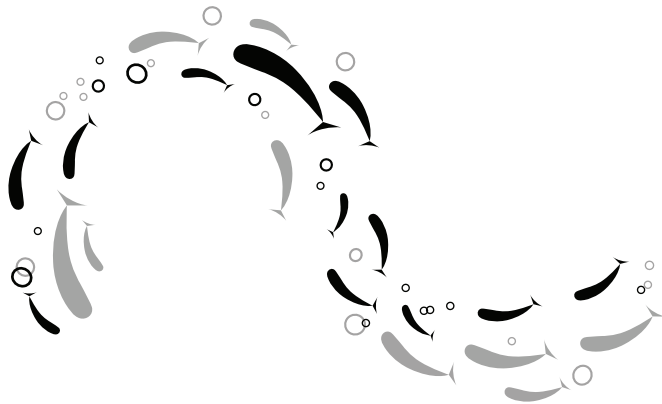
Quantifying volcanism and organic carbon burial across Oceanic Anoxic Event 2

Quantifying volcanism and organic carbon burial across Oceanic Anoxic Event 2

Nina M. Papadomanolaki, Niels A.G.M. van Helmond, Heiko Pälike, Appy Sluijs, Caroline P. Slomp

ABSTRACT

Oceanic Anoxic Event 2 (~94 Ma; OAE2) was characterized by one of the largest carbon cycle perturbations of the Phanerozoic, but associated carbon emissions and marine burial fluxes are poorly constrained. Here, we use the carbon cycle box model LOSCAR-P to quantify the role of Large Igneous Province (LIP) volcanism and enhanced marine organic carbon (C_{org}) burial. We constrain the simulations by the magnitude and shape of the positive stable carbon isotope ($\delta^{13}C$) excursion (CIE) in the exogenic carbon reservoir, and atmospheric pCO_2 reconstructions. In the best fit scenario two pulses of volcanic carbon input — 0.065 Pg C yr^{-1} over 170 kyr and 0.075 Pg C yr^{-1} over 40 kyr, separated by an 80 kyr interval with an input of 0.02 Pg C yr^{-1} — are required to simulate observed changes in $\delta^{13}C$ and pCO_2. About 9 x 10^3 Pg of excess C_{org} burial produces a ~3‰ CIE during the first volcanic pulse. Combined with reduced LIP activity, Corg burial leads to pronounced pCO_2 reductions at the termination of both volcanic pulses, consistent with widespread evidence for cooling, and ultimately leading to a temporal negative trend in the global exogenic $\delta^{13}C$ record. Finally, we show that observed leads and lags between such features in the records and simulations are explained by differences in response time of carbon cycle components to volcanic forcing.

1. INTRODUCTION

Oceanic Anoxic Event 2 (OAE2) was a ~430 — 930 kyr (Voigt *et al.*, 2008; Gangl *et al.*, 2019) long interval of high atmospheric pCO_2 and temperatures, linked to Large Igneous Province (LIP) volcanism (Turgeon and Creaser, 2008; Jenkyns, 2010). The greenhouse conditions and resulting intensification of the hydrological cycle (e.g. van Helmond *et al.*, 2014) stimulated continental weathering (Poulton *et al.*, 2015), which, together with enhanced hydrothermal input due to accelerated seafloor spreading and/or LIP emplacement (Owens *et al.*, 2012), increased the supply of nutrients to the oceans. Consequently, widespread increased primary productivity, deoxygenation and redox-driven nutrient recycling led to enhanced burial of organic matter (Kuypers *et al.*, 2002), particularly in the proto-North Atlantic and epicontinental seas (Takashima *et al.*, 2006).
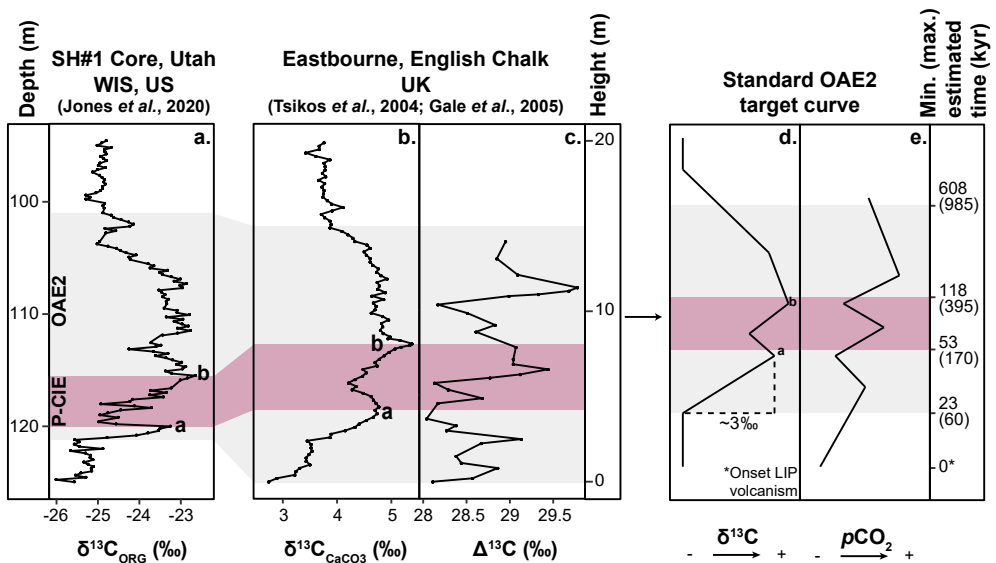
Figure 5.1| Stable carbon isotope records across OAE2 for the Western Interior Seaway (WIS) (a) (organic $\delta^{13}C$ for the SH#1 Core, Utah, USA; Jones *et al.*, 2020) and the English Chalk (b) (carbonate $\delta^{13}C$ for Eastbourne, UK; Tsikos *et al.*, 2004). The two distinct $\delta^{13}C$ maxima are labelled "a" and "b". The difference between $\delta^{13}C_{org}$ and $\delta^{13}C_{carb}$ for Eastbourne (c) is shown as a proxy for pCO_2 (Gale *et al.*, 2005). Right panel: Target curves for our simulations as idealized records of the CIE, with an initial 3‰ increase, and pCO_2. Grey band: extent of OAE2. Purple band: Plenus $\delta^{13}C$ trough. Minimum and, in brackets, maximum ages, relative to the onset of the main pulse of enhanced volcanism (0 kyr; see Supplementary Materials for age derivations).

The burial of organic carbon (C_{org}) during OAE2 marks a positive carbon isotope ($\delta^{13}C$) excursion (CIE) in sedimentary archives (e.g. Jenkyns, 2010) with an average magnitude of 3‰ (Owens *et al.*, 2018). This CIE typically consists of an initial (stepped) increase to a maximum ("a"), often followed by a negative excursion ("trough"; termed the Plenus CIE;

O'Connor *et al.*, 2020), a second maximum ("b"), a plateau and a gradual return to pre-OAE2 values (Figure 5.1). Records of pCO_2 show an increase across the onset of OAE2, and two phases of lower values associated to these carbon isotope maxima (e.g. Sinninghe Damsté *et al.*, 2008; Barclay *et al.*, 2010; Kuhnt *et al.*, 2017). Presumably, both these drops in pCO_2 are associated with cooling phases, one of which is the stratigraphically complex Plenus Cold Event (Supplementary Materials; O'Connor *et al.*, 2020).

The changes in $\delta^{13}C$ and pCO_2 during OAE2, and the timing of key features in the two records, are due to the relative impact of LIP volcanism and enhanced burial of C_{org}. Increased rates of C_{org} burial (e.g. Kolonic *et al.*, 2005) suggest a total burial of at least 41×10^3 Pg C across OAE2 (Owens *et al.*, 2018). Large Igneous Province emission rates are estimated between 0.03 Pg C yr^{-1} and 4.7 Pg C yr^{-1} and total emission masses between 14×10^3 Pg C and 46×10^3 Pg C (Supplementary Table 5.1). The ~25% reduction in atmospheric CO_2 that is associated with $\delta^{13}C$ maximum "a" has been attributed to increased C_{org} burial (e.g. Barclay *et al.*, 2010) and/or decreased LIP volcanism (e.g. Clarkson *et al.*, 2018). Similarly, the Plenus CIE is hypothesized to be the result of decreased C_{org} burial, following the reduction in atmospheric pCO_2, and/or an increase in LIP volcanism. However, a comprehensive, mechanistically plausible scenario for volcanic input and excess C_{org} burial that explains all observations is still lacking.

In this study, we present the first attempt to constrain a scenario for LIP volcanism and C_{org} burial for OAE2 that reproduces the shape and magnitude of the CIE, as well as the timing of its major features relative to reconstructions of atmospheric pCO_2 (Fig. 5.1). We use the carbon cycle box model LOSCAR-P (Komar and Zeebe, 2017) to assess the impact of a range of volcanic emission scenarios on bulk $\delta^{13}C$, atmospheric pCO_2 and C_{org} burial.

2. CARBON CYCLE MODEL SETUP

The LOSCAR-P model with the Paleocene – Eocene model configuration including the Tethys Ocean (Zeebe, 2012; Komar and Zeebe, 2017) enables us to study bulk carbonate $\delta^{13}C$ and atmospheric pCO_2 as a function of volcanism, carbonate and silicate weathering and C_{org} burial. In this model, the burial of both C_{org} and P is redox-dependent, resulting in enhanced recycling of P relative to C_{org} upon ocean deoxygenation. LOSCAR-P does not account for the restricted proto-North Atlantic and epicontinental seaways where anoxic conditions and black shale deposition prevailed (Takashima *et al.*, 2006). We used most values and parameterizations of Komar and Zeebe (2017) but increased the initial steady state concentrations of calcium and magnesium to 25 mmol kg^{-1} and 35 mmol kg^{-1}, respectively (Zeebe and Tyrrel, 2019), and use a $\delta^{13}C_{org}$ value of -28‰ (Kump and Arthur, 1999), in line with the Mid-Cretaceous.

We force the model from steady state (atmospheric pCO_2: 1000 ppm) with an increased volcanic CO_2 flux associated with LIP emplacement assuming modern $\delta^{13}C_{volc}$ of -5‰. Initially, we run our simulation for 90 kyr with a maximum excess input rate of 0.2 Pg C yr^{-1} to test the impact of C_{org} burial on $\delta^{13}C$ with and without redox-dependent C_{org} and P burial. To test the effect of input rate, we force the model, including redox dependent burial, for 90 kyr and 540 kyr with maximum emission rates of 0.2 Pg C yr^{-1} and 0.04 Pg C yr^{-1}. All scenarios start with a linear increase to these rates over 20 kyr, which in LOSCAR-P produces the 60 kyr
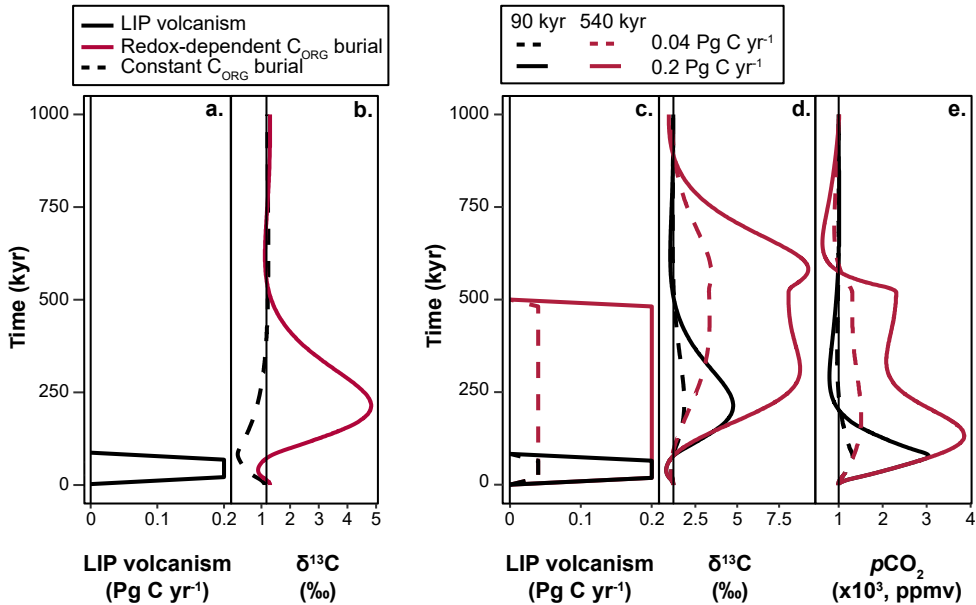
Figure 5.2| Increased LIP volcanism and simulated changes in $\delta^{13}C$ and pCO_2. The effect of excess volcanic emissions (black, solid) of 14,000 Pg C (90 kyr) (a) on $\delta^{13}C$, with constant C_{org} and P burial (black, dashed) and redox-dependent burial (red) (b). The effect of additional LIP volcanism scenarios (c), with maximum rates of 0.04 Pg C yr^{-1} (dashed) and 0.2 Pg C yr^{-1} (solid) over 90 kyr (black) and 540 kyr (red), on $\delta^{13}C$ and pCO_2 (d,e), with redox-dependent burial. Vertical lines indicate the steady state value in each panel.

lag between the onset of volcanism and the increase in $\delta^{13}C$ proposed by Jones *et al.* (2020). We use the same timeframe (20 kyr) for the gradual drop to zero. Following these scenarios we test a large number of possible combinations of rates, masses and durations of LIP activity (Supp. Fig. 5.1) in sensitivity simulation and derive a best-fit scenario for OAE2 $\delta^{13}C_{bulk}$ and pCO_2. The scenarios and results of our sensitivity analyses are included in the Supplementary Materials, with the exception of one scenario with a "stepped" increase in volcanic input (Supplementary Table 5.2) that is presented in the main text for direct comparison.

3. RESULTS

All the scenarios that include LIP volcanism, result in a small negative CIE (**Fig. 2**), followed by a larger positive CIE that is mainly caused by enhanced, redox-dependent C_{org} burial (Fig. 5.2a, b, d). The magnitude of the negative CIE decreases in the simulations with variable C_{org} burial, due to the large difference between $\delta^{13}C_{volc}$ and $\delta^{13}C_{org}$. The peak in $\delta^{13}C$ is preceded by a peak in pCO_2 in all cases (Fig. 5.2e). Following the cessation of LIP activity, $\delta^{13}C$ and pCO_2 values recover to background values on time scales of 400 kyr and 100 kyr, respectively.

The maximum value of the positive CIE and pCO_2 increase varies, depending on the duration and rate of volcanic input (Fig. 5.2c – e). The shorter LIP scenarios (90 kyr) result in a pCO_2

peak towards the end of the negative CIE interval, before $\delta^{13}C$ values increase above the steady state value. In contrast, for the same rate of volcanism, the pCO_2 peak of the longer scenarios (540 kyr) occurs within the interval of increasing $\delta^{13}C$ values of the positive CIE. In the 90 kyr scenarios, the recovery of pCO_2 and $\delta^{13}C$ to background values begins immediately after their maximum value. For the longer LIP scenarios, the first peak in $\delta^{13}C$ is followed by a decrease and a second peak, before the final recovery to the steady state value. In these simulations, pCO_2 decreases and stabilizes within the OAE2 interval, before recovering. The minimum in pCO_2 coincides with the first $\delta^{13}C$ maximum. Notably, the first maximum in the 540 kyr scenarios occurs within the interval of LIP activity. In these scenarios, volcanism decreases within the $\delta^{13}C$ trough, whereas for the 90 kyr simulations it decreases prior to the first $\delta^{13}C$ maximum.

4. TWO VOLCANIC PULSES

Our simulations produce a negative pre-OAE2 CIE, which is present in several carbon isotope records (e.g. Kuroda *et al.*, 2007; Jenkyns *et al.*, 2007), although it is not a common feature (e.g. Tsikos *et al.*, 2004). It may have been enhanced or masked by site-specific processes. The simulations show that it could be forced by volcanic CO_2 emissions alone.

The two $\delta^{13}C$ maxima ("a" and "b"), Plenus CIE and pCO_2 decrease near "a" (Fig. 5.1) are reproduced by the longer (540 kyr) forcing scenarios only, and most distinct in the high emission scenario (0.2 Pg C yr^{-1}). The large positive CIE (~7.9‰), high maximum pCO_2 (~4000 ppmv) and large drop in pCO_2 (45%) that accompany this scenario far exceed the estimates of variability for OAE2, however (Fig. 5.1). Lastly, even this scenario does not reproduce a clear increase in pCO_2 within the Plenus CIE (Fig. 5.1). A variable emissions scenario is therefore required to reproduce all the key features of the $\delta^{13}C_{bulk}$ and pCO_2 records for OAE2.

In our best-fit scenario, LIP volcanism consists of two pulses: 0.065 Pg C yr^{-1} over 170 kyr and 0.075 Pg C yr^{-1} over 40 kyr, separated by an 80 kyr interval of 0.02 Pg C yr^{-1} (Fig. 5.3a). The onset to the first pulse is 20 kyr, as is the decrease to the reduced rate plateau, while the increase and termination of the second pulse is 80 kyr. This amounts to a total duration of LIP activity of 490 kyr, consistent with inferences from osmium isotope records (Du Vivier *et al.*, 2014; 2015; Joo *et al.*, 2020), and a total mass of emitted C of ~24 x 10^3 Pg C (for comparison, see Supp. Table 5.1). Evidence for multiple pulses of volcanism is found in osmium records (Sullivan *et al.*, 2020), and a two-pulse setup also reproduces uranium isotope records across OAE2 (Clarkson *et al.* 2018).

Our two-pulse scenario causes a minor negative CIE, followed by a positive CIE to "a", a trough (Plenus CIE) and another $\delta^{13}C$ increase to "b" (Fig. 5.3b), in agreement with carbon isotope records (Fig. 1). Two distinct peaks in atmospheric pCO_2 are recorded. The first peak coincides with the positive CIE and the second peak coincides with the Plenus CIE (Fig. 5.3c). The initial $\delta^{13}C$ increase to "a" (2.96‰) is equal to the global average of 3‰ (Owens *et al.*, 2018). Additionally, our simulated Plenus CIE (0.52‰) has the same order of magnitude as the trough observed in $\delta^{13}C_{carb}$ at Eastbourne (Tsikos *et al.*, 2004) and in $\delta^{13}C_{org}$ at ODP 1276 (Sinninghe Damsté *et al.*, 2010). The simulated 35% (660 ppmv) decrease in atmospheric
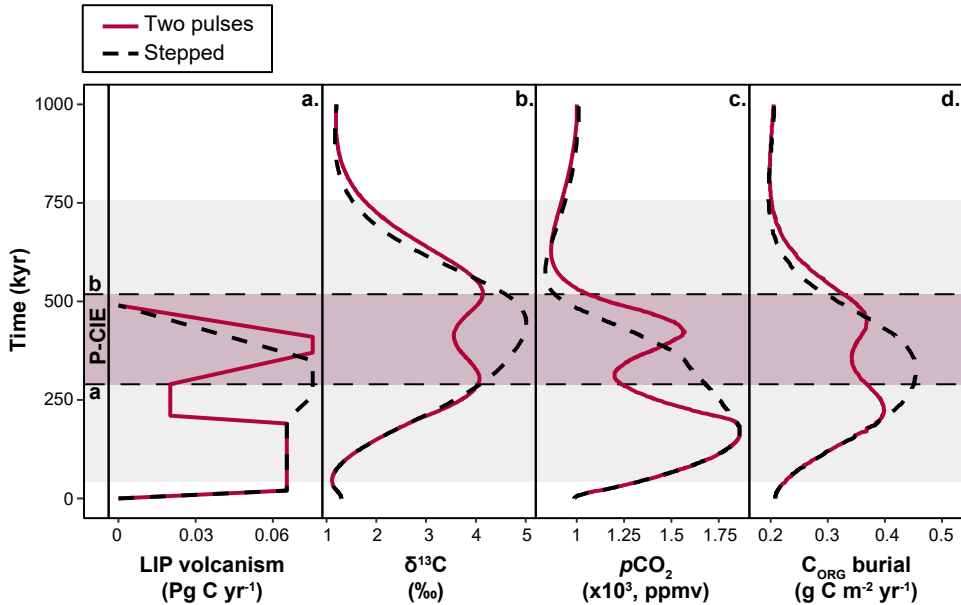
Figure 5.3| Key model output for OAE2 simulations, showing the volcanic forcing (Pg C yr^{-1}; a), bulk $\delta^{13}C$ (‰; b), atmospheric pCO$_2$ (ppm; c) and C$_{org}$ burial rates (g C m^{-2} yr^{-1}; d). Two forcing scenarios are used: two pulses separated by a reduction (purple, solid line) and a stepped increase (black, dashed). Horizontal dashed lines indicate the positions of the two $\delta^{13}C$ maxima "a" and "b". The grey area represents the approximate extent of OAE2 and the purple bar delineates the P-CIE.

pCO$_2$ is also in line with previous, proxy-based reconstructions (Sinninghe Damsté *et al.*, 2008; Barclay *et al.*, 2010; Jarvis *et al.*, 2011) to explain recorded cooling phases during OAE2 (Supplementary Materials).

Our simulated OAE2, from onset to "b", has an overall duration of ~500 kyr. Assuming that the plateau and recovery phases lasted several hundreds of kyr (Gangl *et al.*, 2019), the duration of our simulated OAE2 is in line with the longer estimates (≥700 kyr; Jones *et al.*, 2020). The onset of our CIE, up to "a", is considerably longer (250 kyr) than the longest estimate of 110 kyr (Li *et al.*, 2017). A possible cause for this longer duration could be the lack of proto-North Atlantic restriction and/or underrepresentation of shallow and restricted environments (e.g. epicontinental seas) where additional C$_{org}$ could be buried relative to our LOSCAR-P simulations. The duration of the Plenus CIE (200 kyr) is in agreement with the estimate from the Western Interior Seaway (Jones *et al.*, 2020), providing additional corroboration for our representation of the OAE2 CIE with a two-pulse volcanism scenario.

5. IMPACT OF VOLCANISM AND ORGANIC CARBON BURIAL
We simulate two distinct maxima in C$_{org}$ accumulation rates, resembling trends in the pCO$_2$ curve (Fig. 5.3d). Rates of C$_{org}$ burial roughly a double (from ~0.2 g C m^{-2} yr^{-1} to ~0.4 g C m^{-2}

yr^{-1}), corroborated by the average increase at Tarfaya (Kolonic *et al.*, 2005). The simulations of Clarkson *et al.* (2018) suggest a smaller increase in C$_{org}$ rates (1.3 times pre-OAE2), but their resulting CIE (1.5‰) is only half the global average value. The simulated maximum C$_{org}$ burial values (~0.125 Pg C yr^{-1}) are lower than those modeled by Nederbragt *et al.* (2004) and Owens *et al.* (2018) (~0.185 Pg C yr^{-1}) but our rates, expressed per unit surface area and the relative change in burial are in general agreement with their work. The amount of excess C$_{org}$ burial required for the 3‰ CIE in LOSCAR is ~9,100 Pg C, roughly equal to the value required in the simulation by Owens *et al.*, (2018) for an equivalent CIE. Our total simulated C$_{org}$ burial from the onset of OAE2 until "b" is ~51.4 x 10^3 Pg C (excess burial: ~20,500 Pg C), which is also consistent with estimates from observations (41,000 – 70.000 Pg C; Owens *et al.*, 2018).

In our stepped scenario, the second peak in volcanism causes an increase in C$_{org}$ burial (Fig. 5.3d), reducing pCO$_2$, but the second peak in pCO$_2$ and δ^{13}C, and the Plenus CIE are not reproduced (Fig. 5.3b, c). In contrast, in the two-pulse scenario, a large decrease in volcanism coupled with high C$_{org}$ burial and silicate increased weathering (21%) forces a reduction in pCO$_2$. The CO$_2$ drawdown subsequently reduces C$_{org}$ burial and the second pulse of LIP activity results in the negative Plenus CIE. A second increase in C$_{org}$ burial, coeval with the final cessation of LIP volcanism, results in the second peak ("b") of δ^{13}C. Hence, the inclusion of a two-pulse LIP scenario is critical to reproduce the Plenus CIE, a large decrease in pCO$_2$ that is consistent with temperature records, as well as the second peaks in δ^{13}C and pCO$_2$, without exceeding the average 3‰ OAE2 CIE (Fig. 5.2, 5.3). Atmospheric CO$_2$ responds directly to changes in LIP activity, whereas the response in C$_{org}$ burial is delayed, modulated by P input and regeneration with longer response time, and leads to a slower response of exogenic δ^{13}C.

6. CONCLUSION

Based on our carbon cycle simulations, two pulses of LIP volcanism, increased supply of P from terrestrial weathering and the redox dependency of C$_{org}$ and P burial are required to explain trends and patterns in global exogenic δ^{13}C, atmospheric pCO$_2$ and C$_{org}$ burial across OAE2. Our best-fit scenario reproduces the characteristic shape of the OAE2 CIE, including its 3 ‰ onset and two distinct maxima ("a" and "b") and the Plenus CIE and a doubling of C$_{org}$ burial. The global pCO$_2$ decrease that occurred around δ^{13}C maximum "a" requires both high C$_{org}$ sequestration and a pause in LIP volcanism. Subsequently, a decrease in C$_{org}$ burial, following lower atmospheric CO$_2$, and elevated volcanic emissions result in the Plenus CIE and an increase in pCO$_2$. The second pCO$_2$ and C$_{org}$ burial maxima are only present in simulations with a second pulse of volcanism. Our scenario of variable volcanism and C$_{org}$ burial quantitatively explains not only the key features of OAE2 carbon cycle and climate dynamics but also the relative timing between maximum δ^{13}C, the Plenus CIE and high pCO$_2$.

Chapter 5
Supplementary Materials

1. THE PLENUS COLD EVENT AND THE PLENUS CIE

The southward migration of boreal fauna (e.g. Gale and Christensen, 1996; van Helmond *et al.*, 2016) and multi-proxy records (e.g. Gale and Christensen, 1996; Forster *et al.*, 2007; Jarvis *et al.*, 2011) provide evidence for decreasing temperatures for one or multiple cooling stages within the first half of OAE2. This interval of cooling is generally referred to as the Plenus Cold Event (Gale and Christensen, 1996) and attributed to decreasing atmospheric CO_2 (e.g. Sinninghe Damsté *et al.*, 2010; Jarvis *et al.*, 2011).

Since its original identification, the nature of the Plenus Cold Event has become more complex. On timescales of thousands of years, a lag between atmospheric pCO_2 and global temperature should be absent. Therefore, the multiple intervals of decreased pCO_2 identified in proxy records (see O'Connor *et al.*, 2020) should have caused multiple phases of cooling. This is indeed observed in several temperature records (Forster *et al.*, 2007; Sinninghe Damsté et al., 2010; van Helmond *et al.*, 2014; 2015; Desmares *et al.*, 2016; Jenkyns *et al.*, 2017; Kuhnt *et al.*, 2017). But the presence of multiple cooling pulses and the timing of major cooling relative to key features of the $\delta^{13}C$ record ("a", "b" and the trough that separates them, i.e. "Plenus CIE") depend on local processes as well as global changes (see O'Connor *et al.*, 2020 for extended discussion). Because global correlations of the various recorded drops in temperature and species migrations at individual locations are currently complicated, O'Connor *et al.* (2020) introduced the Plenus CIE as a suitable stratigraphic marker for global correlations.

In this study, our best-fit scenario simulates two maxima in pCO_2, both followed by a decrease, and a $\delta^{13}C$ curve with a 200-kyr trough separating "a" and "b", in line with recent orbital timescales (e.g. Jones *et al.*, 2020). Two intervals with lower atmospheric pCO_2, around "a" and "b", are consistent with records of multiple phases of cooling. The second phase of lower atmospheric pCO_2 should match with the Plenus Cold Event (*sensu stricto*) at Eastbourne (see O'Connor *et al.*, 2020) that is marked by the incursion of boreal fauna. As a result of the (stratigraphic) uncertainties concerning the use of the term Plenus Cold Event, we avoid linking it to our simulation results.

2. OCEANIC ANOXIC EVENT 2 AGE MODEL

Age models for OAE2 based on orbitally tuned sediment records provide a range of durations from 430 kyr (Voigt *et al.*, 2008) to 955 kyr (Gangl *et al.*, 2019). The duration of key sections of the positive carbon isotope excursion (CIE) thus varies depending on the applied age model. In the main text we provide minimum and maximum values for the duration of the lag between the onset of volcanism and the CIE, the total CIE, the onset to "a" and the Plenus CIE from "a" to "b" (Figure 5.1), taking into account the range in age estimates.
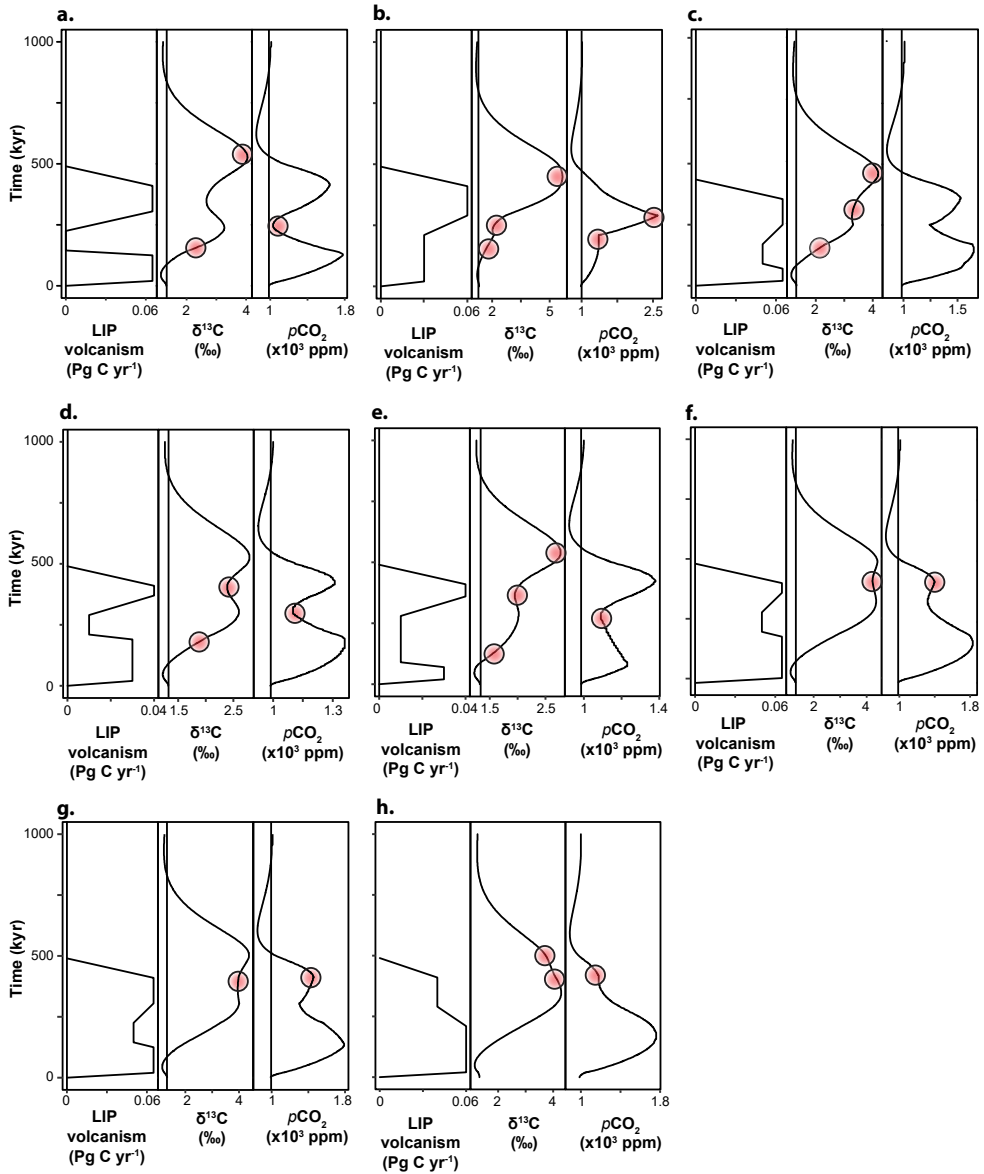
Supplementary Figure 5.1| LIP volcanism, bulk $\delta^{13}C$ and atmospheric pCO_2 for key sensitivity simulations. Vertical lines indicate the steady state value in each panel. Circles indicate the section of the $\delta^{13}C$ or pCO_2 curve that does not match the target curve for OAE2 (Fig. 1) for each LIP volcanism scenario from (a) to (h). For further details, see text.

The onset of Large Igneous Province (LIP) activity is set at 0 kyr. The minimum value for the time between the onset of volcanism and the positive CIE is 23 kyr (Turgeon and Creaser, 2008), and the maximum is 60 kyr (Jones *et al*., 2020). The duration of the onset of OAE2,

up to point "a" is between ~30 kyr (Gangl *et al.*, 2019) and 110 kyr (Li *et al.*, 2017). Jones *et al.* (2020) give a duration of 50 kyr and Kuhnt *et al.* (2017) estimate it to be between 80 and 100 kyr. This places δ^{13}C maximum "a" between 63 kyr and 170 kyr after LIP onset. Li *et al.* (2017) calculate a minimum duration of 55 kyr for the Plenus CIE, similar to Kuhnt *et al.* (2017), which is considerably shorter than the 200 kyr of Jones *et al.* (2020) and maximum 225 kyr of Gangl *et al.* (2019). Taking all these values into account, the δ^{13}C maximum "b" occurs between 118 kyr and 395 kyr after LIP onset. With a duration of 490 kyr to 590 kyr (Li *et al.*, 2017; Gangl *et al.*, 2019) for the δ^{13}C plateau and recovery, the end of the OAE2 CIE at the end of the recovery phase falls between 608 kyr (minimum) and 985 kyr (maximum) after LIP onset.

3. TWO-PULSE SENSITIVITY TESTS

To derive an emission scenario with two pulses of LIP activity that accurately reproduces the characteristics of the δ^{13}C and pCO$_2$ records for OAE2 we performed a large number of sensitivity simulations. We tested different durations and rates for the different parts of a two-pulse scenario, with and without a trough separating the two pulses. The term "stepped" is used to refer to scenarios with two pulses unequal in their rate of emission but without a trough. We present key examples here (Supplementary Fig. 5.1), while the best-fit scenario, and one "stepped" scenario are presented in the main text (Fig. 5.3). The positive CIE of OAE2 is less than 3‰ in scenarios (a) – (e). Scenarios (b) – (h) fail to reconstruct the Plenus CIE. The second maximum in δ^{13}C is much higher than the first in scenarios (a) – (c) and (e), whereas it is not present in (h). A second peak in pCO$_2$, following a clear decrease, is not present in scenarios (f) and (h). This peak is much higher than the first pCO$_2$ maximum in scenario (b), which does not reproduce the decrease after the first peak. The relative decrease in pCO$_2$ is too large in scenario (a) and too small in scenarios (d) and (e).

5

Supplementary Table 5.1| Overview of estimates of volcanic emissions for OAE 2, with rates in Pg yr^{-1}, masses in Pg and the duration of emissions in kyr, together with the estimated pulses and the method of calculation.

Reference	Rate (Pg/yr)	Mass (Pg)	Duration (kyr)	Pulses	Calculation
Clarkson *et al.*, 2018	0.072 – 0.18	10.8 – 27 x10^3	150	2	Model – Uranium
	0.048 – 0.126	7.2 – 18.9 x10^3	150		
Joo *et al.*, 2020	0.028	14.16 x10^3	500	1	LIP volume
Kuroda *et al.*, 2007	1.27 – 4.67	19 – 32.7 x10^3	7 – 15	1	Model – δ^{13}C

Supplementary Table 5.2| Large Igneous Province (LIP) volcanism forcing and key values and characteristics for $\delta^{13}C$ and pCO_2. The value for negative CIE is calculated from the starting value to the minimum value of the excursion. The value for the positive CIE is calculated from the minimum value of the negative to the maximum value of the positive excursion, if the positive CIE exceeds the background value. The Plenus CIE is calculated from the value at "a" to the minimum value. A recovery of pCO_2 to background values is not equal to a CO_2 decrease. A cross indicates that a certain characteristic is present in the records or simulation output. The scenarios presented in this table correspond to the simulations presented in **Figs. 2 – 4** in the main text.

Simulation	LIP Onset Mass (x10³ Pg)	LIP Onset Duration (kyr)	LIP pulse Number	LIP pulse Mass (x10³ Pg)	LIP pulse Duration (kyr)	LIP recovery Mass (x10³ Pg)	LIP recovery Duration (kyr)	CIE (‰) Positive	CIE (‰) Negative	CIE (‰) Plenus	CO₂ decrease (%) [ppmv]	Duration (kyr) Lag first pCO_2 - $\delta^{13}C$ max.	Duration (kyr) OAE2 onset	Duration (kyr) Plenus CIE	Peak CO₂ in OAE2 onset	CO₂ decrease/min. at "a"	CO₂ increase/max. in Plenus CIE	"a" and "b" present
Target OAE2 (Fig. 5.1)	-	-	-	-	-	-	-	3[a]	3[b]	-	25[d]	-	50[c]	65 - 200[c]	X[f]	X[f]	X[f]	X[f]
Base OAE2 w/o C-O₂-P (Fig. 5.2a, b)	-	-	-	-	-	-	-	0.94	-	-	-	-	-	-	-	-	-	-
Base OAE2 w/ C-O₂-P (Fig. 5.2a, b)	2	20	1	10	50	2	20	0.4	4.4	-	-	-	170.7	-	-	-	-	-

5

Chapter 5

															c	d	e	f
Short emissions (Fig. 5.2c, d)	2	20	1	10	50	2	20	0.4	4.4	-	150	170.7	-	-	-	-	-	-
	0.4	20	1	2	50	0.4	20	0.12	0.77	-	145	173	-	-	-	-	-	-
Long emissions (Fig. 5.2c, d)	2	20	1	100	500	2	20	0.4	7.89	0.67	45	310	286.8	271	X	X	X	-
	0.4	20	1	20	500	0.4	20	0.13	2.26	0.03	13 [200]	440	412	138	X	X	X	-
Stepped increase (Fig. 5.4)	0.65	20	2*	22.65	330	5.25	140	0.19	3.89	-	16 [300]	280	396.8	-	X	X	X	-
Best fit (Fig. 5.4)	0.65	20	2**	20.3	390	3	80	0.19	2.96	0.52	35 [660]	145	260		X	X	X	X

a: Kuroda et al., 2007. b: Owens et al., 2018. c: e.g. Forster et al., 2007; Sinninghe Damsté et al., 2010; Jarvis et al., 2011. d: e.g. Barclay et al., 2010. e: Kuhnt et al., 2017; Jones et al., 2020. f: e.g. O'Connor et al., 2020. *: no trough. **: with trough.

5

Oh my heart be strong
And guide when eyes grow dim
When ears grow deaf with empty words
When I know there's life within
Loreena McKennitt - Breaking the Silence

I
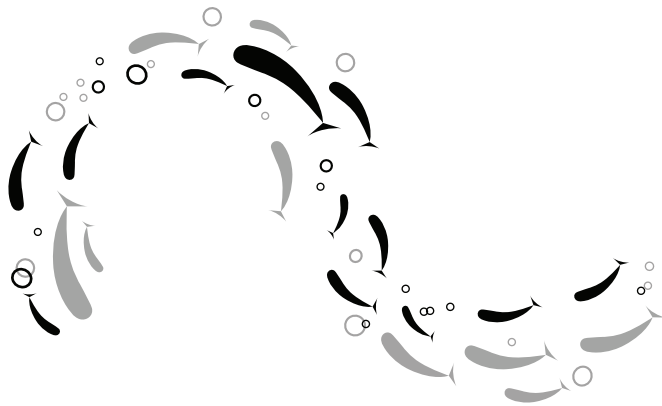
Appendix I: References

Abdel-Halim, A. M., & Aly-Eldeen, M. A. (2016). Characteristics of Mediterranean Sea water in vicinity of Sidikerir Region, west of Alexandria, Egypt. The Egyptian Journal of Aquatic Research, 42(2), 133-140.

Abulaitijiang, A., Andersen, O. B., & Sandwell, D. (2019). Improved Arctic Ocean bathymetry derived from DTU17 gravity model. Earth and Space Science, 6(8), 1336-1347.

Agnini, C., Fornaciari, E., Rio, D., Tateo, F., Backman, J., & Giusberti, L. (2007). Responses of calcareous nannofossil assemblages, mineralogy and geochemistry to the environmental perturbations across the Paleocene/Eocene boundary in the Venetian Pre-Alps. Marine Micropaleontology, 63(1-2), 19-38.

Alegret, L., Ortiz, S., Arenillas, I., & Molina, E. (2010). What happens when the ocean is overheated? The foraminiferal response across the Paleocene–Eocene Thermal Maximum at the Alamedilla section (Spain). GSA Bulletin, 122(9-10), 1616-1624.

Algeo, T. J., & Ingall, E. (2007). Sedimentary Corg: P ratios, paleocean ventilation, and Phanerozoic atmospheric pO2. Palaeogeography, Palaeoclimatology, Palaeoecology, 256(3-4), 130-155.

Algeo, T. J., & Lyons, T. W. (2006). Mo–total organic carbon covariation in modern anoxic marine environments: Implications for analysis of paleoredox and paleohydrographic conditions. Paleoceanography, 21(1).

Alperin, M. J., Suayah, I. B., Benninger, L. K., & Martens, C. S. (2002). Modern organic carbon burial fluxes, recent sedimentation rates, and particle mixing rates from the upper continental slope near Cape Hatteras, North Carolina (USA). Deep Sea Research Part II: Topical Studies in Oceanography, 49(20), 4645-4665.

Andersen, J.H., Carstensen, J., Conley, D.J., Dromph, K., Fleming-Lehtinen, V., Gustafsson, B.G., Josefson, A.B., Norkko, A., Villnäs, A., Murray, C., 2017. Longterm temporal and spatial trends in eutrophication status of the Baltic Sea. Biol. Rev. 92 (1), 135–149.

Andersen, M. B., Matthews, A., Bar-Matthews, M., & Vance, D. (2020). Rapid onset of ocean anoxia shown by high U and low Mo isotope compositions of sapropel S1. Geochemical Perspectives Letters, 15, 10-14.

Anderson, L. D., Delaney, M. L., & Faul, K. L. (2001). Carbon to phosphorus ratios in sediments: Implications for nutrient cycling. Global Biogeochemical Cycles, 15(1), 65-79.

Anderson, P.M., Barnosky, C.D., Bartlein, P.J., Behling, P.J., Brubaker, L., Cushing, E.J., Dodson, J., Dworetsky, B., Guetter, P.J., Harrison, S.P., Huntley, B., Kutzbach, J.E., Markgraf, V., Marvel, R., McGlone, M.S., Mix, A., Moar, N.T., Morley, J., Perrott, R.A., Peterson, G.M., Prell, W.L., Prentice, I.C., Ritchie, J.C., Roberts, N., Ruddiman, W.F., Salinger, M.J., Spaulding, W.G., Street-Perrott, F.A., Thompson, R.S., Wang, P.K., Webb III, T., Winkler, M.G., Wright

Jr, H.E., 1988. Climatic changes of the last 18,000 years: observations and model simulations. Science 241, 1043–1052.

Andersson, A., Meier, H.M., Ripszam, M., Rowe, O., Wikner, J., Haglund, P., Eilola, K., Legrand, C., Figueroa, D., Paczkowska, J., Lindehoff, E., Tysklind, M., Elmgren, R., 2015. Projected future climate change and Baltic Sea ecosystem management. Ambio 44 (3), 345–356.

Andrén, E., Andrén, T., & Kunzendorf, H. (2000). Holocene history of the Baltic Sea as a background for assessing records of human impact in the sediments of the Gotland Basin. *The Holocene*, *10*(6), 687-702.

Andrén, T., Björck, S., Andrén, E., Conley, D., Zillén, L., & Anjar, J. (2011). The development of the Baltic Sea Basin during the last 130 ka. In *The Baltic Sea Basin* (pp. 75-97). Springer, Berlin, Heidelberg.

Andrén, T., Jørgensen, B.B., Cotterill, C., Green, S., Andrén, E., Ash, J., Bauersachs, T., Cragg, B., Fanget, A.S., Fehr, A., Granoszewski, W., Groeneveld, J., Hardisty, D., Herrero-Bervera, E., Hyttinen, O., Jensen, J.B., Johnson, S., Kenzler, M., Kotilainen, A., Kotthoff, U., Marshall, I.P.G., Martin, E., Obrochta, S., Passchier, S., Quintana Krupinski, N., Riedinger, N., Slomp, C., Snowball, I., Stepanova, A., Strano, S., Torti, A., Warnock, J., Xiao, N., Zhang, R., 2015a. Summary. In: Andrén, T., Jørgensen, B.B., Cotterill, C., Green, S., Expedition 347 Scientists (Eds.), Proc. IODP, 347: College Station, TX (Integrated Ocean Drilling Program).

Andrén, T., Jørgensen, B.B., Cotterill, C., Green, S., Andrén, E., Ash, J., Bauersachs, T., Cragg, B., Fanget, A.S., Fehr, A., Granoszewski, W., Groeneveld, J., Hardisty, D., Herrero-Bervera, E., Hyttinen, O., Jensen, J.B., Johnson, S., Kenzler, M., Kotilainen, A., Kotthoff, U., Marshall, I.P.G., Martin, E., Obrochta, S., Passchier, S., Quintana Krupinski, N., Riedinger, N., Slomp, C., Snowball, I., Stepanova, A., Strano, S., Torti, A., Warnock, J., Xiao, N., Zhang, R., 2015b. Site M0063. In: Andrén, T., Jørgensen, B.B., Cotterill, C., Green, S., Expedition 347 Scientists (Eds.), Proc. IODP, 347: College Station, TX (Integrated Ocean Drilling Program).

Appelo, C. A. J., & Postma, D. (2004). Geochemistry, groundwater and pollution. CRC press. ISBN: 9780415364287

Arreguín-Rodríguez, G. J., Alegret, L., Sepúlveda, J., Newman, S., & Summons, R. E. (2014). Enhanced terrestrial input supporting the Glomospira acme across the Paleocene-Eocene boundary in Southern Spain. Micropaleontology, 43-51.

Arthur, M. A., Brumsack, H. J., Jenkyns, H. C., & Schlanger, S. O. (1990). Stratigraphy, geochemistry, and paleoceanography of organic carbon-rich Cretaceous sequences. In *Cretaceous resources, events and rhythms* (pp. 75-119). Springer, Dordrecht.

Aze, T., Pearson, P. N., Dickson, A. J., Badger, M. P., Bown, P. R., Pancost, R. D., ... & Cohen, A. S. (2014). Extreme warming of tropical waters during the Paleocene–Eocene Thermal Maximum. Geology, 42(9), 739-742.

I

Aziz, H. A., Hilgen, F. J., van Luijk, G. M., Sluijs, A., Kraus, M. J., Pares, J. M., & Gingerich, P. D. (2008). Astronomical climate control on paleosol stacking patterns in the upper Paleocene–lower Eocene Willwood Formation, Bighorn Basin, Wyoming. Geology, 36(7), 531-534.Algeo and Ingall, 2007

BACC II Author Team, 2015. Second Assessment of Climate Change for the Baltic Sea Basin. Springer International Publishing, AG Switzerland.

Bailey, T. R., Rosenthal, Y., McArthur, J. M., Van de Schootbrugge, B., & Thirlwall, M. F. (2003). Paleoceanographic changes of the Late Pliensbachian–Early Toarcian interval: a possible link to the genesis of an Oceanic Anoxic Event. Earth and Planetary Science Letters, 212(3-4), 307-320.

Bains, S., Norris, R. D., Corfield, R. M., & Faul, K. L. (2000). Termination of global warmth at the Palaeocene/Eocene boundary through productivity feedback. *Nature*, *407*(6801), 171-174.

Bąk, K. (2004). Deep-water agglutinated foraminiferal changes across the Cretaceous/Tertiary and Paleocene/Eocene transitions in the deep flysch environment; eastern Outer Carpathians (Bieszczady Mts, Poland). In Proceedings of the Sixth International Workshop on Agglutinated Foraminifera. Grzybowski Foundation Special Publication (Vol. 8, pp. 1-56). Grzybowski Foundation.

Barclay, R. S., McElwain, J. C., & Sageman, B. B. (2010). Carbon sequestration activated by a volcanic CO_2 pulse during Ocean Anoxic Event 2. *Nature Geoscience*, *3*(3), 205-208.

Bates, N. R., Astor, Y. M., Church, M. J., Currie, K., Dore, J. E., González-Dávila, M., ... & Santana-Casiano, J. M. (2014). A Time-Series View of Changing Surface Ocean Chemistry Due to Ocean Uptake of Anthropogenic CO_2 and Ocean Acidification. *Oceanography*, *27*(1), 126-141.

Bauer, K. W., Zeebe, R. E., & Wortmann, U. G. (2017). Quantifying the volcanic emissions which triggered Oceanic Anoxic Event 1a and their effect on ocean acidification. *Sedimentology*, *64*(1), 204-214.

Beerling, D. J., Lomas, M. R., & Gröcke, D. R. (2002). On the nature of methane gas-hydrate dissociation during the Toarcian and Aptian oceanic anoxic events. American Journal of Science, 302(1), 28-49.

Beil, S., Kuhnt, W., Holbourn, A., Scholz, F., Oxmann, J., Wallmann, K., ... & Chellai, E. H. (2020). Cretaceous oceanic anoxic events prolonged by phosphorus cycle feedbacks. Climate of the Past, 16(2), 757-782.

Berggren, W. A., & Aubert, J. (1983). Paleogene benthonic foraminiferal biostratigraphy and bathymetry of the Central Coast Ranges of California.

Bergström, S., Carlsson, B., 1994. River runoff to the Baltic Sea – 1950–1990. Ambio 23 (4–5), 280–287.

Berner, R. A., & Berner, E. K. (1997). Silicate weathering and climate. In *Tectonic uplift and climate change* (pp. 353-365). Springer, Boston, MA.

Bernhard, J. M., & Gupta, B. K. S. (1999). Foraminifera of oxygen-depleted environments. In Modern foraminifera (pp. 201-216). Springer, Dordrecht.

Berry, W. B., & Wilde, P. (1978). Progressive ventilation of the oceans; an explanation for the distribution of the lower Paleozoic black shales. *American Journal of Science*, *278*(3), 257-275.

Bertine, K. K. (1972). The deposition of molybdenum in anoxic waters. Marine Chemistry, 1(1), 43-53.

Bianchi, T.S., Engelhaupt, E., Westman, P., Andrén, T., Rolff, C., Elmgren, R., 2000. Cyanobacterial blooms in the Baltic Sea: natural or human-induced? Limnol. Oceanogr. 45 (3), 716–726.

Bice, K. L., & Marotzke, J. (2001). Numerical evidence against reversed thermohaline circulation in the warm Paleocene/Eocene ocean. Journal of Geophysical Research: Oceans, 106(C6), 11529-11542.

Bindoff, N.L., W.W.L. Cheung, J.G. Kairo, J. Arístegui, V.A. Guinder, R. Hallberg, N. Hilmi, N. Jiao, M.S. Karim, L. Levin, S. O'Donoghue, S.R. Purca Cuicapusa, B. Rinkevich, T. Suga, A. Tagliabue, and P. Williamson, 2019: Changing Ocean, Marine Ecosystems, and Dependent Communities. In: IPCC 2019: Special Report on the Ocean and Cryosphere in a Changing Climate [H.-O. Pörtner, D.C. Roberts, V. Masson-Delmotte, P. Zhai, M. Tignor, E. Poloczanska, K. Mintenbeck, A. Alegría, M. Nicolai, A. Okem, J. Petzold, B. Rama, N.M. Weyer (eds.)].

Björck, S., 1995. A review of the history of the Baltic Sea, 13.0–8.0 ka BP. Quat. Int. 27 (94), 19–40.

Bolle, M. P., & Adatte, T. (2001). Palaeocene-early Eocene climatic evolution in the Tethyan realm: clay mineral evidence. Clay minerals, 36(2), 249-261.

Bolle, M. P., Tantawy, A. A., Pardo, A., Adatte, T. H. E. R. R. Y., Burns, S., & Kassab, A. (2000). Climatic and environmental changes documented in the upper Paleocene to lower Eocene of Egypt. Ecologae Geologicae Helvetiae, 93(1), 33-52.

Bopp, L., Le Quéré, C., Heimann, M., Manning, A. C., & Monfray, P. (2002). Climate-induced oceanic oxygen fluxes: Implications for the contemporary carbon budget. *Global Biogeochemical Cycles*, *16*(2), 6-1.

I

Bouttes, N., Roche, D. M., & Paillard, D. (2009). Impact of strong deep ocean stratification on the glacial carbon cycle. Paleoceanography, 24(3).

Bowen, G. J. (2013). Up in smoke: A role for organic carbon feedbacks in Paleogene hyperthermals. Global and Planetary Change, 109, 18-29.

Bowen, G. J., & Zachos, J. C. (2010). Rapid carbon sequestration at the termination of the Palaeocene–Eocene Thermal Maximum. *Nature Geoscience*, *3*(12), 866-869.

Bowen, G. J., Beerling, D. J., Koch, P. L., Zachos, J. C., & Quattlebaum, T. (2004). A humid climate state during the Palaeocene/Eocene thermal maximum. Nature, 432(7016), 495-499.

Bowen, G. J., Koch, P. L., Gingerich, P. D., Norris, R. D., Bains, S., & Corfield, R. M. (2001). Refined isotope stratigraphy across the continental Paleocene-Eocene boundary on Polecat Bench in the northern Bighorn Basin. Paleocene-Eocene Stratigraphy and Biotic Change in the Bighorn and Clarks Fork Basins, Wyoming. University of Michigan Papers on Paleontology, 33, 73-88.

Bown, P., & Pearson, P. (2009). Calcareous plankton evolution and the Paleocene/Eocene thermal maximum event: New evidence from Tanzania. Marine Micropaleontology, 71(1-2), 60-70.

Bralower, T. J. (2002). Evidence of surface water oligotrophy during the Paleocene-Eocene thermal maximum: Nannofossil assemblage data from Ocean Drilling Program Site 690, Maud Rise, Weddell Sea. Paleoceanography, 17(2), 13-1.

Bralower, T. J., Thomas, D. J., Zachos, J. C., Hirschmann, M. M., Rohl, U., Sigurdsson, H., ... & Whitney, D. L. (1997). High-resolution records of the late Paleocene thermal maximum and circum-Caribbean volcanism: Is there a causal link?. *Geology*, *25*(11), 963-966.

Breitburg, D., Levin, L. A., Oschlies, A., Grégoire, M., Chavez, F. P., Conley, D. J., ... & Zhang, J. (2018). Declining oxygen in the global ocean and coastal waters. *Science*, *359*(6371).

Brenner, W.W., 2005. Holocene environmental history of the Gotland Basin (Baltic Sea)—a micropalaeontological model. Palaeogeogr. Palaeoclimatol. Palaeoecol. 220 (3), 227–241.

Broecker, W. S. (1982). Ocean chemistry during glacial time. *Geochimica et Cosmochimica Acta*, *46*(10), 1689-1705.

Broecker, W., & Clark, E. (2001). A dramatic Atlantic dissolution event at the onset of the last glaciation. *Geochemistry, Geophysics, Geosystems*, *2*(11).

Brumsack, H. J. (2006). The trace metal content of recent organic carbon-rich sediments: implications for Cretaceous black shale formation. *Palaeogeography, Palaeoclimatology, Palaeoecology*, *232*(2-4), 344-361.

Burdige, D. J. (2005). Burial of terrestrial organic matter in marine sediments: A re-assessment. Global Biogeochemical Cycles, 19(4).

Burdige, D. J. (2007). Preservation of organic matter in marine sediments: controls, mechanisms, and an imbalance in sediment organic carbon budgets?. Chemical reviews, 107(2), 467-485.

Burke, K. D., Williams, J. W., Chandler, M. A., Haywood, A. M., Lunt, D. J., & Otto-Bliesner, B. L. (2018). Pliocene and Eocene provide best analogs for near-future climates. *Proceedings of the National Academy of Sciences*, *115*(52), 13288-13293.

Caesar, L., McCarthy, G. D., Thornalley, D. J. R., Cahill, N., & Rahmstorf, S. (2021). Current Atlantic Meridional Overturning Circulation weakest in last millennium. *Nature Geoscience*, 1-3.

Caldeira, K., & Wickett, M. E. (2003). Anthropogenic carbon and ocean pH. *Nature*, *425*(6956), 365-365.

Calvert, S. E., & Pedersen, T. F. (1993). Geochemistry of recent oxic and anoxic marine sediments: implications for the geological record. *Marine geology*, *113*(1-2), 67-88.

Canudo, J., Keller, G., Molina, E., & Ortiz, N. (1995). Planktic foraminiferal turnover and $\delta 13C$ isotopes across the Paleocene-Eocene transition at Caravaca and Zumaya, Spain. Palaeogeography, Palaeoclimatology, Palaeoecology, 114(1), 75-100.

Carmichael, M. J., Inglis, G. N., Badger, M. P., Naafs, B. D. A., Behrooz, L., Remmelzwaal, S., ... & Pancost, R. D. (2017). Hydrological and associated biogeochemical consequences of rapid global warming during the Paleocene-Eocene Thermal Maximum. *Global and Planetary Change*, *157*, 114-138.

Carstensen, J., Andersen, J. H., Gustafsson, B. G., & Conley, D. J. (2014). Deoxygenation of the Baltic Sea during the last century. *Proceedings of the National Academy of Sciences*, *111*(15), 5628-5633.

Carstensen, J., Conley, D.J., Bonsdorff, E., Gustafsson, B.G., Hietanen, S., Janas, U., Jilbert, T., Maximov, A., Norkko, A., Norkko, J., Reed, D.C., Slomp, C.P., Timmermann, K., Voss, M., 2014a. Hypoxia in the Baltic Sea: biogeochemical cycles, benthic fauna, and management. Ambio 43, 26–36.

Cartapanis, O., Bianchi, D., Jaccard, S. L., & Galbraith, E. D. (2016). Global pulses of organic carbon burial in deep-sea sediments during glacial maxima. *Nature communications*, *7*(1), 1-7.

Chen, C., Guerit, L., Foreman, B. Z., Hassenruck-Gudipati, H. J., Adatte, T., Honegger, L., ... & Castelltort, S. (2018). Estimating regional flood discharge during Palaeocene-Eocene global warming. Scientific reports, 8(1), 1-8.

I

Cheng, M., Li, C., Jin, C., Wang, H., Algeo, T. J., Lyons, T. W., ... & Anbar, A. (2020). Evidence for high organic carbon export to the early Cambrian seafloor. *Geochimica et Cosmochimica Acta*, *287*, 125-140.

Chun, C. O., Delaney, M. L., & Zachos, J. C. (2010). Paleoredox changes across the Paleocene-Eocene thermal maximum, Walvis Ridge (ODP Sites 1262, 1263, and 1266): Evidence from Mn and U enrichment factors. Paleoceanography, 25(4).

Clarkson, M. O., Lenton, T. M., Andersen, M. B., Bagard, M. L., Dickson, A. J., & Vance, D. (2021). Upper limits on the extent of seafloor anoxia during the PETM from uranium isotopes. *Nature Communications*, *12*(1), 1-9.

Clarkson, M. O., Stirling, C. H., Jenkyns, H. C., Dickson, A. J., Porcelli, D., Moy, C. M., ... & Lenton, T. M. (2018). Uranium isotope evidence for two episodes of deoxygenation during Oceanic Anoxic Event 2. *Proceedings of the National Academy of Sciences*, *115*(12), 2918-2923.

Kelly, D.C., Bralower, T. J., Zachos, J. C., Silva, I. P., & Thomas, E. (1996). Rapid diversification of planktonic foraminifera in the tropical Pacific (ODP Site 865) during the late Paleocene thermal maximum. Geology, 24(5), 423-426.

Colbourn, G., Ridgwell, A., & Lenton, T. M. (2015). The time scale of the silicate weathering negative feedback on atmospheric CO2. *Global Biogeochemical Cycles*, *29*(5), 583-596.

Colosimo, A. B., Bralower, T., & Zachos, J. C. (2005). Evidence for lysocline shoaling at the Paleocene/Eocene thermal maximum on Shatsky Rise, northwest Pacific. In Proceedings of the Ocean Drilling Program: Scientific Results (Vol. 198). Texas A & M University.

Condie, K. C., Des Marais, D. J., & Abbott, D. (2001). Precambrian superplumes and supercontinents: a record in black shales, carbon isotopes, and paleoclimates?. *Precambrian Research*, *106*(3-4), 239-260.

Conley, D. J., Humborg, C., Rahm, L., Savchuk, O. P., & Wulff, F. (2002). Hypoxia in the Baltic Sea and basin-scale changes in phosphorus biogeochemistry. *Environmental science & technology*, *36*(24), 5315-5320.

Conley, D.J., Bjo rck, S., Bonsdorff, E., Carstensen, J., Destouni, G., Gustafsson, B.G., Hietanen, S., Kortekaas, M., Kuosa, H., Meier, H.E.M., Müller-Karulis, B., Nordberg, K., Norkko, A., Nürnberg, G., Pitkänen, H., Rabalais, N.N., Rosenberg, R., Savchuk, O.P., Slomp, C.P., Voss, M., Wulff, F., Zillén, L., 2009. Hypoxia-related processes in the Baltic Sea. Environ. Sci. Technol. 43, 3412–3420.

Conley, D.J., Humborg, C., Rahm, L., Savchuk, O.P., Wulff, F., 2002. Hypoxia in the Baltic Sea and basin-scale changes in phosphorus biogeochemistry. Environ. Sci. Technol. 36 (24), 5315–5320.

Cramer, B. S., Aubry, M. P., Miller, K. G., Olsson, R. K., Wright, J. D., & Kent, D. V. (1999). An exceptional chronologic, isotopic, and clay mineralogic record of the latest Paleocene thermal maximum, Bass River, NJ, ODP 174AX. Bulletin de la Société géologique de France, 170(6), 883-897.

Cramwinckel, M. J., Huber, M., Kocken, I. J., Agnini, C., Bijl, P. K., Bohaty, S. M., ... & Peterse, F. (2018). Synchronous tropical and polar temperature evolution in the Eocene. Nature, 559(7714), 382-386.

Crouch, E. M., & Brinkhuis, H. (2005). Environmental change across the Paleocene–Eocene transition from eastern New Zealand: a marine palynological approach. Marine Micropaleontology, 56(3-4), 138-160.

Crouch, E. M., Dickens, G. R., Brinkhuis, H., Aubry, M. P., Hollis, C. J., Rogers, K. M., & Visscher, H. (2003). The Apectodinium acme and terrestrial discharge during the Paleocene–Eocene thermal maximum: new palynological, geochemical and calcareous nannoplankton observations at Tawanui, New Zealand. Palaeogeography, Palaeoclimatology, Palaeoecology, 194(4), 387-403.

Crusius, J., Calvert, S., Pedersen, T., & Sage, D. (1996). Rhenium and molybdenum enrichments in sediments as indicators of oxic, suboxic and sulfidic conditions of deposition. Earth and Planetary Science Letters, 145(1-4), 65-78.

Cubasch, U., & Cess, R. D. (1990). Processes and modelling. *Climate Change: The IPCC Scientific Assessment*, *69*, 72.

Cui, Y., Kump, L. R., Ridgwell, A. J., Charles, A. J., Junium, C. K., Diefendorf, A. F., ... & Harding, I. C. (2011). Slow release of fossil carbon during the Palaeocene–Eocene Thermal Maximum. Nature Geoscience, 4(7), 481-485.

de Madron, X. D., Radakovitch, O., Heussner, S., Loye-Pilot, M. D., & Monaco, A. (1999). Role of the climatological and current variability on shelf-slope exchanges of particulate matter: Evidence from the Rhône continental margin (NW Mediterranean). Deep Sea Research Part I: Oceanographic Research Papers, 46(9), 1513-1538.

de Vernal, A., Marret, F., 2007. Organic-walled dinoflagellate cysts: tracers of sea-surface conditions. Dev. Marine Geol. 1, 371–408.

De Vries, W. (2014). Nutrients trigger carbon storage. *Nature Climate Change*, *4*(6), 425-426.

DeConto, R. M., Galeotti, S., Pagani, M., Tracy, D., Schaefer, K., Zhang, T., ... & Beerling, D. J. (2012). Past extreme warming events linked to massive carbon release from thawing permafrost. Nature, 484(7392), 87-91.

Desmares, D., Crognier, N., Bardin, J., Testé, M., Beaudoin, B., & Grosheny, D. (2016). A new proxy for Cretaceous paleoceanographic and paleoclimatic reconstructions: Coiling direction

I

changes in the planktonic foraminifera Muricohedbergella delrioensis. *Palaeogeography, Palaeoclimatology, Palaeoecology*, 445, 8-17.

Diaz, R.J., Rosenberg, R., 2008. Spreading dead zones and consequences for marine ecosystems. Science 321 (5891), 926–929.

Dickens, G. R. (2001). Sulfate profiles and barium fronts in sediment on the Blake Ridge: present and past methane fluxes through a large gas hydrate reservoir. *Geochimica et cosmochimica Acta*, *65*(4), 529-543.

Dickens, G. R., Castillo, M. M., & Walker, J. C. (1997). A blast of gas in the latest Paleocene: Simulating first-order effects of massive dissociation of oceanic methane hydrate. Geology, 25(3), 259-262.

Dickens, G. R., Fewless, T., Thomas, E., & Bralower, T. J. (2003). Excess barite accumulation during the Paleocene-Eocene Thermal Maximum: Massive input of dissolved barium from seafloor gas hydrate reservoirs. Geol. Soc. Am. Spec. Pap., 11-24.

Dickens, G. R., O'Neil, J. R., Rea, D. K., & Owen, R. M. (1995). Dissociation of oceanic methane hydrate as a cause of the carbon isotope excursion at the end of the Paleocene. Paleoceanography, 10(6), 965-971.

Dickson, A. J. (2017). A molybdenum-isotope perspective on Phanerozoic deoxygenation events. *Nature Geoscience*, *10*(10), 721-726.

Dickson, A. J., Cohen, A. S., & Coe, A. L. (2012). Seawater oxygenation during the Paleocene-Eocene thermal maximum. Geology, 40(7), 639-642.

Dickson, A. J., Gill, B. C., Ruhl, M., Jenkyns, H. C., Porcelli, D., Idiz, E., ... & van den Boorn, S. H. (2017). Molybdenum-isotope chemostratigraphy and paleoceanography of the Toarcian Oceanic Anoxic Event (Early Jurassic). Paleoceanography, 32(8), 813-829.

Dickson, A. J., Jenkyns, H. C., Porcelli, D., van den Boorn, S., & Idiz, E. (2016). Basin-scale controls on the molybdenum-isotope composition of seawater during Oceanic Anoxic Event 2 (Late Cretaceous). *Geochimica et Cosmochimica Acta*, *178*, 291-306.

Dickson, A. J., Rees-Owen, R. L., März, C., Coe, A. L., Cohen, A. S., Pancost, R. D., ... & Shcherbinina, E. (2014). The spread of marine anoxia on the northern Tethys margin during the Paleocene-Eocene Thermal Maximum. Paleoceanography, 29(6), 471-488.

Dijkstra, N., Slomp, C.P., Behrends, T., 347 scientists, Expedition, 2016. Vivianite is a key sink for phosphorus in sediments of the Landsort Deep, an intermittently anoxic deep basin in the Baltic Sea. Chem. Geol. 438, 58–72.

Doney, S. C., Fabry, V. J., Feely, R. A., & Kleypas, J. A. (2009). Ocean acidification: the other CO2 problem. *Annual review of marine science*, *1*, 169-192.

Döös, K., Meier, H. M., & Döscher, R. (2004). The Baltic haline conveyor belt or the overturning circulation and mixing in the Baltic. *AMBIO: A Journal of the Human Environment*, *33*(4), 261-266.

Du Vivier, A. D. C., Selby, D., Condon, D. J., Takashima, R., & Nishi, H. (2015). Pacific $^{187}Os/^{188}Os$ isotope chemistry and U–Pb geochronology: Synchroneity of global Os isotope change across OAE 2. *Earth and Planetary Science Letters*, *428*, 204-216.

Du Vivier, A. D., Selby, D., Sageman, B. B., Jarvis, I., Gröcke, D. R., & Voigt, S. (2014). Marine $^{187}Os/^{188}Os$ isotope stratigraphy reveals the interaction of volcanism and ocean circulation during Oceanic Anoxic Event 2. *Earth and Planetary Science Letters*, *389*, 23-33.

Dunkley Jones, T., Manners, H. R., Hoggett, M., Kirtland Turner, S., Westerhold, T., Leng, M. J., ... & Grimes, S. T. (2018). Dynamics of sediment flux to a bathyal continental margin section through the Paleocene–Eocene Thermal Maximum. Climate of the Past, 14(7), 1035-1049.

Dwyer, G. S., Cronin, T. M., Baker, P. A., Raymo, M. E., Buzas, J. S., & Corrège, T. (1995). North Atlantic deepwater temperature change during late Pliocene and late Quaternary climatic cycles. Science, 270(5240), 1347-1351.

Dypvik, H., Riber, L., Burca, F., Rüther, D., Jargvoll, D., Nagy, J., & Jochmann, M. (2011). The Paleocene–Eocene thermal maximum (PETM) in Svalbard—clay mineral and geochemical signals. Palaeogeography, Palaeoclimatology, Palaeoecology, 302(3-4), 156-169.

Ebelmen, J. J. (1845). Sur les produits de la de   composition des espe`ces mine   rales de la famille des silicates. *Annales des Mines*, v. 7, p. 3–66.

Egger, H., Fenner, J., Heilmann-Clausen, C., Rögl, F., Sachsenhofer, R.F. & Schmitz, B. (2003) Paleoproductivity of the northwestern Tethyan margin (Anthering section, Austria) across the Paleocene-Eocene transition. Geol. Soc. Am. Spec. Pap., 369 (2003), pp. 133-146.

Egger, H., Homayoun, M., Huber, H., Rögl, F., & Schmitz, B. (2005). Early Eocene climatic, volcanic, and biotic events in the northwestern Tethyan Untersberg section, Austria. Palaeogeography, Palaeoclimatology, Palaeoecology, 217(3-4), 243-264.

Egger, M., Hagens, M., Sapart, C.J., Dijkstra, N., van Helmond, N.A.G.M., Mogollón, J.M., Risgaard-Petersen, N., van der Veen, C., Kasten, S., Riedinger, N., Böttcher, M.E., Röckmann, T., Jrgensen, B.B., Slomp, C.P., 2017. Iron oxide reduction in methanerich deep Baltic Sea sediments. Geochim. Cosmochim. Acta 207, 256–276.

Eijsink, L. M., Krom, M. D., & Herut, B. (2000). Speciation and burial flux of phosphorus in the surface sediments of the eastern Mediterranean. American Journal of Science, 300(6), 483-503.

I

Eilola, K., Meier, H. M., & Almroth, E. (2009). On the dynamics of oxygen, phosphorus and cyanobacteria in the Baltic Sea; A model study. *Journal of Marine Systems*, *75*(1-2), 163-184.

Emeis, K. C., Schulz, H., Struck, U., Rossignol-Strick, M., Erlenkeuser, H., Howell, M. W., ... & Sakamoto, T. (2003). Eastern Mediterranean surface water temperatures and $\delta18O$ composition during deposition of sapropels in the late Quaternary. Paleoceanography, 18(1).

Emeis, K. C., Struck, U., Blanz, T., Kohly, A., & Voβ, M. (2003). Salinity changes in the central Baltic Sea (NW Europe) over the last 10000 years. *The Holocene*, *13*(3), 411-421.

Erba, E., & Tremolada, F. (2004). Nannofossil carbonate fluxes during the Early Cretaceous: Phytoplankton response to nutrification episodes, atmospheric CO2, and anoxia. Paleoceanography, 19(1).

Ernst, S. R., Guasti, E., Dupuis, C., & Speijer, R. P. (2006). Environmental perturbation in the southern Tethys across the Paleocene/Eocene boundary (Dababiya, Egypt): Foraminiferal and clay mineral records. Marine Micropaleontology, 60(1), 89-111.

Ettinger, N. P., Larson, T. E., Kerans, C., Thibodeau, A. M., Hattori, K. E., Kacur, S. M., & Martindale, R. C. (2020). Ocean acidification and photic-zone anoxia at the Toarcian Oceanic Anoxic Event: Insights from the Adriatic Carbonate Platform. Sedimentology.

Evitt, W.R., Gocht, H., Netzel, H., 1985. Gonyaulax cysts from lake Zürich sediments. Rev. Palaeobot. Palynol. 45 (1–2), 35–46.

Farley, K. A., & Eltgroth, S. F. (2003). An alternative age model for the Paleocene–Eocene thermal maximum using extraterrestrial 3He. Earth and Planetary Science Letters, 208(3-4), 135-148.

Farouk, S., Askalany, M., Ahmad, F., Youssef, M., Taha, S., & El-Sorogy, A. (2019). Micropalaeontological and isotopic analyses of the middle Palaeocene succession at Gebel Nezzi (Luxor, Egypt): Implications for eustatic changes. Geological Journal, 54(3), 1435-1453.

Fensome, R.A., Williams, G.L., 2004. The Lentin and Williams Index of Fossil Dinoflagellates, 2004 Edition. AASP Contrib. Ser., 42, Am. Assoc. of Stratigr. Palynol. Found., Dartmouth, Nova Scotia, Canada.

Flögel, S., Wallmann, K., Poulsen, C. J., Zhou, J., Oschlies, A., Voigt, S., & Kuhnt, W. (2011). Simulating the biogeochemical effects of volcanic CO2 degassing on the oxygen-state of the deep ocean during the Cenomanian/Turonian Anoxic Event (OAE2). Earth and Planetary Science Letters, 305(3-4), 371-384.

Foreman, B. Z., Heller, P. L., & Clementz, M. T. (2012). Fluvial response to abrupt global warming at the Palaeocene/Eocene boundary. Nature, 491(7422), 92-95.

Forster, A., Kuypers, M. M., Turgeon, S. C., Brumsack, H. J., Petrizzo, M. R., & Sinninghe Damsté, J. S. (2008). The Cenomanian/Turonian oceanic anoxic event in the South Atlantic: New insights from a geochemical study of DSDP Site 530A. Palaeogeography, Palaeoclimatology, Palaeoecology, 267(3-4), 256-283.

Forster, A., Schouten, S., Moriya, K., Wilson, P. A., & Sinninghe Damsté, J. S. (2007). Tropical warming and intermittent cooling during the Cenomanian/Turonian oceanic anoxic event 2: Sea surface temperature records from the equatorial Atlantic. *Paleoceanography*, *22*(1).

Foster, G. L., Royer, D. L., & Lunt, D. J. (2017). Future climate forcing potentially without precedent in the last 420 million years. *Nature communications*, *8*(1), 1-8.

Fricke, H. C., Clyde, W. C., O'Neil, J. R., & Gingerich, P. D. (1998). Evidence for rapid climate change in North America during the latest Paleocene thermal maximum: oxygen isotope compositions of biogenic phosphate from the Bighorn Basin (Wyoming). *Earth and Planetary Science Letters*, *160*(1-2), 193-208.

Friedrich, O., Erbacher, J., & Mutterlose, J. (2006). Paleoenvironmental changes across the Cenomanian/Turonian boundary event (oceanic anoxic event 2) as indicated by benthic foraminifera from the Demerara Rise (ODP Leg 207). *Revue de micropaléontologie*, *49*(3), 121-139.

Friedrich, O., Erbacher, J., Moriya, K., Wilson, P. A., & Kuhnert, H. (2008). Warm saline intermediate waters in the Cretaceous tropical Atlantic Ocean. Nature Geoscience, 1(7), 453-457.

Friedrich, O., Norris, R. D., & Erbacher, J. (2012). Evolution of middle to Late Cretaceous oceans—a 55 my record of Earth's temperature and carbon cycle. Geology, 40(2), 107-110.

Frieling, J., Gebhardt, H., Huber, M., Adekeye, O. A., Akande, S. O., Reichart, G. J., ... & Sluijs, A. (2017). Extreme warmth and heat-stressed plankton in the tropics during the Paleocene-Eocene Thermal Maximum. Science advances, 3(3), e1600891.

Frieling, J., Iakovleva, A. I., Reichart, G. J., Aleksandrova, G. N., Gnibidenko, Z. N., Schouten, S., & Sluijs, A. (2014). Paleocene–Eocene warming and biotic response in the epicontinental West Siberian Sea. Geology, 42(9), 767-770.

Frieling, J., Peterse, F., Lunt, D. J., Bohaty, S. M., Sinninghe Damsté, J. S., Reichart, G. J., & Sluijs, A. (2019). Widespread warming before and elevated barium burial during the Paleocene-Eocene Thermal Maximum: Evidence for methane hydrate release?. Paleoceanography and paleoclimatology, 34(4), 546-566.

Frieling, J., Reichart, G. J., Middelburg, J. J., Röhl, U., Westerhold, T., Bohaty, S. M., & Sluijs, A. (2018). Tropical Atlantic climate and ecosystem regime shifts during the Paleocene–Eocene Thermal Maximum. Climate of the Past, 14(1), 39-55.

I

Frieling, J., Svensen, H. H., Planke, S., Cramwinckel, M. J., Selnes, H., & Sluijs, A. (2016). Thermogenic methane release as a cause for the long duration of the PETM. Proceedings of the National Academy of Sciences, 113(43), 12059-12064.

Froelich, P. N., Bender, M. L., Luedtke, N. A., Heath, G. R., & DeVries, T. (1982). The marine phosphorus cycle. *Am. J. Sci*, *282*(4), 474-511.

Funkey, C. P., Conley, D. J., Reuss, N. S., Humborg, C., Jilbert, T., & Slomp, C. P. (2014). Hypoxia sustains cyanobacteria blooms in the Baltic Sea. *Environmental science & technology*, *48*(5), 2598-2602.

Gächter, R., & Meyer, J. S. (1993). The role of microorganisms in mobilization and fixation of phosphorus in sediments. In *Proceedings of the third international workshop on phosphorus in sediments* (pp. 103-121). Springer, Dordrecht.

Gale, A. S., & Christensen, W. K. (1996). Occurrence of the belemnite Actinocamax plenus in the. *Bulletin of the Geological Society of Denmark*, *43*(1), 68-77.

Gangl, S. K., Moy, C. M., Stirling, C. H., Jenkyns, H. C., Crampton, J. S., Clarkson, M. O., ... & Porcelli, D. (2019). High-resolution records of Oceanic Anoxic Event 2: insights into the timing, duration and extent of environmental perturbations from the palaeo-South Pacific Ocean. *Earth and Planetary Science Letters*, 518, 172-182.

Ganopolski, A., & Calov, R. (2011). The role of orbital forcing, carbon dioxide and regolith in 100 kyr glacial cycles. *Climate of the Past*, *7*(4), 1415-1425.

Garcia, H. E., K. Weathers, C. R. Paver, I. Smolyar, T. P. Boyer, R. A. Locarnini, M. M. Zweng, A. V. Mishonov, O. K. Baranova, D. Seidov, and J. R. Reagan (2018). World Ocean Atlas 2018, Volume 3: Dissolved Oxygen, Apparent Oxygen Utilization, and Oxygen Saturation. A. Mishonov Technical Ed.; NOAA Atlas NESDIS, 83, 38 pp.

Garcia, H. E., K. Weathers, C. R. Paver, I. Smolyar, T. P. Boyer, R. A. Locarnini, M. M. Zweng, A. V. Mishonov, O. K. Baranova, D. Seidov, and J. R. Reagan (2018). World Ocean Atlas 2018, Volume 4: Dissolved Inorganic Nutrients (phosphate, nitrate and nitrate+nitrite, silicate). A. Mishonov Technical Ed.; NOAA Atlas NESDIS, 84, 35 pp.

Gasse, F. (2000). Hydrological changes in the African tropics since the Last Glacial Maximum. *Quaternary Science Reviews*, *19*(1-5), 189-211.

Gavrilov, Y. O., Kodina, L. A., Lubchenko, I. Y., & Muzylev, N. G. (1997). The late Paleocene anoxic event in epicontinental seas of Peri-Tethys and formation of the sapropelite unit: Sedimentology and geochemistry. Lithology and Mineral Resources C/C of Litologiia I Poleznye Iskopaemye 32, 427-450.

Gavrilov, Y. O., Shcherbinina, E. A., & Oberhansli, H. (2003). Paleocene-Eocene boundary events in the northeastern Peri-Tethys. Special Papers – Geological Society of America, 147-168.

Gerlach, S. A. (1994). Oxygen conditions improve when the salinity in the Baltic Sea decreases. *Marine Pollution Bulletin*, *28*(7), 413-416.

Gibbs, S. J., Bralower, T. J., Bown, P. R., Zachos, J. C., & Bybell, L. M. (2006). Shelf and open ocean calcareous phytoplankton assemblages across the Paleocene-Eocene Thermal Maximum: Implications for global productivity gradients. *Geology*, *34*(4), 233-236.

Gibbs, S. J., Stoll, H. M., Bown, P. R., & Bralower, T. J. (2010). Ocean acidification and surface water carbonate production across the Paleocene–Eocene thermal maximum. *Earth and Planetary Science Letters*, *295*(3-4), 583-592.

Gill, B. C., Lyons, T. W., & Jenkyns, H. C. (2011). A global perturbation to the sulfur cycle during the Toarcian Oceanic Anoxic Event. Earth and Planetary Science Letters, 312(3-4), 484-496.

Giusberti, L., Boscolo Galazzo, F., & Thomas, E. (2016). Variability in climate and productivity during the Paleocene-Eocene Thermal Maximum in the western Tethys (Forada section). Climate of the Past, 12(2), 213-240.

Giusberti, L., Rio, D., Agnini, C., Backman, J., Fornaciari, E., Tateo, F., & Oddone, M. (2007). Mode and tempo of the Paleocene-Eocene thermal maximum in an expanded section from the Venetian pre-Alps. GSA Bulletin, 119(3-4), 391-412.

Goldberg, T., Poulton, S. W., Wagner, T., Kolonic, S. F., & Rehkämper, M. (2016). Molybdenum drawdown during cretaceous oceanic anoxic event 2. Earth and Planetary Science Letters, 440, 81-91.

Gradstein, F. M., Ogg, J. G., Schmitz, M. D., & Ogg, G. M. (Eds.). (2012). *The geologic time scale 2012*. Elsevier.

Grant, K. M., Grimm, R., Mikolajewicz, U., Marino, G., Ziegler, M., & Rohling, E. J. (2016). The timing of Mediterranean sapropel deposition relative to insolation, sea-level and African monsoon changes. Quaternary Science Reviews, 140, 125-141.

Grothe, A., Andreetto, F., Reichart, G. J., Wolthers, M., Van Baak, C. G., Vasiliev, I., ... & Krijgsman, W. (2020). Paratethys pacing of the Messinian Salinity Crisis: Low salinity waters contributing to gypsum precipitation?. Earth and Planetary Science Letters, 532, 116029.

Guidry, M. W., & Mackenzie, F. T. (2000). Apatite weathering and the Phanerozoic phosphorus cycle. *Geology*, *28*(7), 631-634.

I

Gunnars, A., Blomqvist, S., & Martinsson, C. (2004). Inorganic formation of apatite in brackish seawater from the Baltic Sea: an experimental approach. Marine Chemistry, 91(1-4), 15-26.

Gustafsson, B. G., Schenk, F., Blenckner, T., Eilola, K., Meier, H. M., Müller-Karulis, B., ... & Zorita, E. (2012). Reconstructing the development of Baltic Sea eutrophication 1850–2006. *Ambio*, *41*(6), 534-548.

Gustafsson, B.G., Westman, P., 2002. On the causes for salinity variations in the Baltic Sea during the last 8500 years. Paleoceanography 17 (3) (12-1).

Gutjahr, M., Ridgwell, A., Sexton, P. F., Anagnostou, E., Pearson, P. N., Pälike, H., ... & Foster, G. L. (2017). Very large release of mostly volcanic carbon during the Palaeocene–Eocene Thermal Maximum. Nature, 548(7669), 573-577.

Hancock, H. J., Dickens, G. R., Strong, C. P., Hollis, C. J., & Field, B. D. (2003). Foraminiferal and carbon isotope stratigraphy through the Paleocene-Eocene transition at Dee Stream, Marlborough, New Zealand. New Zealand Journal of Geology and Geophysics, 46(1), 1-19.

Hänninen, J., Vuorinen, I., Hjelt, P., 2000. Climatic factors in the Atlantic control the oceanographic and ecological changes in the Baltic Sea. Limnol. Oceanogr. 45 (3), 703–710.

Harding, I. C., Charles, A. J., Marshall, J. E., Pälike, H., Roberts, A. P., Wilson, P. A., ... & Pearce, R. B. (2011). Sea-level and salinity fluctuations during the Paleocene–Eocene thermal maximum in Arctic Spitsbergen. Earth and Planetary Science Letters, 303(1-2), 97-107.

Harding, S. M. (2004). The Toarcian Oceanic Anoxic Event: Organic and inorganic geochemical anomalies in organic-carbon-rich mudrocks from the North Yorkshire coast, UK and Dotternhausen Quarry, SW Germany (Doctoral dissertation). The Open University, UK.

Hartnett, H. E. (1998). Organic carbon input, degradation, and preservation in continental margin sediments: an assessment of the role of a strong oxygen deficient zone (Doctoral dissertation).

Hartnett, H. E., Keil, R. G., Hedges, J. I., & Devol, A. H. (1998). Influence of oxygen exposure time on organic carbon preservation in continental margin sediments. *Nature*, *391*(6667), 572-575.

Harvey, B. P., Gwynn-Jones, D., & Moore, P. J. (2013). Meta-analysis reveals complex marine biological responses to the interactive effects of ocean acidification and warming. *Ecology and evolution*, *3*(4), 1016-1030.

Haupt, B. J., & Seidov, D. (2001). Warm deep-water ocean conveyor during Cretaceous time. Geology, 29(4), 295-298.

Hayes, J. M., Strauss, H., & Kaufman, A. J. (1999). The abundance of 13C in marine organic matter and isotopic fractionation in the global biogeochemical cycle of carbon during the past 800 Ma. Chemical Geology, 161(1-3), 103-125.

Head, M.J., 1996. Late Cenozoic dinoflagellates from the Royal Society borehole at Ludham, Norfolk, eastern England. J. Paleontol. 70 (04), 543–570.

Hedges, J. I., & Keil, R. G. (1995). Sedimentary organic matter preservation: an assessment and speculative synthesis. *Marine chemistry*, *49*(2-3), 81-115.

HELCOM, B. (2007). HELCOM Baltic Sea action plan. *Krakow, Poland*, *November 15*, 2007.

Helz, G.R., Miller, C.V., Charnock, J.M., Mosselmans, J.F.W., Pattrick, R.A.D., Garner, C.D., Vaughan, D.J., 1996. Mechanism of molybdenum removal from the sea and its concentration in black shales: EXAFS evidence. Geochim. Cosmochim. Acta 60 (19), 3631–3642.

Hendriks, I. E., Duarte, C. M., & Álvarez, M. (2010). Vulnerability of marine biodiversity to ocean acidification: a meta-analysis. *Estuarine, Coastal and Shelf Science*, *86*(2), 157-164.

Hennekam, R. (2020) Personal communication.

Herbert, T. D., Ng, G., & Peterson, L. C. (2015). Evolution of Mediterranean sea surface temperatures 3.5–1.5 Ma: regional and hemispheric influences. Earth and Planetary Science Letters, 409, 307-318.

Hetzel, A., März, C., Vogt, C., & Brumsack, H. J. (2011). Geochemical environment of Cenomanian-Turonian black shale deposition at Wunstorf (northern Germany). Cretaceous Research, 32(4), 480-494.

Heyng, A.M., Mayr, C., Lücke, A., Moschen, R., Wissel, H., Striewski, B., Bauersachs, T., 2015. Middle and Late Holocene paleotemperatures reconstructed from oxygen isotopes and GDGTs of sediments from Lake Pupuke, New Zealand. Quat. Int. 374, 3–14.

Hilgen, F. J. (1991). Astronomical calibration of Gauss to Matuyama sapropels in the Mediterranean and implication for the geomagnetic polarity time scale. *Earth and planetary science letters*, *104*(2-4), 226-244.

Hollis, C. J., Dickens, G. R., Field, B. D., Jones, C. M., & Strong, C. P. (2005). The Paleocene–Eocene transition at Mead Stream, New Zealand: a southern Pacific record of early Cenozoic global change. Palaeogeography, Palaeoclimatology, Palaeoecology, 215(3-4), 313-343.

Homoky, W. B., Severmann, S., McManus, J., Berelson, W. M., Riedel, T. E., Statham, P. J., & Mills, R. A. (2012). Dissolved oxygen and suspended particles regulate the benthic flux of iron from continental margins. Marine Chemistry, 134, 59-70.

I

Hönisch, B., Ridgwell, A., Schmidt, D. N., Thomas, E., Gibbs, S. J., Sluijs, A., ... & Williams, B. (2012). The geological record of ocean acidification. *science*, *335*(6072), 1058-1063.

Hopmans, E.C., Schouten, S., Pancost, R.D., van der Meer, M.T.J., Sinnnghe Damsté, J.S., 2000. Analysis of intact tetraether lipids in archaeal cell material and sediments by high performance liquid chromatography/atmospheric pressure chemical ionization mass spectrometry. Rapid Commun. Mass Spectrom. 14, 585–589.

Hopmans, E.C., Weijers, J.W., Schefuß, E., Herfort, L., Damsté, J.S.S., Schouten, S., 2004. A novel proxy for terrestrial organic matter in sediments based on branched and isoprenoid tetraether lipids. Earth Planet. Sci. Lett. 224 (1), 107–116.

Hurrell, J. W., & Deser, C. (2010). North Atlantic climate variability: the role of the North Atlantic Oscillation. *Journal of marine systems*, *79*(3-4), 231-244.

Ingall, E. D., Bustin, R. M., & Van Cappellen, P. (1993). Influence of water column anoxia on the burial and preservation of carbon and phosphorus in marine shales. Geochimica et Cosmochimica Acta, 57(2), 303-316.

Ingall, E., & Jahnke, R. (1997). Influence of water-column anoxia on the elemental fractionation of carbon and phosphorus during sediment diagenesis. *Marine Geology*, *139*(1-4), 219-229.

Ingram, B. L., Coccioni, R., Montanari, A., & Richter, F. M. (1994). Strontium isotopic composition of mid-Cretaceous seawater. *Science*, *264*(5158), 546-550.

IPCC, 2013: Climate Change 2013: The Physical Science Basis. Contribution of Working Group I to the Fifth Assessment Report of the Intergovernmental Panel on Climate Change [Stocker, T.F., D. Qin, G.-K. Plattner, M. Tignor, S.K. Allen, J. Boschung, A. Nauels, Y. Xia, V. Bex and P.M. Midgley (eds.)]. Cambridge University Press, Cambridge, United Kingdom and New York, NY, USA, 1535 pp.

Jacobs, S. S., Giulivi, C. F., & Mele, P. A. (2002). Freshening of the Ross Sea during the late 20th century. *Science*, *297*(5580), 386-389.

Jahnke, R. A. (1984). The synthesis and solubility of carbonate fluorapatite. American Journal of science, 284(1), 58-78.

Jahnke, R. A., Emerson, S. R., Roe, K. K., & Burnett, W. C. (1983). The present day formation of apatite in Mexican continental margin sediments. Geochimica et Cosmochimica Acta, 47(2), 259-266.

Jansson, I.M., Mertens, K.N., Head, M.J., de Vernal, A., Londeix, L., Marret, F., Matthiessen, J., Sangiorgi, F., 2014. Statistically assessing the correlation between salinity and morphology in cysts produced by the dinoflagellate Protoceratium reticulatum from surface sediments of

the North Atlantic Ocean, Mediterranean–Marmara–Black Sea region, and Baltic–Kattegat–Skagerrak estuarine system. Palaeogeogr. Palaeoclimatol. Palaeoecol. 399, 202–213.

Jarvis, I., Burnett, W., & Baturin, G. N. (1994). Geochemistry of phosphorite - state of the art. Eclogae Geol. Helv, 87(3), 643-671.

Jarvis, I., Lignum, J. S., Gröcke, D. R., Jenkyns, H. C., & Pearce, M. A. (2011). Black shale deposition, atmospheric CO2 drawdown, and cooling during the Cenomanian-Turonian Oceanic Anoxic Event. *Paleoceanography*, *26*(3).

Jefferies, R. P. S. (1962). The palaeoecology of the Actinocamax plenus subzone (lowest Turonian) in the Anglo-Paris Basin. *Palaeontology*, 4, 609-647.

Jefferies, R. P. S. (1963). The stratigraphy of the Actinocamax plenus subzone (Turonian) in the Anglo-Paris Basin. *Proceedings of the Geologists' Association*, 74(1), 1-IN4.

Jenkyns, H. C. (2010). Geochemistry of oceanic anoxic events. *Geochemistry, Geophysics, Geosystems*, *11*(3).

Jenkyns, H. C., Dickson, A. J., Ruhl, M., & Van den Boorn, S. H. (2017). Basalt-seawater interaction, the Plenus Cold Event, enhanced weathering and geochemical change: deconstructing Oceanic Anoxic Event 2 (Cenomanian–Turonian, Late Cretaceous). *Sedimentology*, *64*(1), 16-43.

Jenkyns, H. C., Dickson, A. J., Ruhl, M., & Van den Boorn, S. H. (2017). Basalt-seawater interaction, the Plenus Cold Event, enhanced weathering and geochemical change: deconstructing Oceanic Anoxic Event 2 (Cenomanian–Turonian, Late Cretaceous). *Sedimentology*, 64(1), 16-43.

Jenkyns, H.C., 2010. Geochemistry of oceanic anoxic events. Geochem. Geophys. Geosyst. 11 (3), 1–30.

Jilbert, T., Conley, D.J., Gustafsson, B.G., Funkey, C.P., Slomp, C.P., 2015. Glacio-isostatic control on hypoxia in a high-latitude shelf basin. Geology 43 (5), 427–430.

Jilbert, T., Slomp, C.P., 2013. Rapid high-amplitude variability in Baltic Sea hypoxia during the Holocene. Geology 41 (11), 1183–1186.

John, C. M., Bohaty, S. M., Zachos, J. C., Sluijs, A., Gibbs, S., Brinkhuis, H., & Bralower, T. J. (2008). North American continental margin records of the Paleocene-Eocene thermal maximum: Implications for global carbon and hydrological cycling. Paleoceanography, 23(2).

Jones, C. E., & Jenkyns, H. C. (2001). Seawater strontium isotopes, oceanic anoxic events, and seafloor hydrothermal activity in the Jurassic and Cretaceous. *American Journal of Science*, *301*(2), 112-149.

I

Jones, M. M., Sageman, B. B., Selby, D., Jicha, B. R., Singer, B. S., & Titus, A. L. (2020). Regional chronostratigraphic synthesis of the Cenomanian-Turonian Oceanic Anoxic Event 2 (OAE2) interval, Western Interior Basin (USA): New Re-Os chemostratigraphy and 40Ar/39Ar geochronology. *GSA Bulletin.*

Jones, T. D., Lunt, D. J., Schmidt, D. N., Ridgwell, A., Sluijs, A., Valdes, P. J., & Maslin, M. (2013). Climate model and proxy data constraints on ocean warming across the Paleocene–Eocene Thermal Maximum. Earth-Science Reviews, 125, 123-145.

Joo, Y. J., Sageman, B. B., & Hurtgen, M. T. (2020). Data-model comparison reveals key environmental changes leading to Cenomanian-Turonian Oceanic Anoxic Event 2. *Earth-Science Reviews*, *203*, 103123.

Junium, C. K., Dickson, A. J., & Uveges, B. T. (2018). Perturbation to the nitrogen cycle during rapid Early Eocene global warming. Nature communications, 9(1), 1-8.

Kabel, K., Moros, M., Porsche, C., Neumann, T., Adolphi, F., Andersen, T. J., ... & Sinninghe Damsté, J. S. (2012). Impact of climate change on the Baltic Sea ecosystem over the past 1,000 years. *Nature Climate Change*, *2*(12), 871-874.

Kaiho, K. (1988). Uppermost Cretaceous to Paleogene bathyal benthic foraminiferal biostratigraphy of Japan and New Zealand: Latest Paleocene-middle Eocene benthic foraminiferal species turnover. Revue de paléobiologie, 553-559.

Kaiho, K., Arinobu, T., Ishiwatari, R., Morgans, H. E., Okada, H., Takeda, N., ... & Hirai, A. (1996). Latest Paleocene benthic foraminiferal extinction and environmental changes at Tawanui, New Zealand. Paleoceanography, 11(4), 447-465.

Kaiho, K., Takeda, K., Petrizzo, M. R., & Zachos, J. C. (2006). Anomalous shifts in tropical Pacific planktonic and benthic foraminiferal test size during the Paleocene–Eocene thermal maximum. Palaeogeography, Palaeoclimatology, Palaeoecology, 237(2-4), 456-464.

Kalinin, G.P., and I.A. Shiklomanov (1974). Exploitation of the Earth's water resources, in World Water Balance and Water Resources of the Earth (in Russian), pp. 575-606, Gidrometeoizdat, St. Petersburg. Russia.

Kasting, J. F., & Richardson, S. M. (1985). Seafloor hydrothermal activity and spreading rates: The Eocene carbon dioxide greenhouse revisited. *Geochimica et cosmochimica acta*, *49*(12), 2541- 2544.

Katz, M. E., Wright, J. D., Miller, K. G., Cramer, B. S., Fennel, K., & Falkowski, P. G. (2005). Biological overprint of the geological carbon cycle. Marine Geology, 217(3-4), 323-338.

Keeling, R. F., & Garcia, H. E. (2002). The change in oceanic O2 inventory associated with recent global warming. *Proceedings of the National Academy of Sciences*, *99*(12), 7848-7853.

Kelly, D. C. (2002). Response of Antarctic (ODP Site 690) planktonic foraminifera to the Paleocene–Eocene thermal maximum: faunal evidence for ocean/climate change. Paleoceanography, 17(4), 23-1.

Kelly, D. C., Zachos, J. C., Bralower, T. J., & Schellenberg, S. A. (2005). Enhanced terrestrial weathering/runoff and surface ocean carbonate production during the recovery stages of the Paleocene-Eocene thermal maximum. Paleoceanography, 20(4).

Kender, S., Stephenson, M. H., Riding, J. B., Leng, M. J., Knox, R. W. B., Peck, V. L., ... & Jamieson, R. (2012). Marine and terrestrial environmental changes in NW Europe preceding carbon release at the Paleocene–Eocene transition. Earth and Planetary Science Letters, 353, 108-120.

Khatiwala, S., Tanhua, T., Mikaloff Fletcher, S., Gerber, M., Doney, S. C., Graven, H. D., ... & Sabine, C. L. (2013). Global ocean storage of anthropogenic carbon. *Biogeosciences*, *10*(4), 2169-2191.

Khozyem, H., Adatte, T., Spangenberg, J. E., Keller, G., Tantawy, A. A., & Ulianov, A. (2015). New geochemical constraints on the Paleocene–Eocene thermal maximum: Dababiya GSSP, Egypt. Palaeogeography, Palaeoclimatology, Palaeoecology, 429, 117-135.

Khozyem, H., Adatte, T., Spangenberg, J. E., Tantawy, A. A., & Keller, G. (2013). Palaeoenvironmental and climatic changes during the Palaeocene–Eocene Thermal Maximum (PETM) at the Wadi Nukhul Section, Sinai, Egypt. Journal of the Geological Society, 170(2), 341-352.

Kim, J.H., van der Meer, J., Schouten, S., Helmke, P., Willmott, V., Sangiorgi, F., Koc, N., Hopmans, E.C., Sinninghe Damsté, J.S., 2010. New indices and calibrations derived from the distribution of crenarchaeal isoprenoid tetraether lipids: implications for past sea surface temperature reconstructions. Geochim. Cosmochim. Acta 74, 4639–4654.

Kirtland Turner, S.. (2018). Constraints on the onset duration of the Paleocene–Eocene Thermal Maximum. Philosophical Transactions of the Royal Society A: Mathematical, Physical and Engineering Sciences, 376(2130), 20170082.

Knies, J., Mann, U., Popp, B. N., Stein, R., & Brumsack, H. J. (2008). Surface water productivity and paleoceanographic implications in the Cenozoic Arctic Ocean. Paleoceanography, 23(1).

Knox, R. W. O. B., Aubry, M. P., Berggren, W. A., Dupuis, C., Ouda, K., Magioncalda, R., & Soliman, M. (2003). The Qreiya section at Gebel Abu Had: lithostratigraphy, clay mineralogy, geochemistry and biostratigraphy. Micropaleontology, 49(Suppl_1), 93-104.

Kolonic, S., Wagner, T., Forster, A., Sinninghe Damsté, J. S., Walsworth-Bell, B., Erba, E., ... & Kuhnt, W. (2005). Black shale deposition on the northwest African Shelf during the Cenomanian/Turonian oceanic anoxic event: Climate coupling and global organic carbon burial. Paleoceanography, 20(1).

I

Kolonic, S., Wagner, T., Forster, A., Sinninghe Damsté, J. S., Walsworth-Bell, B., Erba, E., Turgeon, S., Brumsack, H.-J., Chellai, E. H., Tsikos, H., Kunht, W., & Kuypers, M. M. (2005). Black shale deposition on the northwest African Shelf during the Cenomanian/Turonian oceanic anoxic event: Climate coupling and global organic carbon burial. *Paleoceanography*, *20*(1).

Komar, N., & Zeebe, R. E. (2017). Redox-controlled carbon and phosphorus burial: A mechanism for enhanced organic carbon sequestration during the PETM. *Earth and Planetary Science Letters*, *479*, 71-82.

Kopp, R. E., Schumann, D., Raub, T. D., Powars, D. S., Godfrey, L. V., Swanson-Hysell, N. L., ... & Vali, H. (2009). An Appalachian Amazon? Magnetofossil evidence for the development of a tropical river-like system in the mid-Atlantic United States during the Paleocene-Eocene thermal maximum. Paleoceanography, 24(4).

Kotthoff, U., Groeneveld, J., Ash, J.L., Fanget, A.S., Quintana Krupinski, N., Peyron, O., Stepanova, A., Warnock, J., van Helmond, N.A.G.M., Passey, B.H., Clausen, O.R., Bennike, O., Andrén, E., Granoszewski, W., Andrén, T., Filipsson, H.L., Seidenkrantz, M., Slomp, C.P., Bauersachs, T., 2017. Reconstructing Holocene temperature and salinity variations in the western Baltic Sea region: A multi-proxy comparison from the Little Belt (IODP Expedition 347, Site M0059). In: Biogeosciences Discussions, (accepted for publication).

Kouli, K., Brinkhuis, H., Dale, B., 2001. Spiniferites cruciformis: a fresh water dinoflagellate cyst? Rev. Palaeobot. Palynol. 113 (4), 273–286.

Koutsoukos, P., Amjad, Z., Tomson, M. B., & Nancollas, G. H. (1980). Crystallization of calcium phosphates. A constant composition study. Journal of the American Chemical Society, 102(5), 1553-1557.

Kraal, P., Dijkstra, N., Behrends, T., & Slomp, C. P. (2017). Phosphorus burial in sediments of the sulfidic deep Black Sea: Key roles for adsorption by calcium carbonate and apatite authigenesis. Geochimica et Cosmochimica Acta, 204, 140-158.

Kraal, P., Slomp, C. P., & de Lange, G. J. (2010). Sedimentary organic carbon to phosphorus ratios as a redox proxy in Quaternary records from the Mediterranean. Chemical Geology, 277(1-2), 167-177.

Kraal, P., Slomp, C. P., Forster, A., & Kuypers, M. M. (2010). Phosphorus cycling from the margin to abyssal depths in the proto-Atlantic during oceanic anoxic event 2. *Palaeogeography, Palaeoclimatology, Palaeoecology*, *295*(1-2), 42-54.

Kraal, P., Slomp, C. P., Forster, A., Kuypers, M. M., & Sluijs, A. (2009). Pyrite oxidation during sample storage determines phosphorus fractionation in carbonate-poor anoxic sediments. Geochimica et Cosmochimica Acta, 73(11), 3277-3290.

Kraal, P., Slomp, C. P., Reed, D. C., Reichart, G. J., & Poulton, S. W. (2012). Sedimentary phosphorus and iron cycling in and below the oxygen minimum zone of the northern Arabian Sea. Biogeosciences, 9(7), 2603-2624.

Krencker, F. N., Bodin, S., Suan, G., Heimhofer, U., Kabiri, L., & Immenhauser, A. (2015). Toarcian extreme warmth led to tropical cyclone intensification. Earth and Planetary Science Letters, 425, 120-130.

Kuhnt, W., Holbourn, A. E., Beil, S., Aquit, M., Krawczyk, T., Flögel, S., Chellai, E. H., & Jabour, H. (2017). Unraveling the onset of Cretaceous Oceanic Anoxic Event 2 in an extended sediment archive from the Tarfaya-Laayoune Basin, Morocco. *Paleoceanography*, *32*(8), 923-946.

Kuhnt, W., Holbourn, A. E., Beil, S., Aquit, M., Krawczyk, T., Flögel, S., ... & Jabour, H. (2017). Unraveling the onset of Cretaceous Oceanic Anoxic Event 2 in an extended sediment archive from the Tarfaya-Laayoune Basin, Morocco. *Paleoceanography*, 32(8), 923-946.

Kump, L. R., & Arthur, M. A. (1999). Interpreting carbon-isotope excursions: carbonates and organic matter. *Chemical Geology*, 161(1-3), 181-198.

Kuroda, J., Ogawa, N. O., Tanimizu, M., Coffin, M. F., Tokuyama, H., Kitazato, H., & Ohkouchi, N. (2007). Contemporaneous massive subaerial volcanism and late cretaceous Oceanic Anoxic Event 2. *Earth and Planetary Science Letters*, *256*(1-2), 211-223.

Kurtz, A. C., Kump, L. R., Arthur, M. A., Zachos, J. C., & Paytan, A. (2003). Early Cenozoic decoupling of the global carbon and sulfur cycles. Paleoceanography, 18(4).

Kuypers, M. M. M., Pancost, R. D., Nijenhuis, I. A., & Sinninghe Damsté, J. S. (2002). Enhanced productivity led to increased organic carbon burial in the euxinic North Atlantic basin during the late Cenomanian oceanic anoxic event. *Paleoceanography*, *17*(4), 3-1.

Kuypers, M. M., Lourens, L. J., Rijpstra, W. I. C., Pancost, R. D., Nijenhuis, I. A., & Sinninghe Damsté, J. S. (2004). Orbital forcing of organic carbon burial in the proto-North Atlantic during oceanic anoxic event 2. Earth and Planetary Science Letters, 228(3-4), 465-482.

Larkin, N. K., & Harrison, D. E. (2005). Global seasonal temperature and precipitation anomalies during El Niño autumn and winter. *Geophysical Research Letters*, *32*(16).

Laws, E. A., D'Sa, E., & Naik, P. (2011). Simple equations to estimate ratios of new or export production to total production from satellite-derived estimates of sea surface temperature and primary production. Limnology and Oceanography: Methods, 9(12), 593-601.

Laws, E. A., Falkowski, P. G., Smith Jr, W. O., Ducklow, H., & McCarthy, J. J. (2000b). Temperature effects on export production in the open ocean. Global Biogeochemical Cycles, 14(4), 1231-1246.

I

Laws, E. A., Landry, M. R., Barber, R. T., Campbell, L., Dickson, M. L., & Marra, J. (2000a). Carbon cycling in primary production bottle incubations: inferences from grazing experiments and photosynthetic studies using 14C and 18O in the Arabian Sea. Deep Sea Research Part II: Topical Studies in Oceanography, 47(7-8), 1339-1352.

Lenstra, W. K., Hermans, M., Séguret, M. J., Witbaard, R., Behrends, T., Dijkstra, N., ... & Slomp, C.P. (2019). The shelf-to-basin iron shuttle in the Black Sea revisited. Chemical Geology, 511, 314-341.

Lenz, C., Jilbert, T., Conley, D.J., Slomp, C.P., 2015. Hypoxia-driven variations in iron and manganese shuttling in the Baltic Sea over the past 8 ka. Geochem. Geophys. Geosyst. 16 (10), 3754–3766.

Li, G., Cheng, L., Zhu, J., Trenberth, K. E., Mann, M. E., & Abraham, J. P. (2020). Increasing oceanstratification over the past half-century. *Nature Climate Change*, *10*(12), 1116-1123.

Li, Y. X., Montanez, I. P., Liu, Z., & Ma, L. (2017). Astronomical constraints on global carbon-cycle perturbation during Oceanic Anoxic Event 2 (OAE2). *Earth and Planetary Science Letters*, 462, 35-46.

Lippert, P. C., & Zachos, J. C. (2007). A biogenic origin for anomalous fine-grained magnetic material at the Paleocene-Eocene boundary at Wilson Lake, New Jersey. Paleoceanography, 22(4).

Liu, X.L., Summons, R.E., Hinrichs, K.U., 2012. Extending the known range of glycerol ether lipids in the environment: structural assignments based on tandem mass spectral fragmentation patterns. Rapid Commun. Mass Spectrom. 26, 2295–2302.

Lønborg, C., Álvarez–Salgado, X. A., Letscher, R. T., & Hansell, D. A. (2018). Large stimulation of recalcitrant dissolved organic carbon degradation by increasing ocean temperatures. *Frontiers in Marine Science*, *4*, 436.

Lougheed, B.C., Snowball, I., Moros, M., Kabel, K., Muscheler, R., Virtasalo, J.J., Wacker, L., 2012. Using an independent geochronology based on palaeomagnetic secular variation (PSV) and atmospheric Pb deposition to date Baltic Sea sediments and infer 14C reservoir age. Quat. Sci. Rev. 42, 43–58.

Lu, G., & Keller, G. (1993). The Paleocene-Eocene transition in the Antarctic Indian Ocean: inference from planktic foraminifera. Marine Micropaleontology, 21(1-3), 101-142.

Luciani, V., Giusberti, L., Agnini, C., Backman, J., Fornaciari, E., & Rio, D. (2007). The Paleocene–Eocene Thermal Maximum as recorded by Tethyan planktonic foraminifera in the Forada section (northern Italy). Marine Micropaleontology, 64(3-4), 189-214.

Lunt, D. J., Ridgwell, A., Sluijs, A., Zachos, J., Hunter, S., & Haywood, A. (2011). A model for orbital pacing of methane hydrate destabilization during the Palaeogene. *Nature Geoscience*, *4*(11), 775-778.

Luo, Y., Boudreau, B. P., Dickens, G. R., Sluijs, A., & Middelburg, J. J. (2016). An alternative model for CaCO3 over-shooting during the PETM: biological carbonate compensation. Earth and Planetary Science Letters, 453, 223-233.

Lüthi, D., Le Floch, M., Bereiter, B., Blunier, T., Barnola, J. M., Siegenthaler, U., ... & Stocker, T. F. (2008). High-resolution carbon dioxide concentration record 650,000–800,000 years before present. *Nature*, *453*(7193), 379-382.

Lyons, S. L., Baczynski, A. A., Babila, T. L., Bralower, T. J., Hajek, E. A., Kump, L. R., ... & Zachos, J. C. (2019). Palaeocene–Eocene Thermal Maximum prolonged by fossil carbon oxidation. Nature Geoscience, 12(1), 54-60.

Lyons, T. W., & Severmann, S. (2006). A critical look at iron paleoredox proxies: New insights from modern euxinic marine basins. Geochimica et Cosmochimica Acta, 70(23), 5698-5722.

Ma, Z., Gray, E., Thomas, E., Murphy, B., Zachos, J., & Paytan, A. (2014). Carbon sequestration during the Palaeocene–Eocene Thermal Maximum by an efficient biological pump. Nature Geoscience, 7(5), 382-388.

Manabe, S., & Stouffer, R. J. (1995). Simulation of abrupt climate change induced by freshwater input to the North Atlantic Ocean. *Nature*, *378*(6553), 165-167.

Mänd, K., Kirsimäe, K., Lepland, A., Crosby, C. H., Bailey, J. V., Konhauser, K. O., ... & Lumiste, K. (2018). Authigenesis of biomorphic apatite particles from Benguela upwelling zone sediments off Namibia: The role of organic matter in sedimentary apatite nucleation and growth. Geobiology, 16(6), 640-658.

Mann, M. E., Zhang, Z., Rutherford, S., Bradley, R. S., Hughes, M. K., Shindell, D., ... & Ni, F. (2009). Global signatures and dynamical origins of the Little Ice Age and Medieval Climate Anomaly. *Science*, *326*(5957), 1256-1260.

Markwick, P. J. (2007). The palaeogeographic and palaeoclimatic significance of climate proxies for data-model comparisons. Deep-time perspectives on climate change: marrying the signal from computer models and biological proxies, 251-312.

Marret, F., Leroy, S., Chalié, F., Françoise, F., 2004. New organic-walled dinoflagellate cysts from recent sediments of Central Asian seas. Rev. Palaeobot. Palynol. 129 (1), 1–20.

Marsay, C. M., Sanders, R. J., Henson, S. A., Pabortsava, K., Achterberg, E. P., & Lampitt, R. S. (2015). Attenuation of sinking particulate organic carbon flux through the mesopelagic ocean. *Proceedings of the National Academy of Sciences*, *112*(4), 1089-1094.

I

Matear, R. J., Hirst, A. C., & McNeil, B. I. (2000). Changes in dissolved oxygen in the Southern Ocean with climate change. *Geochemistry, Geophysics, Geosystems*, *1*(11).

Matthäus, W., & Franck, H. (1992). Characteristics of major Baltic inflows—a statistical analysis. *Continental Shelf Research*, *12*(12), 1375-1400.

McArthur, J. M., Algeo, T. J., Van de Schootbrugge, B., Li, Q., & Howarth, R. J. (2008). Basinal restriction, black shales, Re-Os dating, and the Early Toarcian (Jurassic) oceanic anoxic event. Paleoceanography, 23(4).

McInerney, F. A., & Wing, S. L. (2011). The Paleocene-Eocene Thermal Maximum: A perturbation of carbon cycle, climate, and biosphere with implications for the future. *Annual Review of Earth and Planetary Sciences*, *39*, 489-516.

McInerney, F. A., & Wing, S. L. (2011). The Paleocene-Eocene Thermal Maximum: a perturbation of carbon cycle, climate, and biosphere with implications for the future. Annual Review of Earth and Planetary Sciences, 39, 489-516.

MEDAR Group. (2003). Medatlas/2002-database: Mediterranean and Black Sea database of temperature, salinity and bio-chemical parameters. Climatological atlas. http://nettuno.ogs. trieste.it/medar/climatologies/DH3/dh3.html Visited in 2020.

Meier, H.E.M., 2006. Baltic Sea climate in the late twenty-first century: a dynamical downscaling approach using two global models and two emission scenarios. Clim. Dyn. 27 (1), 39–68.

Meier, H.E.M., Andersson, H.C., Arheimer, B., Blenckner, T., Chubarenko, B., Donnelly, C., Eilola, K., Gustafsson, B.G., Hansson, A., Havenhand, J., Höglund, A., Kuznetsov, I., MacKenzie, B.R., Müller-Karulis, B., Neumann, T., Niiranen, S., Piwowarczyk, J., Raudsepp, U., Reckermann, M., Ruoho-Airola, T., Savchuk, O.P., Schenk, F., Schimanke, S., Väli, G., Weslawski, J.-M., Zorita, E., 2012. Comparing reconstructed past variations and future projections of the Baltic Sea ecosystem—first results from multi-model ensemble simulations. Environ. Res. Lett. 7, 34005.

Meier, H.E.M., Andersson, H.C., Eilola, K., Gustafsson, B.G., Kuznetsov, I., Mller-Karulis, B., Neumann, T., Savchuk, O.P., 2011. Hypoxia in future climates: a model ensemble study for the Baltic Sea. Geophys. Res. Lett. 38, 1–6.

Meier, H.E.M., Höglund, A., Eilola, K., Almroth-Rosell, E., 2016. Impact of accelerated future global mean sea level rise on hypoxia in the Baltic Sea. Clim. Dyn. 1–10.

Mertens, K.N., Dale, B., Ellegaard, M., Jansson, I., Godhe, A., Kremp, A., Louwye, S., 2011. Process length variation in cysts of the dinoflagellate Protoceratium reticulatum, from surface sediments of the Baltic–Kattegat–Skagerrak estuarine system: a regional salinity proxy. Boreas 40 (2), 242–255.

Mertens, K.N., Verhoeven, K., Verleye, T., Louwye, S., Amorim, A., Ribeiro, S., Deaf, A.S., Harding, I.C., De Schepper, S., González, C., Kodrans-Nsiah, M., De Vernal, A., Henry, M., Radi, T., Dybkjaer, K., Poulsen, N.E., Feist-Burkhardt, S., Chitolie, J., Heilmann- Clausen, C., Londeix, L., Turon, J.-L., Marret, F., Matthiessen, J., McCarthy, F.M.G., Prasad, V., Pospelova, V., Kyffin Hughes, J.E., Riding, J.B., Rochon, A., Sangiorgi, F., Welters, N., Sinclair, N., Thun, C., Soliman, A., Van Nieuwenhove, N., Vink, A., Young, M., 2009. Determining the absolute abundance of dinoflagellate cysts in recent marine sediments: the Lycopodium marker-grain method put to the test. Rev. Palaeobot. Palynol. 157, 238–252.

Middelburg, J. J. (2019). Marine carbon biogeochemistry: a primer for earth system scientists (p. 118). Springer Nature.

Miller, K. G., Browning, J. V., Schmelz, W. J., Kopp, R. E., Mountain, G. S., & Wright, J. D. (2020). Cenozoic sea-level and cryospheric evolution from deep-sea geochemical and continental margin records. Science advances, 6(20), 1346.

Miller, K. G., Sugarman, P. J., Browning, J. V., Kominz, M. A., Olsson, R. K., Feigenson, M. D., & Hernández, J. C. (2004). Upper Cretaceous sequences and sea-level history, New Jersey coastal plain. GSA Bulletin, 116(3-4), 368-393.

Miller, K. G., Sugarman, P. J., Browning, J. V., Olsson, R. K., Pekar, S. F., Reilly, T. J., ... & Stewart, M. (1998). Bass river site. In Miller, KG, Sugarman, PJ, Browning, JV, et al., Proc. ODP, Init. Repts., 174AX: College Station, TX (Ocean Drilling Program) (pp. 5-43).

Milliman, J. D., & Farnsworth, K. L. (2013). River discharge to the coastal ocean: a global synthesis. Cambridge University Press.

Monteiro, F. M., Pancost, R. D., Ridgwell, A., & Donnadieu, Y. (2012). Nutrients as the dominant control on the spread of anoxia and euxinia across the Cenomanian-Turonian oceanic anoxic event (OAE2): Model-data comparison. Paleoceanography, 27(4).

Montero-Serrano, J. C., Föllmi, K. B., Adatte, T., Spangenberg, J. E., Tribovillard, N., Fantasia, A., & Suan, G. (2015). Continental weathering and redox conditions during the early Toarcian Oceanic Anoxic Event in the northwestern Tethys: Insight from the Posidonia Shale section in the Swiss Jura Mountains. Palaeogeography, Palaeoclimatology, Palaeoecology, 429, 83-99.

Morsi, A. M. M., Speijer, R. P., Stassen, P., & Steurbaut, E. (2011). Shallow marine ostracode turnover in response to environmental change during the Paleocene–Eocene thermal maximum in northwest Tunisia. Journal of African Earth Sciences, 59(2-3), 243-268.

Mort, H. P., Adatte, T., Föllmi, K. B., Keller, G., Steinmann, P., Matera, V., ... & Stüben, D. (2007). Phosphorus and the roles of productivity and nutrient recycling during oceanic anoxic event 2. *Geology*, *35*(6), 483-486.

I

Mort, H. P., Slomp, C. P., Gustafsson, B. G., & Andersen, T. J. (2010). Phosphorus recycling and burial in Baltic Sea sediments with contrasting redox conditions. *Geochimica et Cosmochimica Acta*, *74*(4), 1350-1362.

Müller, R. D., Sdrolias, M., Gaina, C., Steinberger, B., & Heine, C. (2008). Long-term sea-level fluctuations driven by ocean basin dynamics. Science, 319(5868), 1357-1362.

Murphy, B. H., Farley, K. A., & Zachos, J. C. (2010). An extraterrestrial 3He-based timescale for the Paleocene–Eocene thermal maximum (PETM) from Walvis Ridge, IODP Site 1266. Geochimica et Cosmochimica Acta, 74(17), 5098-5108.

Mutterlose, J., Linnert, C., & Norris, R. (2007). Calcareous nannofossils from the Paleocene–Eocene Thermal Maximum of the equatorial Atlantic (ODP Site 1260B): evidence for tropical warming. Marine Micropaleontology, 65(1-2), 13-31.

Nagy, J., Jargvoll, D., Dypvik, H., Jochmann, M., & Riber, L. (2013). Environmental changes during the Paleocene–Eocene Thermal Maximum in Spitsbergen as reflected by benthic foraminifera. Polar Research, 32(1), 19737.

Nederbragt, A. J., Thurow, J., Vonhof, H., & Brumsack, H. J. (2004). Modelling oceanic carbon and phosphorus fluxes: implications for the cause of the late Cenomanian Oceanic Anoxic Event (OAE2). *Journal of the Geological Society*, *161*(4), 721-728.

Nesje, A., 2009. Latest Pleistocene and Holocene alpine glacier fluctuations in Scandinavia. Quat. Sci. Rev. 28 (21), 2119–2136.

Nicolo, M. J., Dickens, G. R., & Hollis, C. J. (2010). South Pacific intermediate water oxygen depletion at the onset of the Paleocene-Eocene thermal maximum as depicted in New Zealand margin sections. Paleoceanography, 25(4).

Ning, W., Andersson, P.S., Ghosh, A., Khan, M., Filipsson, H.L., 2015. Quantitative salinity reconstructions of the Baltic Sea during the mid-Holocene. Boreas 46, 100–110.

Nomura, R., Takata, H., Wilson, P. A., Lyle, M., & Firth, J. V. (2005). Data report: Paleocene/Eocene benthic foraminifers, ODP Leg 199 Sites 1215, 1220, and 1221, equatorial central Pacific Ocean. In Proceedings of the Ocean Drilling Program, Scientific Results, 199, 1-34. College Station, TX: Ocean Drilling Program.

Norris, R.D., Wilson, P.A., Blum, P., Fehr, A., Agnini, C., Bornemann, A., Boulila, S., Bown, P.R., Cournede, C., Friedrich, O., Ghosh, A.K., Hollis, C.J., Hull, P.M., Jo, K., Junium, C.K., Kaneko, M., Liebrand, D., Lippert, P.C., Liu, Z., Matsui, H., Moriya, K., Nishi, H., Opdyke, B.N., Penman, D., Romans, B., Scher, H.D., Sexton, P., Takagi, H., Turner, S.K., Whiteside, J.H., Yamaguchi, T., and Yamamoto, Y., 2014. Site U1403. In Norris, R.D., Wilson, P.A., Blum, P., and the Expedition 342 Scientists, Proc. IODP, 342: College Station, TX (Integrated Ocean Drilling Program).

Obrochta, S.P., Andrén, T., Fazekas, S.Z., Lougheed, B.C., Snowball, I., Yokoyama, Y., Miyairi, Y., Kondo, R., Kotilainen, A.T., Hyttinen, O., Fehr, A., 2017. The undatables: quantifying uncertainty in a highly expanded Late Glacial-Holocene sediment sequence recovered from the deepest Baltic Sea basin—IODP Site M0063. Geochem. Geophys. Geosyst. 18 (3), 858–871.

O'Connor, L. K., Jenkyns, H. C., Robinson, S. A., Remmelzwaal, S. R., Batenburg, S. J., Parkinson, I. J., & Gale, A. S. (2020). A re-evaluation of the Plenus Cold Event, and the links between CO2, temperature, and seawater chemistry during OAE 2. *Paleoceanography and Paleoclimatology*, 35(4), e2019PA003631.

Orr, J. C., Fabry, V. J., Aumont, O., Bopp, L., Doney, S. C., Feely, R. A., ... & Yool, A. (2005). Anthropogenic ocean acidification over the twenty-first century and its impact on calcifying organisms. *Nature*, *437*(7059), 681-686.

Owens, J. D., Gill, B. C., Jenkyns, H. C., Bates, S. M., Severmann, S., Kuypers, M. M., ... & Lyons, T. W. (2013). Sulfur isotopes track the global extent and dynamics of euxinia during Cretaceous Oceanic Anoxic Event 2. Proceedings of the National Academy of Sciences, 110(46), 18407-18412.

Owens, J. D., Lyons, T. W., & Lowery, C. M. (2018). Quantifying the missing sink for global organic carbon burial during a Cretaceous oceanic anoxic event. *Earth and Planetary Science Letters*, *499*, 83-94.

Owens, J. D., Lyons, T. W., Li, X., Macleod, K. G., Gordon, G., Kuypers, M. M., ... & Severmann, S. (2012). Iron isotope and trace metal records of iron cycling in the proto-North Atlantic during the Cenomanian-Turonian oceanic anoxic event (OAE-2). Paleoceanography, 27(3).

Owens, J. D., Lyons, T. W., Li, X., Macleod, K. G., Gordon, G., Kuypers, M. M. M., Anbar, A., Kuhnt, W., & Severmann, S. (2012). Iron isotope and trace metal records of iron cycling in the proto-North Atlantic during the Cenomanian-Turonian oceanic anoxic event (OAE-2). *Paleoceanography*, *27*(3).

Pagani, M., Pedentchouk, N., Huber, M., Sluijs, A., Schouten, S., Brinkhuis, H., ... & Dickens, G. R. (2006). Arctic hydrology during global warming at the Palaeocene/Eocene thermal maximum. Nature, 442(7103), 671-675.

Pak, D. K., & Miller, K. G. (1992). Paleocene to Eocene benthic foraminiferal isotopes and assemblages: Implications for deepwater circulation. Paleoceanography, 7(4), 405-422.

Palastanga, V., Slomp, C. P., & Heinze, C. (2013). Glacial-interglacial variability in ocean oxygen and phosphorus in a global biogeochemical model. Biogeosciences, 10(2), 945-958.

Pälike, C., Delaney, M. L., & Zachos, J. C. (2014). Deep-sea redox across the Paleocene-Eocene thermal maximum. Geochemistry, Geophysics, Geosystems, 15(4), 1038-1053.

I

Panchuk, K., Ridgwell, A., & Kump, L. R. (2008). Sedimentary response to Paleocene-Eocene Thermal Maximum carbon release: A model-data comparison. Geology, 36(4), 315-318.

Papadomanolaki, N.M., Sluijs, A. and Slomp, C.P. (2020). Corg/Ptot, Fe/Al and CaCO3 data for the PETM of Bass River, Forada, IODP M004 (ACEX), ODP 752, ODP 1172 and IODP 1403. PANGEA.

Parkhurst, D. L., & Appelo, C. A. J. (2013). Description of input and examples for PHREEQC version 3: a computer program for speciation, batch-reaction, one-dimensional transport, and inverse geochemical calculations (No. 6-A43). US Geological Survey.

Passier, H. F., Dekkers, M. J., & de Lange, G. J. (1998). Sediment chemistry and magnetic properties in an anomalously reducing core from the eastern Mediterranean Sea. Chemical Geology, 152(3-4), 287-306.

Penman, D. E., Turner, S. K., Sexton, P. F., Norris, R. D., Dickson, A. J., Boulila, S., ... & Westerhold, T. (2016). An abyssal carbonate compensation depth overshoot in the aftermath of the Palaeocene–Eocene Thermal Maximum. Nature Geoscience, 9(8), 575-580.

Percival, L. M. E., van Helmond, N. A. G. M., Selby, D., Goderis, S., & Claeys, P. (2020). Complex Interactions Between Large Igneous Province Emplacement and Global-Temperature Changes During the Cenomanian-Turonian Oceanic Anoxic Event (OAE 2). *Paleoceanography and Paleoclimatology*, *35*(10), e2020PA004016.

Petrizzo, M. R. (2007). The onset of the Paleocene–Eocene Thermal Maximum (PETM) at Sites 1209 and 1210 (Shatsky Rise, Pacific Ocean) as recorded by planktonic foraminifera. Marine Micropaleontology, 63(3-4), 187-200.

Pierrehumbert, R. T. (2002). The hydrologic cycle in deep-time climate problems. Nature, 419(6903), 191-198.

Poulton, S. W., Henkel, S., März, C., Urquhart, H., Flögel, S., Kasten, S., Sinninghe Damsté, J. S., & Wagner, T. (2015). A continental-weathering control on orbitally driven redox-nutrient cycling during Cretaceous Oceanic Anoxic Event 2. *Geology*, *43*(11), 963-966.

Poulton, S.W., Canfield, D.E., 2011. Ferruginous conditions: a dominant feature of the ocean through Earth's history. Elements 7 (2), 107–112.

Prasad, V., Garg, R., Khowaja-Ateequzzaman, S. I., & Joachimski, M. (2006). Apectodinium acme and the palynofacies characteristics in the latest Palaeocene-earliest Eocene of northeastern India: Biotic response to Palaeocene-Eocene Thermal maxima (PETM) in low latitude. J. Palaeontol. Soc. India, 51(7).

Rabalais, N.N., Diaz, R.J., Levin, L.A., Turner, R.E., Gilbert, D., Zhang, J., 2010. Dynamics and distribution of natural and human-caused hypoxia. Biogeosciences 7 (2), 585–619.

Raffi, I., & De Bernardi, B. (2008). Response of calcareous nannofossils to the Paleocene–Eocene Thermal Maximum: Observations on composition, preservation and calcification in sediments from ODP Site 1263 (Walvis Ridge—SW Atlantic). Marine Micropaleontology, 69(2), 119-138.

Raiswell, R., & Canfield, D. E. (2012). The iron biogeochemical cycle past and present. Geochemical perspectives, 1(1), 1-2.

Raiswell, R., Buckley, F., Berner, R.A., Anderson, T.F., 1988. Degree of pyritization of iron as a paleoenvironmental indicator of bottom-water oxygenation. J. Sediment. Res. 58 (5), 812–819.

Raiswell, R., Canfield, D.E., 2012. The iron biogeochemical cycle past and present. Geochem. Perspect. 1 (1), 1–2.

Raiswell, R., Hardisty, D. S., Lyons, T. W., Canfield, D. E., Owens, J. D., Planavsky, N. J., ... & Reinhard, C. T. (2018). The iron paleoredox proxies: A guide to the pitfalls, problems and proper practice. American Journal of Science, 318(5), 491-526.

Ravizza, G., Norris, R. N., Blusztajn, J., & Aubry, M. P. (2001). An osmium isotope excursion associated with the late Paleocene thermal maximum: Evidence of intensified chemical weathering. Paleoceanography, 16(2), 155-163.

Reed, D. C., Slomp, C. P., & de Lange, G. J. (2011). A quantitative reconstruction of organic matter and nutrient diagenesis in Mediterranean Sea sediments over the Holocene. Geochimica et Cosmochimica Acta, 75(19), 5540-5558.

Renssen, H., Seppä, H., Crosta, X., Goosse, H., Roche, D.M., 2012. Global characterization of the Holocene thermal maximum. Quat. Sci. Rev. 48, 7–19.

Robinson, S. A., Dickson, A. J., Pain, A., Jenkyns, H. C., O'Brien, C. L., Farnsworth, A., & Lunt, D. J. (2019). Southern Hemisphere sea-surface temperatures during the Cenomanian–Turonian: Implications for the termination of Oceanic Anoxic Event 2. *Geology*, *47*(2), 131-134.

Rochon, A., Vernal, A.D., Turon, J.L., Matthießen, J., Head, M.J., 1999. Distribution of Recent Dinoflagellate Cysts in Surface Sediments From the North Atlantic Ocean and Adjacent Seas in Relation to Sea-surface Parameters. American Association of Stratigraphic Palynologists Contribution Series 35. pp. 1–146.

Rodríguez-Tovar, F. J., Uchman, A., Alegret, L., & Molina, E. (2011). Impact of the Paleocene–Eocene Thermal Maximum on the macrobenthic community: Ichnological record from the Zumaia section, northern Spain. Marine Geology, 282(3-4), 178-187.

Röhl, U., Brinkhuis, H., Fuller, M. D., Schellenberg, S. A., Stickley, C. E., & Williams, G. L. (2004). Cyclostratigraphy of middle and late Eocene sediments drilled on the East Tasman

I

Plateau (Site 1172). In Exon, N.F., Kennett, J.P., and Malone, M.J. (Eds.), The Cenozoic Southern Ocean: Tectonics, Sedimentation and Climate Change between Australia and Antarctica. Am. Geophys. Union, Geophys. Monogr., 151:127-151.

Röhl, U., Westerhold, T., Bralower, T. J., & Zachos, J. C. (2007). On the duration of the Paleocene- Eocene thermal maximum (PETM). *Geochemistry, Geophysics, Geosystems*, *8*(12).

Rohling, E. J. (1994). Review and new aspects concerning the formation of eastern Mediterranean sapropels. Marine Geology, 122(1-2), 1-28.

Rohling, E. J., & Hilgen, F.J. (1991). The eastern Mediterranean climate at times of sapropel formation: a review. *Geologie en Mijnbouw*, *70*, 253-264.

Rohling, E. J., Marino, G., & Grant, K. M. (2015). Mediterranean climate and oceanography, and the periodic development of anoxic events (sapropels). Earth – Science Reviews, 143, 62-97

Rosenberg, R. (1990). Negative oxygen trends in Swedish coastal bottom waters. *Marine Pollution Bulletin*, *21*(7), 335-339.

Rossignol-Strick, M. (1985). Mediterranean Quaternary sapropels, an immediate response of the African monsoon to variation of insolation. *Palaeogeography, palaeoclimatology, palaeoecology*, *49*(3-4), 237-263.

Roychoudhury, A. N., Kostka, J. E., & Van Cappellen, P. (2003). Pyritization: a palaeoenvironmental and redox proxy reevaluated. Estuarine, Coastal and Shelf Science, 57(5-6), 1183-1193.

Ruttenberg, K. C. (1993). Reassessment of the oceanic residence time of phosphorus. *Chemical Geology*, *107*(3-4), 405-409.

Ruttenberg, K. C. (2003). The global phosphorus cycle. *Treatise on geochemistry*, *8*, 682.

Ruttenberg, K. C., & Berner, R. A. (1993). Authigenic apatite formation and burial in sediments from non-upwelling, continental margin environments. Geochimica et cosmochimica acta, 57(5), 991-1007.

Ruttenberg, K. C., & Berner, R. A. (1993). Authigenic apatite formation and burial in sediments from non-upwelling, continental margin environments. Geochimica et cosmochimica acta, 57(5), 991-1007.

Ruttenberg, K. C., & Goni, M. A. (1997). Phosphorus distribution, C: N: P ratios, and δ13Coc in arctic, temperate, and tropical coastal sediments: tools for characterizing bulk sedimentary organic matter. Marine Geology, 139(1-4), 123-145.

Rütters, H., Sass, H., Cypionka, H., Rullkötter, J., 2002. Phospholipid analysis as a tool to study complex microbial communities in marine sediments. J. Microbiol. Methods 48, 149–160.

Ruvalcaba Baroni, I., Pohl, A., van Helmond, N. A., Papadomanolaki, N. M., Coe, A. L., Cohen, A. S., ... & Slomp, C. P. (2018). Ocean circulation in the Toarcian (Early Jurassic): A key control on deoxygenation and carbon burial on the European shelf. Paleoceanography and Paleoclimatology, 33(9), 994-1012.

Ruvalcaba Baroni, I., Topper, R. P. M., Van Helmond, N. A. G. M., Brinkhuis, H., & Slomp, C. P. (2014). Biogeochemistry of the North Atlantic during oceanic anoxic event 2: role of changes in ocean circulation and phosphorus input. Biogeosciences, 11(4), 977-993.

Sabine, C. L., & Feely, R. A. (2007). The oceanic sink for carbon dioxide. *Greenhouse gas sinks*, 31.

Sabine, C. L., Feely, R. A., Gruber, N., Key, R. M., Lee, K., Bullister, J. L., ... & Rios, A. F. (2004). The oceanic sink for anthropogenic CO2. *science*, *305*(5682), 367-371.

Sangiorgi, F., Dinelli, E., Maffioli, P., Capotondi, L., Giunta, S., Morigi, C., ... & Corselli, C. (2006). Geochemical and micropaleontological characterisation of a Mediterranean sapropel S5: a case study from core BAN89GC09 (south of Crete). Palaeogeography, Palaeoclimatology, Palaeoecology, 235(1-3), 192-207.

Sarmiento, J. L., & Gruber, N. (2006). *Ocean biogeochemical dynamics*. Princeton university press.

Sarmiento, J. L., Hughes, T. M., Stouffer, R. J., & Manabe, S. (1998). Simulated response of the ocean carbon cycle to anthropogenic climate warming. *Nature*, *393*(6682), 245-249.

Savrda, C. E., & Bottjer, D. J. (1991). Oxygen-related biofacies in marine strata: an overview and update. Geological Society, London, Special Publications, 58(1), 201-219.

Schimanke, S., Meier, H.E.M., Kjellström, E., Strandberg, G., Hordoir, R., 2012. The climate in the Baltic Sea region during the last millennium simulated with a regional climate model. Clim. Past 8 (5), 1419–1433.

Schlanger, S. O., & Jenkyns, H. C. (1976). Cretaceous oceanic anoxic events: causes and consequences. *Geologie en Mijnbouw*, *55*(3-4), 179-184.

Schmidtko, S., Stramma, L., & Visbeck, M. (2017). Decline in global oceanic oxygen content during the past five decades. *Nature*, *542*(7641), 335-339.

Schmitz, B., & Pujalte, V. (2007). Abrupt increase in seasonal extreme precipitation at the Paleocene-Eocene boundary. Geology, 35(3), 215-218.

I

Schmitz, B., Asaro, F., Molina, E., Monechi, S., von Salis, K., & Speijer, R. P. (1997b). High-resolution iridium, δ13C, δ18O, foraminifera and nannofossil profiles across the latest Paleocene benthic extinction event at Zumaya, Spain. Palaeogeography, Palaeoclimatology, Palaeoecology, 133(1-2), 49-68.

Schmitz, B., Charisi, S. D., Thompson, E. I., & Speijer, R. P. (1997a). Barium, SiO2 (excess), and P2O5 as proxies of biological productivity in the Middle East during the Palaeocene and the latest Palaeocene benthic extinction event. Terra Nova, 9(2), 95-99.

Schneider, L. J., Bralower, T. J., Kump, L. R., & Patzkowsky, M. E. (2013). Calcareous nannoplankton ecology and community change across the Paleocene-Eocene Thermal Maximum. Paleobiology, 39(4), 628-647.

Schobben, M., Foster, W. J., Sleveland, A. R., Zuchuat, V., Svensen, H. H., Planke, S., ... & Poulton, S. W. (2020). A nutrient control on marine anoxia during the end-Permian mass extinction. Nature Geoscience, 13(9), 640-646.

Schoon, P. L., Heilmann-Clausen, C., Schultz, B. P., Sinninghe Damsté, J. S., & Schouten, S. (2015). Warming and environmental changes in the eastern North Sea Basin during the Palaeocene–Eocene Thermal Maximum as revealed by biomarker lipids. Organic Geochemistry, 78, 79-88.

Schouten, S., Hopmans, E.C., Rosell-Melé, A., Pearson, A., Adam, P., Bauersachs, T., Bard, E., Bernasconi, S.M., Bianchi, T.S., Brocks, J.J., Carlson, L.T., Derenne, S., Selver, A.D., Dutta, K., Eglinton, T., Fosse, C., Galy, V., Grice, K., Hinrichs, K.U., Huang, Y., Huguet, A., Huguet, C., Hurley, S., Ingalls, A., Jia, G., Keely, B., Knappy, C., Kondo, M., Krishnan, S., Lincoln, S., Lipps, J., Mangelsdorf, K., Martínez-García, A., Ménot, G., Mets, A., Mollenhauer, G., Ossebaar, J., Pagani, M., Pancost, R.D., Pearson, E.J., Peterse, F., Reichart, G.J., Schaeffer, P., Schmitt, G., Schwark, L., Shah, S.R., Smith, R.W., Smittenberg, R.H., Summons, R.E., Takano, Y., Talbot, H.M., Taylor, K.W.R., Tarozo, R., Uchida, M., van Dongen, B.E., Van Mooy, B.A.S., Wang, J., Warren, C., Weijers, J.W.H., Werne, J.P., Woltering, M., Xie, S., Yamamoto, M., Yang, H., Zhang, C.L., Zhang, Y., Zhao, M., Sinninghe Damsté, J.S., 2013. An interlaboratory study of TEX86 and BIT analysis of sediments, extracts, and standard mixtures. Geochem. Geophys. Geosyst. 14, 1–23.

Schouten, S., Huguet, C., Hopmans, E.C., Kienhuis, M.V.M., Sinninghe Damsté, J.S., 2007. Analytical methodology for TEX86 paleothermometry by high-performance liquid chromatography/atmospheric pressure chemical ionization-mass spectrometry. Anal. Chem. 79, 2940–2944.

Schuffert, J. D., Kastner, M., Emanuele, G., & Jahnke, R. A. (1990). Carbonate-ion substitution in francolite: A new equation. Geochimica et Cosmochimica Acta, 54(8), 2323-2328.

Schulte, P., Schwark, L., Stassen, P., Kouwenhoven, T. J., Bornemann, A., & Speijer, R. P. (2013). Black shale formation during the Latest Danian Event and the Paleocene–Eocene

Thermal Maximum in central Egypt: Two of a kind?. Palaeogeography, Palaeoclimatology, Palaeoecology, 371, 9-25.

Scott, C., Lyons, T.W., 2012. Contrasting molybdenum cycling and isotopic properties in euxinic versus non-euxinic sediments and sedimentary rocks: refining the paleoproxies. Chem. Geol. 324, 19–27.

Self-Trail, J. M., Robinson, M. M., Bralower, T. J., Sessa, J. A., Hajek, E. A., Kump, L. R., ... & Wandless, G. A. (2017). Shallow marine response to global climate change during the Paleocene-Eocene Thermal Maximum, Salisbury Embayment, USA. Paleoceanography, 32(7), 710-728.

Seppä, H., Bjune, A.E., Telford, R.J., Birks, H.J.B., Veski, S., 2009. Last nine-thousand years of temperature variability in northern Europe. Clim. Past 5 (3), 523–535.

Sepúlveda, J., Wendler, J., Leider, A., Kuss, H. J., Summons, R. E., & Hinrichs, K. U. (2009). Molecular isotopic evidence of environmental and ecological changes across the Cenomanian–Turonian boundary in the Levant Platform of central Jordan. *Organic Geochemistry*, *40*(5), 553-568.

Seto, K., Nomura, R., and Niitsuma, N., 1991. Data report: oxygen and carbon isotope records of the upper Maestrichtian to lower Eocene benthic foraminifers at Site 752 in the eastern Indian Ocean. In Weissel, J., Peirce, J., Taylor, E., Alt, J., et al., Proc. ODP, Sci. Results, 121: College Station, TX (Ocean Drilling Program), 885–889.

Seton, M., Müller, R. D., Zahirovic, S., Gaina, C., Torsvik, T., Shephard, G., ... & Chandler, M. (2012). Global continental and ocean basin reconstructions since 200 Ma. Earth-Science Reviews, 113(3-4), 212-270.

Shao, C., Sui, Y., Tang, D., & Legendre, L. (2016). Spatial variability of surface-sediment porewater pH and related water-column characteristics in deep waters of the northern South China Sea. Progress in Oceanography, 149, 134-144.

Shcherbinina, E., Gavrilov, Y., Iakovleva, A., Pokrovsky, B., Golovanova, O., & Aleksandrova, G. (2016). Environmental dynamics during the Paleocene–Eocene thermal maximum (PETM) in the northeastern Peri-Tethys revealed by high-resolution micropalaeontological and geochemical studies of a Caucasian key section. Palaeogeography, Palaeoclimatology, Palaeoecology, 456, 60-81.

Shipboard Scientific Party (1985). Site 549. In Graciansky, P. C. de, Poag, C. W., et al., Init. Repts. DSDP, 80: Washington (U.S.Govt. Printing Office).

Shipboard Scientific Party (1989). Site 738. In Barron, J., Larsen, B., et al., Proc. ODP, Init. Repts., 119: College Station, TX (Ocean Drilling Program), 229–288.

I

Shipboard Scientific Party (2002). Site 1215. In Lyle, M.W., Wilson, P.A., Janecek, T.R., et al., Proc. ODP, Init. Repts., 199: College Station TX (Ocean Drilling Program), 1–87.

Shipboard Scientific Party (2004). Site 1260. In Erbacher, J., Mosher, D.C., Malone, M.J., et al., Proc. ODP, Init. Repts., 207: College Station, TX (Ocean Drilling Program), 1–113.

Shipboard Scientific Party, 1989. Site 752. In Peirce, J., Weissel, J., et al., Proc. ODP, Init. Repts., 121: College Station, TX (Ocean Drilling Program), 111–169.

Shipboard Scientific Party, 2001. Site 1172. In Exon, N.F., Kennett, J.P., Malone, M.J., et al., Proc. ODP, Init. Repts., 189: College Station TX (Ocean Drilling Program), 1–98.

Sildever, S., Andersen, T.J., Ribeiro, S., Ellegaard, M., 2015. Influence of surface water salinity gradient on dinoflagellate cyst community structure, abundance and morphology in the Baltic Sea, Kattegat and Skagerrak. Estuar. Coast. Shelf Sci. 155, 1–7.

Sinninghe Damsté, J. S., Kuypers, M. M., Pancost, R. D., & Schouten, S. (2008). The carbon isotopic response of algae,(cyano) bacteria, archaea and higher plants to the late Cenomanian perturbation of the global carbon cycle: Insights from biomarkers in black shales from the Cape Verde Basin (DSDP Site 367). *Organic Geochemistry*, *39*(12), 1703-1718.

Sinninghe Damsté, J. S., Kuypers, M. M., Pancost, R. D., & Schouten, S. (2008). The carbon isotopic response of algae,(cyano) bacteria, archaea and higher plants to the late Cenomanian perturbation of the global carbon cycle: Insights from biomarkers in black shales from the Cape Verde Basin (DSDP Site 367). *Organic Geochemistry*, 39(12), 1703-1718.

Sinninghe Damsté, J. S., van Bentum, E. C., Reichart, G. J., Pross, J., & Schouten, S. (2010). A CO2 decrease-driven cooling and increased latitudinal temperature gradient during the mid-Cretaceous Oceanic Anoxic Event 2. *Earth and Planetary Science Letters*, 293(1-2), 97-103.

Sinton, C. W., & Duncan, R. A. (1997). Potential links between ocean plateau volcanism and global ocean anoxia at the Cenomanian-Turonian boundary. *Economic Geology*, *92*(7-8), 836-842.

Slomp, C. P., & Cappellen, P. V. (2007). The global marine phosphorus cycle: sensitivity to oceanic circulation. *Biogeosciences*, *4*(2), 155-171.

Slomp, C. P., Epping, E. H., Helder, W., & Raaphorst, W. V. (1996). A key role for iron-bound phosphorus in authigenic apatite formation in North Atlantic continental platform sediments. Journal of marine Research, 54(6), 1179-1205.

Slomp, C. P., Thomson, J., & de Lange, G. J. (2002). Enhanced regeneration of phosphorus during formation of the most recent eastern Mediterranean sapropel (S1). *Geochimica et Cosmochimica Acta*, *66*(7), 1171-1184.

Slomp, C. P., Thomson, J., & de Lange, G. J. (2004). Controls on phosphorus regeneration and burial during formation of eastern Mediterranean sapropels. Marine Geology, 203(1-2), 141-159.

Sluijs, A., & Brinkhuis, H. (2009). A dynamic climate and ecosystem state during the Paleocene–Eocene Thermal Maximum: inferences from dinoflagellate cyst assemblages on the New Jersey shelf. Biogeosciences, 6, 1755-1781.

Sluijs, A., Brinkhuis, H., Crouch, E. M., John, C. M., Handley, L., Munsterman, D., ... & Pancost, R. D. (2008). Eustatic variations during the Paleocene-Eocene greenhouse world. Paleoceanography, 23(4).

Sluijs, A., Brinkhuis, H., Schouten, S., Bohaty, S. M., John, C. M., Zachos, J. C., ... & Dickens, G. R. (2007). Environmental precursors to rapid light carbon injection at the Palaeocene/ Eocene boundary. *Nature*, *450*(7173), 1218-1221.

Sluijs, A., Röhl, U., Schouten, S., Brumsack, H. J., Sangiorgi, F., Sinninghe Damsté, J. S., & Brinkhuis, H. (2008a). Arctic late Paleocene–early Eocene paleoenvironments with special emphasis on the Paleocene-Eocene thermal maximum (Lomonosov Ridge, Integrated Ocean Drilling Program Expedition 302). Paleoceanography, 23(1).

Sluijs, A., Schouten, S., Pagani, M., Woltering, M., Brinkhuis, H., Sinninghe Damsté, J. S., ... & Matthiessen, J. (2006). Subtropical Arctic Ocean temperatures during the Palaeocene/Eocene thermal maximum. Nature, 441(7093), 610-613.

Sluijs, A., van Roij, L., Harrington, G. J., Schouten, S., Sessa, J. A., LeVay, L. J., ... & Slomp, C. P. (2014). Warming, euxinia and sea level rise during the Paleocene-Eocene Thermal Maximum on the Gulf Coastal Plain: implications for ocean oxygenation and nutrient cycling. Climate of the Past, 10(4), 1421-1421.

Sohlenius, G., Emeis, K.C., Andrén, E., Andrén, T., Kohly, A., 2001. Development of anoxia during the Holocene fresh–brackish water transition in the Baltic Sea. Mar. Geol. 177 (3), 221–242.

Soliman, M. F. (2003). Chemostratigraphy of the Paleocene/Eocene (P/E) boundary sediments at Gabal el-Qreiya, Nile Valley, Egypt. Micropaleontology, 49(Suppl_1), 123-138.

Soliman, M. F., Aubry, M. P., Schmitz, B., & Sherrell, R. M. (2011). Enhanced coastal paleoproductivity and nutrient supply in Upper Egypt during the Paleocene/Eocene Thermal Maximum (PETM): Mineralogical and geochemical evidence. Palaeogeography, Palaeoclimatology, Palaeoecology, 310(3-4), 365-377.

Speijer, R. P., & Schmitz, B. (1998). A benthic foraminiferal record of Paleocene sea level and trophic/redox conditions at Gebel Aweina, Egypt. Palaeogeography, Palaeoclimatology, Palaeoecology, 137(1-2), 79-101.

I

Speijer, R. P., Schmitz, B., & van der Zwaan, G. J. (1997). Benthic foraminiferal extinction and repopulation in response to latest Paleocene Tethyan anoxia. Geology, 25(8), 683-686.

Speijer, R. P., Van der Zwaan, G. J., & Schmitz, B. (1996). The impact of Paleocene/Eocene boundary events on middle neritic benthic foraminiferal assemblages from Egypt. Marine Micropaleontology, 28(2), 99-132.

Speijer, R., & Wagner, T. (2002). Sea-level changes and black shales associated with the late Paleocene thermal maximum: Organic-geochemical and micropaleontologic evidence from the southern Tethyan margin (Egypt-Israel). Catastrophic events and mass extinctions: Impacts and beyond, 356, 533-549.

Speijer, R., Schmitz, B., Aubry, M. P., & Charisi, S. D. (1995). The latest Paleocene benthic extinction event: punctuated turnover in outer neritic benthic foraminiferal faunas from Gebel Aweina, Egypt. Israel Journal of Earth Sciences, 44(4), 207-222.

Stassen, P., Dupuis, C., Steurbaut, E., Yans, J., & Speijer, R. P. (2012). Perturbation of a Tethyan coastal environment during the Paleocene–Eocene thermal maximum in Tunisia (Sidi Nasseur and Wadi Mezaz). Palaeogeography, Palaeoclimatology, Palaeoecology, 317, 66-92.

Stassen, P., Thomas, E., & Speijer, R. P. (2012). Integrated stratigraphy of the Paleocene-Eocene thermal maximum in the New Jersey Coastal Plain: Toward understanding the effects of global warming in a shelf environment. Paleoceanography, 27(4).

Stassen, P., Thomas, E., & Speijer, R. P. (2015). Paleocene–Eocene Thermal Maximum environmental change in the New Jersey Coastal Plain: benthic foraminiferal biotic events. Marine Micropaleontology, 115, 1-23.

Steckbauer, A., Klein, S. G., & Duarte, C. M. (2020). Additive impacts of deoxygenation and acidification threaten marine biota. *Global change biology*, *26*(10), 5602-5612.

Steenbergh, A. K., Bodelier, P. L., Hoogveld, H. L., Slomp, C. P., & Laanbroek, H. J. (2011). Phosphatases relieve carbon limitation of microbial activity in Baltic Sea sediments along a redox-gradient. Limnology and Oceanography, 56(6), 2018-2026.

Stein, R., Boucsein, B., & Meyer, H. (2006). Anoxia and high primary production in the Paleogene central Arctic Ocean: First detailed records from Lomonosov Ridge. Geophysical Research Letters, 33(18).

Stigebrandt, A., & Gustafsson, B. G. (2003). Response of the Baltic Sea to climate change—theory and observations. *Journal of Sea Research*, *49*(4), 243-256.

Stoll, H. M., & Bains, S. (2003). Coccolith Sr/Ca records of productivity during the Paleocene-Eocene thermal maximum from the Weddell Sea. Paleoceanography, 18(2).

Stoll, H. M., Shimizu, N., Archer, D., & Ziveri, P. (2007). Coccolithophore productivity response to greenhouse event of the Paleocene–Eocene Thermal Maximum. Earth and Planetary Science Letters, 258(1-2), 192-206.

Stramma, L., Prince, E. D., Schmidtko, S., Luo, J., Hoolihan, J. P., Visbeck, M., ... & Körtzinger, A. (2012). Expansion of oxygen minimum zones may reduce available habitat for tropical pelagic fishes. *Nature Climate Change*, *2*(1), 33-37.

Stramma, L., Schmidtko, S., Levin, L. A., & Johnson, G. C. (2010). Ocean oxygen minima expansions and their biological impacts. *Deep Sea Research Part I: Oceanographic Research Papers*, *57*(4), 587-595.

Suan, G., Pittet, B., Bour, I., Mattioli, E., Duarte, L. V., & Mailliot, S. (2008). Duration of the Early Toarcian carbon isotope excursion deduced from spectral analysis: consequence for its possible causes. Earth and Planetary Science Letters, 267(3-4), 666-679.

Sullivan, D. L., Brandon, A. D., Eldrett, J., Bergman, S. C., Wright, S., & Minisini, D. (2020). High resolution osmium data record three distinct pulses of magmatic activity during cretaceous Oceanic Anoxic Event 2 (OAE-2). Geochimica et Cosmochimica Acta.

Sulpis, O., Boudreau, B. P., Mucci, A., Jenkins, C., Trossman, D. S., Arbic, B. K., & Key, R. M. (2018). Current CaCO3 dissolution at the seafloor caused by anthropogenic CO2. *Proceedings of the National Academy of Sciences*, *115*(46), 11700-11705.

Sundquist, E. T. (1991). Steady-and non-steady-state carbonate-silicate controls on atmospheric CO2. *Quaternary Science Reviews*, *10*(2-3), 283-296.

Svensen, H., Planke, S., Malthe-Sørenssen, A., Jamtveit, B., Myklebust, R., Eidem, T. R., & Rey, S. S. (2004). Release of methane from a volcanic basin as a mechanism for initial Eocene global warming. Nature, 429(6991), 542-545.

Sweere, T. C., Dickson, A. J., Jenkyns, H. C., Porcelli, D., Elrick, M., van den Boorn, S. H., & Henderson, G. M. (2018). Isotopic evidence for changes in the zinc cycle during Oceanic Anoxic Event 2 (Late Cretaceous). *Geology*, *46*(5), 463-466.

Takashima, R., Nishi, H., Huber, B. T., & Leckie, R. M. (2006). Greenhouse world and the Mesozoic ocean. *Oceanography*.

Takeda, K., & Kaiho, K. (2007). Faunal turnovers in central Pacific benthic foraminifera during the Paleocene–Eocene thermal maximum. Palaeogeography, Palaeoclimatology, Palaeoecology, 251(2), 175-197.

Techtmann, S. M., Fortney, J. L., Ayers, K. A., Joyner, D. C., Linley, T. D., Pfiffner, S. M., & Hazen, T. C. (2015). The unique chemistry of Eastern Mediterranean water masses selects for distinct microbial communities by depth. PLoS One, 10(3).

I

Thomas, D. J., Bralower, T. J., & Jones, C. E. (2003). Neodymium isotopic reconstruction of late Paleocene–early Eocene thermohaline circulation. Earth and Planetary Science Letters, 209(3-4), 309-322.

Thomas, D. J., Bralower, T. J., & Jones, C. E. (2003). Neodymium isotopic reconstruction of late Paleocene–

Evidence for the thermal dissociation of methane hydrate during the Paleocene-Eocene thermal maximum. Geology, 30(12), 1067-1070.

Thomas, E. (1989). Development of Cenozoic deep-sea benthic foraminiferal faunas in Antarctic waters. *Geological Society, London, Special Publications*, *47*(1), 283-296.

Thomas, E. (2007). Cenozoic mass extinctions in the deep sea: What perturbs the largest habitat on Earth?. *Special papers – Geological Society of America*, *424*, 1.

Thomas, E., & Shackleton, N. J. (1996). The Paleocene-Eocene benthic foraminiferal extinction and stable isotope anomalies. *Geological Society, London, Special Publications*, *101*(1), 401-441.

Torfstein, A., Winckler, G., & Tripati, A. (2010). Productivity feedback did not terminate the Paleocene-Eocene Thermal Maximum (PETM). Climate of the Past, 6(2), 265-272.

Trabucho Alexandre, J., Tuenter, E., Henstra, G. A., van der Zwan, K. J., van de Wal, R. S., Dijkstra, H. A., & de Boer, P. L. (2010). The mid-Cretaceous North Atlantic nutrient trap: black shales and OAEs. *Paleoceanography*, *25*(4).

Trecalli, A., Spangenberg, J., Adatte, T., Föllmi, K. B., & Parente, M. (2012). Carbonate platform evidence of ocean acidification at the onset of the early Toarcian oceanic anoxic event. *Earth and Planetary Science Letters*, *357*, 214-225.

Trecalli, A., Spangenberg, J., Adatte, T., Föllmi, K. B., & Parente, M. (2012). Carbonate platform evidence of ocean acidification at the onset of the early Toarcian oceanic anoxic event. Earth and Planetary Science Letters, 357, 214-225.

Tremolada, F., & Bralower, T. J. (2004). Nannofossil assemblage fluctuations during the Paleocene–Eocene thermal maximum at Sites 213 (Indian Ocean) and 401 (North Atlantic Ocean): palaeoceanographic implications. Marine Micropaleontology, 52(1-4), 107-116.

Tribovillard, N., Algeo, T. J., Lyons, T., & Riboulleau, A. (2006). Trace metals as paleoredox and paleoproductivity proxies: an update. *Chemical geology*, *232*(1-2), 12-32.

Tripati, A., & Elderfield, H. (2005). Deep-sea temperature and circulation changes at the Paleocene-Eocene thermal maximum. Science, 308(5730), 1894-1898.

Tsandev, I., & Slomp, C. P. (2009). Modeling phosphorus cycling and carbon burial during Cretaceous Oceanic Anoxic Events. *Earth and Planetary Science Letters*, *286*(1-2), 71-79.

Tsandev, I., Slomp, C. P., & Van Cappellen, P. (2008). Glacial-interglacial variations in marine phosphorus cycling: Implications for ocean productivity. Global Biogeochemical Cycles, 22(4).

Tsikos, H., Jenkyns, H. C., Walsworth-Bell, B., Petrizzo, M. R., Forster, A., Kolonic, S., Erba, E., Premoli Silva, I., Baas, M., Wagner, T., & Damsté, J. S. (2004). Carbon-isotope stratigraphy recorded by the Cenomanian–Turonian Oceanic Anoxic Event: correlation and implications based on three key localities. *Journal of the Geological Society*, *161*(4), 711-719.

Turgeon, S. C., & Creaser, R. A. (2008). Cretaceous oceanic anoxic event 2 triggered by a massive magmatic episode. *Nature*, *454*(7202), 323-326.

Tyrrell, T. (1999). The relative influences of nitrogen and phosphorus on oceanic primary production. Nature, 400(6744), 525-531.

Ullmann, C. V., Boyle, R., Duarte, L. V., Hesselbo, S. P., Kasemann, S. A., Klein, T., ... & Aberhan, M. (2020). Warm afterglow from the Toarcian Oceanic Anoxic Event drives the success of deep-adapted brachiopods. Scientific reports, 10(1), 1-11.

Urey, H.C., (1952). On the early chemical history of the Earth and the origin of life. *Proceedings of the National Academy of Sciences of the United States of America,* 38, 351–363.

van Bentum, E. C., Hetzel, A., Brumsack, H. J., Forster, A., Reichart, G. J., & Sinninghe Damsté, J. S. (2009). Reconstruction of water column anoxia in the equatorial Atlantic during the Cenomanian–Turonian oceanic anoxic event using biomarker and trace metal proxies. Palaeogeography, Palaeoclimatology, Palaeoecology, 280(3-4), 489-498.

Van Cappellen, P., & Berner, R. A. (1991). Fluorapatite crystal growth from modified seawater solutions. Geochimica et Cosmochimica Acta, 55(5), 1219-1234.

Van Cappellen, P., & Ingall, E. D. (1994). Benthic phosphorus regeneration, net primary production, and ocean anoxia: A model of the coupled marine biogeochemical cycles of carbon and phosphorus. *Paleoceanography*, *9*(5), 677-692.

Van Cappellen, P., & Ingall, E. D. (1996). Redox stabilization of the atmosphere and oceans by phosphorus-limited marine productivity. Science, 271(5248), 493-496.

van Helmond, N. A. G. M., Ruvalcaba Baroni, I., Sluijs, A., Sinninghe Damsté, J. S., & Slomp, C. P. (2014). Spatial extent and degree of oxygen depletion in the deep proto-North Atlantic basin during Oceanic Anoxic Event 2. *Geochemistry, Geophysics, Geosystems*, *15*(11), 4254-4266.

I

van Helmond, N. A. G. M., Sluijs, A., Reichart, G. J., Sinninghe Damsté, J. S., Slomp, C. P., & Brinkhuis, H. (2014). A perturbed hydrological cycle during Oceanic Anoxic Event 2. *Geology*, *42*(2), 123-126.

Van Helmond, N. A. G. M., Sluijs, A., Sinninghe Damsté, J. S., Reichart, G. J., Voigt, S., Erbacher, J., ... & Brinkhuis, H. (2015). Freshwater discharge controlled deposition of Cenomanian–Turonian black shales on the NW European epicontinental shelf (Wunstorf, northern Germany). *Climate of the Past*, *11*(3), 495-508.

van Helmond, N. A., Ruvalcaba Baroni, I., Sluijs, A., Sinninghe Damsté, J. S., & Slomp, C. P. (2014). Spatial extent and degree of oxygen depletion in the deep proto-N orth A tlantic basin during Oceanic Anoxic vent 2. Geochemistry, Geophysics, Geosystems, 15(11), 4254-4266.

van Helmond, N. A., Sluijs, A., Sinninghe Damsté, J. S., Reichart, G. J., Voigt, S., Erbacher, J., ... & Brinkhuis, H. (2015). Freshwater discharge controlled deposition of Cenomanian–Turonian black shales on the NW European epicontinental shelf (Wunstorf, northern Germany). Climate of the Past, 11, 495-508.

Van Santvoort, P. J. M., De Lange, G. J., Thomson, J., Colley, S., Meysman, F. J. R., & Slomp, C. P. (2002). Oxidation and origin of organic matter in surficial Eastern Mediterranean hemipelagic sediments. Aquatic Geochemistry, 8(3), 153-175.

Voigt, S., Erbacher, J., Mutterlose, J., Weiss, W., Westerhold, T., Wiese, F., Wilmsen, M., & Wonik, T. (2008). The Cenomanian-Turonian of the Wunstorf section-(North Germany): global stratigraphic reference section and new orbital time scale for Oceanic Anoxic Event 2. *Newsletters in Stratigraphy*, 43(1), 65.

Voigt, S., Gale, A. S., & Flögel, S. (2004). Midlatitude shelf seas in the Cenomanian-Turonian greenhouse world: Temperature evolution and North Atlantic circulation. *Paleoceanography*, *19*(4).

Von Strandmann, P. A. P., Jenkyns, H. C., & Woodfine, R. G. (2013). Lithium isotope evidence for enhanced weathering during Oceanic Anoxic Event 2. *Nature Geoscience*, *6*(8), 668-672.

Walker, J. C., & Kasting, J. F. (1992). Effects of fuel and forest conservation on future levels of atmospheric carbon dioxide. Global and planetary change, 5(3), 151-189.

Wallmann, K. (2003). Feedbacks between oceanic redox states and marine productivity: A model perspective focused on benthic phosphorus cycling. *Global biogeochemical cycles*, *17*(3).

Walsh, J. J., Rowe, G. T., Iverson, R. L., & McRoy, C. P. (1981). Biological export of shelf carbon is a sink of the global CO_2 cycle. *Nature*, *291*(5812), 196-201.

Wanner, H., Beer, J., Bütikofer, J., Crowley, T. J., Cubasch, U., Flückiger, J., ... & Widmann, M. (2008). Mid-to Late Holocene climate change: an overview. *Quaternary Science Reviews*, *27*(19-20), 1791-1828.

Warnock, J.P., Bauersachs, T., Kotthoff, U., Brandt, H.T., Andrén, E., 2017. Holocene environmental history of the Ångermanälven Estuary, northern Baltic Sea. Boreas. http://dx.doi.org/10.1111/bor.12281.

Wasmund, N., 1997. Occurrence of cyanobacterial blooms in the Baltic Sea in relation to environmental conditions. Int. Rev. Hydrobiol. Hydrogr. 82 (2), 169–184.

Weijers, J.W., Schouten, S., Spaargaren, O.C., Sinninghe Damsté, J.S., 2006. Occurrence and distribution of tetraether membrane lipids in soils: implications for the use of the TEX86 proxy and the BIT index. Org. Geochem. 37 (12), 1680–1693.

Weiss, R. F. (1970). The solubility of nitrogen, oxygen and argon in water and seawater. In Deep sea research and oceanographic abstracts, 17(4),721-735.

Westman, P., Borgendahl, J., Bianchi, T.S., Chen, N., 2003. Probable causes for cyanobacterial expansion in the Baltic Sea: role of anoxia and phosphorus retention. Estuaries 26 (3), 680–689.

Wilkin, R. T., Arthur, M. A., & Dean, W. E. (1997). History of water-column anoxia in the Black Sea indicated by pyrite framboid size distributions. *Earth and Planetary Science Letters*, *148*(3-4), 517-525.

Willumsen, P.I., Filipsson, H.L., Reinholdsson, M., Lenz, C., 2013. Surface salinity and nutrient variations during the Littorina stage in the Fårö deep, Baltic Sea. Boreas 42 (1), 210–223.

Wing, S. L., Harrington, G. J., Smith, F. A., Bloch, J. I., Boyer, D. M., & Freeman, K. H. (2005). Transient floral change and rapid global warming at the Paleocene-Eocene boundary. *Science*, *310*(5750), 993-996.

Winnick, M. J., & Maher, K. (2018). Relationships between CO2, thermodynamic limits on silicate weathering, and the strength of the silicate weathering feedback. *Earth and Planetary Science Letters*, *485*, 111-120.

Wolthers, M. (2020). Personal observations.

Wood, G.D., Gabriel, A.M., Lawson, J.C., 1996. Palynological techniques—processing and microscopy. Palynol. Princ. Appl. 1, 29–50.

Yao, W., Paytan, A., & Wortmann, U. G. (2018). Large-scale ocean deoxygenation during the Paleocene-Eocene Thermal Maximum. *Science*, *361*(6404), 804-806.

I

Zachos, J. C., Dickens, G. R., & Zeebe, R. E. (2008). An early Cenozoic perspective on greenhouse warming and carbon-cycle dynamics. Nature, 451(7176), 279-283.

Zachos, J. C., Röhl, U., Schellenberg, S. A., Sluijs, A., Hodell, D. A., Kelly, D. C., ... & Kroon, D. (2005). Rapid acidification of the ocean during the Paleocene-Eocene thermal maximum. *Science*, *308*(5728), 1611-1615.

Zeebe, R. E. (2012). LOSCAR: Long-term ocean-atmosphere-sediment carbon cycle reservoir model v2. 0.4. *Geoscientific Model Development*, *5*(1), 149-166.

Zeebe, R. E. (2013). What caused the long duration of the Paleocene-Eocene Thermal Maximum?. Paleoceanography, 28(3), 440-452.

Zeebe, R. E., & Lourens, L. J. (2019). Solar System chaos and the Paleocene–Eocene boundary age constrained by geology and astronomy. *Science*, *365*(6456), 926-929.

Zeebe, R. E., & Tyrrell, T. (2019). History of carbonate ion concentration over the last 100 million years II: Revised calculations and new data. Geochimica et Cosmochimica Acta, 257, 373-392.

Zeebe, R. E., & Zachos, J. C. (2007). Reversed deep-sea carbonate ion basin gradient during Paleocene-Eocene thermal maximum. Paleoceanography, 22(3).

Zeebe, R. E., Ridgwell, A., & Zachos, J. C. (2016). Anthropogenic carbon release rate unprecedented during the past 66 million years. *Nature Geoscience*, *9*(4), 325-329.

Zeebe, R. E., Zachos, J. C., & Dickens, G. R. (2009). Carbon dioxide forcing alone insufficient to explain Palaeocene–Eocene Thermal Maximum warming. *Nature Geoscience*, *2*(8), 576-580.

Zhao, M., Zhang, S., Tarhan, L. G., Reinhard, C. T., & Planavsky, N. (2020). The role of calcium in regulating marine phosphorus burial and atmospheric oxygenation. Nature communications, 11(1), 1-8.

Zheng, X. Y., Jenkyns, H. C., Gale, A. S., Ward, D. J., & Henderson, G. M. (2013). Changing ocean circulation and hydrothermal inputs during Ocean Anoxic Event 2 (Cenomanian–Turonian): evidence from Nd-isotopes in the European shelf sea. *Earth and Planetary Science Letters*, *375*, 338-348.

Zheng, X. Y., Jenkyns, H. C., Gale, A. S., Ward, D. J., & Henderson, G. M. (2016). A climatic control on reorganization of ocean circulation during the mid-Cenomanian event and Cenomanian-Turonian oceanic anoxic event (OAE 2): Nd isotope evidence. *Geology*, *44*(2), 151-154.

Zillén, L., Conley, D. J., Andrén, T., Andrén, E., & Björck, S. (2008). Past occurrences of hypoxia in the Baltic Sea and the role of climate variability, environmental change and human impact. *Earth-Science Reviews*, *91*(1-4), 77-92.

Zillén, L., Conley, D.J., 2010. Hypoxia and cyanobacteria blooms-are they really natural features of the late Holocene history of the Baltic Sea? Biogeosciences 7 (8), 2567–2580.

Zillén, L., Conley, D.J., Andrén, T., Andrén, E., Björck, S., 2008. Past occurrences of hypoxia in the Baltic Sea and the role of climate variability, environmental change and human impact. Earth Sci. Rev. 91 (1–4).

Zonneveld, K. A., Marret, F., Versteegh, G. J., Bogus, K., Bonnet, S., Bouimetarhan, I., ... & Young, M. (2013). Atlas of modern dinoflagellate cyst distribution based on 2405 data points. *Review of Palaeobotany and Palynology*, *191*, 1-197.

Zonneveld, K.A.F., Marret, F., Versteegh, G.J.M., Bogus, K., Bonnet, S., Bouimetarhan, I., Crouch, E., de Vernal, A., Elshanawany, R., Edwards, L., Esper, O., Forke, S., Grøsfjeld, K., Henry, M., Holzwarth, U., Kielt, J.F., Kim, S.Y., Ladouceur, S., Ledu, D., Chen, L., Limoges, A., Londeix, L., Lu, S.H., Mahmoud, M.S., Marino, G., Matsouka, K., Matthiessen, J., Mildenhal, D.C., Mudie, P., Neil, H.L., Pospelova, V., Qi, Y., Radi, T., Richerol, T., Rochon, A., Sangiorgi, F., Solignac, S., Turon, J.L., Verleye, T., Wang, Y., Wang, Z., Young, M., 2013. Atlas of modern dinoflagellate cyst distribution based on 2405 data points. Rev. Palaeobot. Palynol. 191, 1–197.

Zwiep, K. L., Hennekam, R., Donders, T. H., Van Helmond, N. A., De Lange, G. J., & Sangiorgi, F. (2018). Marine productivity, water column processes and seafloor anoxia in relation to Nile discharge during sapropels S1 and S3. Quaternary Science Reviews, 200, 178-190.

I

Happiness can be foundn even in the darkest of places,
if one only remembers to turn on the light.
J.K. Rowling – Harry Potter and the Prisoner of Azkaban
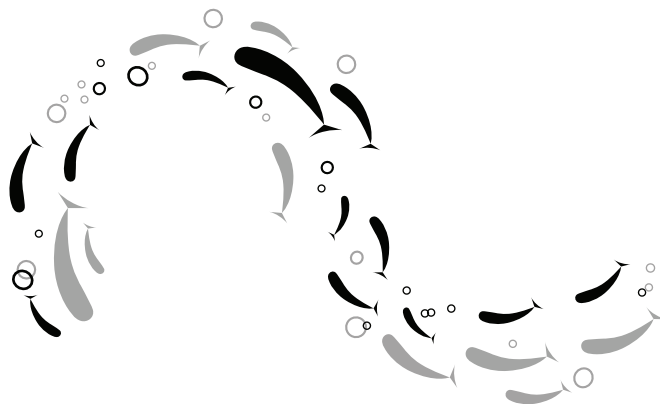
Appendix II: Samenvatting in het Nederlands

1. ACHTERGROND

Onze planeet bestaat voor meer dan 70% uit zeeën en oceanen. Deze spelen een belangrijke rol in de cycli van verscheidene chemische elementen. Drie van deze elementen, koolstof, zuurstof en fosfor, zijn essentiële bouwstenen voor het leven op aarde. Zuurstof is ook noodzakelijk voor de ademhaling van de meeste meercellige organismen. Deze drie elementen worden aan het oceaanoppervlak gebruikt voor fotosynthese, wat resulteert in de productie van organisch materiaal. Hierbij wordt koolstofdioxide (CO_2), een broeikasgas, opgenomen en omgezet naar organische vormen van koolstof. Het merendeel van het organische materiaal wordt in de diepe oceaan afgebroken, via een proces dat zuurstof verbruikt. Een klein percentage wordt afgezet op de oceaanbodem en uiteindelijk begraven in diepere sedimentlagen. Daar kan het voor miljoenen jaren bewaard blijven, zodat de opgenomen CO_2 niet terug kan keren naar de atmosfeer. Hierdoor is de begraving van organisch koolstof een proces dat de levensduur van CO_2 in de atmosfeer kan beïnvloeden. Ons kwantitatief begrip van organisch koolstof begraving bepaalt dan ook mede hoe accuraat de lange termijn projecties van de effecten van CO_2 uitstoot door de mens en de daardoor aangedreven klimaatverandering zullen zijn.

De begraving van organisch koolstof kan op twee manieren gestimuleerd worden: door verhoogde productie of verminderde afbraak. De hoeveelheid organisch koolstof die geproduceerd wordt is sterk afhankelijk van de beschikbaarheid van fosfor, een belangrijke voedingsstof die voornamelijk in de vorm van fosfaat door rivieren aangeleverd wordt. Hoge fosfaatconcentraties stimuleren fotosynthese zodat meer organisch koolstof geproduceerd en begraven kan worden. Tegelijkertijd neemt de consumptie van zuurstof door de afbraak van organisch koolstof toe. We spreken in zo'n geval van eutrofiëring. Ook klimaatverandering kan mariene zuurstofconcentraties negatief beïnvloeden. De atmosfeer is de belangrijkste bron van zuurstof voor de oceaan, maar bij hogere temperaturen lost zuurstof minder goed op in oppervlaktewateren. Zo neemt de toevoer van zuurstof naar de oceaan af. Hoge temperaturen en lage zoutgehaltes, die veroorzaakt kunnen worden door het smelten van ijskappen en toegenomen neerslag, verlagen de dichtheid van het oppervlaktewater en veroorzaken een sterke gelaagdheid (stratificatie). Stratificatie belemmert de menging van oppervlaktewateren met de diepe oceaan en zo ook de toevoer van zuurstof naar de diepe oceaanlagen. Als zuurstofarme of zuurstofloze condities ontstaan, neemt de efficiëntie van organisch koolstof afbraak af en de begraving toe. De begraving van fosfaat neemt dan juist af zodat concentraties van fosfaat in oppervlaktewateren langer verhoogd blijven. Zo ontstaat er een positieve, zelfversterkende kringloop (positieve feedback) waarbij de toename in fosfaat zuurstofloosheid, organisch koolstof begraving en een verdere toename in fosfaat veroorzaakt. Toenemende eutrofiëring heeft sinds de jaren zestig geleid tot een exponentiele stijging in het oppervlak van zuurstofarme wateren langs de kusten (Diaz en Rosenberg, 2008). In de open oceaan zijn zuurstofconcentraties de afgelopen 50 jaar met ~2% afgenomen (Schmidtko *et al*., 2017) en zijn zones van zuurstofschaarste sterk uitgebreid (Stramma *et al*., 2012). De huidige zuurstofafname in de oceanen zal naar verwachting doorzetten, tenzij de uitstoot van broeikasgassen en de lozing van nutriënten aanzienlijk worden verminderd (bijv. Breitburg *et al*., 2018).

De huidige uitstoot van broeikasgassen is zonder precedent in de laatste 66 miljoen jaar (Myr) en dit verschuift het klimaatsysteem naar een toestand die voor de mensheid ongekend is (bijv. IPCC, 2013; Zeebe *et al.*, 2016). Om de impact van verstoringen in de mondiale koolstofcyclus op het klimaat en de mariene biogeochemie te beoordelen, worden tijdperken uit het geologische verleden die soortgelijke veranderingen ondergingen bestudeerd (bijv. Burke *et al.*, 2018). Voor dit proefschrift zijn meerdere tijdperken van belang, voornamelijk het Holocene Temperatuurs Maximum (HTM), het Middeleeuwse klimaatoptimum (MCA), het Paleoceen-Eoceen Temperatuurs Maximum (PETM) en het Cenomaan-Turoons Oceanic Anoxic Event 2 (OAE2).

De primaire methoden binnen het onderzoek naar klimaat- en oceaansveranderingen uit het verleden zijn de chemische analyse van sedimentarchieven en simulaties door biogeochemische computermodellen. De chemische eigenschappen van mineralen en de fossiele resten van organismen die bewaard gebleven zijn in mariene sedimenten kunnen gebruikt worden om veranderingen in het klimaat en de biogeochemie van de oceaan te reconstrueren (proxy). Zo kunnen de fossiele resten van algen en diverse moleculen die zij produceren worden gebruikt als proxy voor de temperatuur en saliniteit van de waterkolom. Koolstofisotopen functioneren als proxy voor veranderingen in de koolstofcyclus en de concentraties van spoormetalen volgen de verspreiding van zuurstofloosheid. Vervolgens worden oceaanmodellen gebruikt om de locatie-gebonden informatie uit sedimentarchieven samen te voegen tot een mondiaal beeld en zo de staat van het klimaat en de oceaan te reconstrueren.

2. SAMENVATTING

In dit proefschrift geef ik een kwalitatieve en kwantitatieve beschrijving van de drijvende krachten achter zuurstofafname in zeewater en de gevolgen van die zuurstofloosheid voor de begraving van organisch koolstof. De belangrijkste onderwerpen die aan de orde komen zijn de oorzaken van zuurstofloosheid op lokale (**Hoofdstuk 2**) en mondiale (**Hoofdstuk 4**) schaal, de invloed van mineraalvorming op de begraving van fosfor onder zuurstofloze condities (**Hoofdstuk 3**) en de mondiale impact van het vrijkomen van fosfaat uit zuurstofloze sedimenten (**Hoofdstukken 3 – 5**), en het effect van zuurstof-afhankelijke organisch koolstof begraving op de mondiale koolstofcyclus (**Hoofdstukken 4 en 5**).

HOOFDSTUK 2 onderzoekt het ontstaan van zuurstofloosheid in de Oostzee tijdens twee afzonderlijke tijdperken van klimaatverandering in de laatste 10.000 jaar: het HTM en de MCA. Het HTM vond plaats aan het einde van het laatste glaciaal, toen het smelten van de ijskappen zeespiegelstijging veroorzaakte waarna zoutwater uit de Noordzee de Oostzee binnenstroomde, destijds nog een zoetwater meer. Mijn onderzoek naar de morfologie en soortensamenstelling van fossiele algenresten, en veranderingen in de spoormetaalsamenstelling van sedimenten uit het diepste punt van de Oostzee toont aan dat een hoger zoutgehalte stratificatie veroorzaakte en zo de toevoer van zuurstof naar het diepe bekken verhinderde. Het herstel van de zuurstofconcentraties aan het einde van de HTM, en de verspreiding en terugtrekking van de zuurstofloosheid tijdens de MCA werden vooral teweeggebracht door temperatuur gedreven stratificatie en een variërende toevoer van voedingsstoffen. Tegenwoordig worden de zuurstofconcentraties in de Oostzee vooral bepaald

II

door de beschikbaarheid van voedingstoffen uit meststoffen, maar de resultaten van dit onderzoek laten zien dat klimaatverandering een grote invloed kan hebben op de uitbreiding van zuurstofloze gebieden in de Oostzee en andere kustzeeën.

In **HOOFDSTUK 3** wordt onderzocht waarom de begraving van fosfaat in organisch-rijke mariene sedimenten in zuurstofloze gebieden in het verleden veel beperkter was dan in de moderne oceaan. Tijdens perioden met lage zuurstofconcentraties in zee zoals OAE2 zijn de waarden van de proxy voor fosfaat begraving tot meer dan een factor vier hoger dan de moderne waarden, wat wijst op verminderd behoud van fosfaat in de oceaanbodem. De gebruikelijke verklaring stelt dat zuurstofloosheid en de aanwezigheid van sulfide dit grote verschil veroorzaakten. Deze verklaring is echter onvoldoende, omdat zuurstofloze bekkens in de moderne oceaan een groot scala aan biogeochemische karakteristieken omvatten, inclusief zeer hoge concentraties van sulfide. Uit onze berekeningen blijkt dat de vorming van het mineraal carbonaat fluorapatiet, de belangrijkste lange-termijn opslagvorm van fosfaat in mariene sedimenten, sterk vermindert onder hoge temperaturen, verzuring van de oceaan en bij een tekort aan calciumcarbonaat. Dit zijn eigenschappen die kenmerkend zijn voor de tijdvakken van zuurstofafname waarin de fosfaatbegraving verminderd was. Hierdoor ontstond er een situatie waarin de toevoer van fosfaat via rivieren toenam en niet werd bijgehouden door afzetting op de oceaanbodem, waardoor hogere concentraties van fosfaat in de oceaan eutrofiëring, zuurstofloosheid en organisch koolstof begraving bevorderden. De huidige opwarming van de aarde en oceaan verzuring zouden dan ook mogelijk kunnen bijdragen aan mondiale zuurstofafname via een soortgelijk mechanisme.

HOOFDSTUK 4 bestudeert de primaire productiviteit en zuurstofloosheid in de oceaan tijdens het PETM, hoe die varieerde in de ruimte en tijd, en de gevolgen daarvan voor organisch koolstof begraving. Het PETM was een tijdperk van sterke klimaatverandering, ongeveer 56 miljoen jaar geleden, en wordt gezien als een analoog voor de hedendaagse opwarming van de aarde. In dit hoofdstuk wordt met behulp van nieuwe chemische sedimentgegevens en een datacompilatie aangetoond dat productieve en zuurstofloze omstandigheden wijdverspreid waren en zich vooral voordeden op het continentale plat en in ingeperkte bekkens. In dezelfde regio's komt men sedimenten tegen die rijk zijn in organisch koolstof. Door de beschikbare data te combineren met modellen voor de koolstofcyclus in de oceaan toon ik aan dat de aanmaak van organisch materiaal en de begraving daarvan zodanig toenam dat het leidde tot onttrekking van CO_2 uit de atmosfeer. De gemodelleerde effecten van begraving van organisch koolstof op atmosferisch CO_2 en de mondiale koolstofisotopen balans bakenen de uitstoot van CO_2 en/of methaan tijdens het PETM verder af.

HOOFDSTUK 5 verdiept zich in één van de belangrijkste perioden van zuurstofloosheid in de oceaan uit de geologische geschiedenis. OAE2 vond circa 94 miljoen jaar geleden plaats en was hoogstwaarschijnlijk het gevolg van vulkanische CO_2 uitstoot. De toename in temperatuur, veranderingen in neerslagpatronen en verwering van fosfaathoudende gesteenten zouden de waargenomen zuurstofloosheid en de afzetting van organisch koolstof-rijke sedimenten veroorzaakt hebben. In dit hoofdstuk presenteer ik het eerste kwantitatieve scenario voor CO_2 uitstoot via vulkanisme en organisch koolstof begraving tijdens OAE2. De resultaten van het daarbij gebruikte koolstofcyclusmodel tonen aan dat de CO_2 uitstoot door vulkanisme tijdens OAE2 variabel was en dat de invloed van organisch koolstof begraving op

atmosferisch CO_2 en andere koolstofcyclus componenten sterk afhankelijk was van de trend in CO_2 uitstoot.

II

Δεν μπορεί τέλος πάντων ο άνθρωπος να κάμει κάτι και χωρίς γιατί;
Έτσι, για το κέφι του.
Νίκος Καζαντζάκης – Βίος και πολιτεία του Α. Ζορμπά

III
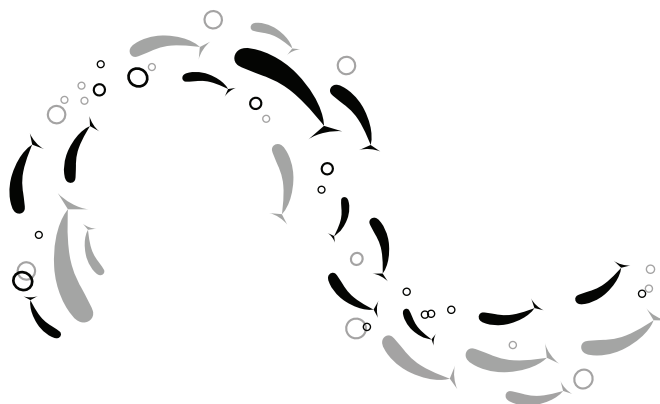
Appendix III: Περίληψη στα ελληνικά

1. ΙΣΤΟΡΙΚΌ

Οι θάλασσες και οι ωκεανοί καλύπτουν περισσότερο από το 70% του πλανήτη μας και διαδραματίζουν σημαντικό ρόλο στους κύκλους πολλών χημικών στοιχείων. Τρία από αυτά τα στοιχεία, ο άνθρακας, το οξυγόνο και ο φώσφορος, είναι βασικά δομικά στοιχεία για τη ζωή στη Γη. Το οξυγόνο είναι επίσης απαραίτητο για την αναπνοή των περισσότερων πολυκύτταρων οργανισμών. Τα τρία αυτά στοιχεία χρησιμοποιούνται στην επιφάνεια του ωκεανού για τη φωτοσύνθεση, που έχει ως αποτέλεσμα την παραγωγή οργανικού υλικού. Η διαδικασία αυτή απορροφά διοξείδιο του άνθρακα (CO_2), ένα αέριο του θερμοκηπίου, και το μετατρέπει σε οργανικές μορφές άνθρακα. Το μεγαλύτερο μέρος της οργανικής ύλης διασπάται στα βάθη του ωκεανού, μέσω μιας διαδικασίας που καταναλώνει οξυγόνο. Ένα μικρό ποσοστό εναποτίθεται στον πυθμένα του ωκεανού και θάβεται τελικά σε βαθύτερα στρώματα ιζημάτων. Εκεί μπορεί να διατηρηθεί για εκατομμύρια χρόνια, εμποδίζοντας την επιστροφή του απορροφημένου CO_2 στην ατμόσφαιρα. Με αυτόν τον τρόπο η ταφή του οργανικού άνθρακα επηρεάζει τη διάρκεια παραμονής του CO_2, συμπεριλαμβανομένου όσου εκπέμπουν οι ανθρώπινες δραστηριότητες, στην ατμόσφαιρα. Επομένως, η ποσοτική έρευνα της ταφής του οργανικού άνθρακα συμβάλλει στον καθορισμό της ακρίβειας των προγνόσεων για τη μελλοντική εξέλιξη της ανθρωπογενούς κλιματικής αλλαγής.

Η ταφή του οργανικού άνθρακα μπορεί να προωθηθεί με δύο τρόπους: μέσω αυξημένης παραγωγής ή μειωμένης αποδόμησης. Η ποσότητα οργανικού άνθρακα που θα παραχθεί εξαρτάται σε μεγάλο βαθμό από τη διαθεσιμότητα φωσφόρου, ενός σημαντικού θρεπτικού συστατικού που παρέχεται κυρίως σε μορφή φωσφορικού ιόντος από την εκροή ποταμών. Η υψηλές συγκεντρώσεις φωσφορικού ιόντος προκαλούν αυξημένη φωτοσύνθεση έτσι ώστε να μπορεί να παραχθεί και να ταφεί μεγαλύτερη ποσότητα οργανικού άνθρακα. Παράλληλα, αυξάνεται η κατανάλωση οξυγόνου μέσω της διάσπασης του οργανικού άνθρακα και προκαλείται ευτροφισμός. Οι θαλάσσιες συγκεντρώσεις οξυγόνου μπορούν να επηρεαστούν αρνητικά και από την κλιματική αλλαγή. Η ατμόσφαιρα είναι η κύρια πηγή οξυγόνου για τον ωκεανό, αλλά σε υψηλότερες θερμοκρασίες το οξυγόνο διαλύεται λιγότερο εύκολα στα επιφανειακά ύδατα. Έτσι μειώνεται η παροχή οξυγόνου στον ωκεανό. Η υψηλές θερμοκρασίες και η χαμηλή αλμυρότητα, που δημιουργείται λόγω του λιώσιμου παγετώνων και της αυξημένης βροχόπτωσης, στην επιφάνεια της θάλασσας χαμηλώνουν την πυκνότητα της και προκαλούν ισχυρή στρωματοποίηση. Η στρωματοποίηση εμποδίζει την ανάμιξη των επιφανειακών υδάτων με τα βαθιά νερά και, συνεπώς, μειώνει την παροχή οξυγόνου στις βαθύτερες στρώσεις του ωκεανού. Σε συνθήκες χαμηλού, ή και έλλειψης, οξυγόνου, η διάσπαση του οργανικού άνθρακα γίνεται λιγότερο αποτελεσματικά και η ταφή περισσότερο. Αντιθέτως, η ταφή του φωσφορικού ιόντος μειώνεται σε τέτοιες καταστάσεις έτσι ώστε οι συγκεντρώσεις του στην επιφάνεια του ωκεανού να παραμένουν αυξημένες. Με αυτόν τον τρόπο η αυξημένη διαθεσιμότητα φωσφορικού ιόντος προωθεί την αποξυγόνωση, την ταφή οργανικού άνθρακα και την περαιτέρω αύξηση φωσφορικού ιόντος μέσω ενός θετικού αυτοενισχυόμενου κύκλου (θετική ανατροφοδότηση). Ο αυξανόμενος ευτροφισμός έχει οδηγήσει σε εκθετική αύξηση της έκτασης των υδάτων με χαμηλή περιεκτικότητα σε οξυγόνο κατά μήκος των ακτών από τη δεκαετία του 1960 (Diaz and Rosenberg, 2008). Στον ανοικτό ωκεανό, οι συγκεντρώσεις οξυγόνου έχουν μειωθεί κατά ~2% τα τελευταία 50 χρόνια (Schmidtko *et al.*, 2017) και φυσικά εμφανιζόμενες ζώνες ελάχιστου οξυγόνου έχουν επεκταθεί σημαντικά (Stramma *et al.*, 2012). Η σημερινή μείωση του οξυγόνου στους

ωκεανούς αναμένεται να συνεχιστεί, εκτός εάν μειωθούν σημαντικά οι εκπομπές αερίων του θερμοκηπίου και η χρήση λιπασμάτων (π.χ. Breitburg *et al.*, 2018).

Η τρέχουσα εκπομπή αερίων του θερμοκηπίου είναι πρωτοφανείς για τα τελευταία 66 εκατομμύρια χρόνια και ωθεί το κλιματικό σύστημα σε μια κατάσταση πρωτόγνωρη για την ανθρωπότητα (π.χ. IPCC, 2013 – Zeebe *et al.*, 2016). Για να εκτιμηθεί ο αντίκτυπος των διαταραχών του παγκόσμιου κύκλο του άνθρακα στο κλίμα και τη θαλάσσια βιογεωχημεία, μελετώνται εποχές από το γεωλογικό παρελθόν που υπέστησαν παρόμοιες αλλαγές (π.χ. Burke *et al.*, 2018). Αρκετές εποχές παρουσιάζουν ενδιαφέρον για την παρούσα διατριβή, κυρίως το Ολόκαινο Θερμοκρασιακό Μέγιστο (HTM), το Μεσαιωνικό Κλιματικό Βέλτιστο (MCA), το Παλαιόκαινο-Ηώκαινο Θερμοκρασιακό Μέγιστο (PETM) και το Κενομάνιο-Τουρώνιο Ωκεάνιο Ανοξικό Γεγονός 2 (OAE2).

Οι κυρίως μέθοδοι που χρησιμοποιούνται για τη μελέτη των παρελθόντων κλιματικών και ωκεάνιων αλλαγών είναι η χημική ανάλυση αρχείων ιζημάτων και η πραγματοποίηση προσομοιώσεων με ηλεκτρονικά βιογεωχημικά μοντέλα. Οι χημικές ιδιότητες των ορυκτών και τα απολιθωμένα υπολείμματα οργανισμών που διατηρούνται σε θαλάσσια ιζήματα μπορούν να χρησιμοποιηθούν για την ανακατασκευή των αλλαγών στο κλίμα και τη βιογεωχημεία των ωκεανών (proxy). Για παράδειγμα, τα απολιθωμένα υπολείμματα φυκών και διαφόρων μορίων που παράγουν μπορούν να χρησιμοποιηθούν ως proxy για αλλαγές της θερμοκρασίας και της αλατότητας της υδάτινης στήλης. Συγκεκριμένα χημικά στοιχεία και τα ισότοπά τους λειτουργούν ως proxy για τις αλλαγές στον κύκλο του άνθρακα και της εμφάνισης ή διάλυσης συνθηκών χαμηλού οξυγόνου και αποξυγονωμένων συνθηκών. Στη συνέχεια χρησιμοποιούνται ηλεκτρονικά μοντέλα για τη σύνθεση των πληροφοριών από τα αρχεία ιζημάτων σε μια συνολική εικόνα για την αναπαραγωγή της κατάστασης του αρχαίου κλίματος και ωκεανού.

2. ΠΕΡΙΛΗΨΗ

Στην παρούσα διατριβή, παρέχω μια ποιοτική και ποσοτική περιγραφή των κινητήριων δυνάμεων πίσω από την εξάντληση του θαλάσσιου οξυγόνου και των συνεπειών αυτής της αποξυγόνωσης για την ταφή του οργανικού άνθρακα. Τα κύρια θέματα που θα θιχτούν είναι τα αίτια της εξάντλησης του οξυγόνου σε τοπική (**2ᵒ Κεφάλαιο**) και παγκόσμια (**4ᵒ Κεφάλαιο**) κλίμακα, η επίδραση του σχηματισμού ορυκτών στην ταφή του φωσφόρου υπό αποξυγονωμένες συνθήκες (**3ᵒ Κεφάλαιο)** και η παγκόσμια επίδραση της αυξημένης απελευθέρωσης φωσφόρου από αποξυγονωμένα ιζήματα (**3ᵒ – 5ᵒ Κεφάλαιο**), καθώς και η επίδραση της ταφής του οργανικού άνθρακα που εξαρτάται από το οξυγόνο στον παγκόσμιο κύκλο του άνθρακα (**4ᵒ και 5ᵒ Κεφάλαιο**).

III

Στο **2ᵒ ΚΕΦΑΛΑΙΟ** διερευνάται η αποξυγόνωση της Βαλτικής Θάλασσας κατά τη διάρκεια δύο ξεχωριστών εποχών κλιματικής αλλαγής των τελευταίων 10.000 χρόνων: το HTM και το MCA. Το HTM έλαβε χώρα στο τέλος της τελευταίας παγετώδους περιόδου, όταν το λιώσιμο των παγετώνων προκάλεσε άνοδο της στάθμης της θάλασσας και μετέπειτα την εισροή αλμυρού νερού από τη Βόρεια Θάλασσα στη Βαλτική Θάλασσα, η οποία εκείνη την εποχή ήταν ακόμη λίμνη γλυκού νερού. Η έρευνά μου σχετικά με τη μορφολογία και τα είδη των απολιθωμένων υπολειμμάτων φυκιών, καθώς και των αλλαγών στις συγκεντρώσεις

ιχνοστοιχείων στα ιζήματα από το βαθύτερο τμήμα της Βαλτικής Θάλασσας υπόδειξε ότι η διαφορά πυκνότητας μεταξύ των αλμυρών και των γλυκών νερών προκάλεσε στρωμάτωση και εμπόδισε έτσι την παροχή οξυγόνου στη βαθιά λεκάνη. Η ανάκαμψη των συγκεντρώσεων του οξυγόνου στο τέλος του HTM και η εξάπλωση και υποχώρηση της αποξυγόνωσης κατά τη διάρκεια του MCA οφείλονται κυρίως στη στρωματοποίηση λόγω θερμοκρασίας και στη μεταβαλλόμενη παροχή θρεπτικών ουσιών. Σήμερα, οι συγκεντρώσεις οξυγόνου στη Βαλτική Θάλασσα καθορίζονται κυρίως από τη διαθεσιμότητα θρεπτικών ουσιών από λιπάσματα, αλλά τα αποτελέσματα της παρούσας μελέτης υπογραμμίζουν την πιθανή επίδραση της κλιματικής αλλαγής στην επέκταση των περιοχών με έλλειψη οξυγόνου στη Βαλτική και σε άλλες παράκτιες θάλασσες.

Το **3ο ΚΕΦΑΛΑΙΟ** εξετάζει τη μειωμένη, σχετικά με τον σύγχρονο ωκεανό, ταφή φωσφορικού ιόντος σε αρχαία θαλάσσια ιζήματα. Κατά τη διάρκεια περιόδων ευρείας αποξυγόνωσης όπως η OAE2, οι αξίες ενός proxy για την ταφή του φωσφόρου είναι περισσότερο από τετραπλάσιες των σημερινών, υποδεικνύοντας μειωμένη κατακράτηση φωσφόρου στον πυθμένα του ωκεανού. Η συνήθης εξήγηση αναφέρει ότι η στέρηση οξυγόνου και η παρουσία υδροθείου προκάλεσαν αυτή τη μεγάλη διαφορά. Ωστόσο, η εξήγηση αυτή είναι ανεπαρκής, διότι οι λεκάνες με έλλειψη οξυγόνου στον σύγχρονο ωκεανό περιλαμβάνουν ένα ευρύ φάσμα βιογεωχημικών χαρακτηριστικών, συμπεριλαμβανομένων πολύ υψηλών συγκεντρώσεων υδροθείου. Οι υπολογισμοί μας δείχνουν ότι ο σχηματισμός ανθρακικού φθοριοπατίτη, της κύριας μορφής μακροχρόνιας αποθήκευσης φωσγορικού ιόντος στα θαλάσσια ιζήματα, μειώνεται σημαντικά υπό υψηλές θερμοκρασίες, οξίνιση των ωκεανών και ανεπάρκεια ανθρακικού ασβεστίου. Τα παραπάνω είναι γνωρίσματα που χαρακτηρίζουν εποχές αποξυγόνωσης κατά τις οποίες η ταφή του φωσγορικού ιόντος ήταν μειωμένη. Έτσι δημιουργήθηκε ένα σύστημα στο οποίο η χερσαία προσφορά φωσγορικού ιόντος αυξήθηκε και δεν καλύφθηκε από την απόθεση στον πυθμένα του ωκεανού, καθιστώντας το φωσγορικό ιόν περισσότερο διαθέσιμο για τη φωτοσύνθεση των φυκών και προωθώντας τον ευτροφισμό. Η σύγχρονη κλιματική αλλαγή και η οξίνιση των ωκεανών θα μπορούσαν ενδεχομένως να συμβάλουν στην παγκόσμια μείωση του οξυγόνου μέσω ενός παρόμοιου μηχανισμού.

Το **4ο ΚΕΦΑΛΑΙΟ** μελετά την πρωτογενή παραγωγικότητα και αποξυγόνωση στον ωκεανό κατά τη διάρκεια του PETM, πώς αυτές μεταβάλλονταν στο χώρο και τον χρόνο, και τον αντίκτυπο αυτών για την ταφή του οργανικού άνθρακα. Το PETM ήταν μια περίοδος έντονης κλιματικής αλλαγής, πριν από περίπου 56 εκατομμύρια χρόνια, και θεωρείται ανάλογη της σύγχρονης υπερθέρμανσης του πλανήτη. Στο κεφάλαιο αυτό επιδεικνύεται, με τη χρήση νέων χημικών αναλύσεων ιζημάτων και τη σύνθεση δεδομένων, ότι οι παραγωγικές και αποξυγονοποιημένες συνθήκες ήταν ευρέως διαδεδομένες και εμφανίζονταν κυρίως κατά μήκος των ηπειρωτικών περιθωρίων και σε περιορισμένες λεκάνες. Στις ίδιες περιοχές απαντώνται ιζήματα πλούσια σε οργανικό άνθρακα. Συνδέοντας τα διαθέσιμα δεδομένα με δύο ηλεκτρονικά μοντέλα για των κύκλου του άνθρακα, το κεφάλαιο αυτό δείχνει ότι η δημιουργία οργανικού υλικού και η ταφή του αυξήθηκε κατά τρόπο που οδήγησε στην μείωση του CO_2 από την ατμόσφαιρα. Η επίδραση της ταφής στο ατμοσφαιρικό CO_2 και στο παγκόσμιο ισοζύγιο ισοτόπων του άνθρακα περιγράφει περαιτέρω τις πιθανές εκπομπές CO_2 ή/και μεθάνιου κατά τη διάρκεια του PETM.

Το **5ο ΚΕΦΑΛΑΙΟ** εξετάζει ένα από τα σημαντικότερα διαστήματα εξάντλησης οξυγόνου στη γεωλογική ιστορία. Η ΟΑΕ2 έλαβε χώρα πριν από περίπου 94 εκατομμύρια χρόνια, πιθανότατα λόγω της αυξημένης εκπομπής CO_2 από ηφαίστεια. Η αύξηση της θερμοκρασίας, η αλλαγμένη βροχόπτωση και η αποσάθρωση φωσφορικών πετρωμάτων προκάλεσαν την παρατηρηθείσα αποξυγώνοση και την απόθεση ιζημάτων με υψηλό περιεχόμενο οργανικού άνθρακα. Σε αυτή το κεφάλαιο, παρουσιάζω το πρώτο ποσοτικό σενάριο για τις ηφαιστειακές εκπομπές CO_2 και της ταφής του οργανικού άνθρακα κατά τη διάρκεια του ΟΑΕ2. Τα αποτελέσματα του ηλεκτρονικού μοντέλου που χρησιμοποιήθηκε δείχνουν ότι η ηφαιστειότητα ήταν μεταβλητή κατά τη διάρκεια του ΟΑΕ2 και ότι η επίδραση της ταφής του οργανικού άνθρακα στο ατμοσφαιρικό CO_2 και σε άλλες συνιστώσες του κύκλου του άνθρακα εξαρτιόταν σε μεγάλο βαθμό από τον ρυθμό εκπομπής CO_2.

III

I don't know half of you half as well as I should like;
and I like less than half of you half as well as you deserve.
J.R.R. Tolkien –The Fellowship of the Ring
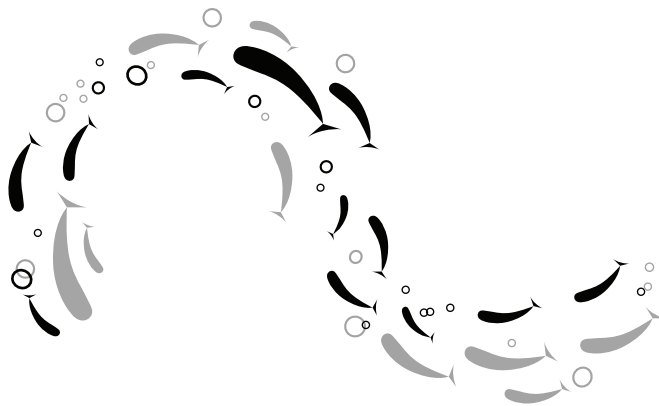
IV

Appendix IV: Acknowledgments

One does not simply finish a PhD on one's own. So, let me thank everyone who made mine possible! And I apologize for the random choice of languages en the many exclamations marks, I write as I think.

First of all, I must thank my two amazing promotors, Caroline Slomp and Appy Sluijs. I'm not sure I would have managed to finish this PhD the way I did without your enthusiasm and patience. You have supported me every step of the way with scientific discussions, encouragement and also acceptance of my need to take time off now and again. Thank you, for everything!

Caroline, you have been my mentor, supervisor and role model. From the beginning of my MSc thesis, you have helped me believe in myself and always done your absolute best to give me the chances I need. From the broad topic of my MSc thesis to the many topics of my PhD, you gave me the opportunity to work on almost anything that interested me and you were always looking for ways to expand my experience, looking also to my post-PhD career. But more than anything you made my PhD an exciting and challenging experience, while always keeping an eye out for my mental wellbeing. A good supervisor can make or break a PhD, and you were the best I could have wished for!

Appy, at the start of my bachelors I wanted to work in terrestrial ecology, but one course on marine sciences was all it took to steer my interest to million-year old ocean sediments. Your enthusiasm during MS1 derailed my plans and turned me into a biogeologist instead. Your support also got me through a lot, going all the way back to the struggles of writing a chapter for a popular science book. During my PhD, you made me feel like I could do anything I set my mind to and took the edge off things that were not going the way I wanted. More than any scientific input and guidance, these two aspects of your supervision is what I'm most grateful for!

I've also been lucky that two very important people agreed to be my paranymfen:

Sietske, ik ken je al bijna zo lang als ik in Nederland woon. Toen ik hierheen verhuisde, was ik bang dat ik heel wat weken alleen op de universiteit zou ronddwalen. Aan die angst maakte jij snel een einde! Sindsdien ben je de beste vriendin waar ik ooit op had kunnen hopen, met je grote glimlach en immense enthousiasme. Ik hoop dat dit nog lang zo zal blijven, of ik in het buitenland woon of in Nederland! En ik zal je zeker blijven spammen met Harry Potter en Buttercup Cumbersnatch memes!

Niels, zonder jouw presentatie over OAE2, in mijn tweede bachelorsjaar, had mijn 'wetenschappelijke' carrière er waarschijnlijk anders uit gezien. Na al die jaren (7+) hulp, advies en inspiratie, is het denk ik niet gek dat ik jou als mijn derde, onofficiële promotor zie. En daar komen de discussies en lol tijdens lunch- en koffiepauzes, en natuurlijk conferenties, bij. Om de diners in Kiel niet te vergeten. Ik ga dit allemaal heel erg missen! Kom vooral langs in het buitenland om samen OAE2 secties te bezoeken!

This is where I thank all the other people who made the four chapters you just read (*of course* you did) scientifically possible. Nikki Dijkstra, for putting so much time and effort into

supervising me and my labwork. Mariette Wolthers, for all your help and valuable lessons in mineral chemistry. Heiko Pälike and Richard Zeebe, for hosting me in Bremen and Hawaiʻi, helping me out with my various modelling and coding exercises and thinking along with me. Francesca Sangiorgi and Bas van de Schootbrugge, for supervising me and guiding me through the murky depths of palynology. Thorsten Bauersachs, Mathilde Hagens and Ulrich Kotthoff, for making my first first-author paper possible. And also a big thanks to everyone at the lab, for guiding me through protocols and performing many measurements: Natasja, Arnold, Helen, Coen, Ton, Thom, Giovanni and anyone else that I may have forgotten.

There have been many people in the Marine Geochemistry and MPP groups that made my PhD a good time, through fun and, occasionally, commiseration. First off, my VMA office buddies, Wytze and Martijn. Thank you for making the office such a comfortable place to be, for putting up with my yawning and for giving me many reasons to laugh and not talk about science during lunch and conferences. Then there's the ever-changing geochemistry lunch group: Olga, Mădălina, Matthias, Olivier, Anne, Nicole, Shaun, Mareike, Melanie, Marie, Signe, Lilia, Bayan and all the other PhD's, postdocs, staff and students that have joined over the years. And when I wasn't spending time with the geochemistry people, I was lucky to be able to hang with the MPP group: Carolien, Joost, Frida, Robin, Lena, Suning, Peter, Martin, Tjerk and all the others. I must also not forget the people from other groups: Pieter, Fabian, Ilja and Γιάννης Ζ.. I also want to thank Annuska, Marjolein, Jan-Willem, Ton Markus and Margot Stoete for taking care of so many practical things during the past five yars. And lastly, I also thank all the NESSC PIs, postdocs and PhDs.

Er zijn een aantal fantastische vriendinnen die ik moet bedanken. Dus, als je in het VK zit en bij het MPP gedeelte denkt: huh, hier mist iemand! Geen angst, Margot, ik ben je niet vergeten! Zodra we weer kunnen reizen, ren/zwem/vlieg ik jouw kant op voor een epische hike en een gezonde portie *staying wild*. Cindy, bedankt voor alle veel te lange koffiepauzes die toch niet lang genoeg waren, voor je geduld, humor en toch ook wel wijsheid, en voor alle gezelligheid in binnen- en buitenland! En natuurlijk voor de filmavonden en japanse diners met Roos. Roos, dank je dat je ervoor gezorgd hebt dat ik zelfs op regenachtige avonden toch nog richting Olympos ging, voor alle katvideos, super gezellige verjaardagsfeestjes en alle andere keren dat we samen op de bank hingen of een stuk gingen lopen! Wineke, zonder jou was ik allang verdwaald in Tokyo en zwierf ik daar waarschijnlijk nogsteeds rond. Ik heb zoveel genoten van onze reis em het beste deel was dat jij en ik zo goed klikte, en dat we nu nogsteeds close zijn (want ja, met wie moet ik anders een bepaalde obsessie delen, *wink wink*). Joyce, ik ben nog altijd zó blij dat jij mijn huisgenoot geweest bent en dat het niet daar bij gebleven is! En Judith, alle pijn en blauwe plekken waren het waard, al was het alleen maar omdat ik jou ontmoet heb! Ik hoop (verwacht) dat jullie allemaal langs gaan komen, als ik naar het buitenland vertrek!

There are many places where you can make friends, some stranger than others. Don't believe people when they tell you you can't make friends through social media, because I did just that! Lauren, it amazes me every time we talk just how similar we are and I can't believe we still haven't met in real life! I cannot imagine what it was like not having you to talk to. Please, stay as awesome as you are forever. And a big thanks to anyone who ever offered me support, advice or a good laugh on social media! Travelling abroad is another way to make friends,

IV

friends who can really turn your stay into something unforgetable. That's what Fiona, Janett, Laurel and Becca did for me. Hope to see you all again soon, here, there, anywhere! And then there's USSP, a summer school for budding paleoceanographers and paleoclimatologists. I thank all the lecturers and attendees for the successful summer school of 2017, but in particular: Chloe, Simone, Lisa, Amy, Ophelie and Ruth (and others that I thanked above).

I think it's customary to end with family, which is what I'll do. Big, no, *huge* thanks to all my uncles, aunts and cousins for all the love and support! Ik wil mijn oma, Auke, Annet, Hans, Evalyn en Judith in het bijzonder bedanken, voor al jullie interesse, advies en enthousiasme door de jaren heen. Bedankt! Ευχαριστώ!

Μπαμπά, σ'ευχαριστώ που με στηρίζεις, έστω και από μακριά, μου λες πως όλα θα πάνε καλά και που θέλεις πάντα το καλύτερο για μένα.

Then there's my brother, Γιώργος. Don't think I have anything to thank you for, so... moving on!

Πλάκα κάνω! Without you, I'd have noone to complain to daily, ask for advice, spam with memes and screenshots of the latest anime I'm watching, and watch crappy action movies with. But also. No.

Last, but really first, *mom*. Zonder jou was ik never nooit zo ver gekomen. Je bent mijn beste vriendin, en de beste en liefste moeder in de wereld! Ik heb nog veel meer te zeggen maar daar heb geen thesis dankwoord voor nodig!!!!

IV

CURRICULUM VITAE

Nina was born on the 3rd of June 1993 in Rethymnon, on the Greek island of Crete. She completed her primary and secondary education in Rethymnon, before moving to the Netherlands to attend university. She obtained her BSc degree in Biology in 2014 and her MSc degree in Environmental Biology (with distinction) in 2016, both from Utrecht University. Her MSc thesis focussed on reconstructing redox conditions and causes of deoxygenation for the Holocene Baltic Sea and a german site during the Toarcian Oceanic Anoxic Event, using palynological and trace elemental tools. During the second year of her MSc, she spend six months abroad for a research internship at MARUM in Bremen, with prof. Heiko Paelike. She began her PhD in October 2016 and completed it in March 2021. In 2019, she spend three months at the University of Manoa, in the USA, learning how to use the carbon-cycle box model LOSCAR, with guidance from prof. Richard E. Zeebe, and working on her final thesis chapter. Her PhD thesis was approved on the 27th of April, 2021 and will be defended on the 24th of June, 2021.
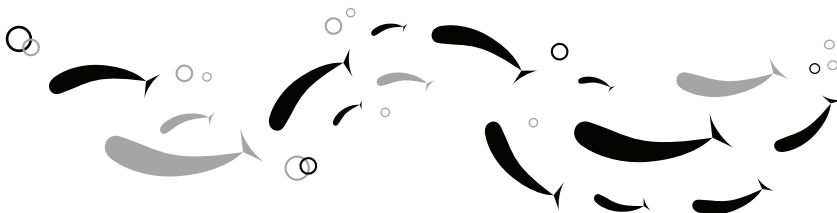
PEER-REVIEWED PUBLICATIONS

van Helmond, N. A., Sluijs, A., **Papadomanolaki, N. M.**, Plint, A. G., Gröcke, D. R., Pearce, M. A., ... & Brinkhuis, H. (2016). Equatorward phytoplankton migration during a cold spell within the Late Cretaceous super-greenhouse. *Biogeosciences*, 13(9), 2859-2872.

Papadomanolaki, N. M., Dijkstra, N., Van Helmond, N. A., Hagens, M., Bauersachs, T., Kotthoff, U., ... & Slomp, C. P. (2018). Controls on the onset and termination of past hypoxia in the Baltic Sea. *Palaeogeography, Palaeoclimatology, Palaeoecology*, 490, 347-354.

Ruvalcaba Baroni, I., Pohl, A., van Helmond, N. A., **Papadomanolaki, N. M.**, Coe, A. L., Cohen, A. S., ... & Slomp, C. P. (2018). Ocean circulation in the Toarcian (Early Jurassic): A key control on deoxygenation and carbon burial on the European shelf. *Paleoceanography and Paleoclimatology*, 33(9), 994-1012.

Papadomanolaki, N. M., Sluijs, A. & Slomp, C. P. (2021). Eutrophication and deoxygenation forcing of marginal marine organic carbon burial during the PETM. *In revision for* Paleoceanography and Paleoclimatology.

Papadomanolaki, N. M., van Helmond, N. A. G. M., Pälike, H., Sluijs, A. & Slomp, C. P. (2021). Quantifying volcanism and organic carbon burial across Oceanic Anoxic Event 2. *In review for* Geology.